East European Journal of Physics. 1. 161–169 (2026)
DOI: 10.26565/2312-4334-2026-1-15 ISSN 2312-4334

INVESTIGATION OF THE ^{14}N(γ,2α)^{6}LI REACTION

Serhii Afanasiev[1], **Inna Afanasieva**[1*,2], **Kateryna Chkuaseli**[2]
[1]*National Science Center "Kharkov Institute of Physics and Technology" 1, Akademicheskaya St., 61108, Kharkiv, Ukraine*
[2]*V.N. Karazin Kharkiv National University, 4, Svoboda Sq., Kharkiv, 61022, Ukraine*
[*]*Corresponding Author e-mail: afaninna@i.ua*
Received December 5, 2025; revised February 2, 2026; accepted February 22, 2026

A digital measurement technique of points coordinates along the tracks was developed for the stereo frame photonuclear reaction data bank created in KIPT. The main procedure is the analysis of pixel intensity in the area of tracks. The ^{14}N(γ,2α)^{6}Li reaction was chosen as a test reaction for measurement. A kinematic scheme for calculating the physical parameters of the reaction was created assuming a two-particle decay mode with the formation of an intermediate excited state. Experimental data and kinematic calculation were compared. Events corresponding to the partial channel of the ^{14}N(γ,^{6}Li)^{8}Be$_0$ reaction with the subsequent two-particle decay ^{8}Be $\rightarrow$ α +α were identified and the partial cross section of this channel was measured. The energy and angular distributions of particles at each decay stage were analyzed.

Keywords: *Photonuclear reactions; Diffusion chamber; Digital measurement technique; Ground state ^{8}Be*

PACS: 25.20.-x

1. INTRODUCTION

Photoreactions on light nuclei are of particular interest to nuclear physics. They are driven by the well-known electromagnetic interaction and therefore their study provides important information about the fundamental properties of the nuclear forces. Photonuclear reactions are also important in nuclear fusion and astrophysical processes [1, 2]. It has been accepted [3, 4] that at quantum energies E_γ up to the meson threshold, nucleus absorption mainly occurs through two different reaction mechanisms: giant dipole resonance (at E_γ < 40 MeV) and quasi-deuteron photoabsorption (at E_γ > 40 MeV, where the photon wavelength is usually smaller than the nucleus size but close to the deuteron size).

The (γ,N) and (γ,NN) reactions were qualitatively explained in the framework of various modifications of these interaction mechanisms. At the same time, in various nuclear reactions, not only protons and neutrons but also other particles such as deuterons, tritons, α-particles, and other light and heavy nuclei, different in composition and properties from the initial nucleus, are observed with significant probability. This led to the development of the model of the interaction of constituent nuclear particles (nucleon associations, cluster model) [5, 6]. The use of this theory made it possible to describe such effects that could not be explained by other methods. The simple cluster model assumes that the atomic nucleus consists of two structureless fragments whose properties coincide or are close to the properties of the corresponding nuclei in the free state. The two-cluster model assumes the presence of only two separate fragments – clusters, between which all nucleons of the nucleus are redistributed. The photon does not enter into strong nuclear interactions with the target nucleus, but only electromagnetic interactions with the cluster structure, the operators of which are exactly known. Therefore, it is possible to take into account only nuclear interactions of related clusters, which greatly simplifies the consideration in comparison with the three-body problem, when it is necessary to include the nuclear interaction of the incoming particle along with intercluster forces.

The ^{14}N nucleus is of interest as an intermediate between ^{12}C and ^{16}O nuclei, which in the cluster model are considered coupled systems of 3α and 4α particles. Previously, we have studied in detail the reactions of ^{12}C(γ,3α) and ^{16}O(γ,4α) [7]. In the present work, we present information on the ^{14}N(γ,2α)^{6}Li reaction, which will provide new information on the evolution of the cluster structure, which becomes more complicated beyond α-clustering. The reaction ^{14}N(γ,2α)^{6}Li has not been studied before, but nuclear reactions with such final particles in the literature are (^{3}He + ^{11}B [8], and d + ^{12}C [9]).

2. EXPERIMENTAL TECHNIQUE

The experiment was performed using a track 4π-detector (the diffusion chamber placed in a magnetic field with a strength of 1.5 T.) [10]. The chamber was exposed to a beam of bremsstrahlung photons with a maximum energy of 150 MeV emitted from a linear electron accelerator (LUE-300). The soft component of the bremsstrahlung spectrum was removed by a beryllium filter 2.5 radiation-length units in thickness. The spectral distribution of photons was assumed to be of a Schiff form corrected for its nonuniform attenuation by the filter.

To reduce the target density, the chamber was filled with a mixture of nitrogen (15%) and helium. This experimental method makes it possible to obtain, for slow final nuclei, track lengths acceptable for measurements and sufficiently high

Cite as: S. Afanasiev, I. Afanasieva, K. Chkuaseli, East Eur. J. Phys. 1, 161 (2026), https://doi.org/10.26565/2312-4334-2026-1-15

sharpness of their image at pressures close to atmospheric pressure (1.5 atmospheres). The target–detector combination made it possible to register the products of a low-energy reaction and analyze it practically from its threshold.

The error in measuring the particle momentum depends on its magnitude and track length, and ranges from 3 to 10%. The energy of the stopped particles was determined from the range-energy relationship. The range in the mixture was obtained taking into account the ion charge exchange with the medium, using tabulated data for several target.

2.1. Digital Measurement of Point Coordinates Along Tracks

In the experiment, during the sessions of irradiation of the camera, the working area of the camera was photographed by two 2-lens cameras. A large amount of information on multiparticle photoreactions was collected and an experimental complex with a digital data bank of stereo frames and a set of graphic programs that allow to restore events and perform physical analysis of the obtained data was created [11]. Photo frames have a structured name with the maximum necessary information about the experiment session.

In [11], a method of digital semi-automatic measurement of the coordinates of points along the track was proposed. This allowed us to compare the digital method and the method using special devices. Also, the procedure of correct obtaining of physical information by digital measurement was created.

In this work, a fully automatic method of obtaining the kinematic parameters of particles is proposed, which reduces the contribution of the meter error and significantly speeds up the image processing. For this purpose, a specialized graphical application was created using the Python programming language on the platform of the Tkinter graphics library with the use of additional modules - PIL, NumPy, SciPY, and Pandas. The PIL module allows you to access a two-dimensional array of numbers, which is a function of the image intensity distribution on the plane. The intensity range is from 0 (black) to 255 (white). The coordinate system starts in the upper left corner. The X coordinate increases from left to right, and the Y coordinate increases from top to bottom. Next, we will present algorithms for the mathematical processing of digital arrays (NumPy and SciPY) with further visualization of the results.

Fig. 1 shows two identical fragments of a photo frame with a three-beam event. The white segments emanating from the same vertex correspond to a three-beam event. It should be noted that there are significant background emissions (light objects in the frame) that can cause distortions during image analysis. They arise due to the complex gas structure of the diffusion chamber. However, such background emissions are not systematic and the total intensity along the tracks should be higher.

To implement an automatic method for obtaining kinematic parameters of reaction particles, an algorithm is proposed in which the pixel intensity is scanned along a circular trajectory of a specified radius and the average intensity value is calculated at each scanning step

$$I_\theta = (\sum_{i=1}^{n} I_i)/n, \tag{1}$$

where n is the number of pixels (length radius), θ - scaning angle, and I_i - is the intensity of the i-th pixel.

In Fig. 1 above, for a visual example, dark segments of 50 pixels in length represent the procedure of scanning in a circle. The scaning was performed along the clockwise trajectory with a step of 15 degrees. In the real study, the scanning step was 1º. For the convenience of data analysis and searching for extremes, we introduced the relative intensity $I^{extr} = I_\theta / I^{aver}$, where I^{aver} - is the average intensity of the circle.

In Fig. 2, the histogram shows the dependence of I^{extr} on the scanning angle in the range from 0 to 360 degrees. There is an irregular structure with several maxima corresponding to the deviation from the background in the scanning area. To automatically determine the position of these maxima, we used the *groupby()* function from the Pandas module, which performs grouping by one or more parameters and determines the inflection points (extremes). The positions of the calculated extremes are shown as solid points. The three maxima in the positive region correspond to the three tracks in Fig. 1, and the position of the maximum gives the value of the departure angle of the corresponding track.

Thus, knowing the top of the event, the angles of departure of the tracks, and the average intensity of the I^{aver} in the selected direction, it is possible to calculate the coordinates of points along each track. For this purpose, the procedure of sequential advancement of the scanning segment along the corresponding track was performed. The pixels in the scanning segment were checked for intensity. A sharp change in intensity compared to I^{aver} made it possible to determine the boundary of the track. If all pixels corresponded to the track, the procedure was performed to move the start of the scan to the last point of the scanning segment, and then the procedure of scanning the intensity of pixels along a circular trajectory was performed again to determine the angle of departure of the track and further advancement along the track. This sequence of actions was performed in a loop until the track boundary was determined. This algorithm allows us to take into account the curvature of the track and at each stage of moving along the track it is possible to refine the departure angle.

In Fig. 1 on the bottom image shows the result of the automatic digitization of all three event tracks. The points describe the trajectory of the tracks well. Subsequently, we performed the functions of fitting the points with a second-order linear curve and refining the coordinates of the middle of the track. After reconstructing the geometry of the event, a

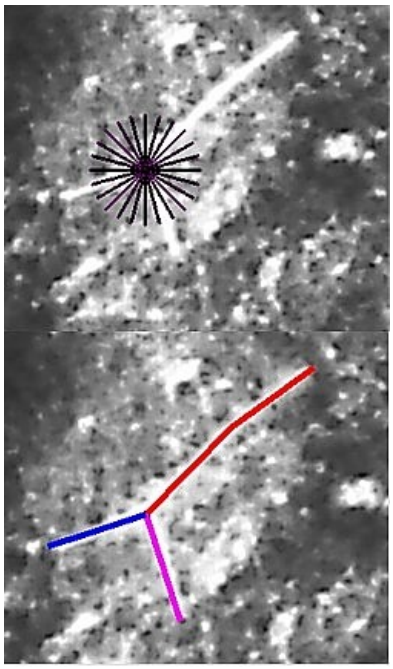

Figure 1. Digital image processing.

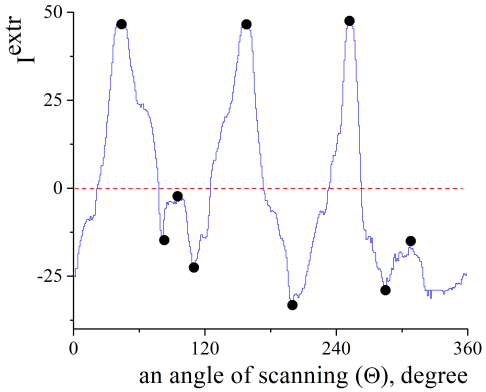

Figure 2. Dependence of pixel intensity on scanning angle.

numerical matrix of this event is created, in which for each track there are guide cosines l, m, n; the radius of curvature and track length.

2.2. $^{14}N(\gamma,2\alpha)^{6}Li$ Reaction Events

For the measurement and processing of the $^{14}N(\gamma,2\alpha)^{6}Li$ reaction, we selected 3-ray stars close to compatibility, two of whose rays belong to two-charged particles and one to a three-charged particle. The ionization density, its change along the track at a known momentum, makes it possible to determine the charge of the particle. This identification was performed visually at the stage of selecting events for measurements. The particle tracks usually ended in the working area of the chamber, so the experimental data of their energy losses (the range-energy relationship) were used to determine the kinetic energy of the particles [12].

The methodology for selecting events is traditional for this method of experiment and has been previously described [13, 14].

Events corresponding to the $^{14}N(\gamma,2\alpha)^{6}Li$ reaction were selected after measurements based on the momentum balance. Boundary conditions were imposed on the quantities $\sum P_x^i$, $\sum P_y^i$, and $\sum P_z^i$, where $P^i_{x(y,z)}$ - are the components of the three-dimensional momentum of the i-th final particle. The projection of the imbalance onto the OX axis, along which the γ-quanta is directed, is equal to the sum of the projections of the momentum onto this axis minus the energy

of the γ-quanta, which was defined as the sum of the kinetic energies of the final particles and the reaction threshold. A clearly pronounced peak in the distributions for $\sum P_{x(y,z)}$ in region 0 corresponds to the events of the examined reaction. The laws of conservation of energy and momentum make it possible to refine the measurement results of one of the tracks, usually the worst measured one. The measurement error of the momentum of charged particles depends on its size and track length and ranges from 3 to 10%.

3. DATA PROCESSING

For the $^{14}N(\gamma,2\alpha)^{6}Li$ reaction events, the excitation energy of a pair of particles was determined as

$$E_x(\alpha\alpha) = M^{eff} - (2m_\alpha) \tag{2}$$

where M^{eff} is effective mass equal to the total energy of a pair of α-particles in their resting state, and m_α is the mass of the α-particle.

In Fig. 3, the histogram shows the distribution of $E_x(\alpha\alpha)$ with a step of 0.25 MeV. The distribution has a structure: a narrow near-threshold maximum and a concentration of events in the region of 3 MeV. The area of the first maximum is 15% of the total area. There are three particles in the final state of the reaction, so three combinations of particle-pair systems are possible. This means that the structure observed in Fig. 3, is formed either by the decay of the intermediate excited state of the ^{8}Be nucleus or is simulated by one of the background pairs during the decay of the intermediate excited state of the ^{10}B nucleus.

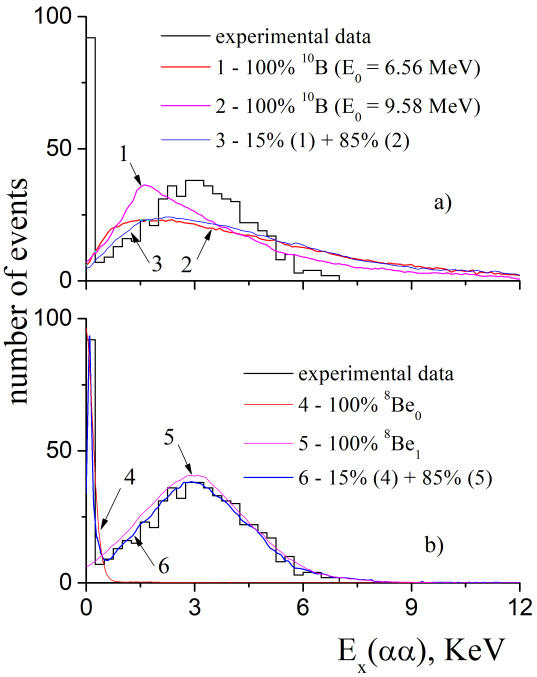

Figure 3. Distribution of events by excitation energy of 2α-particles. The curves are explained in the text

3.1. Kinematic Calculation

Experimental studies of nuclear reactions on light nuclei are usually accompanied by a mathematical model of the process under study [15-16].

To analyze the experimental data and compare it with the kinematic calculation, a graphical application in the Python programming language was created for this work. The matplotlib library is used for data visualization.

The kinematic model of the $^{14}N(\gamma,2\alpha)^{6}Li$ reaction was developed under the assumption of two-particle decay with the formation of an intermediate excited state. In the system of the center of mass (s.c.m.) of a two-particle reaction, the kinematics is determined by the fact that, regardless of the specific type of interaction, the reaction products scatter at an angle of 180° and have equal modulus momentum, and their energies in the same system depend only on the masses of the particles and the total energy of the system.

For the reaction of $^{14}N(\gamma,2\alpha)^{6}Li$, decay through two channels is possible:

$\gamma + {}^{14}N \rightarrow \alpha_1 + {}^{10}B^* \rightarrow \alpha_1 + \alpha_2 + {}^6Li$ (I)

and

$\gamma + {}^{14}N \rightarrow {}^6Li + {}^8Be^* \rightarrow \alpha_1 + \alpha_2 + {}^6Li$ (II)

The mathematical calculation is based on the literature data on the parameters of the levels of ^{10}B and ^8Be nuclei [17] and the corresponding assumptions about the angular distributions in the system of the reaction center of the particle that first left the ^{14}N nucleus and the particles in the intermediate state resting state. Each decay mode is reduced to three two-particle systems:

- $(\gamma + {}^{14}N)$ – the initial,
- $(\alpha + {}^{10}B^*)$ or $({}^6Li + {}^8Be^*)$ – the intermediate,
- $({}^6Li + \alpha)$ or $(\alpha + \alpha)$ – the final.

To generate random values, a set of functions of the standard random library of the Python programming language was used. Several excited states of ^{10}B and ^8Be nuclei can contribute to the reaction. A scheme was created that allows you to select both the relative contribution for each channel (1) or (2) and the contribution of a separate level in each channel. To do this, we used the random.randint(0,100) function, which creates random, uncorrelated numbers evenly distributed in the range from 0 to 100. For the initial system, the numerical function of the distribution of the number of events on the energy of quanta $N(E_\gamma)$ was taken from a real experiment, and random values of E_γ were generated by the random.choice() function. The excitation curves $f(E_x)$ of the ^{10}B and ^8Be states of the nuclei were taken as Gaussian functions with a maximum position E_0 and half-width at half-height (σ) from a compilation of spectroscopic data [17]. Random values were generated by the function random.gauss(E_0,σ).

In the non-relativistic approximation, in the case of a two-particle channel, the law of conservation of energy is $E_\gamma = T_{P1} + T_{P2} + E_x + Q$, where T is the kinetic energy of particles P_1 and P_2 ($P_1 = \alpha_1$, $P_2 = {}^{10}B$ or $P_1 = {}^6Li$, $P_2 = {}^8Be$), E_x is the excitation energy of the intermediate particle ($E_x({}^{10}B)$ in the case of channel (I) or $E_x({}^8Be)$ for channel (II)), and Q is the energy threshold of the corresponding channel.

Using a two-particle channel and an unambiguous connection between the particles, we obtain:

$$T_{P1} = \frac{M_{P1}}{M_{P1} + M_{P2}}(E_\gamma - Q - E_x) \tag{3}$$

After the procedures for generating E_γ and E_x, T_{P1} and, accordingly, the particle momentum P_{P1} was determined.

The distributions over the polar angle θ for particle P_1 were taken in form $f(\theta)=c_1 sin^2\theta + c_2 sin^2\theta cos\theta + c_3 sin^2\theta cos^2\theta + c_4$, where c_{1-4} - are coefficients containing information about the reaction mechanism and wave functions of the nuclei. Parameters c_{1-4} were determined from the quantum values of the intermediate excited nucleus [18]. The distribution in the azimuthal angle ϕ is isotropic and was generated by multiplying the random number random.randint(0,1) by 2π.

The longitudinal and transverse projections of the particle P_1's momentum were determined, based on the generated values of the polar (θ) and azimuthal (ϕ) angles. The values of the projections and the total momentum of nucleus P_2 were calculated from the two-particle process.

A similar procedure was carried out for the final system, provided that the energy of the system is the excitation energy of the particle P_2. The kinematic parameters of the particles were transferred from the s.c.m. reaction to the laboratory system. The laws of conservation of energy and momentum for the kinematic parameters of the particles were checked. An event was considered formed if it satisfied the conservation laws.

3.2. Decay Channel Identification

For example, let us compare the kinematic calculation with the experiment (Fig. 3). Using the kinematic model, we constructed several distributions of events according to $E_x(\alpha\alpha)$ under the assumption of each decay channel - (I) or (II).

In Fig. 3a, three curves are presented in the framework of decay through a channel (I): curve 1 - with 100% production of the narrow ^{10}B nucleus level (E_0 = 6.56 MeV, σ = 0.025 MeV); curve 2 - with 100% formation of the broad ^{10}B nucleus level (E_0 = 9.58 MeV, σ = 0.257 MeV); curve 3 - with 15% of the narrow ^{10}B nucleus level and 85% of the broad ^{10}B nucleus level formation. Level parameters are taken from a compilation of spectroscopic data [17]. The dependence of 15% and 85% is taken from the ratio of the areas of the maxima of the distribution of the number of events for $E_x(\alpha\alpha)$ in the experiment (Fig. 3, histogram). The calculated curves were normalized to the experimental area distribution. The curves do not fully describe the near-threshold maximum at $E_x(\alpha\alpha) < 0.25$ MeV. In addition, they give only one maximum, which has almost the same position (at ~ 1.5 MeV) with different widths. It was checked that any combinations of the relative contributions of curves 1 and 2 also do not describe the experimental distribution.

Two levels of ^8Be nucleus were chosen for a channel (II): the ground state (GS) with E_0 = 0.092 MeV, σ = 0.025 MeV, and 1^{st} excited state with E_0 = 3.04 MeV, σ = 0.75 MeV. Fig. 3b shows three curves corresponding to the following ratios: curve 4 - with 100% GS; curve 5 - with 100% of the 1^{st} level of the ^8Be nucleus; curve 6 - with 15% GS and 85% of the 1^{st} level of the ^8Be nucleus. Curves 4 and 5 are consistent with the experiment when describing the first and second maxima, respectively. And curve 6 satisfactorily describes the total experimental distribution. Thus, it can be concluded that in the $^{14}N(\gamma,2\alpha)^6Li$ reaction, decay occurs mainly through the formation of an intermediate excited ^8Be nucleus.

4. ^{8}BE GROUND STATE FORMATION CHANNEL

The maximum up to 0.25 MeV (Fig. 3) is shown in Fig. 4b as data points with a 20 keV step. The errors are statistical. A fit was performed using a Gaussian distribution (solid curve) with a peak position E_0 = 0.096 ± 0.005 MeV and full width at half maximum σ = 0.064 ± 0.01 MeV. From spectrometric measurements [17], it is known that the parameters of the ground state (GS) of the ^{8}Be nucleus: E_0 = 0.092 MeV, Γ = 5.57 eV, quantum numbers - $J^\pi = 0^+$.

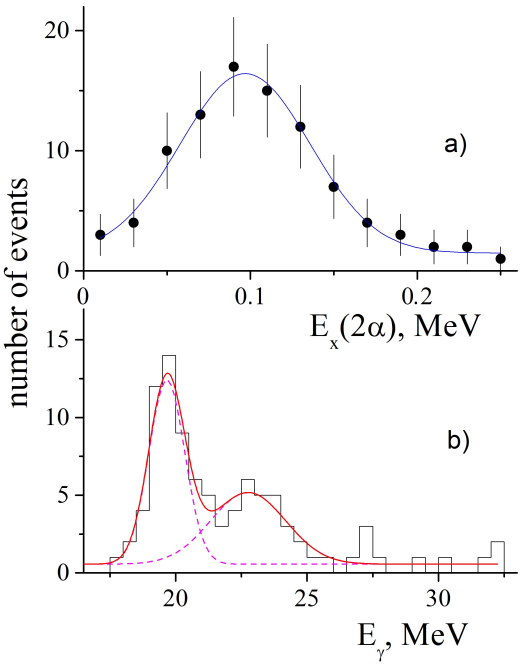

Figure 4. a) ground state ^{8}Be nucleus, b) partial cross-section of the channel for the formation of the ground state of the ^{8}Be nucleus in the ^{14}N(γ,2α)^{6}Li reaction.

The positions of the maxima (experimental and tabular) coincide within the error. Therefore, the concentration of events in the region of 0.1 MeV can be explained by the formation of the GS of the ^{8}Be nucleus. Due to insufficient energy resolution and low statistical power, the task of specifying the GS parameters was not set in this experiment. The width observed in this experiment is instrumental. Events (N^{GS}), in which a pair of α-particles corresponds to the formation of the GS of the ^{8}Be, nucleus, are reliably distinguished. The relative yield of this partial channel is – η=14.98% (η=N^{GS}/N, where N – is the total number of reaction events). The histogram in Fig. 4b presents the partial cross-section for the formation channel of the ^{8}Be nucleus GS in the ^{14}N(γ,^{6}Li)^{8}Be$_0$ reaction with a 0.5 MeV step for E_γ. A structure is observed in the distribution. The solid line shows the fit of the cross-section with a combination of two Gaussian functions (dashed lines), which resulted in the determination of the energy positions of the maxima and their widths - $E_\gamma{}^1$ = 19.66 ± 0.25 MeV, Γ^1 = 1.25 ± 0.29 MeV and $E_\gamma{}^2$ = 22.75 ± 0.42 MeV, Γ^2 = 2.79 ± 0.51 MeV.

Sequential two-particle decay allows us to determine the energy and angular distributions at each stage of decay.

In Fig. 5a, solid circles are used to exhibit the dependence of the number of events on the escape angle of the GS of ^{8}Be nucleus, θ(^{8}Be), in the center of the mass coordinate frame for the reaction in whole. After, the circles are drawn in the middle of the histogram steps, and vertical bars mark statistical errors. The figure demonstrates that the GS of ^{8}Be nucleus yield is symmetric about 90° and looks similar to $sin^2\theta cos^2\theta$. We performed the Legendre polynomial fit:

$$f(\theta) = a \cdot f_1 + b \cdot f_2 + c \cdot f_3 + d \cdot f_4 \tag{4}$$

where a, b, c, d – are coefficients containing information about the reaction mechanism and wave functions of the nuclei, and, $f_1 = sin^2\theta$, $f_2 = sin^2\theta cos\theta$, $f_3 = sin^2\theta cos^2\theta$, f_4 =1. In the figure, the solid curve represents the function f(θ) with a = 3.84 ± 0.87, b = 0.23 ± 1.98, c = 39.29 ± 4.35, d = 0.46 ± 0.55. For the parameters b and d, the values and errors of their measurements are close and their contribution to the fit is insignificant. The main contribution is given by the parameter c. The data obtained allows us to estimate the multipole amplitudes of the photoprocess in the future, since for this two-particle process we know the spin-parity of the particles - 1^+ for ^{6}Li and 0^+ for ^{8}Be.

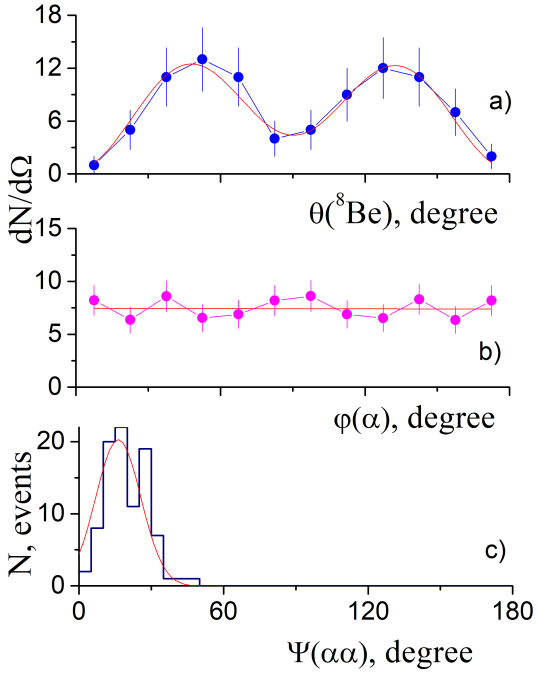

Figure 5. a) event distribution over the escape angle of the GS of the ^{8}Be nucleus, b) angular distributions of α-particles in the system of the center of mass of the ^{8}Be nucleus, c) dependence of the angle of separation of two α-particles.

In Fig. 5b, the solid circles represent the angular distributions of α-particles in the system of the center of mass of the ^{8}Be nucleus. The polar angle ($\phi(\alpha)$) is reckoned from the direction of the ^{8}Be nucleus motion. The angular distributions are isotropic (solid line in Fig. 3b is a fit with a linear function with a slope of -0.004 ± 0.012). This means that the orbital momentum l=0. It follows that the quantum numbers $J^{\pi} = 0^{+}$, is in the GS of ^{8}Be nucleus.

In Fig. 5c, the histogram shows the distribution of the number of events as a function of the angle of departure (ψ) of the α-particle pair. Fitting with the Gaussian function gave the values of the maximum and width at the half-height - $\psi_0 = 16.28^{\circ} \pm 0.71^{\circ}$ and $\Gamma(\psi) = 18.71^{\circ} \pm 1.52^{\circ}$.

The relative energies of α-particles were determined as the ratio:

$$\epsilon_i = T_i/T_0 \tag{5}$$

where i – is the particle identifier.

To test the possible mechanisms of interaction of the γ-quantum with the nucleus, the particles forming in the GS of ^{8}Be nucleus were sorted by energy for each event as $T_{\alpha}^{max} > T_{\alpha}^{min}$.

Fig. 6a demonstrates the distribution of the number of events over the relative energy ϵ for the α-particles (squares - $\epsilon(\alpha^{min})$, circles - $\epsilon(\alpha^{max})$ and asterisks - $\epsilon(^{6}\text{Li})$. The distributions were fitted with the Gaussian function and the values of the corresponding maxima were obtained: - $\epsilon(\alpha^{min}) = 0.17 \pm 0.03$, $\epsilon(\alpha^{max}) = 0.25 \pm 0.03$, $\epsilon(^{6}\text{Li}) = 0.55 \pm 0.02$. The slight deviation between α^{min} and α^{max}, taking into account the small value of the angle of separation between α-particles (Fig. 5c), explains the formation of a narrow near-threshold state (Fig. 3a).

Details of the mechanisms of the channel of formation of the GS of the ^{8}Be nucleus can be studied with the help of the symmetric Dalitz plot. This technique is particularly suitable for the geometric visualization of the decay into three particles with identical masses and makes it possible to illustrate the population of the available phase space at three-body decays. If the decay is a true direct 3-particle decay, the distribution of events in the Dalitz diagram must be uniform. However, as a rule, 3-particle decays occur via resonances, i.e., the excited particle decays into a resonance and α-particle, and then the resonance, in turn, decays into two other particles. In this case, the distribution of events in the Dalitz diagram reveals an essentially non-uniform structure, with an increased concentration of events in the region of invariant masses coinciding with the resonance masses.

The Dalitz diagram is a convenient tool for studying the dynamics of 3-particle decays. The Cartesian coordinates for plotting a Dalitz diagram can be obtained as follows [10]:

$$x = \sqrt{3}(\epsilon_j - \epsilon_k); y = 2\epsilon_i - \epsilon_j - \epsilon_k \tag{6}$$

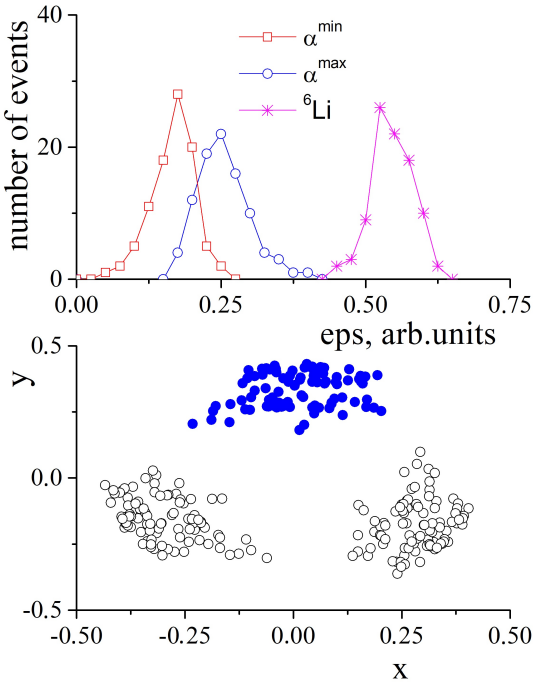

Figure 6. a) dependence of the number of events on the relative energy of particles ϵ, b) Dalitz diagram for the channel of formation of the GS of the ^{8}Be nucleus.

By definition, the sum of the relative energies of three particles equals 1. In our experiment, the contribution of each component can be evaluated from the general plot.

In Fig. 6b, the solid dots represent the dependence in the case where α-particles were used in the x coordinate, and the open dots represent combinations with ^{6}Li. The Dalitz distribution confirms the presence of an intermediate excited particle (^{8}Be) and correlates with the distribution in Fig. 6a.

5. CONCLUSIONS

A systematic study of the ^{14}N(γ,2α)^{6}Li reaction was performed. To obtain the physical parameters of the events, a graphical application was created in the Python programming language with the ability to automatically measure the coordinates of points along the tracks on digital photo frames. The main procedure is the analysis of the pixel intensity in the track area along a circular trajectory of a certain radius.

The excitation energy of the 2α-particle system was determined and a structure with two maxima was found in the distribution of the number of events by $E_x(\alpha\alpha)$. It was assumed that this structure is formed either as a result of the decay of the intermediate excited state of the ^{8}Be nucleus or is simulated by one of the background pairs during the decay of the intermediate excited state of the ^{10}B nucleus.

A kinematic scheme for calculating the physical parameters of the reaction has been created assuming a two-particle decay mode with the formation of an intermediate excited state. A comparison of experimental data and kinematic calculation has been performed and it has been determined that with high probability the decay process with the formation of an intermediate excited nucleus ^{8}Be in the ground and 1^{st} excited states occurs.

In the distribution of events by the energy of the relative motion of two a particles, a resonance was found, identified as the ground state of ^{8}Be nucleus. Events corresponding to the partial channel of the ^{14}N(γ,^{6}Li)^{8}Be$_0$ reaction with the subsequent two-particle decay $^{8}\text{Be} \rightarrow \alpha + \alpha$ were identified and the partial cross section of this channel was measured. An analysis of the energy and angular distributions of particles at each stage of decay was performed.

ORCID

Serhii Afanasiev, https://orcid.org/0000-0003-1682-4621; **Inna Afanasieva**, https://orcid.org/0000-0002-9523-9780; **Kateryna Chkuaseli**, https://orcid.org/0009-0008-1972-9148

REFERENCES

[1] A. Coc, C. Angulo, E. Vangioni-Flam, P. Descouvemont, and A. Adahchour, Nucl. Phys. A, **752**, 522 (2005). https://doi.org/10.1016/j.nuclphysa.2005.02.057.

[2] F.-K. Thielemann, F. Brachwitz, C. Freiburghaus, *et al.*, Prog. Part. Nucl. Phys. **46**, 22 (2001). https://doi.org/10.1016/S0146-6410(01)00103-X.

[3] E.G. Fuller, Physics Reports, **127**, 185 (1985). https://doi.org/10.1016/0370-1573(85)90145-0

[4] D.J.S. Findlay, Nucl. Instr. and Meth. in Phys. Res. Section B: Beam Interactions with Materials and Atoms, **50**, 314 (1990). https://doi.org/10.1016/0168-583X(90)90374-4

[5] O.F. Nemets, V.G. Neudachin, and A.T. Rudchik, *et al.*, (Naukova Dumka, Kiyev, 1988). (in russian)

[6] M. Freer, H. Horiuchi, Y. Kanada-En'yo, *et al.*, Rev. Mod. Phys. **90**, 035004, (2018). https://doi.org/10.1103/RevModPhys.90.035004

[7] S.N. Afanasyev, Ukrainian Journal of Physics, **64**, 787 (2019). https://doi.org/10.15407/ujpe64.9.787

[8] F.C. Young, P.D. Forsyth, and J.B. Marion, Nucl. Phys. A, **91**, 209, (1967). https://doi.org/10.1016/0375-9474(67)90462-9

[9] L. Jarczyk, B. Kamys, Z. Rudy, *et al.*, Nucl. Phys. A, **459**, 52, (1986). https://doi.org/10.1016/0375-9474(86)90055-2

[10] Yu.M. Arkatov, P.I. Vatset, V.I. Voloshchuk, *et al.*, Prib. Tekh. Eksp. **3**, 205, (1969). (in russian).

[11] S.N. Afanasiev, and I.A. Afanasieva, Problems of Atomic Science and Technology, Series "Nuclear Physics Investigations", (5)(141), 87, (2022). https://doi.org/10.46813/2022-141-087

[12] O.F. Nemets, and Yu.V. Gofman, (Naukova Dumka, Kiyev, 1975). (in russian).

[13] V.V. Kirichenko, A.F. Khodyachikh, P.I. Vatset, *et al.*, Yad. Fiz. **29**, 572, (1979).

[14] S.N. Afanasyev, and A.F. Khodyachikh, Yad. Fiz. **71**, 1859, (2008). https://doi.org/10.1134/-S106377880811001X

[15] D. Dell'Aquila, I. Lombardo, and G. Verde, *et al.*, Phys. Rev. Lett. **119**, 132501, (2017). https://doi.org/10.1103/PhysRevLett.119.132501

[16] S.N. Afanasyev, in: *Proceedings of the 5rd International Conference "Computer modeling of high-technology (CMHT-2018)*, (2018), pp.37.

[17] D.R. Tilley, J.H. Kelley, J.L. Godwin, *et al.*, Nucl. Phys. A, **745**, 155, (2004). https://doi.org/10.1016/j.nuclphysa.2004.09.059

[18] A.M. Baldin, V.I. Gol'danskii, V.M. Maksimenko, and I.L. Rosenthal, *Kinematics of nuclear reactions*, (Atomizdat, Moscow, 1968). (in russian).

ДОСЛІДЖЕННЯ РЕАКЦІЇ $^{14}N(\gamma,2\alpha)^{6}Li$

Сергій Афанасьєв[1], **Інна Афанасьєва**[1,2], **Катерина Чкуаселі**[2]

[1]*Національний Науковий Центр "Харківський Фізико-Технічний Інститут", вул. Академічна, 1, 61108, Харків, Україна*

[2]*Харківський національний університет ім. В.Н. Каразіна, майдан Свободи, 4, 61022, Харків, Україна*

Для створеного в ННЦ ХФТІ банку даних стереокадрів фотоядерних реакцій розроблено методику цифрового вимірювання координат точок уздовж треків. Основною процедурою є аналіз інтенсивності пікселів в області треків. Як тестову для вимірювання обрано реакцію $^{14}N(\gamma,2\alpha)^{6}Li$. Створено кінематичну схему розрахунку фізичних параметрів реакції в припущенні двочастинкової моди розпаду з утворенням проміжного збудженого стану. Виконано порівняння експериментальних даних і кінематичного розрахунку. Виділено події, що відповідають парціальному каналу реакції $^{14}N(\gamma,^{6}Li)^{8}Be_0$ з наступним двочастинковим розпадом $^{8}Be \rightarrow \alpha + \alpha$ і виміряно парціальний перетин цього каналу. Виконано аналіз енергетичних і кутових розподілів частинок на кожному етапі розпаду.

Ключові слова: *фотоядерні реакції; дифузійна камера; цифрова техніка вимірювання; основний стан ядра* ^{8}Be

East European Journal of Physics. 1. 170–175 (2026)

DOI: 10.26565/2312-4334-2026-1-16 ISSN 2312-4334

DETERMINATION OF $^{10}B/^{11}B$ ISOTOPIC RATIO AND CONCENTRATION OF BORON IN STAINLESS STEEL BY ICP MS

Inna Afanasieva[1,2], **Serhii Afanasiev**[1], **Dmytro Kutnii**[1], **Dmytro Burdeinyi**[1], **Stanislav Vanzha**[1], **Nataliia Rud'**[1], **Oleksandr Medvediev**[1]

[1]*National Science Center "Kharkov Institute of Physics and Technology" 1, Akademicheskaya St., 61108, Kharkiv, Ukraine*

[2]*V.N. Karazin Kharkiv National University, 4, Svoboda Sq., Kharkiv, 61022, Ukraine*

[*]*Corresponding Author e-mail: afaninna@i.ua*

Received January 8, 2026; revised February 7, 2026; accepted February 19, 2026

The large thermal neutron absorption cross-section of the ^{10}B enables the use of boron as a neutron absorber for reactivity control in nuclear reactors. Precise information on both the isotopic composition and boron concentration in absorbing materials is crucial, as the degree of reactivity control depends directly on the ^{10}B content. In the work, a series of experiments were conducted to determine the boron concentration and isotopic ratio in samples of corrosion-resistant chromium-nickel stainless steel, which is used in the control and protection system rods of nuclear reactors. The study was performed using an inductively coupled plasma mass spectrometer on 5 stainless steel samples with a certified boron mass fraction. The external standard method was used to determine the $^{10}B/^{11}B$ isotopic ratio, using the ICP-MS-68A Standard (with a natural ^{10}B:^{11}B ratio of 19.9:80.1) as a reference. To determine the boron concentration in steel, the isotope dilution method (internal standard method) was used. A known amount of a spike with a specific isotopic ratio was added to samples of unknown boron content. Elemental amorphous boron powder with a ^{10}B:^{11}B isotopic ratio of 95.0:5.0 was used as the spike. The proposed methods allow determining the isotope ratio and boron concentration in a sample by measuring only the ^{10}B and ^{11}B isotopes. The results obtained were compared with the manufacturer's certified data. The values coincide within the measurement uncertainty, confirming the reliability of the proposed methods for steel analysis.

Keywords: *Boron isotopic ratio; Boronated steel; ICP MS; Isotope dilution*

PACS: 29.30.-h

1. INTRODUCTION

Due to the large cross-section of absorbing the thermal neutrons in the ^{10}B isotope, boron in various forms is used to control nuclear reactor reactivity by absorbing neutrons [1]. Since the degree of reactivity control depends on the amount of ^{10}B, precise knowledge of both the isotopic composition and the concentration of boron in the neutron-absorbing material is highly important for the nuclear industry [2, 3]. In addition, information about the isotopic composition and the concentration of boron in different samples is important for other fields of science, such as archaeology, geology, and medicine [4-6].

Various methods are used to determine isotopic ratios, such as atomic absorption spectrometry [7], thermal ionization mass spectrometry (TIMS) [8], secondary ion mass spectrometry (SIMS) [9], as well as others. Each of these methods has its own specific advantages and disadvantages.Among them, TIMS is renowned for providing extremely high accuracy and precision in isotope ratio measurements. However, the high ionization potential of boron prevents the production of singly charged boron ions using TIMS. Attempts are made to bypass this problem by using different sample preparation procedures, but this complicates the sample preparation process and degrades the accuracy of isotope ratio measurement.

An alternative to TIMS for precise boron isotope ratio measurements is high-resolution inductively coupled plasma mass spectrometry (ICP MS) [10].

In this study, a methodology for determining both the boron isotope ratio and the boron concentration in samples of corrosion-resistant chromium-nickel stainless steel alloyed with boron using a single-collector inductively coupled plasma mass spectrometer will be presented. Boronated steel is one of the promising materials for use as a neutron absorber for control and safety rod systems in a nuclear reactor [11].

A feature of this study for determining the boron content in the sample is the use of the isotope dilution method [12,13], which is based on the internal standard principle. This method yields a faster result with fewer calculation steps, which reduces the error in determining the required data. Isotope dilution method is an analytical technique, the essence of which lies in introducing a known amount of a tracer (spike) with a different boron isotopic composition into a sample that has a defined boron isotopic composition but an unknown elemental mass content. After the addition of the spike, the boron isotopic ratio changes, and the boron content in the initial sample can be calculated from the magnitude of this change. As is known, boron has two stable isotopes (^{10}B and ^{11}B), which makes it an excellent candidate for using this method.

Cite as: I. Afanasieva, S. Afanasiev, D. Kutnii, D. Burdeinyi, S. Vanzha, N. Rud', O. Medvediev, East Eur. J. Phys. 1, 170 (2026), https://doi.org/10.26565/2312-4334-2026-1-16

2. EXPERIMENTAL TECHNIQUE

2.1. Instrumentation

Measurements were conducted using a single-collector inductively coupled plasma mass spectrometer, the ICP-SFMS ELEMENT 2, whose technical characteristics are described in [14, 15]. A substantial advantage of this mass spectrometer is its high resolution and high sensitivity (~ 10 cps per 1 ppb ^{115}In), which allows for the analysis of extremely low element contents. The high-resolution mode (10000 imp. at 10 % peak height) was used in the work, and the signal stability was better than 1 % over 10 minutes.

Physicochemical sample preparation methods were used for sample investigation, involving the conversion of samples into liquid form using high-purity distilled water, acids, and organic solvents. Liquid solutions containing the analyzed sample were introduced into an argon torch in the form of an aerosol using a peristaltic pump. Sample injection occurred for a certain number of iterations N with a uniform time interval $\triangle t$. The analytical signal is the mass spectrum of the analyzed elements, whose peak areas were measured after subtracting the average background value, which was measured before the start of the sample investigation.

2.2. Materials

For the inductively coupled plasma mass spectrometric method of analysis, the required concentrations of the measured samples are displayed in the ppm and ppb ranges. To obtain such concentrations, we used small aliquots of the investigated material, namely 0.1 g. This allowed us, on the one hand, to accurately measure the sample mass, and on the other, to minimize the consumption of acids and other reagents used for sample preparation (sample dissolution). Chemical analytical glassware of Class 1 was used during sample preparation to reduce measurement error. To prepare the solution of the investigated boronated steel sample, steel chips with an increased boron content up to 2 % (limits specified in the manufacturer's certificate for boronated steel samples:1.6÷2.0 %) were collected and crushed. Sampling was performed in several places of the investigated sample to obtain a representative sample and a reliable analysis result.

For the external standard method, a solution of the multicomponent standard 48 Component ICP-MS-68A Standard at 10 µg/mL in 2% HNO_3 (High Purity Standards (USA)) [16] was used. The solution was prepared by diluting the standards in ultrapure concentrated nitric acid (HNO_3) to achieve an element concentration of 1 ppm.

Amorphous boron powder, enriched up to 95 % in the ^{10}B isotope (manufactured by the National High Technology Center of Georgia) [17], was used as the internal standard (spike). The reference material was not subjected to additional drying or homogenization. A portion of amorphous boron weighing 0.1001 ± 0.0001 g was dissolved in 10 ml of HNO_3 with the addition of a small amount of distilled water under slight heating and stirring. The boron concentration in the resulting solution (spike) was 10 ppm.

In parallel, a blank solution was prepared in the same way, but without dissolving the investigated material. All the procedures mentioned above were followed during its preparation, except for the addition of the aliquot. The blank solution was used in the studies to avoid the influence of impurities contained in the reagents used for dissolution on the sample measurement results.

2.3. Procedure

Table 1 presents the sequence (column 1) of the measurements performed (column 2).

Table 1. The measurement procedure for boron isotope ratios

Step	Procedure
0	Rinsing of sample introduction tube, spray chamber and nebulizer by argon (600 s)
1	Measure signal of ^{10}B and ^{11}B of blank solution ($^{10}B_{blank}$, $^{11}B_{blank}$)
2	Rinsing of sample introduction tube, spray chamber and nebulizer by argon (600 s)
3	Measure $^{10}B/^{11}B$ of ICP-MS-68A Standard ($R_{standart}$)
4	Rinsing of sample introduction tube, spray chamber and nebulizer by argon (600 s)
5	Measure $^{10}B/^{11}B$ of sample solution ($R_{sample}{}^{meas}$)
6	Rinsing of sample introduction tube, spray chamber and nebulizer by argon (600 s)
7	Measure $^{10}B/^{11}B$ of spike solution ($R_{spike}{}^{meas}$)
8	Rinsing of sample introduction tube, spray chamber and nebulizer by argon (600 s)
9	Measure $^{10}B/^{11}B$ of mix solution ($R_{mix}{}^{meas}$)

The signal intensity of ^{10}B and ^{11}B in the blank solution is represented as $^{10}B_{blank}$ and $^{11}B_{blank}$ (step 1).

The determination of the ^{10}B/^{11}B isotopic ratio for the standard ($R_{standart}$), sample (R_{sample}), spike (R_{spike}) and mix (R_{mix}) solutions was performed using the formula:

$$R = \frac{I(^{10}B) - ^{10}B_{blank}}{I(^{11}B) - ^{11}B_{blank}}, \quad (1)$$

Where I(^{10}B) and I(^{11}B) are the signal intensities of ^{10}B and ^{11}B in the investigated solutions (steps 3, 5, 7, 9).

To reduce the influence of the background signal between measurements of different samples, the mass spectrometer was rinsing with argon for 10 minutes (steps 2, 4, 6, 8).

To determine the boron concentration in the steel sample, the enriched boron solution (mix) with a boron concentration of 0.01 ppm was added to the stainless steel solutions (sample). The measurement of the ^{10}B/^{11}B isotopic ratio for the mixture (mix) was performed last (step 9).

3. DETERMINATION THE BORON ISOTOPE RATIOS

To determine the isotopic composition of the samples (sample, spike and mix), the mass spectrometer was calibrated using a standard of known elemental composition (ICP-MS-68A Standard). For the boron isotopes (^{10}B and ^{11}B) the calibration characteristic — the relative sensitivity coefficient of the boron isotopes — was experimentally determined under specific conditions. This coefficient reflects the dependence of the analytical signal of the corresponding peaks on the content of these isotopes in the standard. In our case, this coefficient corresponds to the value of $R_{standart}$ (step 3 in Table 1). The stability of the $R_{standart}$ value was analyzed over a year in different measurement sessions, and Fig. 1 presents the dependence of $R_{standart}$ on the measurement session number.

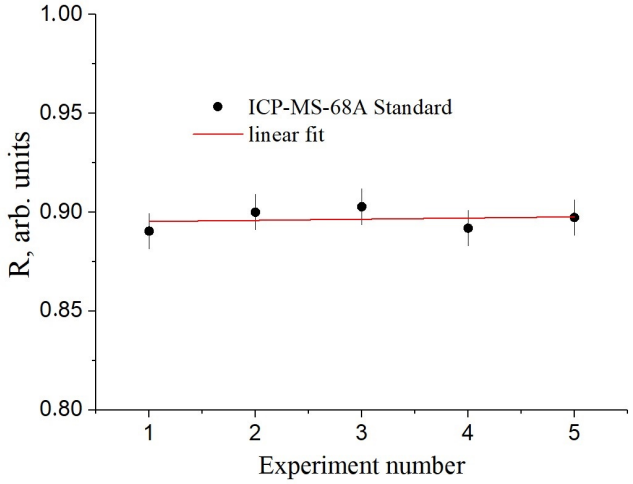

Figure 1. Dependence of $R_{standart}$ in different measurement sessions.

Fitting was performed using a linear function R = a+b·N, where a = 0.895 ± 0.006 and b = 0.001 ± 0.002. The slope (b) is insignificant. Also, it is visible from the figure that the $R_{standart}$ for different measurement sessions coincide within the error.

Considering the mass spectrometer calibration, the isotopic ratio of the samples was determined as R^{corr}=R^{meas} / $R_{standart}$, where R^{meas} corresponds to the measured value $R_{sample}{}^{meas}$, $R_{spike}{}^{meas}$ or $R_{mix}{}^{meas}$. The obtained results for the isotopic ratio values were compared with the certified data of the investigated samples: sample with a natural ratio of 19.9 % : 80.1 % (R = 0.248) and spike with a ^{10}B-enriched ratio of 95.0 % : 5.0 % (R = 25.316).

Table 2 presents the values of $R_{sample}{}^{corr}$ and $R_{spike}{}^{corr}$ for the same 5 measurement sessions (Fig. 1), calculated using $R_{standart}$ according to the measurement session.

Within the errors, the determined R_{sample} and R_{spike} coincide with the certified values (0.248 and 25.316 respectively).

4. DETERMINATION OF BORON CONCENTRATION IN STAINLESS STEEL

The isotope dilution method, based on the internal standard principle [11, 12], was used to determine the boron content in the boronated steel. This method yields a quick result with fewer calculation steps, which reduces the error in determining the required data. Isotope dilution method is an analytical technique, the essence of which lies in introducing

Table 2. Determination the boron isotope ratios

Session	$R_{sample}{}^{corr}$	$R_{spike}{}^{corr}$
1	0.247±0.004	24.922±0.549
2	0.246±0.005	25.033±0.581
3	0.249±0.004	24.845±0.535
4	0.246±0.004	25.201±0.490
5	0.247±0.004	24.877±0.542

a known amount of a tracer (M_{spike}) with a different boron isotopic composition (R_{spike}) into a sample with a defined boron isotopic composition (R_{sample}) but an unknown elemental mass content (M_{sample}) (Fig. 2). After the addition of the spike, the boron isotopic ratio (R_{mix}) changes, and the boron content in the initial sample can be calculated from the magnitude of this change.

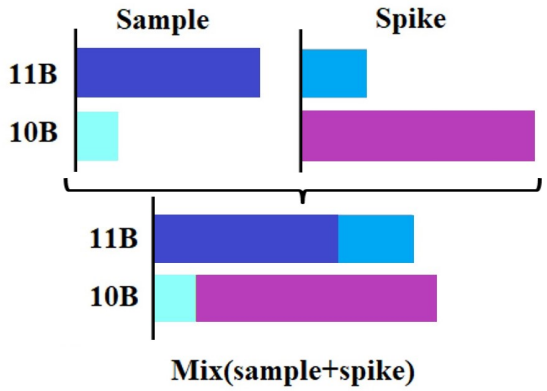

Figure 2. Schematic representation of the isotope dilution method.

For the resulting mixture (mix diagram at Fig.2), the mass content is $M_{mix} = M_{sample} + M_{spike}$. The introduction of the spike changes the isotopic ratio of the element, and the content of the element in the initial sample can be calculated from the magnitude of this change using the formula:

$$M_{sample} = M_{spike} \frac{1 + R_{sample}}{1 + R_{spike}} \frac{R_{spike} - R_{mix}}{R_{mix} - R_{sample}}. \tag{2}$$

Thus, if we add a known amount M_{spike}, the unknown mass content of boron in the sample, M_{sample}, can be determined from the measured R values using formula (2).

In our study, the boron content (concentration) in the boronated steel samples was measured for 5 different measurement sessions. An equal amount of the tracer (spike) was added to each sample, resulting in 5 mix samples. Thus, 5 combinations, each with 3 data sets (sample, spike and mix), were measured.

Fig. 3 shows the dependence of the peak intensity of the ^{10}B and ^{11}B isotopes as a function of measurement time for all components for one combination: sample (Fig. 3a), spike (Fig. 3b) and mix (Fig. 3c). The figure shows that the intensity dependence is linear without significant fluctuations.

The change in the relative contribution of each of the ^{10}B and ^{11}B isotopes in Fig. 3a, 3b and 3c is consistent with the logic of the isotope dilution method (Fig.2). The integrated value of the ratios $R(^{10}B/^{11}B)$ according to formula (1) was determined as the average over the entire measurement time.

In the next stage, the boron content value was calculated using formula (2). The calculation results are presented in the last column of the table. The uncertainties are statistical, taking into account the root mean square deviations for the distributions in Fig. 3.

From Table 3, it is evident that all values fall within the range specified in the manufacturer's certificate for boronated steel samples, 1.6÷2.0 %, which confirms the relevance of using this method for determining the boron content in the sample.

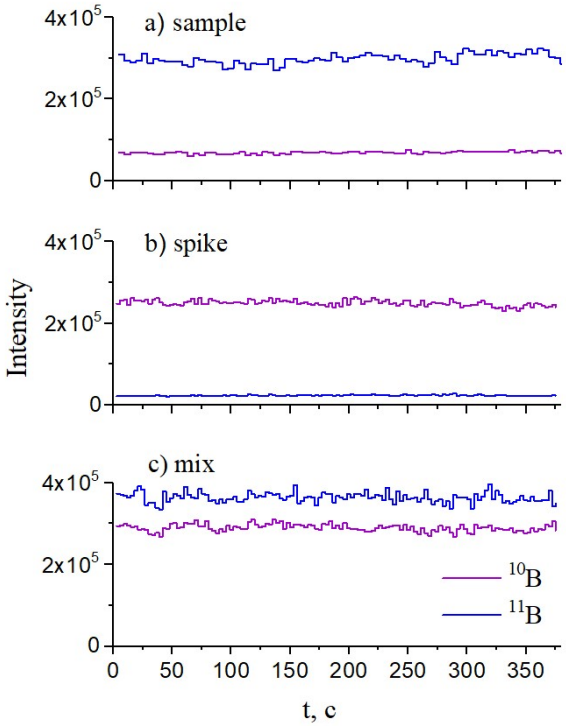

Figure 3. Values of the mass peak intensity for ^{10}B and ^{11}B isotopes as a function of measurement time for the three components: a) sample, b) spike, c) mix.

Table 3. Boron content in stainless steel.

Session	Boron content, wt.%
1	1.844±0.085
2	1.748±0.041
3	1.919±0.096
4	1.624±0.062
5	1.784±0.099

5. CONCLUSION

This work presents a methodology for measuring the isotopic ratio and concentration of boron in a multicomponent sample (stainless steel) based on the use of an inductively coupled plasma mass spectrometer (ICP-MS). A feature of the methodology is the use of external and internal calibration exclusively based on boron isotopes.

The multicomponent standard 48 Component ICP-MS-68A Standard at 10 µg/mL in 2% HNO3 (High Purity Standards (USA)) was used for external calibration, and amorphous boron powder, enriched up to 95 % in the ^{10}B isotope (manufactured by the National High Technology Center of Georgia), was used for internal calibration.

The determination of the boron isotope ratio was performed using the external calibration method. Measurements were carried out during 5 time-separated sessions. The obtained results were compared with the certified values (19.9 % : 80.1 %, R = 0.248) for boronated steel and highly enriched boron powder (95.0 % : 5.0 %, R = 25.316). The measurement results agree with the certified data within the uncertain.

The isotope dilution method (internal calibration) was used to determine the concentration of boron in the steel sample, where a known amount of the element with a different isotopic composition is added to a sample with an unknown concentration of the element. By measuring the isotopic ratio in the resulting mixture, the unknown concentration of the element in the sample can be determined. An additional advantage of the method is its simplicity and speed, as it does not require measuring all elements of the steel and has fewer calculation steps, which reduces the error in determining the necessary data.

Measurements were performed for five different stainless steel samples in different measurement sessions and

compared with the certified data presented by the manufacturer. The data agree within the measurement uncertainty, which indicates the reliability of the method for determining the boron content in steel samples.

ORCID

Inna Afanasieva, https://orcid.org/0000-0002-9523-9780; **Serhii Afanasiev**, https://orcid.org/0000-0003-1682-4621; **Dmytro Kutnii**, https://orcid.org/0000-0001-9591-4013; **Dmytro Burdeinyi**, https://orcid.org/0000-0003-4431-7264; **Stanislav Vanzha**, https://orcid.org/0000-0003-0949-947X; **Nataliia Rud'**, https://orcid.org/0000-0002-2958-3524; **Oleksandr Medvediev**, https://orcid.org/0009-0004-8896-2817

REFERENCES

[1] J.A. Evans, M.D. DeHart, K.D. Weaver, *et al.*, Nucl. Eng. and Des. **391**, 111726 (2022). https://doi.org/10.1016/j.nucengdes.2022.111726

[2] L. Desgranges, J.M. Escleine, P. Bienvenu, *et al.*, Nucl. Instr. and Meth. in Phys. Res. Section B: Beam Interactions with Materials and Atoms, **432**, 42 (2017). https://doi.org/10.1016/j.nimb.2018.07.011

[3] C. Subramanian, A.K. Suri, and T.S.R. Ch Murthy, BARC Newsletter, **313**, 42, (2010). https://inis.iaea.org/records/wb5s0-j1n27

[4] G.L. Foster, H.R. Marschall, and M.R. Palmer, *Boron Isotope Analysis of Geological Materials*, (Springer, 2018). https://doi.org/10.1007/978-3-319-64666-4_2

[5] L.B. Williams, and R.L. Hervig, Appl. Geochem. **19**, 1625 (2004). https://doi.org/10.1016/j.apgeochem.2004.02.007

[6] A.M. Hughes, and N. Hu, Cancers, **15**, 4091 (2023). https://doi.org/10.3390/cancers15164091

[7] H. Wiltsche, K. Prattes, M. Zischka, and G. Knapp, Spectrochim. A. Part B: Atomic Spectroscopy, **64**, 341, (2009). https://doi.org/10.1016/j.sab.2009.03.008

[8] T. Ishikawa, and K. Nagaishi, J. Anal. At. Spectrom. **26**, 359 (2011). https://doi.org/10.1039/C0JA00060D

[9] V. Karki, M. Singh, K.S. Bhushan, *et al.*, Intern. J. of Mass Spectrum, **460**, 116475, (2021). https://doi.org/10.1016/j.ijms.2020.116475

[10] D. Malinovsky, P.J.H. Dunn, and H. Goenaga-Infante, Nucl. Eng. and Des. **35**, 2723, (2020). https://doi.org/10.1039/D0JA00145G

[11] A. Saeed, Nucl. Eng. and Des. **413**, 112515 (2023). https://doi.org/10.1016/j.nucengdes.2023.112515

[12] P. Rodríguez-González, and J.I. García Alonso, J. Anal. At. Spectrom. **25**, 239, (2010). https://doi.org/10.1039/B924261A

[13] A. Quemet, A. Hubert, and A. Gourgiotis, *et al.*, J. Anal. At. Spectrom. **39**, 1665 (2024). https://doi.org/10.1039/D4JA00029C

[14] D.V. Kutnii, D.D. Burdeynyi, S.A. Vanzha, and N.V. Rud., East Europ. J. of Phys. (2), 104, (2020). https://doi.org/10.26565/2312-4334-2020-2-09

[15] D.V. Kutnii, S.A. Vanzha, D.D. Burdeynyi, *et al.*, East Europ. J. of Phys. (2), 75, (2022). https://doi.org/10.26565/2312-4334-2022-2-08

[16] ZeptoMetrix, ICP-MS Multi Element Solution Standard with 48 Components at 10 µg/mL, https://www.zeptometrix.com/us/en/icp-ms-standard-at-10-g-ml-solution-a-100-ml-ICP-MS-68A-A.

[17] National High Technology Center of Georgia, Amorphous boron powder with boron-10 isotope, http://geoisotopes.com/ka/bori-ge/b10-am-ge.

ВИЗНАЧЕННЯ ІЗОТОПНОГО ВІДНОШЕННЯ $^{10}B/^{11}B$ ТА КОНЦЕНТРАЦІЇ БОРУ В НЕРЖАВІЮЧІЙ СТАЛІ ЗА ДОПОМОГОЮ ICP MS

Інна Афанасьєва[1,2], **Сергій Афанасьєв**[1], **Дмитро Кутній**[1], **Дмитро Бурдейний**[1], **Станіслав Ванжа**[1], **Наталя Рудь**[1], **Олександр Медведєв**[1]

[1]*Національний Науковий Центр "Харківський Фізико-Технічний Інститут", вул. Академічна, 1, 61108, Харків, Україна*

[2]*Харківський національний університет ім. В.Н. Каразіна, майдан Свободи, 4, 61022, Харків, Україна*

Великий переріз поглинання теплових нейтронів ізотопом ^{10}B дозволяє використовувати бор у якості поглинача нейтронів для контролю реактивності в ядерних реакторах. Інформація про точне значення як ізотопного складу, так і концентрації бору в нейтронпоглинаючому матеріалі є дуже важливою, адже ступінь регулювання реактивності залежить від кількості ^{10}B. В роботі проведено серію експериментів з визначення концентрації бору та його ізотопного відношення в зразках корозійностійкої хромонікелевої неіржавіючої сталі, яка використовується як матеріал поглинаючих стрижнів системи управління та захисту ядерного реактора. Дослідження виконано з використанням мас-спектрометра з індуктивно-зв'язаною плазмою на 5 зразках неіржавіючої сталі з сертифікованим значенням масової частки бору. Для визначення ізотопного відношення $^{10}B/^{11}B$ використовувався метод зовнішнього стандарту. В якості зовнішнього стандарту використовувався спеціалізований багатокомпонентний калібрувальний розчин ICP-MS-68A Standard з природним ізотопним співвідношенням бору ^{10}B:^{11}B=19.9:80.1. Для визначення концентрації бору в сталі використовувався метод ізотопного розбавлення (метод внутрішнього стандарту). До невідомого за вмістом бору зразка з природнім співвідношенням його ізотопів додавали відому кількість індикатора з іншим ізотопним відношенням. У якості індикатора використовували порошок елементарного аморфного бору зі співвідношенням ізотопів ^{10}B:^{11}B=95.0:5.0. Запропоновані методи дозволяють визначити ізотопне відношення та концентрацію бору в зразку вимірюючи лише ізотопи ^{10}B та ^{11}B. Отримані в роботі значення порівнювались з паспортними даними, представленими виробником. У межах невизначеності вимірювань дані співпадають, що може свідчити про надійність запропонованих методів для визначення ізотопного співвідношення та вмісту бору в зразках сталі.

Ключові слова: *ізотопне співвідношення бору; борована сталь; ICP MS; ізотопне розведення*

East European Journal of Physics. **1.** 176-186 (2026)
DOI:10.26565/2312-4334-2026-1-17 ISSN 2312-4334

A PYTHAGOREAN-FUZZY NONLOCAL REFORMULATION OF QUANTUM ELECTRODYNAMICS

Supratim Mukherjee
Department of Mathematics, Government General Degree College, Tehatta, India
Corresponding Author email: raja_lalbagh@yahoo.co.in
Received October 13, 2025; revised February 8, 2026; accepted February 25, 2026

Quantum Electrodynamics (QED) is the most precise theory in physics, yet its assumption of pointlike interactions between charged particles and photons leads to ultraviolet divergences that require renormalization. This paper proposes a Pythagorean-Fuzzy Nonlocal Reformulation of QED, embedding structured uncertainty directly into the interaction framework. Each spacetime region is described by a Pythagorean fuzzy field with degrees of membership, non-membership, and hesitation, quantifying how strongly an event participates in an interaction and how precisely it can be localized. The conventional point vertex is replaced by a smooth, gauge-covariant nonlocal coupling modulated by a Lorentz-invariant kernel and the fuzzy field's defuzzified weight. This structure preserves all symmetries of QED while automatically suppressing short-distance divergences. Ultraviolet divergences are suppressed at their origin, yielding finite self-energy and vacuum-polarization contributions within the nonlocal framework, without the appearance of divergent counter terms. Physically, the formulation interprets quantum interactions as finite "fuzzy" processes distributed over regions of limited definability. Mathematically, it unites the logic of Pythagorean fuzzy sets with the geometry of field theory, providing a natural regularization mechanism that remains fully consistent with standard QED in the sharp-local limit.
Keywords: *Nonlocal quantum field theory; Gauge-covariant regularization; Lorentz-invariant smearing; Wilson lines; Renormalization group; Pythagorean fuzzy field; Ultraviolet convergence*
PACS: 11.10.Lm; 11.15.-q; 11.10.Gh; 12.20.-m

1. INTRODUCTION

Quantum Electrodynamics (QED) is the most precisely verified theory in the history of science ([12]). It provides the framework within which the interactions of charged particles and electromagnetic fields are described with astonishing accuracy. From the Lamb shift to the electron's anomalous magnetic moment ([12]), QED's predictions agree with experiment to more than one part in a billion. Despite this success, the theory rests on a profound mathematical idealization that has always carried physical discomfort: it assumes that the interaction between particles occurs at *exact* points in spacetime.

This assumption of pointlike interaction gives the theory its elegant simplicity but also creates its deepest problem. When the distance between interacting fields is treated as infinitesimally small, the energy density and self-interaction terms diverge. The resulting ultraviolet infinities are removed through renormalization, a procedure that replaces infinite bare quantities with finite, measurable ones. Although renormalization works extraordinarily well in practice, it leaves open an unresolved conceptual question: why should a physically meaningful theory require infinite subtractions at all? The problem is not in the mathematics of QED but in its philosophical foundation, the assumption that spacetime and field values can be defined with infinite precision.

Physical measurement, and arguably nature itself, never operates at such absolute precision. Quantum uncertainty limits the accuracy with which position, momentum, and energy can be defined. Every measurement, every event, occupies a *finite* spacetime region whose boundaries are blurred by intrinsic indeterminacy. The local field description of QED does not account for this fundamental imprecision; it treats uncertainty as a statistical feature of measurement rather than as a structural property of the theory. This disconnect motivates a search for a framework in which uncertainty is embedded into the fabric of field interactions, rather than added externally through probabilistic interpretation.

Nonlocal quantum field theories and regularization techniques ([7], [8], [9]) have long attempted to soften the ultraviolet behavior of QED by smearing interactions over finite distances. These approaches introduce cutoff scales or modified propagators, but they remain within the rigid logic of classical mathematics ([7], [8], [9]): their spacetime points and interaction kernels are defined with crisp equality and deterministic structure. What they lack is an explicit representation of *imprecision itself* ([1], [2], [3], [4]), a formal language to express the degree to which an event both belongs and does not belong to a region of interaction.

This paper develops such a language through a Pythagorean-Fuzzy Nonlocal Reformulation of QED ([1], [2], [3], [4], [5], [6]). The central idea is that interactions should not be viewed as absolute coincidences of fields at single points but as processes distributed over fuzzy spacetime regions characterized by partial membership and hesitation. Each spacetime location is associated with a *Pythagorean fuzzy field*, specified by a pair of parameters that quantify the degree of inclusion and exclusion of that point in the interaction domain ([1], [2], [3]). The remaining "hesitation" represents intrinsic localization indeterminacy—an objective measure of how sharply an event can be defined in spacetime.

Cite as: S. Mukherjee, East Eur. J. Phys. 1, 176 (2026), https://doi.org/10.26565/2312-4334-2026-1-17

This fuzzy structure does not replace quantum probability; rather, it complements it. Probability captures stochastic uncertainty—how likely an event is to occur. Fuzziness captures ontological uncertainty—how precisely an event can be said to occur at all. Incorporating this second form of uncertainty into QED acknowledges that perfect locality is an idealization, not a physical reality. By treating field interactions as fuzzy, the theory gains an internal mechanism for moderating short-distance behavior. Contributions from extremely high momenta are automatically damped because the interaction is spread over a finite region whose effective size is governed by a "fuzziness scale." The result is a natural regularization of ultraviolet divergences without the need for artificial counterterms.

Crucially, the proposed formulation preserves the symmetries and structure that make QED reliable. Gauge invariance is maintained through a covariant construction that links spatially separated points by a Wilson line ([10], [11]), and Lorentz invariance is respected by using isotropic smearing kernels ([9]). The modified interaction term introduces no arbitrary cutoffs or external parameters; the extent of nonlocality emerges directly from the fuzzy field itself. When the fuzziness parameters vanish, the interaction contracts to a point and standard QED is recovered exactly ([12]). Thus, the new theory is not a replacement for QED but a smooth generalization of it, reducing to the classical formulation as a special limit. Beyond its technical implications, the Pythagorean-fuzzy approach carries conceptual significance. It offers a unified way to think about uncertainty that bridges logic and physics. Fuzzy logic, originally designed to formalize human reasoning under imprecise information, becomes here a framework for describing physical indeterminacy in the quantum vacuum. The degrees of membership and hesitation translate naturally into physical language: participation strength, field overlap, and localization ambiguity. In this view, renormalization is not a mathematical patch but a manifestation of the fact that interactions never achieve complete certainty in spacetime. By replacing infinite precision with structured hesitation, the theory removes the very conditions that give rise to divergences.

This reformulation also points toward broader generalizations. The same principles that regularize QED can, in principle, be applied to non-Abelian gauge fields, where self-interaction divergences are even more severe. A Pythagorean-fuzzy framework could provide a unified description of structured uncertainty across the Standard Model, and perhaps offer hints toward quantum gravity, where spacetime discreteness and minimum-length hypotheses already suggest a limit to localization.

The objective of this paper is therefore twofold: to construct a mathematically consistent, gauge-invariant nonlocal QED in which the interaction vertex is weighted by a Pythagorean-fuzzy field, and to demonstrate that this structure yields ultraviolet-finite amplitudes without contradicting established physics. The formulation is built to preserve empirical consistency while deepening conceptual coherence: uncertainty becomes not an obstacle to precision, but the mechanism that makes precision possible.

The paper is organized as follows. Section 2 defines the Pythagorean-fuzzy field and its defuzzification operator, describing how fuzzy membership, non-membership, and hesitation are represented in spacetime. Section 3 constructs the gauge-covariant nonlocal interaction and outlines the modified Feynman rules. Section 4 analyzes the one-loop corrections and demonstrates the built-in ultraviolet convergence. Section 5 discusses the preservation of Lorentz and gauge symmetries and examines the recovery of conventional QED in the local limit. Section 6 provides a suitable example to understand the proposed approach. Section 7 considers conceptual implications and possible extensions to other gauge theories and gravitational contexts. Finally, Section 8 summarizes the findings and reflects on how integrating structured uncertainty into field theory may offer a more complete picture of quantum reality.

2. THEORETICAL FRAMEWORK: THE PYTHAGOREAN-FUZZY FIELD

The central difference between this work and conventional Quantum Electrodynamics lies in how uncertainty is treated. Here, uncertainty is not a limitation of measurement but an intrinsic property of the interaction itself. To express this idea without losing contact with familiar field-theoretic language, every point in spacetime is assigned a Pythagorean-fuzzy field, written as $\Phi(x)$. Each value of Φ represents the degree to which a spacetime element participates in an electromagnetic interaction. It is not a probability amplitude in the quantum-mechanical sense but a logical weight that measures inclusion and exclusion within an interaction region.

The Pythagorean-fuzzy structure differs from classical fuzzy logic because it uses two independent parameters: the degree of membership $\mu(x)$ and the degree of non-membership $\nu(x)$. Their squared magnitudes sum to at most one, leaving a residual quantity, called hesitation, defined by $\pi(x) = \sqrt{(1 - \mu^2 - \nu^2)}$. This hesitation describes how indeterminate the localization of an interaction is at that point. When μ equals one and both ν and π vanish, the event is perfectly defined and the theory reduces locally to ordinary QED. When μ and ν are comparable in size, the system reflects the dual character of quantum processes: partly present, partly absent, and accompanied by a finite zone of ambiguity.

Physically, μ can be viewed as the extent to which the electromagnetic field occupies a spacetime cell, while ν represents its complementary exclusion. The hesitation term π expresses the intrinsic vagueness in where and when the interaction occurs. Together these quantities describe a kind of ontological uncertainty—uncertainty about the very existence of a sharp boundary between interaction and non-interaction. In this sense the Pythagorean-fuzzy field extends the probabilistic description of quantum theory by assigning structure to the indeterminacy itself.

To link this logical framework with dynamics, the fuzzy field $\Phi(x)$ is mapped to a scalar weight through a defuzzification operator $D(\Phi)$. This operator provides an effective measure of how intense or "real" an interaction is at each location. Its exact mathematical form is flexible, but conceptually it captures the combined influence of membership,

non-membership, and hesitation. When D equals one, the region behaves as fully defined and interacts with complete strength; when D is smaller, the interaction is correspondingly weaker. This scalar weight multiplies the interaction term in the Lagrangian, replacing the implicit assumption of perfect unity that characterizes the pointlike vertex of standard QED. The physical meaning of D(Φ) is straightforward. In conventional QED, the electron and photon fields couple with a fixed charge e at every point, independent of any uncertainty in their localization. In the present formulation, the effective coupling becomes position-dependent through D(Φ), which modulates interaction strength according to local hesitation. Well-defined regions yield D close to one, while regions with high uncertainty give smaller values. The fuzzy field thus acts as a spatially distributed regulator that embodies the limits of physical precision.

Although the fuzzy structure introduces new variables, it does not alter the continuous nature of spacetime or the linear structure of the quantum fields. The function Φ(x) varies smoothly, and its effect enters the theory as a multiplicative factor rather than by changing dimensionality or topology. This construction remains consistent with Lorentz invariance once the defuzzification operator and the associated smearing kernel depend only on invariant intervals. The resulting theory preserves relativistic covariance while allowing the coupling strength to reflect the degree of localization uncertainty. The Pythagorean-fuzzy field unifies two distinct notions of uncertainty. Quantum mechanics describes stochastic uncertainty through probabilities of outcomes, whereas fuzzy logic expresses epistemic uncertainty through partial belonging to sets. When a quantum field is described through a fuzzy framework, the amplitude indicates whether a process occurs, while the fuzzy weight describes how sharply that process can be said to occur in spacetime. This distinction permits a layered view of reality: probabilistic at the level of events, fuzzy at the level of their definition.

Once fuzziness is introduced, strict locality cannot be maintained. Each spacetime element now represents a region of finite extension, and interactions between fields must occur over small domains determined by both the smearing scale and the local hesitation encoded in π(x). This reinterpretation eliminates the singular self-interaction that arises when two fields coincide exactly. The divergence associated with exact coincidence is replaced by a finite overlap integral weighted by the fuzzy participation functions of the interacting fields. In this way, the Pythagorean-fuzzy field forms a conceptual and mathematical bridge between logical uncertainty and geometric nonlocality. In practice, the detailed behavior of Φ(x) does not need to be specified globally. It can be treated as a slowly varying background field that modulates interaction strength without adding new dynamical degrees of freedom. Its gradients can be neglected when the fuzziness scale is small compared with macroscopic distances but still larger than the Planck length, ensuring that ordinary QED predictions remain valid at accessible energies. At very high energies, where localization approaches the limits imposed by π(x) and by the smearing scale σ, the modification becomes significant and provides an intrinsic regularization that suppresses ultraviolet divergences.

The Pythagorean-fuzzy field, therefore, plays two complementary roles. Conceptually, it expresses the idea that no physical interaction is infinitely precise. Mathematically, it supplies a smooth, symmetry-preserving cutoff that eliminates the need for arbitrary renormalization constants. By redefining what it means for fields to coincide, it turns singular interactions into controlled overlaps. The next section develops this idea explicitly by constructing the gauge-covariant nonlocal interaction that incorporates D(Φ) into the QED Lagrangian while preserving the fundamental symmetries of the theory.

3. GAUGE-COVARIANT NONLOCAL INTERACTION

Having introduced the Pythagorean-fuzzy field as a measure of structured uncertainty, the next step is to express how it modifies the basic interaction between the charged fermion and the electromagnetic field. The guiding principle is that the new formulation must preserve the two pillars of QED: Lorentz invariance and local gauge symmetry. Any mechanism that softens locality must do so without violating the conservation laws and symmetry relations that those invariances guarantee.

In conventional QED, the interaction is described by the term $\mathcal{L}_{\text{int}} = -e\,\bar{\psi}(x)\gamma^{\mu}\psi(x)A_{\mu}(x)$, which assumes that the electron and photon fields meet at the same spacetime point. The strength of the coupling, represented by the electric charge e, is taken to be universal and exact. This idealization of coincidence, although mathematically convenient, is precisely what produces ultraviolet divergences when loop integrals explore arbitrarily small separations. The goal of the present framework is to preserve the same interaction in form but to replace exact coincidence with a physically meaningful overlap governed by the fuzziness of spacetime.

To achieve this, the local product of fields is replaced by a nonlocal convolution in which each field interacts not at a single point but across a small region surrounding it. The extent of this region is controlled by a Lorentz-invariant smearing function that depends only on the invariant separation between points. The Pythagorean-fuzzy weight D(Φ) enters as a modulating factor that adjusts the effective coupling according to the local degree of hesitation. In this way, the interaction is distributed smoothly over spacetime rather than being concentrated at a single geometric point.

The nonlocal form of the interaction can be written schematically as an integral over pairs of nearby points. The contribution of any pair is weighted by two elements: the smearing kernel, which determines the geometric proximity, and the fuzzy weight, which measures how strongly the interaction at that midpoint participates in physical reality. To preserve local $U(1)$gauge symmetry in this nonlocal structure, the separated fermion fields are connected by an open Wilson line. The Wilson line between spacetime points $x$and $y$is defined as

$$W(x,y) = \mathcal{P}\exp\left[-ie\int_y^x A_\mu(\xi)\, d\xi^\mu\right],$$

where $\mathcal{P}$ denotes path ordering along an arbitrary smooth curve from $y$to x.

Under a local gauge transformation, the Wilson line transforms covariantly so that the bilinear combination $\bar{\psi}(y)W(x,y)\psi(x)$ remains gauge invariant. This guarantees preservation of gauge symmetry and the associated conservation laws.

Conceptually, the Wilson line plays the role of a bridge linking the two separated field evaluations. It compensates for the phase difference that would otherwise arise when the gauge potential varies between the two points. Without it, the nonlocal product would not transform properly under local changes of phase, and the delicate algebraic structure that underlies the conservation of electric charge would collapse. Including this connector allows the theory to remain consistent with the established gauge structure of QED while relaxing its assumption of strict locality.

The existence of a conserved fermion current follows directly from the gauge invariance of the nonlocal action. Consider an infinitesimal local $U(1)$gauge transformation,

$$\psi(x) \to e^{ie\alpha(x)}\psi(x), \bar{\psi}(x) \to \bar{\psi}(x)e^{-ie\alpha(x)}, A_\mu(x) \to A_\mu(x) - \partial_\mu\alpha(x).$$

Because the separated fermion fields are connected by a Wilson line, the phase acquired at one spacetime point is transported consistently to the other. The variation of the fermion bilinear is therefore exactly compensated by the variation of the gauge field along the path. The nonlocal interaction term remains invariant under this transformation.

Gauge invariance of the full action implies, through Noether's theorem, the continuity equation $\partial_\mu J^\mu(x) = 0$, where the conserved current is defined by functional differentiation of the action with respect to the gauge field, $J^\mu(x) = \frac{\delta S}{\delta A_\mu(x)}$. The nonlocal structure modifies the detailed expression of the current by introducing a smeared contribution weighted by the kernel and the fuzzy field, but its divergence vanishes identically due to gauge symmetry. In the limit $\sigma \to 0$and $D(\Phi) \to 1$, the current reduces smoothly to the standard QED expression $J^\mu = \bar{\psi}\gamma^\mu\psi$.

Thus, charge conservation is preserved exactly within the Pythagorean-fuzzy nonlocal framework, despite the relaxation of strict pointwise locality.

The smearing kernel itself is chosen to depend only on the Lorentz-invariant distance between the two points, so that the nonlocal term does not privilege any particular reference frame. A convenient and physically transparent choice is a Gaussian function whose width σ defines the typical scale of fuzziness. This choice ensures that contributions from widely separated points fall off rapidly and that the limit of σ approaching zero reproduces the local interaction of standard QED. The parameter σ thus sets the smallest physically meaningful resolution of the theory. It can be regarded as the characteristic size of an interaction region—a minimal coherence length below which the concept of a distinct spacetime event loses meaning.

More explicitly, the smearing kernel is defined in terms of the invariant spacetime interval between the interaction points. A convenient covariant choice is

$$K(x-y) = \frac{1}{(2\pi\sigma^2)^2}\exp\left(-\frac{(x-y)_\mu(x-y)^\mu}{2\sigma^2}\right),$$

where $(x-y)_\mu(x-y)^\mu$denotes the Minkowski scalar interval.

Because the exponent depends only on this Lorentz scalar quantity, the kernel transforms as a scalar under Lorentz transformations. The parameter $\sigma$is treated as a universal scalar length scale characterizing the minimal definable interaction region. It does not transform under Lorentz transformations and therefore introduces no preferred reference frame. In the limit $\sigma \to 0$, the kernel approaches a spacetime delta distribution, and the interaction reduces continuously to the local QED vertex.

When the interaction is expressed in momentum space, the smearing kernel introduces a smooth form factor that multiplies the vertex function. This form factor decays exponentially at high momentum transfer, which means that processes involving extremely short distances are naturally suppressed. The result is a built-in ultraviolet regularization that requires no artificial cutoffs and no renormalization subtractions. The theory remains finite because it acknowledges, at a structural level, that interactions cannot occur at distances smaller than the fuzziness scale implied by σ and by the hesitation encoded in the fuzzy field. From a physical standpoint, this modification can be interpreted as a refinement of how electromagnetic coupling operates in regions of strong quantum fluctuation. In ordinary QED the vacuum polarization around a charge extends indefinitely, limited only by the need for renormalization. In the fuzzy formulation, the same polarization cloud acquires a finite core determined by σ, while its strength varies locally with D(Φ). Where spacetime is well defined, the interaction behaves as usual; where hesitation increases, the effective coupling softens. The theory thus captures a dynamic interplay between certainty and uncertainty in the fabric of spacetime.

An important feature of this construction is that it leaves the overall theoretical architecture of QED intact. The field content, gauge symmetry, and form of the Dirac and Maxwell equations remain unchanged. What differs is the microscopic texture of interaction: the vertices are no longer mathematical points but small regions weighted by fuzzy

logic. This minimal change has far-reaching consequences. It introduces finiteness without new particles or dimensions, and it does so in a manner that remains analytically continuous with the established framework of quantum field theory.

A closed Wilson loop is not required in this construction, since the Wilson line appears between charged fields and serves to restore gauge covariance of a nonlocal fermion bilinear rather than to define an independent gauge-invariant observable.

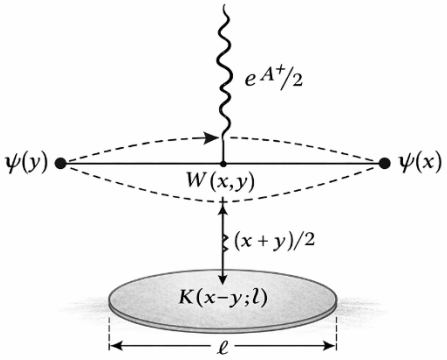

Figure 1. Gauge-covariant nonlocal vertex. The fermion fields at spacetime points $x$and $y$are connected by an open Wilson line $W(x,y)$; the photon couples at the midpoint within a Gaussian smearing region of scale ℓ

The diagram in Fig 1 illustrates how the interaction between two fermion field points $\psi(x)$and $\psi(y)$is extended over a finite region of spacetime rather than confined to a single point. The two points are connected by a Wilson line that ensures gauge covariance by transporting the local phase consistently between them. The photon field $A_\mu((x+y)/2)$interacts at the geometric midpoint, where the Pythagorean-fuzzy weight $D(\Phi((x+y)/2))$modulates the interaction strength according to local structural uncertainty. The Gaussian kernel $f_\sigma(x-y)$defines the nonlocal spread, with width controlled by the fuzziness scale σ. Together, these elements form a smooth, Lorentz-invariant vertex that preserves charge conservation while replacing pointlike coincidence with an overlap of finite extent. In the limit $\sigma \to 0$and $D(\Phi) \to 1$, the interaction reduces continuously to the local QED vertex.

In summary, the gauge-covariant nonlocal interaction translates the idea of the Pythagorean-fuzzy field into the dynamical language of QED. It replaces pointwise coincidence with controlled overlap, introduces a smooth Lorentz-invariant kernel that regularizes short-distance behavior, and maintains gauge invariance through Wilson-line connections. The result is a theory that is both mathematically finite and physically interpretable, one that respects all known symmetries while giving uncertainty a structural role. The following section examines how this modification affects the behavior of radiative corrections and how the built-in fuzziness manifests as natural ultraviolet convergence in quantum processes.

4. RADIATIVE CORRECTIONS AND ULTRAVIOLET CONVERGENCE

A convincing field theory must demonstrate not only conceptual elegance but also technical consistency when confronted with radiative corrections. In Quantum Electrodynamics, such corrections arise from virtual processes in which particles momentarily emit and reabsorb photons, altering their observed properties. These loops generate the self-energy of the electron, the vacuum polarization of the photon field, and vertex corrections that renormalize the charge. In the standard formulation, each of these quantities diverges because the integration extends over arbitrarily large momenta corresponding to infinitely short distances. Renormalization rescues the theory numerically, but at the cost of introducing formally infinite counterterms and a dependence on subtraction procedures that lack intrinsic physical meaning.

In the Pythagorean-fuzzy reformulation, the situation changes in a fundamental way. The modified interaction, being nonlocal and weighted by the fuzzy field, naturally limits the contribution of very short-distance fluctuations. The smearing kernel acts as a soft regulator that suppresses amplitudes for processes involving extremely large momentum transfers, while the fuzzy weight D(Φ) scales the effective coupling according to the degree of local hesitation. These two features together replace the artificial cutoffs of conventional regularization with a built-in physical mechanism rooted in the finite precision of spacetime itself.

The key difference appears most clearly in the behavior of the vertex function. In momentum space, each interaction vertex carries a smooth form factor that decays exponentially with the squared momentum transfer. This factor multiplies the usual vertex term and ensures that loop integrals converge automatically. Whereas the ordinary electron self-energy integral diverges quadratically, the presence of the fuzzy kernel transforms it into a finite expression whose value depends on the fuzziness scale σ. The same reasoning applies to vacuum polarization: the divergence at high momentum is replaced by a rapidly converging integral that reflects the finite spread of interaction regions. In effect, the fuzziness of spacetime removes the unphysical contribution of modes whose wavelength is shorter than the minimal interaction scale.

It is important to note that this finiteness does not come at the expense of physical principles. Gauge invariance, which is responsible for the Ward identity linking the vertex and self-energy corrections, is preserved by the gauge-covariant structure of the nonlocal term. The Wilson line connecting separated points ensures that the phase relationships

between fields remain consistent under local gauge transformations. As a result, charge conservation and current continuity still hold exactly. Lorentz invariance is likewise preserved because the smearing kernel depends only on the invariant distance between points, not on any preferred frame or direction. The theory remains fully relativistic, though its interpretation of locality is softened. The emergence of ultraviolet convergence can therefore be understood as a direct consequence of the theory's physical premises. In a world where interactions occupy regions of finite extent, fields cannot influence each other at separations smaller than that extent. The mathematical divergences of local QED simply record the absence of such a bound. By introducing a fuzziness parameter σ and a field-dependent hesitation π(x), the new formulation restores this bound in a continuous and covariant manner. The parameter σ defines a universal lower limit to meaningful spatial separation, while π(x) encodes local variations arising from the intrinsic uncertainty of the interaction environment. The resulting field theory is finite not by construction but by necessity: it respects the physical impossibility of absolute localization.

One may view the smearing kernel as a kind of physical filter that distinguishes between fluctuations that can be physically realized and those that cannot. Short-wavelength modes that would require resolving spacetime beyond its own uncertainty simply contribute negligibly. The structure of the form factor ensures that this filtering occurs smoothly, without introducing discontinuities or arbitrary thresholds. In practice, this means that the usual loop integrals of QED can be performed in the same manner as before, but their integrands are now multiplied by rapidly decaying functions that render them finite. The presence of the nonlocal smearing replaces divergent renormalization procedures with finite parameter matching governed by the intrinsic scale σ, while preserving the renormalization group structure of the theory.

The presence of ultraviolet convergence in the nonlocal formulation does not eliminate the role of the renormalization group or the β-function. The running of the effective coupling with energy scale remains a meaningful concept, since vacuum polarization effects still modify the interaction strength at different momentum transfers. What changes is the ultraviolet behavior of these corrections. Because each interaction vertex carries a smooth momentum-dependent form factor originating from the smearing kernel, the high-energy contribution to the vacuum polarization is exponentially suppressed. As a result, the growth of the effective coupling at large momentum is moderated relative to local QED.

The β-function can therefore be defined in the usual way from the scale dependence of the effective charge, but its asymptotic behavior is altered by the intrinsic nonlocal scale σ. In particular, the exponential damping of large momenta prevents the unbounded logarithmic growth that leads to the Landau pole in conventional QED. Instead of a divergence at finite energy, the running coupling approaches a softened high-energy behavior controlled by σ. In the limit $\sigma \to 0$, the standard perturbative β-function and its associated Landau pole are recovered continuously. The fuzzy nonlocal framework thus preserves the renormalization group structure while modifying its extreme ultraviolet regime.

Because σ and D(Φ) have clear physical interpretations, their presence does not diminish the predictive power of the theory. On the contrary, they provide an additional level of explanation. The fuzziness scale σ may be associated with a minimal localization length, perhaps related to fundamental constants such as the Compton wavelength or a yet-unobserved substructure of spacetime. The variation of D(Φ) with position could reflect fluctuations of vacuum uncertainty or local field coherence. Both quantities carry meaning that can, in principle, be probed indirectly through high-precision measurements that test the limits of standard QED. The theory is therefore falsifiable in the same sense as any effective field theory: it reproduces known results in its appropriate limit and predicts finite, calculable deviations near its intrinsic scale.

From a broader perspective, the natural regularization achieved here illustrates the power of reinterpreting uncertainty as geometry rather than as probability. The divergence problem, long treated as a mathematical nuisance, emerges as a symptom of an overly idealized view of spacetime. Once the assumption of perfect locality is relaxed, infinities vanish of their own accord. The Pythagorean-fuzzy reformulation therefore provides both a technical advantage and a philosophical resolution. It asserts that what appears as infinite energy density in local QED is simply the attempt to define an interaction within a region smaller than what nature allows.

The implications of this built-in finiteness extend beyond QED itself. Any gauge theory that relies on local field interactions can, in principle, adopt a similar fuzzy nonlocal structure. The same reasoning that renders the electromagnetic self-energy finite would apply to the gluon self-interaction in Quantum Chromodynamics or to the ultraviolet behavior of the electroweak sector. If extended further, this approach might provide a bridge toward quantum gravity, where the unification of general relativity and quantum mechanics almost certainly requires a departure from strict locality. The present model offers a mathematically consistent pathway toward that departure while preserving the operational structure that has made quantum field theory so successful.

In summary, the analysis of radiative corrections in the Pythagorean-fuzzy formulation shows that the theory is finite, symmetric, and physically interpretable. The fuzziness of spacetime acts as an intrinsic regulator that replaces renormalization with geometry. Gauge and Lorentz invariance remain intact, and all known low-energy predictions of QED are recovered when the fuzziness parameters approach zero. What changes is the meaning of interaction itself: it becomes a phenomenon with measurable extent, defined not by exact coincidence but by controlled overlap. The next section turns to the deeper significance of this result, examining how the preservation of symmetry, the continuity of limits, and the physical interpretation of fuzziness come together to form a coherent picture of electromagnetic interaction under uncertainty.

5. SYMMETRY, LOCAL LIMIT, AND PHYSICAL INTERPRETATION

A theoretical framework gains credibility only when its innovations preserve the essential symmetries on which physical laws are built. Gauge and Lorentz invariance lie at the heart of Quantum Electrodynamics, and any modification that compromises them would amount to replacing, not extending, the theory. The Pythagorean-fuzzy formulation was constructed with this constraint in mind. It introduces structural uncertainty into the interaction without disturbing the symmetries that make QED both predictive and coherent.

Gauge invariance is preserved through the use of a covariant nonlocal construction. The interaction between the electron and photon fields, though extended in spacetime, is linked by a Wilson line that transports phase information consistently from one point to another. Under a local gauge transformation, both the matter field and the gauge field change in a correlated way, and the Wilson line precisely compensates for this shift. As a result, the entire nonlocal interaction term transforms as a scalar under gauge transformations, maintaining current conservation and ensuring that the Ward identity still holds. In practical terms, this means that the charge of the electron remains conserved, and the physical content of the gauge principle is untouched. Lorentz invariance is equally secure. The smearing kernel depends only on the invariant spacetime interval between points, so its form is the same in all inertial frames. This prevents any preferred direction or reference frame from entering the theory. Observers related by Lorentz transformations will agree on the functional form of the interaction, differing only in their coordinates. In this respect, the fuzzy nonlocal modification alters the geometry of interaction but not the symmetry of spacetime. The resulting dynamics are covariant, and the classical limit of relativistic field theory remains intact.

Preserving these symmetries is more than a mathematical exercise; it carries deep physical meaning. It shows that the introduction of fuzziness does not imply disorder or violation of conservation laws. Instead, it represents a refinement of structure within the same logical framework. The electron's motion, the propagation of light, and the invariance of physical laws under changes of inertial frame all remain as they were. What changes is the microscopic interpretation of what it means for two fields to "meet" or for an interaction to "occur." The new theory interprets these events not as infinitely precise coincidences but as overlapping regions of finite extent. In that reinterpretation, the mathematical singularities of local field theory lose their physical relevance. The recovery of standard QED as a limiting case confirms this continuity. When the fuzziness parameters vanish—when σ tends to zero and the fuzzy weights approach unity—the smearing kernel collapses to a delta function, and the interaction term reduces exactly to its local form. All predictions of conventional QED are then reproduced with no residual modification. This behavior distinguishes the present formulation from more radical proposals that alter the structure of space or field operators themselves. Here, the fuzziness does not redefine the laws of motion; it modifies only their domain of applicability by recognizing that perfect locality is an abstraction rather than a property of nature.

The parameters that define the fuzzy regime have clear physical interpretations. The smearing scale σ represents the minimal region within which an electromagnetic interaction can be meaningfully defined. It can be thought of as a measure of the smallest coherent volume of spacetime available to an exchange of virtual photons. The fuzzy weight $D(\Phi)$, which depends on the local configuration of the Pythagorean field, expresses how strongly a region participates in that interaction. Together they define a kind of "uncertainty texture" on spacetime: a landscape of participation that varies continuously but never permits infinite precision. This view replaces the rigid geometric fabric of classical spacetime with one that is softly structured, yet remains smooth and differentiable on scales larger than σ. From a conceptual standpoint, the preservation of gauge and Lorentz symmetries while introducing fuzziness suggests a deeper harmony between uncertainty and order. The formalism shows that indeterminacy need not imply violation of symmetry or breakdown of predictability. Instead, uncertainty can be built into the geometry of the theory in a way that reinforces its consistency. The Pythagorean-fuzzy parameters simply limit the resolution at which spacetime can be meaningfully probed. They do not alter the governing equations, only the domain over which those equations can be applied without contradiction.

This perspective offers a natural interpretation of renormalization. In standard QED, divergent integrals are rendered finite by redefining mass and charge. Here, those same divergences never appear because the theory refuses to describe interactions at scales smaller than its intrinsic uncertainty. Renormalization becomes unnecessary, not because the divergences are subtracted away, but because the physical situation they would describe no longer exists. The fuzziness of spacetime acts as a built-in acknowledgment of the limits of definability. In this sense, the Pythagorean-fuzzy formulation achieves what renormalization merely enforces: a finite theory consistent with observation. The smooth local limit also clarifies the theory's empirical standing. Since standard QED is recovered exactly when fuzziness vanishes, all existing experimental confirmations of QED remain valid. Any deviation from those results would occur only at energy scales high enough to probe the structure associated with σ. Detecting such effects would require precision beyond current capabilities, though in principle small corrections could manifest in extremely high-energy scattering or in the behavior of quantum vacuum polarization at short distances. The theory therefore remains compatible with all known data while offering a testable direction for future exploration.

There is also a philosophical resonance in this formulation. It challenges the long-standing notion that fundamental theories must rest on perfectly sharp mathematical points. By demonstrating that gauge and Lorentz symmetries survive even when locality is softened, it suggests that the essential features of physics do not depend on infinitesimal precision. Symmetry, not exactness, is what preserves the coherence of natural law. The fuzziness embedded in $\Phi(x)$ may thus be

viewed as a more faithful representation of physical reality—one where uncertainty is not a flaw to be corrected but a property to be understood.

In conclusion, the Pythagorean-fuzzy QED framework preserves the structural integrity of the standard theory while reinterpreting its foundations. Gauge invariance, Lorentz symmetry, and current conservation remain exact. The local limit reproduces every verified prediction of conventional QED. Yet the theory replaces the need for renormalization with a geometric acknowledgment of uncertainty. It retains the beauty and coherence of the original structure but grounds it in a more physically realistic picture of spacetime, one that is finite in its precision and self-consistent in its logic. The next section extends this discussion to broader implications, exploring how the same principles may generalize to other interactions and how they might inform future approaches to unifying quantum fields with the geometry of spacetime itself.

6. EXEMPLIFICATION: ONE-LOOP ELECTRON SELF-ENERGY IN PYTHAGOREAN-FUZZY QED

To illustrate the operational implications of the Pythagorean-fuzzy reformulation, we consider the one-loop correction to the electron self-energy — one of the canonical processes in quantum electrodynamics (QED) where ultraviolet divergences traditionally occur.

In this framework, the interaction vertex is not a pointlike coincidence in spacetime, but a gauge-covariant nonlocal overlap modulated by the Pythagorean-fuzzy field and a Lorentz-invariant Gaussian kernel characterized by a finite width ℓ.

The corresponding effective interaction Lagrangian is expressed as

$$\mathcal{L}_{\text{int}}^{\text{fuzzy}} = e\, D(x) \int d^4y\, K(x,y;\ell)\, \bar{\psi}(y)\, W(x,y)\, \gamma^\mu\, \psi(x)\, A_\mu(y),$$

where $K(x,y;\ell) = \frac{1}{(2\pi\ell^2)^2} \exp\left[-\frac{(x-y)^2}{2\ell^2}\right]$ is the smearing kernel that ensures smooth nonlocality, $D(x)$is the defuzzification operator encoding the local participation and hesitation degrees, and $W(x,y)$is the Wilson line that guarantees gauge invariance between the points $x$and y.

Within this formalism, the one-loop electron self-energy amplitude in momentum space takes the modified form

$$\Sigma_{\text{fuzzy}}(p) = \int \frac{d^4k}{(2\pi)^4}\, e^{-\ell^2 k^2}\, D(x)\, \frac{\gamma^\mu\, (\gamma^\nu p_\nu - \gamma^\nu k_\nu + m)\, \gamma_\mu}{[(p-k)^2 - m^2]\,[k^2 - \mu^2]}.$$

The exponential damping factor originating from the Gaussian kernel suppresses high-momentum modes, ensuring convergence of the integral without introducing any *ad hoc* cut-offs or counter terms. In this sense, ultraviolet divergences are regularized dynamically by the intrinsic nonlocality of the interaction vertex.

Physically, the Pythagorean-fuzzy field $D(x)$modulates the effective coupling strength according to the intrinsic uncertainty at each spacetime point, reflecting finite participation rather than exact pointwise localization.

In the local limit, when $\ell \to 0$and $D(x) \to 1$, the interaction reduces continuously to the standard pointlike QED vertex, and the familiar self-energy expression is recovered, reproducing all empirical results of conventional QED.

This explicit calculation demonstrates that the Pythagorean-fuzzy extension of QED provides a natural and symmetry-preserving ultraviolet regularization. By embedding structured uncertainty directly into the interaction vertex, it resolves the divergence problem at its conceptual origin, rather than by external renormalization prescriptions.

The Figure 2 illustrates the one-loop electron self-energy correction within the Pythagorean-fuzzy nonlocal quantum electrodynamics framework.

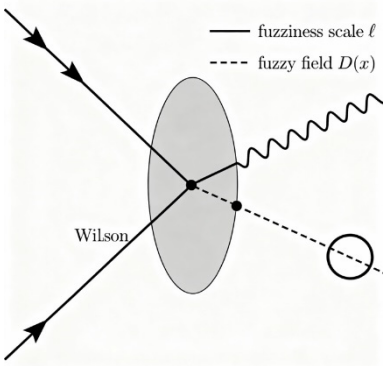

Figure 2. One-loop Electron Self-Energy in Pythagorean-Fuzzy QED with Nonlocal Fuzzy Vertex

The electron line enters and exits through a nonlocal interaction vertex represented as a smooth elliptical Gaussian-shaped region, marked by the fuzziness scale ℓ and the fuzzy field defuzzification parameter $D(x)$. The electron emits and reabsorbs a virtual photon in the loop, depicted by the wavy photon line. A dashed Wilson line connects interaction points inside the fuzzy vertex region, ensuring gauge covariance. This visual conveys how the

interaction vertex in fuzzy QED is extended over a finite spacetime region, providing a physical mechanism for ultraviolet regularization without the need for renormalization counterterms.

7. BROADER IMPLICATIONS AND EXTENSIONS

The reformulation of Quantum Electrodynamics within a Pythagorean-fuzzy framework does more than provide an elegant solution to the problem of ultraviolet divergence. It invites a wider reconsideration of how uncertainty, locality, and interaction are connected across the structure of physical theory. The idea that fuzziness is intrinsic to spacetime rather than a by-product of measurement suggests that the same reasoning can extend far beyond electrodynamics, potentially reshaping how other interactions and even spacetime itself are described.

A natural first direction of extension lies in the non-Abelian gauge theories that form the backbone of the Standard Model. Quantum Chromodynamics, for example, inherits many of the mathematical strengths and weaknesses of QED. Its self-interacting gluon fields make the ultraviolet behavior even more intricate, requiring renormalization of both the gauge coupling and the field propagators. Introducing a Pythagorean-fuzzy structure into QCD could regularize these interactions in the same spirit as it does for QED. Each color field could carry its own fuzzy participation factor, reflecting the limited definability of color charge at sub-hadronic scales. The resulting theory would still respect SU(3) gauge symmetry because the fuzzy weights, if constructed as color-invariant scalars, would not interfere with the group structure. The expected outcome would be a finite, gauge-covariant formulation that preserves asymptotic freedom while softening the behavior of the coupling at extremely short distances.

The same conceptual framework could apply to the electroweak interaction, where the unification of electromagnetic and weak forces already relies on a symmetry-breaking mechanism to introduce mass. Here, the fuzzy field could interact with the Higgs sector, providing a new interpretation of spontaneous symmetry breaking. Instead of attributing mass generation solely to the vacuum expectation value of a scalar field, one might view it as emerging partly from the finite resolution of spacetime, encoded in the hesitation of interaction itself. The interplay between Pythagorean-fuzzy geometry and symmetry breaking could open a subtle but interesting route toward a deeper understanding of how vacuum structure and particle mass arise. A more speculative but equally important direction concerns the relation between fuzzy field theory and the problem of quantum gravity. The core difficulty of unifying gravity with quantum mechanics lies in the clash between continuous spacetime geometry and the discrete, probabilistic nature of quantum events. Most approaches to quantum gravity—whether through loop quantization, string theory, or causal sets—try to impose discreteness from the top down by redefining the underlying manifold. The Pythagorean-fuzzy approach offers a different route. It replaces discreteness with gradation, introducing a minimal definable region not through lattice spacing but through degrees of participation. The fuzziness scale σ then acquires a natural interpretation as a measure of the smallest meaningful region of spacetime curvature. Such a description could, in principle, regularize the singularities of general relativity by recognizing that the notion of a spacetime point ceases to make sense below a certain level of hesitation.

At a conceptual level, the theory aligns with the broader movement toward "quantum geometry," where space and time are understood not as passive backgrounds but as dynamical entities shaped by uncertainty. In a fuzzy spacetime, the metric tensor could itself be replaced by a field of graded relations, describing how strongly or weakly regions of the universe belong to one another. The Pythagorean-fuzzy formalism, already equipped with membership, non-membership, and hesitation, provides a ready-made language for this idea. It can express not only how fields interact but also how spacetime itself may participate in those interactions to varying degrees. This perspective naturally bridges the gap between geometric and logical descriptions of the universe, placing both within a single, coherent framework. Beyond high-energy physics, the implications of this approach extend to the philosophy of science. The fuzzy reformulation suggests that the pursuit of absolute precision in theoretical constructs may be misplaced. Nature seems to operate through balance rather than absolutes—probability in outcomes and hesitation in definitions. The classical ideal of exact points and instantaneous events has always been a convenient abstraction, but the success of fuzzy logic in modeling real physical behavior hints that the underlying world is inherently continuous yet never perfectly sharp. This reinterpretation does not weaken physics; it grounds it more firmly in the conditions of observation and the finite character of information. It shifts emphasis from exactness to coherence, from mathematical idealization to physical plausibility.

There are also practical consequences for computation and modeling. Nonlocal interactions with fuzzy weights are naturally stable under numerical evaluation, as the exponential suppression of high-momentum modes removes the need for artificial cutoffs in simulations. This could simplify lattice and perturbative calculations, offering a more physical alternative to regularization schemes that introduce arbitrary parameters. Moreover, the Pythagorean-fuzzy representation of uncertainty could inspire new numerical methods that blend logical and probabilistic elements—methods that might be particularly suited to multiscale phenomena where classical and quantum regimes overlap. While the present study has focused on QED as a conceptual prototype, the framework's flexibility suggests that it could be extended in stages. The first stage would involve detailed computation of higher-order corrections to verify that gauge symmetry and finiteness persist in all perturbative orders. The second would apply the same logic to other gauge groups, exploring whether the fuzzy structure modifies running couplings in a way that naturally unifies them at high energies. The third, more ambitious stage, would attempt to couple the fuzzy field to gravity, allowing the fuzziness of spacetime to participate directly in curvature and energy-momentum balance. Each of these developments would test the extent to which uncertainty, once promoted to a structural feature, can serve as a universal regularizing principle across physical theory.

The broader message of the Pythagorean-fuzzy formulation is that uncertainty and symmetry need not be opposing ideas. A theory can respect the deepest conservation laws while admitting that nature forbids infinite precision. When formulated carefully, this recognition does not obscure physics; it clarifies it. It shows that finiteness and coherence can emerge from the same mathematical structures that once produced infinities, provided those structures are interpreted with the appropriate degree of softness. The fuzziness field, viewed as an extension of geometry and logic, thus becomes not merely a regularization device but a statement about the character of physical law.

The next and final section summarizes the essential achievements of this framework, restating its conceptual motivations, technical results, and potential avenues for further investigation.

8. CONCLUSIONS

This study has developed a Pythagorean-fuzzy reformulation of Quantum Electrodynamics in which uncertainty is treated not as an afterthought but as an inherent property of spacetime and interaction. The central motivation was to confront the conceptual tension between the empirical success of QED and its mathematical dependence on renormalization. In the standard theory, pointlike interactions produce divergences that must be cancelled by counterterms. The present work addresses those infinities at their source by replacing the idealization of perfect locality with a structured form of uncertainty. By introducing a Pythagorean-fuzzy field $\Phi(x)$, each spacetime region acquires measurable degrees of participation, exclusion, and hesitation. These parameters quantify how strongly an event belongs to an interaction and how sharply it can be localized. When mapped through the defuzzification operator $D(\Phi)$, they define an effective coupling that varies smoothly across spacetime, modulating the strength of interaction in proportion to local uncertainty. The resulting theory is nonlocal but gauge-covariant: the Wilson line preserves local phase relations, and the smearing kernel depends only on invariant distance, ensuring Lorentz symmetry. The modification is therefore not a replacement for QED but a consistent generalization that introduces structural finiteness while leaving the underlying symmetries intact.

The physical consequences of this reformulation are both technical and conceptual. At the technical level, the fuzzy smearing of interaction vertices introduces a smooth form factor in momentum space that suppresses contributions from extremely short distances. All loop integrals that would diverge in the local theory become finite, eliminating the need for renormalization. Ultraviolet convergence emerges naturally from the finite resolution of spacetime itself. At the conceptual level, this framework replaces the idea of exact pointwise coincidence with that of finite overlap, transforming the notion of interaction from an instantaneous event to a process extended in space and time. The divergence problem is resolved not by subtraction but by recognizing that perfect locality has no physical meaning.

The preservation of gauge and Lorentz invariance demonstrates that uncertainty and symmetry can coexist without conflict. Fuzziness does not imply disorder; it represents a more accurate reflection of physical reality, where no measurement or process can achieve infinite precision. The local limit of the theory, obtained when the fuzziness parameters vanish, reproduces every verified prediction of QED, guaranteeing empirical consistency. Yet the framework goes beyond existing formalism by providing a physically interpretable regularization that requires no arbitrary cutoffs or counterterms. It unites probabilistic and logical forms of uncertainty under a single mathematical structure and anchors them in the geometry of spacetime. The broader implications are significant. The same logic that regularizes QED could be applied to non-Abelian gauge theories, where self-interactions make divergences more severe, or to gravity, where the notion of a spacetime point may itself break down. The Pythagorean-fuzzy formalism offers a path toward such generalization by interpreting minimal length not as a discrete unit but as a degree of definability. It suggests that the continuum description of nature remains valid, but only when enriched with a graded notion of existence that prevents infinitesimal idealizations from producing unphysical infinities.

At a deeper level, this work argues that the mathematical structure of physics need not be built on sharp boundaries and exact points. Reality, as revealed by quantum mechanics, operates through balance rather than absolutes: probabilities govern outcomes, and fuzziness governs definitions. By incorporating this principle into the very geometry of field interactions, the Pythagorean-fuzzy approach offers a self-consistent and finite extension of quantum field theory that remains faithful to its empirical core. It transforms uncertainty from a source of limitation into a source of regularity. The framework developed here does not claim to complete the story of quantum theory, but it provides a direction that reconciles precision with finiteness and logic with geometry. Its continuity with established physics ensures that it can be explored without speculative leaps, and its conceptual foundations invite reexamination of how mathematical idealization shapes physical understanding. If the universe indeed prohibits perfect exactness, then a theory that builds this prohibition into its structure is not merely a mathematical convenience—it is a closer representation of nature itself.

Statement on Novelty and Scientific Importance

The present work introduces a novel theoretical framework that integrates Pythagorean fuzzy set theory into the structural formulation of quantum electrodynamics. Rather than treating uncertainty solely as a probabilistic feature of quantum amplitudes, the proposed approach embeds a graded notion of participation directly into the interaction vertex of the theory. In this framework, spacetime regions are characterized by degrees of membership, non-membership, and hesitation, providing a quantitative representation of finite definability in field interactions.

Unlike conventional nonlocal regularization schemes that introduce external cutoffs or modified propagators, the present formulation derives ultraviolet suppression from an intrinsic geometric mechanism. The nonlocal interaction vertex is constructed in a gauge-covariant manner using Wilson-line connections and a Lorentz-invariant smearing kernel. As a result, ultraviolet divergences are moderated through exponential damping while preserving gauge symmetry and Lorentz covariance. The framework therefore offers a structurally consistent alternative to purely formal renormalization procedures.

From a foundational perspective, the work reframes the divergence problem of QED as a consequence of idealized pointlike locality. By replacing exact coincidence with finite overlap governed by a fuzziness scale, the theory incorporates minimal interaction resolution without altering the core dynamical equations. In the appropriate local limit, all standard results of QED are recovered continuously.

The methodology does not modify the axioms of quantum field theory but operates as an extension within the established Hilbert-space formalism. Its significance lies in providing a unified language that connects logical uncertainty with geometric nonlocality in gauge theories. The approach may serve as a conceptual bridge toward broader applications in non-Abelian gauge fields or theories where strict locality is expected to break down.

In summary, the novelty of this work lies in embedding structured uncertainty directly into the interaction geometry of quantum electrodynamics, yielding a finite and symmetry-preserving nonlocal formulation. Its scientific importance rests on offering a coherent mechanism for ultraviolet moderation while maintaining the foundational principles of gauge field theory.

ORCID

Supratim Mukherjee, https://orcid.org/0000-0003-2190-2831

REFERENCES

[1] R.R. Yager, "Pythagorean fuzzy subsets," in: *Proc. 2013 Joint IFSA/NAFIPS World Congress and Annual Meeting*, (IEEE, Edmonton, AB, Canada), pp. 57–61. https://doi.org/10.1109/IFSA-NAFIPS.2013.6608375

[2] R.R. Yager, "Pythagorean membership grades in multicriteria decision making," IEEE Trans. Fuzzy Syst. **22**(4), 958–965 (2014). https://doi.org/10.1109/TFUZZ.2013.2278989

[3] X. Peng, and Y. Yang, "Some results for Pythagorean fuzzy sets," Int. J. Intell. Syst. **30**(11), 1133–1160 (2015). https://doi.org/10.1002/int.21738

[4] J. Mahanta, and S. Panda, "Distance measure for Pythagorean fuzzy sets with varied applications," Neural Comput. Appl. **33**(24), 17161–17171 (2021). https://doi.org/10.1007/s00521-021-06308-9 (PMID: 34376923, PMCID: PMC8339398)

[5] M. Kirişci, "New type Pythagorean fuzzy soft set and decision-making application," arXiv:1904.04064 [math.GM].

[6] M.C. Bozyiğit, M. Olgun, and M. Ünver, "Circular Pythagorean fuzzy sets and applications to multi-criteria decision making," Informatica, **34**(4), 713–742 (2023). https://doi.org/10.15388/23-INFOR529

[7] G.V. Efimov, "Nonlocal quantum field theory, nonlinear interaction Lagrangians, and the convergence of the perturbation-theory series," Theor. Math. Phys. **2**, 217–223 (1970). https://doi.org/10.1007/BF01038039

[8] N.V. Krasnikov, "Introduction to nonlocal field theory including gravity," Phys. Part. Nucl. **55**, 1467–1473 (2024). https://doi.org/10.1134/S1063779624701107

[9] V.A. Alebastrov, and G.V. Efimov, "Causality in quantum field theory with nonlocal interaction," Commun. Math. Phys. **38**(1), 11–28 (1974). https://doi.org/10.1007/BF01651546

[10] A. Idilbi, and I. Scimemi, "Singular and regular gauges in soft-collinear effective theory: the introduction of the new Wilson line T," Phys. Lett. B, **695**, 463–468 (2011). https://doi.org/10.1016/j.physletb.2010.11.060; arXiv:1009.2776 [hep-ph]. https://doi.org/10.48550/arXiv.1009.2776

[11] S. Gukov, and A. Kapustin, "Topological quantum field theory, nonlocal operators, and gapped phases of gauge theories," arXiv:1307.4793 [hep-th]. https://doi.org/10.48550/arXiv.1307.4793

[12] M.E. Peskin, and D.V. Schroeder, *An Introduction to Quantum Field Theory*, (Westview Press, Boulder, CO, 1995).

ПІФАГОРІЙСЬКО-НЕЧІТКЕ НЕЛОКАЛЬНЕ ПЕРЕФОРМУЛЮВАННЯ КВАНТОВОЇ ЕЛЕКТРОДИНАМІКИ

Супратім Мукерджі

Кафедра математики, Державний коледж загальної освіти, Техатта, Індія

Квантова електродинаміка (КЕД) є найточнішою теорією у фізиці, проте її припущення про точкові взаємодії між зарядженими частинками та фотонами призводить до ультрафіолетових розбіжностей, які потребують перенормування. У цій статті пропонується піфагорійсько-нечітка нелокальна переформуляція КЕД, що вбудовує структуровану невизначеність безпосередньо в структуру взаємодії. Кожна область простору-часу описується піфагорійським нечітким полем зі ступенями належності, неналежності та вагань, що кількісно визначає, наскільки сильно подія бере участь у взаємодії та наскільки точно її можна локалізувати. Звичайна точкова вершина замінюється гладким, калібрувально-коваріантним нелокальним зв'язком, модульованим лоренц-інваріантним ядром та дефазифікованою вагою нечіткого поля. Ця структура зберігає всі симетрії КЕД, автоматично пригнічуючи розбіжності на коротких відстанях. Ультрафіолетові розбіжності пригнічуються у своєму виникненні, що призводить до скінченних внесків власної енергії та вакуумної поляризації в нелокальних рамках, без появи розбіжних контрчленів. Фізично, це формулювання інтерпретує квантові взаємодії як скінченні «нечіткі» процеси, розподілені по областях обмеженої визначеності. Математично, воно об'єднує логіку піфагорових нечітких множин з геометрією теорії поля, забезпечуючи природний механізм регуляризації, який повністю відповідає стандартній КЕД у різко-локальній границі.

Ключові слова: *нелокальна квантова теорія поля; калібрувально-коваріантна регуляризація; Лоренц-інваріантне розмиття; лінії Вілсона; ренормгрупа; Піфагорове нечітке поле; ультрафіолетова збіжність*

EAST EUROPEAN JOURNAL OF PHYSICS. **1.** 187-190 (2026)
DOI:10.26565/2312-4334-2026-1-18 ISSN 2312-4334

FISSION TIME SCALES AND DISTRIBUTIONS STUDIED USING A LANGEVIN DYNAMICAL MODEL

Charmi Vadagama[1]*, Pruthul Desai[1], M.T. Senthil Kannan[2]
[1]*Department of Physics, Sir P.T. Sarvajanik College of Science, Surat-395007, India*
[2]*Department of Physics, Christ the King Engineering College, Karamadai - 641104, India*
**Corresponding Author E-mail: charmy1612@gmail.com*
Received January 1, 2026; revised February 16, 2026; accepted February 18, 2026

The fission time scale and associated distributions play a crucial role in investigating the full dynamical evolution of the excited compound nucleus. In the present work, we have performed a one-dimensional Langevin dynamical model calculation to simulate the fission time scale and corresponding fission time distributions (FTDs) for ^{125}Cs, ^{213}Fr, and ^{243}Am. The time evolution of the collective deformation coordinate from the ground state to scission is followed under the influence of dissipation, fluctuations, and realistic fission barriers, and a large ensemble of trajectories is used to construct fission–time distributions for each compound nucleus. The results reveal distinct differences in the shapes and widths of the distributions, characterized by extended long-time components that significantly impact the average fission time. Particle evaporation is found to play an important role in shaping the fission time distributions by modifying the excitation energy during the dynamical evolution. These findings emphasize the importance of analyzing the full fission time distribution, rather than relying solely on average values, for a realistic description of fission dynamics.
Keywords: *Nuclear fission; Fission time scale; Fission time distribution; Langevin dynamical model; Neutron multiplicities*
PACS: 24.75. +i, 25.85 -w, 24.60.ky

INTRODUCTION

Nuclear fission is a complex many-body process in which an excited compound nucleus evolves from its ground-state configuration to scission under the combined influence of the mean nuclear potential, dissipation, fluctuation, and statistical particle emission. It has been a topic of great interest and has been extensively studied both theoretically and experimentally [1-3]. Also, the study of nuclear fission dynamics is a challenging subject due to the intricate nature of this process. A compound nucleus may undergo fission depending on the excitation energy, angular momentum, fission barrier, and other factors. The dynamics of the fission process are governed primarily by the target–projectile combination, viz -a- viz., the total mass and the excitation energy. This relevance can be examined by using the fission timescale (τ_f), which is the time required for the CN to reach the scission configuration from the ground state shape. Significant effort has been made to comprehend fission timescales through various experimental techniques. Fission time (τ_f) of an excited compound nucleus can be inferred from the measured particle multiplicities such as pre-scission neutron multiplicities [4, 5], charged particles (proton and α) [6], and γ-rays [7]. Also, the average fission time (τ_f) can be estimated from observables such as the evaporation residue (ER) cross-section [8] and fission probabilities [9]. All these nuclear probes are considered indirect probes, and with a proper model, they are used to evaluate the fission time in the range of 10^{-21}s (1 zs = 10^{-21}s). On the other hand, direct probes, including crystal blocking and K-shell X-ray measurements, determine significantly longer lifetimes in the order of 10^{-18}s (attosecond) scales. This apparent discrepancy has motivated renewed interest in dynamical approaches that explicitly follow the time evolution of the fissioning system, incorporating fluctuations, dissipation, and particle evaporation on an event-by-event basis. A one-dimensional Langevin dynamical model has been used recently to resolve this discrepancy [10]. In this work, a similar study is extended for a wide range of masses with different excitation energies.

THEORETICAL MODEL

In the present work, a stochastic one-dimensional Langevin dynamical model is utilized to describe the full dynamical evolution of an excited compound nucleus, with the elongation of the nucleus considered as a collective coordinate and usually defined in terms of the Funny-Hill shape parameter *c* [11]. The one-dimensional Langevin equation in terms of *c* is given by,

$$\frac{dp}{dt} = -\frac{p^2}{2}\frac{dm^{-1}(c)}{dc} - \frac{dF(c)}{dc} - \beta p + g\Gamma(t),$$
$$\frac{dc}{dt} = \frac{p}{m(c)}, \quad (1)$$

where *c* is the collective coordinate defining the deformation of a fissioning nucleus, and p is the collective momentum conjugate to *c*. The shape-dependent collective inertia *m(c)* is calculated by employing the Werner-Wheeler approximation [12] for the irrotational flow of incompressible nuclear fluid. The parameter β appearing in Eq. (1) is the

Cite as: C. Vadagama, P. Desai, M.T. S. Kannan, East Eur. J. Phys. 1, 186 (2026), https://doi.org/10.26565/2312-4334-2026-1-18

shape-independent reduced dissipation coefficient that represents the coupling between collective and intrinsic nuclear degrees of freedom and governs the irreversible energy flow from collective to the intrinsic excitation and is denoted by the ratio of the dissipation coefficient η to the inertia parameter m (β =η/m). Since nuclear dissipation governs the fission time scale and the time available for prescission neutron emission, the prescission neutron multiplicity (ν_{pre}) is highly sensitive to β. Therefore, β is treated as the only adjustable parameter and is constrained by reproducing the experimental (ν_{pre}). The product $g\Gamma(t)$ is the random force, with $\Gamma(t)$ being the time-dependent stochastic part with time average $\langle\Gamma|(t)\rangle = 0$ and time-correlation $\langle\Gamma(t)\Gamma(t')\rangle = \delta(t - t')$. g is the strength of the random force, and it is related to the dissipation coefficient η through the fluctuation-dissipation theorem: $g^2 = \eta T$ [13].

The driving force for the collective motion is extracted from the Helmholtz free energy:

$$F(c) = V(c) - \{a(c) - a_0\}T^2, \tag{2}$$

where $V(c)$ and $a(c)$ are the deformation-dependent potential energy and level density parameter, respectively. a_0 is the value of $a(c)$ at the spherical shape (c = 1).

The shell correction in the level density parameter $a(c)$ is incorporated using Ignatyuk's prescription [14]. The nuclear temperature T in the above Eq. (2) is calculated from the ground state excitation energy (E^*) and the ground state level density parameter a_0 by using the Fermi gas relation: $T = \sqrt{E^*/a_0}$. The deformation-dependent shell correction energy in $V(c)$ is obtained by solving a two-centered Woods-Saxon mean field [15], followed by the application of Strutinsky's prescription [16].

A large number of Langevin trajectories, approximately 10^6, are sampled to reduce statistical uncertainties. For each event, dynamics are followed numerically up to 10^{-15}s with a time-step of 10^{-25}s. At each time step, evaporation of light particles (n, p, α) and GDR γ-rays are sampled with the Monte-Carlo technique. The standard statistical model prescription is considered to calculate the widths for these evaporation channels. The initial collective coordinate is that of a spherical nucleus, and its initial momentum distribution follows from an equilibrated thermal system. A Langevin trajectory is judged as a scission when the neck radius reaches its critical value $C_{sc} = 0.3R_0$; (R_0 being the spherical nucleus radius). For each fission event, fission time is evaluated with associated neutron evaporation fission channels. If c_f^i is the fission time for the ith fission event, then the average fission time is calculated as $\langle c_f\rangle = \frac{\sum_{i=1}^{N_f} c_f^i}{N_f}$, where, N_f is the total number of fission events.

RESULTS AND DISCUSSION

The details of the reactions chosen for the present work are given in Table I. For each compound nucleus excitation energy (E*), the reduced dissipation coefficient (β) – determined by accurately reproducing experimental prescission ν_{pre}(Exp) along with the average fission time $\langle c_f\rangle$, and barrier height (B_f) are listed. These nuclei were chosen to provide a systematic comparison of fission dynamics across a wide range of masses.

Table I: Details of the reactions

CN	E^*(MeV)	ν_{pre} (Exp)	ν_{pre}(Cal)	β(Mev/ħ)	$\langle c_f\rangle$ zs	B_f (MeV)	Ref.
^{125}Cs	241.78	4.0 ± 0.5	4.0676	4	1.45×10^3	34.64	[5]
^{213}Fr	72.19	3.28 ± 0.30	3.30	5.5	1.53×10^4	18.44	[17]
^{243}Am	54.1	1.35 ± 0.14	1.4312	0.5	3.28×10^1	7.50	[18]

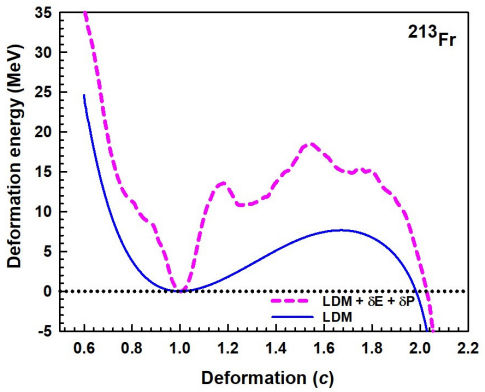

Figure 1. The Potential-energy landscape of the ^{213}Fr nucleus calculated using the Liquid drop model (LDM) (solid line) and the LDM plus microscopic corrections (dashed line) as a function of the collective deformation coordinate c

Fig. 1 shows the deformation energy landscape of ^{213}Fr as a function of the deformation parameter c, incorporating shell and pairing corrections. The height and shape of the fission barrier play a crucial role in governing the fission dynamics by controlling both the barrier penetration probability and the residence time of the compound nucleus in the pre-scission region. The deformation-dependent microscopic corrections significantly modify the macroscopic LDM barrier, converting the originally single-humped fission barrier into a characteristic double-humped shape. This barrier structure leads to a competition between fission and particle evaporation, which strongly influences the average fission time and fission time distributions discussed below.

Fig. 2 depicts the total fission yields of ^{125}Cs, ^{213}Fr, and ^{243}Am as a function of fission time. The fission time distribution is sharply peaked at short times around 10^{-20}s

with a very small non-vanishing tail up to 10^5 zs (zeptosecond) for the ^{125}Cs compound system. Further, the distribution for ^{213}Fr has a broader width with a peak around 10^{-19}s, and has a considerably longer tail up to the maximum dynamical time. The pronounced long-time tail is correlated with the structured fission barrier of Fig. 1, where the second hump and the shallow intermediate minimum trap a non-negligible fraction of trajectories and allow for additional neutron evaporation before scission. Conversely, the actinide nucleus ^{243}Am shows a narrower peak with a shorter τ_f ~ 10^{-20} s without any long tail structure. From these distributions, we have observed the average fission time $\langle\tau_f\rangle$, 1.45×10^3 zs, 1.53×10^4 zs and 3.28×10^1 s for the systems ^{125}Cs, ^{213}Fr and ^{243}Am, respectively. The $\langle\tau_f\rangle$ are mainly contributed by the long tail part of fission yields.

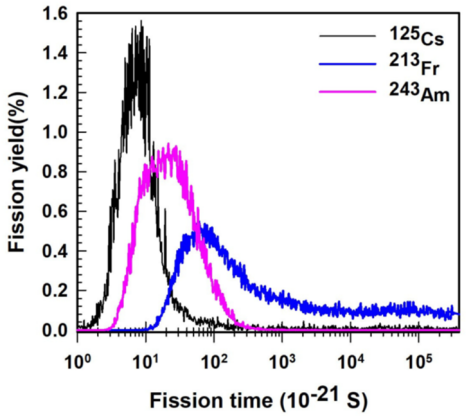

Figure 2. Fission yield distribution as a function of time for ^{125}Cs, ^{213}Fr, and ^{243}Am

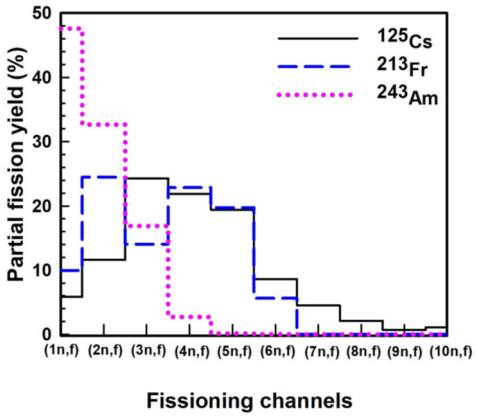

Figure 3. Partial fission yields from different isotopes of ^{125}Cs, ^{213}Fr, and ^{243}Am through neutron evaporation

Further, to understand the behaviour τ_f more clearly, partial fission yields of different fission channels are depicted in Fig. 3. For ^{125}Cs, fission channels up to *(8n, f)* have contributed, which indicates that the CN has survived for a longer dynamical time after the last particle evaporated. This behavior is consistent with the relatively higher fission barrier of ^{125}Cs, which hinders early saddle crossing and allows successive neutron evaporations to occur. Since each neutron usually reduces the CN excitation by 8 to 10 MeV (separation energy kinetic energy), it makes the fission process slower. The same scenario is valid for ^{213}Fr up to *(6n, f)* fission channel. For this system, the available E^* falls between 15 – 25 MeV, hence a substantial percentage of CN persists for a longer time. In contrast, a larger partial fission yield is observed for the *(1n, f)* and *(2n, f)* channels for ^{243}Am, resulting in a very short fission timescale. Also, this behavior can be directly related to the comparatively lower fission barrier of ^{243}Am, which allows rapid saddle crossing and suppresses higher-order evaporation chains.

CONCLUSIONS

The present Langevin dynamical study demonstrates that the fission decay of the compound systems ^{125}Cs, ^{213}Fr, and ^{243}Am is governed by a subtle interplay between excitation energy, fission barrier structure, and dissipation strength. From this study, we conclude that the fission timescale primarily depends on CN mass, which determines the potential energy surface (PES). Consequently, the fission timescale of each nucleus is determined by the shape of the PES near the ground state configuration.

ORCID

Charmi Vadagama, https://orcid.org/0009-0001-4603-8616

REFERENCES

[1] G. Mohanto, M. T. Senthil Kannan, J. Sadhukhan, and B. Srinivasan, Phys. Rev. C, **110**, 034604 (2024). https://doi.org/10.1103/PhysRevC.110.034604
[2] P. Fröbrich, and I. Gontchar, Phys. Rep. **292**, 131 (1998). https://doi.org/10.1016/S0370-1573(97)00042-2
[3] Y. Jia, and J.-D. Bao, Phys. Rev. C, **75**, 034601 (2007). https://doi.org/10.1103/PhysRevC.75.034601.
[4] K. Kapoor, S. Verma, P. Sharma, R. Mahajan, N. Kaur, G. Kaur, B. Behera, *et al.*, Phys. Rev. C, **96**, 054605 (2017). https://doi.org/10.1103/PhysRevC.96.054605
[5] D. Hinde, D. Hilscher, H. Rossner, B. Gebauer, M. Lehmann, and M. Wilpert, Phys. Rev. C, **45**, 1229 (1992). https://doi.org/10.1103/PhysRevC.45.1229
[6] K. Ramachandran, A. Chatterjee, A. Navin, K. Mahata, A. Shrivastava, V. Tripathi, *et al.*, Pramana, **85**, 335 (2015). https://doi.org/10.1007/s12043-015-0988-6
[7] P. Paul, Nucl. Phys. A, **569**, 73 (1994). https://doi.org/10.1016/0375-9474(94)90097-3
[8] B. B. Back, D. J. Blumenthal, *et. al.*, Phys. Rev. C, **60**, 044602 (1999). https://doi.org/10.1103/PhysRevC.60.044602
[9] V. Tishchenko, C.-M. Herbach, D. Hilscher, U. Jahnke, J. Galin, F. Goldenbaum, *et al.*, Phys. Rev. Lett. **95**, 162701 (2005). https://doi.org/10.1103/PhysRevLett.95.162701
[10] M. T. Senthil Kannan, *et al.*, Phys. Rev. C, **98**, 021601 (2018). https://doi.org/10.1103/PhysRevC.98.021601

[11] M. Brack, J. Damgaard, A.S. Jensen, H.C. Pauli, V.M. Strutinsky, and C.Y. Wong, Rev. Mod. Phys. **44**, 320 (1972). https://doi.org/10.1103/RevModPhys.44.320
[12] J. R. Nix, Nucl. Phys. A, **130**, 241 (1969). https://doi.org/10.1016/0375-9474(69)90730-1
[13] Y. Abe, S. Ayik, P.-G. Reinhard, and E. Suraud, Phys. Rep. **275**, 49 (1996). https://doi.org/10.1016/0370-1573(96)00003-8
[14] A. Ignatyuk, M. Itkis, V. Okolovich, G. Smirenkin, and A. Tishin, Sov. J. Nucl. Phys. **21**, 255 (1975).
[15] F. Garcia, O. Rodriguez, J. Mesa, J.D.T. Arruda-Neto, V.P. Likhachev, E. Garrote, *et al.*, Comput. Phys. Commun. **120**, 57 (1999). https://doi.org/10.1016/S0010-4655(99)00199-X
[16] V.M. Strutinsky, Nucl. Phys. A, **122**, 1 (1968). https://doi.org/10.1016/0375-9474(68)90699-4
[17] J.O. Newton, D.J. Hinde, R.J. Charity, J.R. Leigh, J. Bokhorst, *et al.*, Nucl. Phys. A, **483**, 126 (1988). https://doi.org/10.1016/0375-9474(88)90068-1
[18] A. Saxena, *et al.*, Phys. Rev. C, **49**, 932 (1994). https://doi.org/10.1103/PhysRevC.49.932

МАСШТАБИ ТА РОЗПОДІЛИ ЧАСУ ПОДІЛУ, ДОСЛІДЖЕНІ З ЗАСТОСУВАННЯМ ДИНАМІЧНОЇ МОДЕЛІ ЛАНЖЕВЕНА

Чармі Вадагама[1], Прутул Десаі[1], М.Т. Сентіл Каннан[2]
[1]Кафедра фізики, коледж наук ім. сера П.Т. Сарваджаніка, Сурат-395007, Індія
[2]Кафедра фізики, інженерний коледж Христа Царя, Карамадай - 641104, Індія

Шкала часу поділу та пов'язані з нею розподіли відіграють вирішальну роль у дослідженні повної динамічної еволюції збудженого складного ядра. У цій роботі ми виконали розрахунок одновимірної динамічної моделі Ланжевена для моделювання шкали часу поділу та відповідних розподілів часу поділу (FTD) для ^{125}Cs, 213Fr та 243Am. Часова еволюція колективної координати деформації від основного стану до розриву відстежується під впливом дисипації, флуктуацій та реалістичних бар'єрів поділу, а для побудови розподілів часу поділу для кожного складного ядра використовується великий ансамбль траєкторій. Результати показують чіткі відмінності у формах та ширині розподілів, що характеризуються протяжними довгочасовими компонентами, які суттєво впливають на середній час поділу. Виявлено, що випаровування частинок відіграє важливу роль у формуванні розподілу часу поділу, змінюючи енергію збудження під час динамічної еволюції. Ці результати підкреслюють важливість аналізу повного розподілу часу поділу, а не покладатися виключно на середні значення, для реалістичного опису динаміки поділу.

Ключові слова: *ядерний поділ; шкала часу поділу; розподіл часу поділу; динамічна модель Ланжевена; нейтронні множинності*

East European Journal of Physics. 1. 191–202 (2026)
DOI: 10.26565/2312-4334-2026-1-19 ISSN 2312-4334

DFT STUDY OF THE STABILITY, ELECTRONIC, OPTICAL, AND THERMAL PROPERTIES OF TWO-DIMENSIONAL $BiBr_3$ SEMICONDUCTOR

Yadgar Hussein Shwan*, **Majida Ali Ameen**, **Aras Saeed Mahmood**
Physics Department, College of Education, University of Sulaimani, Sulaymaniyah 46001, Kurdistan Region, Iraq
*Corresponding Author e-mail: yadgar.shwan@univsul.edu.iq
Received September 24, 2025; revised February 14, 2026; accepted February 17, 2026

Density functional theory (DFT) serves as a first-principles method to thoroughly investigate the stability of the structure and analyse the electronic, optical, and thermal characteristics of two-dimensional bismuth tribromide (2D $BiBr_3$). Ab-initio molecular dynamic (AIMD) simulations reveal that the structure is thermally stable at 300 K. The $BiBr_3$ behaves as a semiconductor with a 2.84 eV band gap according to its electronic band structure and partial density of state (PDOS) analysis. Optical characterisation reveals that $BiBr_3$ has strong interactions in visible and ultraviolet wavelength domains, which shows its potential in the next-generation of optical and optoelectronic devices. A remarkable Seebeck value estimated via Boltzmann transport calculations, highlights the promise of $BiBr_3$ in low-temperature thermoelectric management. This investigation implies temperature-driven power factor improvement, peaking at 3.25×10^{12} W/K^2·cm·s at 300K. The $BiBr_3$ exhibits moderate heat capacity at intermediate to high temperatures while keeping very low thermal conductivity. This highlights its ability to effectively manage heat and serve as an insulator in various applications. The detailed results show that 2D $BiBr_3$ is a potentially favorable material with diverse possibilities in most technological applications.

Keywords: *$BiBr_3$ structure; DFT; Stability; Electronic characteristics; Thermal properties; Optical characteristics*

PACS: 71.15.Mb, 71.20.-b, 78.20.-e, 72.20.Pa, 65.40.-b

1. INTRODUCTION

Andre Geim and Konstantin Novoselov made an extraordinary discovery of graphene through their conventional mechanical exfoliation process known as the "Scotch tape method" in 2004. This discovery started the exploration of two-dimensional (2D) materials. A breakthrough in materials research is sparked by graphene, just one sheet of atoms of carbon organized in a hexagonal lattice, which demonstrated remarkable hardness, thermal characteristics, and electrical conductivity. After discovering graphene, scientists look for more 2D substances with special features. Molybdenum disulfide (MoS_2) is one example of a transitional metals dichalcogenide (TMD), a family of semiconducting materials having adjustable optical and electronic characteristics. Additional types of 2D materials follow these [1, 2].

In the past few years, the interest in 2D compounds is increasing because of their distinctive characteristics and prospective uses. Black phosphorus, Hexagonal Nitride of Boron (h-BN), and other metallic halides are among the 2D materials, their outstanding electronic characteristics and their use in future technology have made them an intriguing group of materials. The lower dimension of 2D structures results in enhanced carriers mobility, adjustable band structures, and quantum-confined effects, which in turn cause the spacial electronic behavior. Following an analysis of the electronic band structures of the crystals by electronic band structure, estimated band gap, and DOS revealed that Mg_3BiBr_3 exhibits semiconductor behavior [3, 4, 5].

An instance of the halide family, bismuth tribromide $BiBr_3$ is developed into a centre of scrutiny over the last decades. Achieving plenty of recognition due to its exceptional properties than its potential applications, setting up such a hybrid framework will enable the efficient calculation of a wide range of materials features, including thermal conductivity, electronic behavior, and optical properties, making it an appealing candidate for photovoltaics and light-emitting diodes, particularly in the fields of materials science and optoelectronics. Moreover, $BiBr_3$ shows potential for eco-friendly solutions in next generation energy devices as a lead-free substitute for conventional perovskites. Triple bromine Br atoms coordinated the bismuth Bi atom in $BiBr_3$ to produce a deformed octahedral shape in a (+3) oxidized state. Because the Bi^{+3} ion has just one pair of electrons, the deformation is caused by unequal bond lengths and angles, because it introduces hybridization effects that affect the position of the valence and conduction bands, this stereochemical activity has a substantial impact on the electronic characteristics [6, 7, 8].

$BiBr_3$ requires thermal stability to be employed in a variety of circumstances. According to DFT calculations, $BiBr_3$ has a sufficiently stable structure under ambient circumstances, which is important for device sustainability and stability in real-world situations as well as efficiency of the device. Theoretical research implies that BiI_3 in a crystalline-monolayer form would have less stability when compared to $BiBr_3$. $BiBr_3$ has been studied for its electronic characteristics, such as band structure and density of state, to better understand material characteristics. The indirect band gap of $BiBr_3$ is around 2.84 eV, positioning it in the visible to ultraviolet wavelengths. $BiBr_3$ has strong optical characteristics, such as UV-visible absorption of light and its high refractive index, they can lead to an enhancement of solar cell performance. Its optical

Cite as: Y.H. Shwan, M.A. Ameen, A.Sa. Mahmood, East Eur. J. Phys. 1, 191 (2026), https://doi.org/10.26565/2312-4334-2026-1-19

band gap and absorption coefficients make it a promising option for use in solar energy harvesting devices, $BiBr_3$ has a large dielectric constant, indicating the ability to storage electrical energy in an electrostatic field [9, 10, 11].

In terms of thermoelectric properties, DFT has emerged as a popular computational approach for studying 2D materials on an atomic scale, which gives information on numerous thermoelectric parameters such as the seebeck coeffcient, S, elecrical conductivity, σ, electronic thermal conductivity, κ, and the power factor, PF, of the system. They are chemical potential-dependent and temperature-dependent behaviors that indicate the components leading to their thermal resilience. In solar cell device, BiBr3 being a lead-free material has been investigated as a safer alternative[12, 13].

Limitations such as incomplete characterisation and insufficient examination of the properties have plagued studies of $BiBr_3$. This work attempts to fill these gaps by conducting a comprehensive and in-depth assessment of $BiBr_3$, which can provide a deeper understanding of its characteristics and its uses. This study uses DFT to analyse the stability, thermal, electronic, and optical characteristics of the $BiBr_3$ structure. DFT provides an excellent basis for studying the electronic structure of $BiBr_3$ at the atomic level, allowing precise predictions of its behaviour in many applications. We utilize AIMD to examine BiBr3's thermal stability and potential tolerance for heat by simulating its thermal properties. While optical feature computation suggests great potential for usage in a range of several areas, also, understanding the light-matter interaction is critical because it allows us to optimise materials for specific uses. Applying BoltzTraP to the Boltzmann transport framework, the thermoelectric performance at low temperatures and the heat capacity, phonon group velocity and lattice thermal conductivity at high temperatures are investigated [5, 14, 15, 16, 17].

2. METHODS AND COMPUTATIONAL TOOLS

We examine a two-dimensional unit cell of $BiBr_3$ with space group $P2_1/c$ consisting of 16 atoms. Quantum espresso utilizes the projector augmented wave (PAW) framework for conducting first-principles calculations. Furthermore, the GGA (generalized gradient approximation) is employed as a method to compute exchange and correlation terms when using PBE conceptual framework. A convergence test establishes the suitable kinetic energy cutoff for Brillouin zone sampling through testing. A combination of a $7\times7\times3$ Monkhorst-Pack k-point grid and a 45 Ry plane-wave cutoff is used as the computational parameters. The *nscf* calculations require a denser k-point grid of $50\times50\times5$ for their execution. Unit cell and atomic arrangements undergo structural relaxation through the relax and vc-relax modes to determine optimal structures suitable for detailed analysis. The relaxation energy reaches convergence at 4×10^{-7} eV [17, 18].

The AIMD simulation run tests thermal stability on a unit cell maintained at 300 K for 5 ps. Structure undergo analysis of their electronic and optical characteristics when they reach full relaxation, where stress are less than 6×10^{-4} eV/Å. The analysis of electronic transport characteristics employs BoltzTraP, which applies Boltzmann transport equations to constant relaxation time condition, important characteristics including the seebeck,S, electrical conductivity, thermal conductivity of electron, and power factor are calculated. Phonopy program calculates entropy and heat capacity by appling the small displacement approach [19]. The Phono3py software is used to calculate the conductivity of lattice vibration and group velocity, employing a q-point mesh of 10×10×7. XCRYSDEN and BURI 1.3. are used to visualize and design structures, as well as to improve our understanding of material characteristics by assuring correct modeling and guiding investigations [12, 20, 21].

3. RESULTS

This part discusses the results of the stability, electronic, optical, and thermal properties of the 2D $BiBr_3$ structure.

3.1. Geometric properties

The $BiBr_3$ crystallizes as a structure that is monoclinic in the $P2_1/c$ space group, arranged in a two-dimensional form. In this arrangement, every bismuth (Bi^+) ion is linked to by triple bromine (Br^-) ions, giving rise to edge-sharing $BiBr_3$ octahedra. Modeling simulations to determine the electronic, thermal, and optical characteristics of $BiBr_3$ needs accurate descriptions of geometric aspects, including unit cell, lattice constants, and lengths of bond. Geometric variation factors significantly influence the electronic band structure, phonon dispersion, and optical response, emphasizing the need for computational studies that include an accurate assessment of the atomic configuration [22, 23].

After fully relaxed structure, the lattice constants are $a = 7.40$Å, $b = 12.79$Å, the z vacuum distance is assumed to be $c = 7.69$ Å, and the Bi-Br bond length is found to be 2.90 Å. They are decsribing the arrangement of atoms in a unit cell. The Fig. 1(a),(b) depicts the top and side perspectives of the structure. The study analyzes the characteristics of $BiBr_3$ by utilizing a relaxation structure-optimized lattice parameter. The findings are consistent with reported data [24].

3.2. Stability

We evaluate formation energy to ensure that the structure becomes energetically stable. The formation energy of a $BiBr_3$ material refers to the overall energy required to develop it based on its separate components in their normal states. Negative formation energy means that the material energetically is great stable, whereas positive formation energy demonstrates the fact that the material is unstable and might degradation, the $BiBr_3$ becomes energiticaly excellent stable at lattice distance of 7.40 Å due to its minimum negative formation energy of -2.45 eV [25].

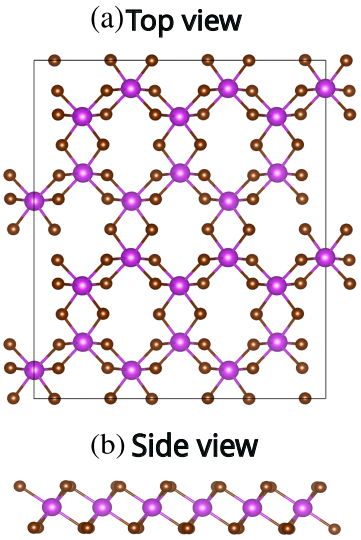

Figure 1. Structure of 2D $BiBr_3$ from top view (a), and side view (b).

To evaluate the thermal stability of $BiBr_3$, we are applied AIMD to compute temperature and total energy versus time (5 ps) in a unit cell at 300 K. The temperature variation increases somewhat at the start of the simulation due to the structure requires only a brief amount of time for reaching equilibrium. Then the fluctuation becomes roughly constant throughout time, indicating that the structure has achieved stability and it is in an equilibrium phase. Additionally, the temperature profile varies little during the simulation, indicating that heat transport is restricted by a $BiBr_3$ structure as seen in Fig. 2(a) . We are noticed no substantial structural disturbances or bond breaks, this corresponding to the system remain stable.

The energy fluctuations of roughly 0.22 Ry, which is inside the range reported in earlier. The $BiBr_3$ structure showed no substantial energetic changes throughout the simulation period, thus avoiding any structural deformation. It is apparent that there is no structural change in terms of energy as illustrates in Fig. 2(b). $BiBr_3$ may have an extremely rigid lattice structure or strong bonds due to its low (temperature and energy) fluctuations. These little fluctuations demonstrate that phase transitions or breakdowns do not take place with time. $BiBr_3$ is stable and crucial for structural integrity. AIMD simulations provide a useful foundation for testing structural stability [26, 27].

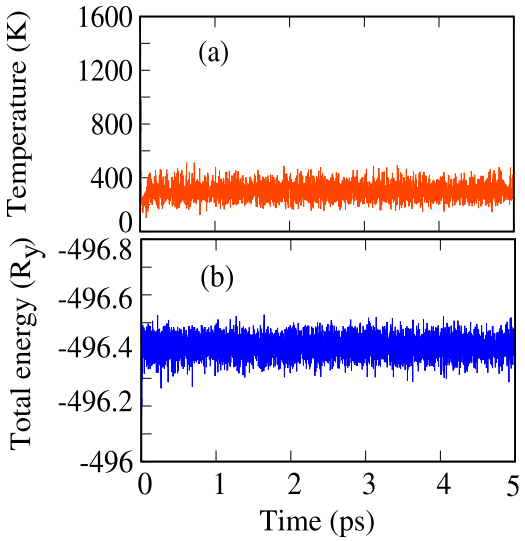

Figure 2. The flactuation of temperature (a), and energy (b) versus time during the AIMD simulation.

3.3. Electronic properties

We first calculated $BiBr_3$'s thermal stability through analysis, then, the electronic properties of $BiBr_3$ are computed. It mostly depends on band structure and partial DOS, which are computed along the path Γ→Y→M→K→H→X. Both are referenced to the same energy level where Fermi energy is taken to be zero, these are shown in Fig. 3 and Fig. 4.

The $BiBr_3$ material exhibits indirect bandgap characteristics because its electronic states are unevenly distributed across the band structure. The valence band's maximum (VBM) is located at the X point and the conduction band minimum (CBM) at the Y point, giving an indirect band gap. In these situations, the transition between the VBM and CBM requires a change in energy as well as momentum. This condition decreases the propensity of direct photon-induced transitions, since phonons are required to achieve momentum conservation. As a consequence, the optoelectronic transition of the material is inherently dictated by the indirect nature of the gap. Fig. 3 shows that the GGA-PBE functional may potentially underestimate the calculated indirect band gap of 2.84 eV. This underestimation is due to the fact that standard DFT that is based on semi-local exchange-correlation functionals is incomplete when it comes to the discontinuity in the exchange-correlation potential and tends to delocalize the electron densities [28].

The obtained band structure of $BiBr_3$ is not flat, which points to the high dispersion, delocalized electronic states, and to the strong variations of energy levels with momentum. The degree of band dispersion is proportional to the effective mass of charged carrier, $m^* = \hbar^2 \left(\frac{\partial^2 E}{\partial k^2}\right)^{-1}$. In such a way, the dispersive character of the band structure of $BiBr_3$, implies quite delocalized electrons and holes, resulting in a higher efficiency of the charge transport. The electronic band structure is determined by the arrangement of the atoms, which is significant in establishing its characteristics. Lower symmetry in $BiBr_3$ causes energy bands to spread widely due to fewer degenerate energy levels and generates substantial band gap, from this perception, this arrangement is not fully symmetrical in a high-symmetry sense, because there are some imperfections. Its depends on the specific observation or crystal phase [29].

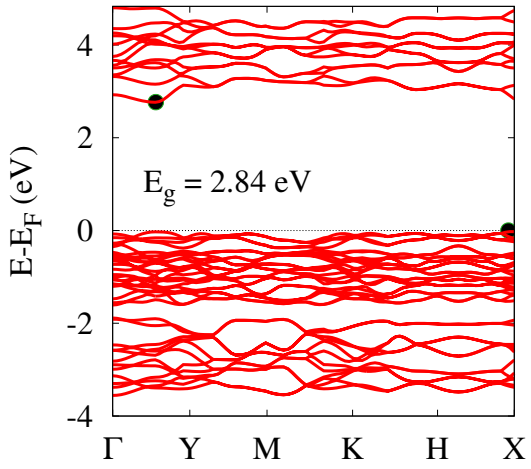

Figure 3. The electronic band structure of 2D $BiBr_3$, with the Fermi level referenced at zero energy.

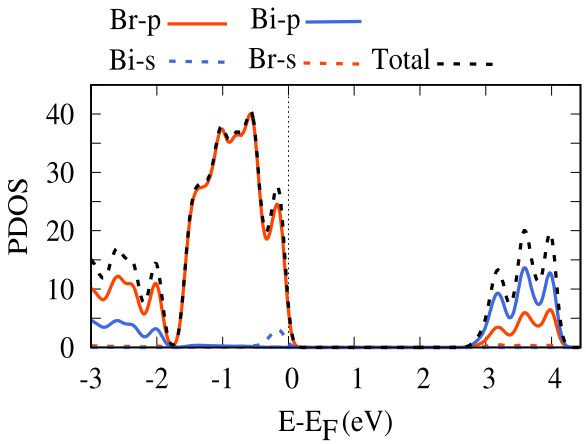

Figure 4. Project density of states (PDOS) and total density of state of 2D $BiBr_3$ material as obtained with DFT calculations.

A PDOS calculation is conducted for the constituent elements in the energy range of (-3 to 4.5) eV, highlighting their orbital contributions to the band structure, which is essential for a comprehensive understanding of bonding properties, as illustrated in Fig. 4. The predominance of Br-p orbitals in the valence band (VB) indicates a strong ionic character, stemming from the robust interaction between the bismuth and bromine atoms. Conversely, in the conduction band (CB),

Bi-p orbitals significantly influence both the electronic and optical characteristics of $BiBr_3$. The considerable electronic character separation between the Br and Bi atoms suggests the ionic nature of bonding in $BiBr_3$. Additionally, the band gap varies from 0 to 2.83 eV, indicating that the PDOS is zero due to the absence of allowed electronic states [30].

We are noticed that the two atomic orbitals involved in the reaction (Bi-p and Br-p) remained distinct due to the orbitals do not normally hybridize. The orbitals work independently without mixed and retain their original features, resulting in a localized disposition in states. The projected density of states (PDOS) calculations show a weak contribution from Bi-s and Br-s orbitals, as these states are at lower energies compared to the p orbitals, which limits their involvement in bonding. In heavy-element compounds, relativistic effects and the larger principal quantum number make s orbitals more contracted and lower in energy, further decreasing their overlap with nearby orbitals. As a result, these s orbitals play a minor role in the bonding framework. Conversely, the Bi-p and Br-p orbitals, which are higher in energy and more spatially extended, primarily drive the bonding interactions, forming the main electronic coupling in the system. In conclusion, $BiBr_3$ has an indirect band gap of about 2.84 eV that is smaller compared to that obtained in Bi_4O_6, reported as 3.12 eV [31].

3.4. Optical properties

This section analyzes optical characteristics (dielectric (ε), absorption coefficient (α), and optical conductivity of 2D $BiBr_3$ shape based on Random Phase Approximation (RPA) across the Brillouin zone with dense mesh grid points at span of energy (0-10)eV. These characteristics describe how a material responds to incoming electromagnetic spectrum. $BiBr_3$'s optical properties can be helpful for a variety of applications. The Fig. 5 shows how dielectric behavior changes with photon energy under both perpendicular (E_z) and parallel (E_x) electric field conditions [32].

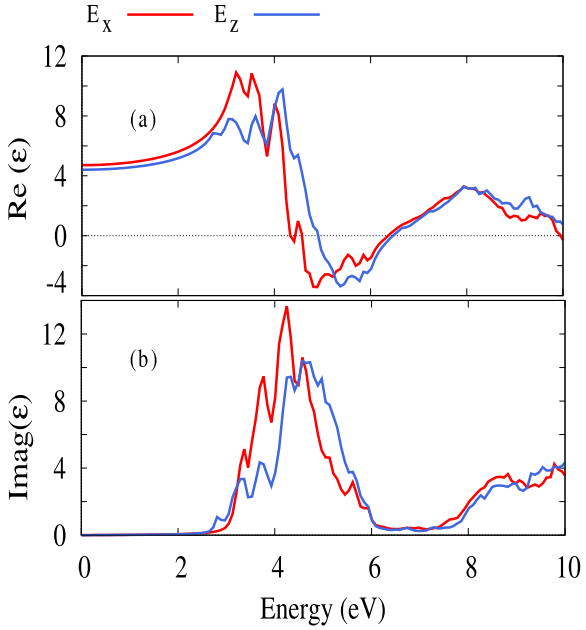

Figure 5. Real part, Re(ε), and Imaginary part, Imag(ε), of the dielectric function of 2D $BiBr_3$ in parallel, E_x (red) and perpendicular, E_z (blue) applied electric field.

It is noteworthy that the results in the x- and y-polarized electric field are comparable showing symmetric optical response of $BiBr_3$. However, the interactions varies in the electric field x-polarization and z-polarization, owing to weak anisotropic structure. The real part Re(ε) refers to the active aspect of structures that respond to electrical energy storage. The stationary dielectric function is 4.9 and 4.7 at zero photon energy for E_x, E_z respectively. This suggests that $BiBr_3$ exhibits strong polarization behavior or is easily polarizable, because of the their atoms are less sensitive to electric fields. The material displays its strongest response at around 3 eV. This occurs at particular photon energies where the electrons in the valence band can be polarized most efficiently by the incident electromagnetic field, typically around the point of interband transitions, the substance exhibits a robust electrical energy storage capacity when observed from this standpoint. At frequencies higher than this, the electrons are no longer able to respond in a meaningful way to the rapidly varying electromagnetic field, and Re(ε) will begin to drop. Around 4 eV, the material attains plasmonic behavior because the Re(ε) becomes negative due to the collective electron oscillation, making the material useful for plasmonic applications, at this point the material does not support propagating wave [33].

The imaginary part of dielectric reacte to a various frequncies, seen in Fig. 5(b). The Imag(ε) of the dielectric function corresponding to how much energy material absorbs. At low frequencies the static value of Imag(ε) is almost equal to zero since there is insufficient energy in the photons at low frequencies to excite electrons across the band gap.

As the energy of photons is successively increased and passes beyond the band gap threshold, Imag(ε) rises sharply because allowed electronic transitions between the valence band and the conduction band can then occur. Peaks at certain energies can be seen, each one being due to a strong optical transition at a critical point in the electronic band structure where the joint density of states is large. Their peaks represent the energy bands at which photon energy absorption is maximum. At higher photon energies Imag(ε) is gradually decreased due to lowering probability of additional elctronic excitations, and the electrons cannot react to the fast oscillations of the external field anymore. The Imag(ε) shares a connection with shielding capabilities through electromagnetic screening mechanisms present in materials. Shielding strength increases while Imag(ε) value increases and vice versa. Therefore the general tendency of Imag(ε) , which begins at nearly zero, increases with energy, reaches maxima associated with characteristic transitions, and decays at high frequencies, characterizes the primary absorption response of the substance [34].

Optical conductivity, descibes a material's capacity to transmit electric current under an oscillating an electric field. The optical conductivity varies significantly with respect to photon energy as it is illustrated in Fig. 6. The key point is, the optical conductivity in the range energy (0-2.82) eV dis effectively zero, because there aren't many electronic states accessible for optical transitions. Also, it is denoted as the optical band gap. The transition from the valence to the conduction band appears clearly with the maximum optical conductivity of $BiBr_3$ happening at 4.1 eV, the material shows strong light-absorbing properties and transition abilities that function at multiple photon frequencies. The photon energy surpassing the band gap plays a vital role in determining the total transition strength and involvement of most interband transitions. Multiple allowable transitions contribute to the observed peak. This information allows us to comprehend charge transfer patterns, which are required by developers for the production of storage device applications. Although photons with more energy can potentially cause promotion across larger energy gaps, the number of available and strongly coupled transitions is reduced. Optical coupling becomes weaker as the reduced joint density of states, which leads directly to a reduced optical conductivity at high energy photons [35].

The refractive index, n, of a substance is a dimensionless number that defines the way light travels through material as displays in Fig. 6, and its govens phase velocity and dispersion. $BiBr_3$ refractive index varies with wavelengths due to frequency-dependent refractive index. The static n is 2.24 at zero photon energy, indicating the material strongly respond to electric field. At low photon energies (below the band gap), no interband transitions happen, so Imag(ε)$\approx$ 0, and Re (ε) remains fairly constant. As a result, the refractive index stays nearly the same. Beyond this point the refractive index grows smoothly because the light phase velocity decreases and normal dispersion. Then at 4 eV, the refractive index gradually reduces because the energy of the photon is more than the band gap of the material, leading to the saturation absorption of the material, As photon energy rises, the oscillation becomes too rapid for bound electrons to react effectively. Then, the Polarisation weakens and declines, resulting in a reduction of n is occur [36].

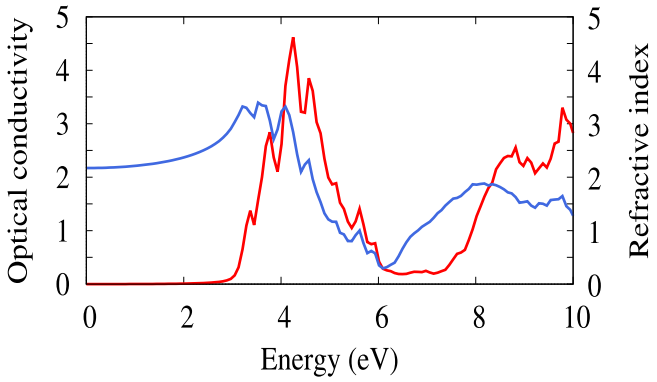

Figure 6. Optical conductivity (red), and refractive index (blue) of 2D $BiBr_3$ in external electric field.

The absorption coefficient α governs a material's ability to absorb photons at various of energy as illustrated Fig. 7. The α value starts at zero during the initial part of the curve since the photon energy lacks sufficient power to promote carriers from VB to CB. A steep rise in α occurs when photon energy matches the band gap energy, which is roughly 2.83 eV, corresponding to the Imag(ε) curve. Analysis indicates the structure demonstrates a distinct absorption peak at around 4.5 eV that belongs to the UV spectrum. The detection of VIS and UV light through this curve is essential for solar enegy applications. $BiBr_3$ has the capacity to absorb in the VIS to extreme-UV spectrum. At extremely high photon energies, the absorption coefficient decrease, mostly because the material no longer has accessible states for electronic transitions at that range of wavelength and he available electronic states become less responsive to photons carrying higher amounts of energy and result in decreased absorption capability [37].

The reflectivity of $BiBr_3$ is displayed in Fig. 7. From 0.0 eV to 2.74 eV, the reflectivity has a value of nearly 0.15%. At low photon energies (below the band gap), the free-electron dielectric response is weak. This means the material doesn't effectively reflect light, leading to very low reflectivity in that range. As photon energy increases above the band gap, reflectivity rises-potentially reaching values as high as 57% on average. This is because electrons can oscillate more strongly in response to the light. The reflectivity can be reduced to levels almost reaching zero at hight frequency. At

this photon energy, the incident light is extremely transparent through it, as reflection is suppressed and absorption is negligible. Provided that this happens at around 7 eV, the material would effectively look transparent in that very limited ultraviolet wavelength. From this analysis, this material can be used as shielding in the UV range.

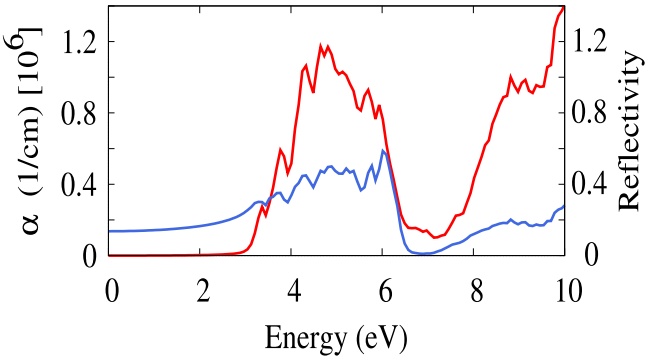

Figure 7. The absorption coefficient,α, (red) and reflectivity (blue) of $BiBr_3$ as a function of the energy of the photon in the presence of external electric field.

3.5. Thermal properties

The thermal properties will be analyzed through two unique temperature ranges known as low temperature and intermediate of high temperature. The analysis of electronic thermal response in materials under low-temperature conditions serves to determine fundamental thermoelectric parameters consisting of S, σ, κ, and PF as a function of chemical potential with energy of Fermi set to zero. $BiBr_3$ supports exceptional thermoelectric stability through Seebeck coefficient calculation across the studied temperature conditions, as shown in Fig. 8(a). The directional aspect of the Seebeck coefficient constitutes a crucial property for understanding material behavior. The sign of S reveals which charge carriers predominate in a material since positive S values indicate holes whereas negative S values indicate electrons. A thermal gradient operating near the E_F with $S > 0$ indicates holes act as dominant charge carriers through which heat transfer occurs by hot holes diffusing toward the cold region. Electron transport between the hot and cold sides results in negative S, indicating the presence of CB [38].

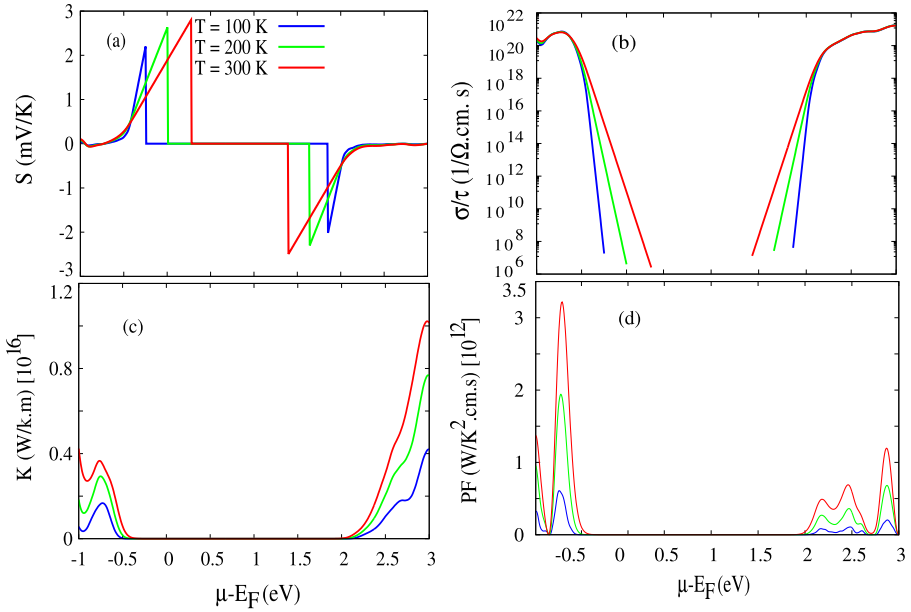

Figure 8. The Seebeck coefficient (a), electrical conductivity,the y-axis is scaled in a logarithms form (b),electronic thermal conductivity κ (c), power factor (d) of $BiBr_3$ versus μ-E_F for the different values of temperature. μ refers to the chemical potential.

The S value shows minimal change when the temperature rises from 100 to 200 K to 300 K since carrier density changes little due to gradients density of states (GDS) and weak scattering. Under a range of chemical potentials from -0.27 to 1.88 eV the S exhibits a plateaus region at 100 K where S equals zero because of unavailable band structure.

Rising temperature causes plateaus to become smaller because carrier excitation becomes more straightforward, resulting in increased sample smearing. The significant S value of $BiBr_3$ shows that it acts as a semiconductor material, and also raises PF while aligning with its application potential for energy conversion [39].

The electrical conductivity, σ, which is shown in Fig. 8(b) is plotted on a log scale because this will help to visualize better and discover a trend where it would be difficult to achieve with a realistic scale. The σ represents the flow of charge carriers within a material. The σ shows a strong correlation with chemical potential and temperature because these factors affect carrier concentration and distribution. The Values of σ that surround the VBM and CBM match the DOS peaks observed in the VB and CB. The σ occurs more efficiently in the CB compared to the VB because of differences in charge carrier behavior and DOS. There exists no density of the state between CB and VB resulting in zero electrical conductivity (null electrical). This state of affairs seems to favor the Seebeck effect. Electricity conductivity responds to temperature variations that modify the number of active charge carriers in the material. When the temperature surpasses zero the number of thermally excited electrons rises leading to increased smearing around the Fermi level that enhances the value of σ, which are roughly 10^{21} and 10^{22} 1/Ω.cm.s for VB and CB respectively. An increase in σ value tends to increase power factor, which corresponds to photovoltaic increase efficiency, especially hybrid solar cell device.

The electronic thermal conductivity,κ, which resembles the power factor pattern, is depicted in Fig. 8(c) in various low temperatures. The κ of $BiBr_3$ through electrons depends on multiple variables like σ behavior, carrier mobility and temperature variations. The thermal transport behavior of this material heavily depends on electron-mediated thermal conductivity. The value of κ increases as temperature rises due to thermal excitation of electrons that creates additional electron involvement in thermal transportation. The percentage values of κ increase by 114% and 150% for VB and CB, respectively, in the temperature range from 100 to 300 K based on Wiedemann–Franz law [40, 41]. The achievement of full κ may have been prevented by the occurrence of electron-electron collisions. Electron mobility changes because of scattering, which affects the value of κ, this interactions result in lower thermal conductivity levels . From this perspective, the excellent thermal conductivity of $BiBr_3$ enhances heat dissipation, which preserves the temperature of solar cells while increasing photovoltaic system efficiency and a long life [42, 43].

From the Fig. 8(d), the power factor of $BiBr_3$ depends on both chemical potential and temperature parameters for evaluating the material's charge carrier transport properties. A temperature increase shifts the chemical potential toward band edge positions, so it changes carrier densities and affects transportation properties. Low power factor values occur at low temperatures since carrier activation remains restricted. Still, as temperature increases leads to improved carrier excitation, which boosts σ and enhances S and that makes PF is high, the power factor shows its maximum value at the band edges VBM or CBM because these areas maintain an ideal balance between Seebeck coefficient and electrical conductivity and optimal carrier concentration. $BiBr_3$ demonstrates a better hole transport efficiency through the fact that its valence band maintains higher power factor values than its conduction band. The high PF value serves excellently for thermoelectric applications and it can be used as a hole transport layer in solar device energy [18].

After verifying thermal stability. At intermediate high temperature ranges, we analyze $BiBr_3$'s thermal properties through temperature-dependent measurements of heat capacity C_V and entropy, which appear in Fig. 9.

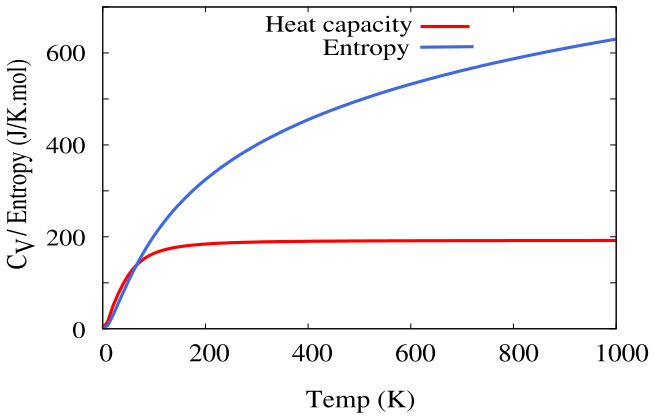

Figure 9. Heat capacity (red) and entropy (blue) as a function of temperature of $BiBr_3$.

$BiBr_3$'s heat capacity increases with temperature because of the continual activation of phonon modes, which is consistent with Debye's T^3 law (T < 300 K), where only low energy phonons contribute to heat capacity. Above 200 K, many of the phonon modes in the low- and mid-frequency spectrum are already excited. Only high-frequency modes are left to participate. Because these high-frequency modes must be excited with much greater energy, the heat capacity of the system grows more slowly with temperature. Consequently, the specific heat becomes nearly constant at high temperatures, this is referred to as the plateau region. The C_V of $BiBr_3$ exhibits moderate heat capacity, making it a potential candidate for energy storage, which is (12.35 J/K.mol at 300 K per atom). Despite this trend, the heat capacity of $BiBr_3$ does not attain the classical Dulong-Petit limit, even at elevated temperatures of 1000 K. This phenomenon can be attributed to an inadequate phonon population that fails to saturate C_V to the classical limit. Additionally, it is possible that the vibrational

modes in $BiBr_3$ do not fully contribute to the heat capacity at high temperatures, a factor that may be influenced by the presence of the heavy Bi atom [44, 45].

When temperatures reach a moderately high level the system entropy achieves an approximate value of 620 J/K·mol, which demonstrates notable lattice disorder. The material performance under extreme conditions would be affected by the elevated disorder since it impacts both structural quality and thermal characteristics. Complete randomness throughout the crystal lattice corresponds to high entropy values. An increase in temperature triggers the combined effects of intensified atomic vibrations and lattice defects and anharmonic interactions which create a disordered state in the lattice.

Lattice thermal conductivity is a measure of the efficiency of the heat conduction through a substance owing to lattice vibration, specifically phonons. Phonons are the main carriers of thermal energy in semiconductors and insulators, as shown in Fig. 10(a) [46]. The lattice thermal conductivity of $BiBr_3$ is temperature dependent. At a temperature of 200K, the lattice usually reaches a maximum of 4.4 W/m.K, this is because the phonon population rises due to normal phonon scattering (N-process) and does not disrupt heat flow much, as well as because of the high group velocity. At higher temperatures, many of the high-frequency phonons transport the majority of the thermal energy and become active, and the Umklapp scattering (U-process) dominates, phonons interact strongly and lose momentum, which reduces their capacity in conducting heat. As a result, conductivity of heat is reduced [47]. Studies indicate that phonons significantly affect the transfer of heat in various 2D monolayers, as demonstrated by research on other 2D materials [48, 49]. The $BiBr_3$ exhibits weak lattice thermal conductivity, which is attributed to the material properties that limit the phonon transport. Due to the presence of the heavy Bi element, atom vibrations occur at very slow rates, ensuring that group phonon velocities are reduced. This leads to reduced efficiency in the transport of heat. In short, $BiBr_3$ has a moderate heat capacity as well as low lattice thermal conductivity, rendering it a good thermal insulator.

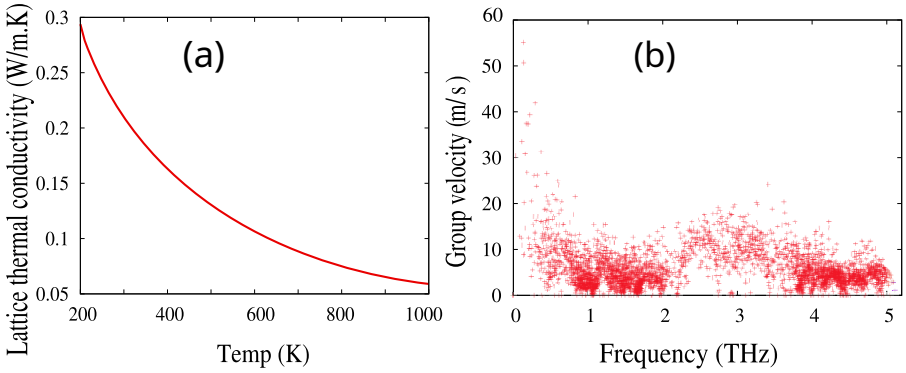

Figure 10. Lattice thermal conductivity (a), and group velocity (b) of $BiBr_3$.

Thermal transport is governed by the group velocity because the lattice thermal conductivity is proportional to the product of the phonon group velocity and the heat capacity. When the temperature rises, the lattice becomes softer, and as a result, the group velocity of phonons reduces, leading to lower lattice thermal conductivity, the trend of this behavior is reflected well based on the trends observed in $BiBr_3$ material, as can be seen in Fig. 10(a) and Fig. 10(b) [50, 51]. Phonon group velocities are large in the low-frequency regime (acoustic), indicating a fast propagation of the respective vibrational modes inside the $BiBr_3$ structure, which corresponds well to the speed of sound in the material. Conversely, at frequencies between (1-2) THz, the phonon group velocity remains mostly constant. This indicates that vibrational speeds stay relatively steady or increase gradually in this high-frequency range, the atoms participate in highly localized 'rattling' motions. The energy remains trapped there temporarily, which reduces thermal conductivity. Overall, the thermal properties of $BiBr_3$ make it an interesting candidate in many thermal management applications, especially when heat absorption and insulation play the most crucial role.

4. CONCLUSIONS

This study offers a comprehensive first-principles investigation of $BiBr_3$, uncovering its diverse properties through the DFT framework. The material exhibits exceptional thermal stability, maintaining structural integrity at high temperatures with minimal energy fluctuations. The $BiBr_3$ material acts as a semiconductor with an indirect band gap of 2.84 eV. Simultaneously, its optical interactions in the Vis-UV regions shows strong light absorption, making it a promising candidate for energy harvesting and lead-free photovoltaic applications. However, it is highly reflected in the UV range, which is roughly (59%). The large peak in the power factor and Seebeck indicates maximum transport efficiency at room temperature, reflecting an optimal balance between electrical and thermal properties suitable for energy conversion and thermal management. Its moderate heat capacity, remaining below the Dulong–Petit limit, combined with low lattice thermal conductivity, further supports its potential as an insulating material. $BiBr_3$'s unique electronic, optical, and thermoelectric properties position it as an ideal material for next-generation optoelectronics, energy harvesting, and thermal management applications.

Acknowledgment

This work was financially supported by the University of Sulaimani. The computations were performed on resources provided by the Computational Science Lab at Research and Developed Center at the University of Sulaimani. YHS has special thanks to Nzar Rauf Abdullah for fruitful discussions. This project is done as a part of PhD thesis.

ORCID

Yadgar Hussein Shwan, https://orcid.org/0000-0002-0020-253x; **Majida Ali Ameen**, https://orcid.org/0009-0004-9641-5186; **Aras Saeed Mahmood**, https://orcid.org/0000-0003-3908-3766

REFERENCES

[1] S.S. Prasad, R.K. Mishra, S. Gupta, S. Prasad, and S. Singh, "Introduction, History, and Origin of Two Dimensional (2D) Materials," in: *Advanced Applications of 2D Nanostructures. Materials Horizons: From Nature to Nanomaterials*, edited by S. Singh, K. Verma, and C. Prakash, (Springer, Singapore, 2021), pp. 1-9. https://doi.org/10.1007/978-981-16-3322-5_1

[2] X. Duan, and H. Zhang, "Introduction: two-dimensional layered transition metal dichalcogenides," Chem. Rev. **124**(19), 10619–10622 (2024). https://doi.org/10.1021/acs.chemrev.4c00586

[3] M. U. Khandaker, H. Osman, S. A. Issa, M. Uddin, M. H. Ullah, H. Wahbi, and M. Hanfi, "Newly predicted halide perovskites Mg_3-AB3 (A= N, Bi; B= F, Br, I) for next-generation photovoltaic applications: a first-principles study," RSC advances, **15**(8), 5766-5780 (2025). https://doi.org/10.1039/D4RA09093D

[4] K. S. Novoselov, A. K. Geim, S. V. Morozov, D.E. Jiang, Y. Zhang, S. V. Dubonos, I. V. Grigorieva, and A. A. Firsov, "Electric field effect in atomically thin carbon films," Science, **306**(5696), 666-669 (2004). https://doi.org/10.1126/science.1102896

[5] S. Abdu, A. Shu'aibu, M. Aboh, and M. Abubakar, "Computations of the band structure and linear optical properties of methylammonium bismuth bromide and methylammonium galluim bromide using FHI-aims code," Science World Journal, **14**(2), 101-105 (2019). https://scienceworldjournal.org/article/view/19450/13175

[6] S. Yosim, L. Ransom, R. Sallach, and L. Topol, "The bismuth-bismuth tribromide and bismuth-bismuth triiodide systems," The Journal of Physical Chemistry, 66(1), 28-31 (1962). https://doi.org/10.1021/j100807a006

[7] K. R. Kurbanov, and N. N. Kurbanova, "Structrural peculiarities and some electrical-and-physical properties of bismuth oxide and antimony trichloride and tribromide," Ph.D. thesis, Sumy State University Publishing House (2011).

[8] G. Huang, Y. Q. Sun, Z. Xu, M. Zeller, and A. D. Hunter, "Structural regularity and diversity in hybrids of aromatic thioethers and $BiBr_3$: from discrete complexes to layers and 3D nets, Dalton Transactions, (26), 5083-5093 (2009). https://doi.org/10.1039/B902490P

[9] Y. Xu, M. Lyu, and J. Zhu, "Surface engineering in CsPbX 3 quantum dots: from materials to solar cells," Materials Chemistry Frontiers, **8**(9), 2029-2055 (2024). https://doi.org/10.1039/D3QM00911D

[10] M. M. R. Al-Fartoos, A. Roy, T. K. Mallick, and A. A. Tahir, "Advancing thermoelectric materials: a comprehensive review exploring the significance of one-dimensional nano structuring," Nanomaterials, **13**(13) 2011 (2023). https://doi.org/10.3390/nano13132011

[11] X. Liu, Z. Wang, G. Yu, Z. Sun, G. Zhang, X. Q. Wang, L. Zhu, *et al.*, "Growth morphology of {1 0 1} surfaces of l-arginine trifluoroacetate crystals investigated by afm," Journal of Physics and Chemistry of Solids, **68**(4), 608-610 (2007). https://doi.org/10.1016/j.jpcs.2007.02.002

[12] P. Giannozzi, S. Baroni, N. Bonini, M. Calandra, R. Car, C. Cavazzoni, D. Ceresoli, *et al.*, "Quantum espresso: a modular and open-source software project for quantumsimulations of materials," Journal of physics: Condensed matter, **21**(39), 395502 (2009). https://doi.org/10.1088/0953-8984/21/39/395502

[13] S. Baroni, S. De Gironcoli, A. Dal Corso, and P. Giannozzi, "Phonons and related crystal properties from density-functional perturbation theory," Reviews of modern Physics, **73**(2), 515 (2001). https://doi.org/10.1103/RevModPhys.73.515

[14] L. Fornaro, C. Maidana, H. B. Pereira, A. Noguera, and A. Olivera, "Bismuth tri-iodide-Graphene 2D material," Journal of Crystal Growth, **639**, 127738 (2024). https://doi.org/10.1016/j.jcrysgro.2024.127738

[15] D. Cubicciotti, "Thermodynamic properties of bismuth (i) bromide and bismuth (iii) bromide," Inorganic Chemistry, **7**(2), 208-211 (1968). https://doi.org/10.1021/ic50060a005

[16] Z. Deng, F. Wei, Y. Wu, R. Seshadri, A. K. Cheetham, and P. Canepa, "Understanding the structural and electronic properties of bismuth trihalides and related compounds," Inorganic Chemistry, **59**(6), 3377-3386 (2020). https://doi.org/10.1021/acs.inorgchem.9b03214

[17] A. Darmawan, E. Suprayoga, A. A. AlShaikhi, and A. R. Nugraha, "Thermoelectric properties of two-dimensional materials with combination of linear and nonlinear band structures," Materials Today Communications, **33**, 104596 (2022). https://doi.org/10.1016/j.mtcomm.2022.104596

[18] N. R. Abdullah, B. J. Abdullah, H. G. Hussein, and V. Gudmundsson, "Novel ZnO nanosheet with buckling stress: First principles study of electronic, structural stability, phonon vibrations, lattice thermal and optical conductivity," Chemical Physics Letters, **844**, 141269 (2024). https://doi.org/10.1016/j.cplett.2024.141269

[19] D. Alfè, "Phon: A program to calculate phonons using the small displacement method," Computer Physics Communications, **180**(12), 2622-2633 (2009). https://doi.org/10.1016/j.cpc.2009.03.010

[20] A. Togo, and I. Tanaka, "First principles phonon calculations in materials science," Scripta Materialia, **108**, 1-5 (2015). https://doi.org/10.1016/j.scriptamat.2015.07.021

[21] J. P. Perdew, K. Burke, and M. Ernzerhof, "Generalized gradient approximation made simple," Physical review letters, **77**(18), 3865 (1996). https://doi.org/10.1103/physrevlett.77.3865

[22] K. Persson, Materials data on $BiBr_3$ (sg:14) by materials project, an optional note, (2016). https://doi.org/10.17188/1288706

[23] Y. Boran, and H. Kara, "A comprehensive density functional theory analysis on structural, electronic, and optical properties of BiOF," Brazilian Journal of Physics, **54**(5), 159 (2024). https://doi.org/10.1007/s13538-024-01523-w

[24] X. He, Y. Wu, S. Liu, W. He, S. Li, G. Huo, L. Jiang, *et al*., "Large-scale ultrastable 2D inorganic molecular crystal $BiBr_3$ and heterostructures with superior photoluminescence enhancement," Advanced Functional Materials, **34**(39), 2403273 (2024). https://doi.org/10.1002/adfm.202403273

[25] A. Jehan, M. Husain, S. Bibi, N. Rahman, V. Tirth, A. Azzouz-Rached, M. Y. Khan, *et al*., "Insight into the structural, optoelectronic, and elastic properties of AuXF3 (X= Ca, Sr) fluoroperovskites: Dft study," Optical and Quantum Electronics, **55**(14), 1242 (2023). https://doi.org/10.1007/s11082-023-05394-4

[26] A. Bafekry, M. Yagmurcukardes, B. Akgenc, M. Ghergherehchi, and B. Mortazavi, "First-principles investigation of electronic, mechanical and thermoelectric properties of graphene-like XBi (X= Si, Ge, Sn) monolayers," Physical Chemistry Chemical Physics, **23**(21), 12471-12478 (2021). https://doi.org/10.1039/d1cp01183a

[27] H. van Gog, W.-F. Li, C. Fang, R. S. Koster, M. Dijkstra, and M. van Huis, "Thermal stability and electronic and magnetic properties of atomically thin 2D transition metal oxides," npj 2D Materials and Applications, **3**(1), 18 (2019). https://doi.org/10.1038/s41699-019-0100-z

[28] N. R. Abdullah, B. J. Abdullah, and V. Gudmundsson, "DFT study of tunable electronic, magnetic, thermal, and optical properties of a Ga_2Si_6 monolayer," Solid State Sciences, **125**, 106835 (2022). https://doi.org/10.1016/j.solidstatesciences.2022.106835

[29] J. Xie, Z. Zhang, D. Yang, D. Xue, and M. Si, "Theoretical prediction of carrier mobility in few-layer BC_2N," The Journal of Physical Chemistry Letters, **5**(23), 4073-4077 (2014). https://doi.org/10.1021/jz502006z

[30] N. R. Abdullah, G. A. Mohammed, H. O. Rashid, and V. Gudmundsson, "Electronic, thermal, and optical properties of graphene like SiC_x structures: Significant effects of Si atom configurations," Physics Letters A, **384**(24), 126578 (2020). https://doi.org/10.1016/j.physleta.2020.126578

[31] Y. H. Shwan, M. A. Ameen, and A. S. Mahmood, "DFT study of electronic, optical, and thermodynamic properties of the 2D shape of Bi_4O_6 structure," Solid State Communications, **404**, 116095 (2025). https://doi.org/10.1016/j.ssc.2025.116095

[32] S. Qi, Y. Zhang, R. Zhang, X. Liu, and H. Xu, "First-principles and experiment investigation of Bi_2O_3/Bi_2WO_6 heterojunctions," Colloid and Interface Science Communications, **44**, 100502 (2021). https://doi.org/10.1016/j.colcom.2021.100502

[33] Y. H. Shwan, B. N. Ghafoor, and G. H. Hamasalih, "Optimization of surface plasmon resonance (SPR) for gold/air interface by using kretschmann configuration," Engineering and Technology Journal, **40**(10), 1334-1341 (2022). https://doi.org/10.30684/etj.2022.132902.1151

[34] H. Lashgari, A. Boochani, A. Shekaari, S. Solaymani, E. Sartipi, and R. T. Mendi, "Electronic and optical properties of 2D graphene-like ZnS: DFT calculations," Applied Surface Science, **369**, 76-81 (2016). https://doi.org/10.1016/j.apsusc.2016.02.042

[35] A. Akrap, J. Teyssier, A. Magrez, P. Bugnon, H. Berger, A. B. Kuzmenko, and D. Van Der Marel, "Optical properties of BiTeBr and BiTeCl," Physical Review B, **90**(3), 035201 (2014). https://doi.org/10.1103/physrevb.90.035201

[36] J.-L. Meyzonnette, J. Mangin, and M. Cathelinaud, ":Refractive index of optical materials," in: *Springer Handbook of Glass*, (Springer, 2019), pp. 997-1045. https://dx.doi.org/10.1007/978-3-319-93728-1_29

[37] A. Ghaleb, and A. Ahmed, "Structural, electronic, and optical properties of sphalerite ZnS compounds calculated using density functional theory (DFT)," Chalcogenide Letters, **19**(5), (2022). https://doi.org/10.15251/cl.2022.195.309

[38] I. T. Witting, T. C. Chasapis, F. Ricci, M. Peters, N. A. Heinz, G. Hautier, and G. J. Snyder, "The thermoelectric properties of bismuth telluride," Advanced Electronic Materials, **5**(6), 1800904 (2019). https://doi.org/10.1002/aelm.201800904

[39] M. Benaadad, A. Nafidi, S. Melkoud, M. S. Khan, and D. Soubane, "First-principles investigations of structural, optoelectronic and thermoelectric properties of Cu-based chalcogenides compounds," Journal of Materials Science, **56**(28), 15882-15897 (2021). https://doi.org/10.1007/s10853-021-06325-y

[40] X. Jiang, C. Ban, L. Li, C. Wang, W. Chen, and X. Liu, "Thermoelectric properties study on the BN nanoribbons via boltztrap first-principles," AIP Advances, **11**(5), 055120 (2021). https://doi.org/10.1063/5.0042555

[41] R. Chegel, "Enhanced electrical conductivity in graphene and boron nitride nanoribbons in large electric fields," Physica B: Condensed Matter, **531**, 206-212 (2018). https://doi.org/10.1016/j.physb.2017.12.053

[42] J. Androulakis, Y. Lee, I. Todorov, D.-Y. Chung, and M. Kanatzidis, "High-temperature thermoelectric properties of n-type pbse doped with Ga, In, and Pb," Physical Review B—Condensed Matter and Materials Physics, **83**(19), 195209 (2011). https://doi.org/10.1103/physrevb.83.195209

[43] J. Wang, L. P. Zhang, and Y. Li, "Preparation and analysis of novel thermoelectric material $(Sr_xCa_{1-x})_3Co_4O_9$," Applied Mechanics and Materials, **492**, 326-330 (2014). https://doi.org/10.4028/www.scientific.net/amm.492.326

[44] X. Tan, H. Shao, T. Hu, G. Liu, J. Jiang, and H. Jiang, "High thermoelectric performance in two-dimensional graphyne sheets predicted by first-principles calculations," Physical Chemistry Chemical Physics, **17**(35), 22872-22881 (2015). https://doi.org/10.1039/c5cp03466c

[45] Z.-X. Xie, L.-M. Tang, C.-N. Pan, Q. Chen, and K.-Q. Chen, "Ballistic thermoelectric properties in boron nitride nanoribbons," Journal of Applied Physics, **114**(14), 144311 (2013). https://doi.org/10.1063/1.4824750

[46] J. J. Plata, P. Nath, D. Usanmaz, J. Carrete, C. Toher, M. de Jong, M. Asta, *et al.*, "An efficient and accurate framework for calculating lattice thermal conductivity of solids: Aflow—aapl automatic anharmonic phonon library," npj Computational Materials, **3**(1), 45 (2017). https://doi.org/10.1038/s41524-017-0046-7

[47] Y.-Y. Wu, Q. Wei, J. Zou, and H. Yang, "Ultra-low thermal conductivity and high thermoelectric performance of monolayer BiP 3: a first principles study," Physical Chemistry Chemical Physics, **23**(35), 19834–19840 (2021). https://doi.org/10.1039/d1cp01383a

[48] M. Markov, Prediction of thermal conductivity and strategies for heat transport reduction in bismuth: an ab initio study., Ph.D. thesis, Universit'e Paris Saclay (COmUE) (2016).

[49] M. Wang, and D. Han, "Thermal properties of 2D dirac materials MN_4 (M= Be and Mg): a first-principles study," ACS omega, **7**(12), 10812-10819 (2022). https://doi.org/10.1021/acsomega.2c00785

[50] Y. Luo, X. Yang, T. Feng, J. Wang, and X. Ruan, "Vibrational hierarchy leads to dual-phonon transport in low thermal conductivity crystals," Nature communications, **11**(1), 2554 (2020). https://doi.org/10.1038/s41467-020-16371-w

[51] A. Togo, "First-principles phonon calculations with phonopy and phono3py," Journal of the Physical Society of Japan, **92**(1), 012001 (2023). https://doi.org/10.7566/jpsj.92.012001

ДОСЛІДЖЕННЯ СТАБІЛЬНОСТІ, ЕЛЕКТРОННИХ, ОПТИЧНИХ ТА ТЕПЛОВИХ ВЛАСТИВОСТЕЙ ДВОВИМІРНОГО НАПІВПРОВІДНИКА $BiBr_3$ ЗА ДОПОМОГОЮ DFT

Ядгар Хуссейн Шван, **Маджида Алі Амін**, **Арас Саїд Махмуд**

Фізичний факультет, Коледж освіти, Університет Сулеймані, Сулейманія 46001, Курдистан, Ірак

Теорія функціоналу густини (DFT) служить методом перших принципів для ретельного дослідження стабільності структури та аналізу електронних, оптичних та теплових характеристик двовимірного трибромiду вісмуту (2D $BiBr_3$). Моделювання молекулярної динаміки ab-initio (AIMD) показує, що структура є термічно стабільною при 300 K. $BiBr_3$ поводиться як напівпровідник із забороненою зоною 2,84 еВ згідно з його електронною зонною структурою та аналізом часткової густини станів (PDOS). Оптична характеристика показує, що $BiBr_3$ має сильні взаємодії у видимому та ультрафіолетовому діапазонах довжин хвиль, що демонструє його потенціал у наступному поколінні оптичних та оптоелектронних пристроїв. Чудове значення термоЕРС, оцінене за допомогою розрахунків переносу Больцмана, підкреслює перспективність $BiBr_3$ у низькотемпературному термоелектричному управлінні. Це дослідження передбачає покращення коефіцієнта потужності, зумовленого температурою, яке досягає піку в 3,25 $\times 10^{12}$ Вт/K^2·см·с при 300K. $BiBr_3$ демонструє помірну теплоємність при середніх та високих температурах, зберігаючи при цьому дуже низьку теплопровідність. Це підкреслює його здатність ефективно керувати теплом та служити ізолятором у різних застосуваннях. Детальні результати показують, що 2D $BiBr_3$ є потенційно сприятливим матеріалом з різноманітними можливостями в більшості технологічних застосувань.

Ключові слова: *структура $BiBr_3$; DFT; стабільність; електронні характеристики; теплові властивості; оптичні характеристики*

EAST EUROPEAN JOURNAL OF PHYSICS. 1. 203-207 (2026)
DOI:10.26565/2312-4334-2026-1-20 ISSN 2312-4334

EFFECT OF IMPURITY CLUSTERS ON OPTICAL PROPERTIES OF NICKEL AND COPPER DOPED SILICON

Sirajidin Z. Zainabidinov[1], N.A. Turgunov[2], Akramjon Y. Boboev[1], Shuhratjon K. Akbarov[1], Raymash M. Turmanova[2], Abdukakhor Arikov[1], Muqaddas O. Kuchkarova[1], Bakhrikhon Tolanova[1], Markhabo B. Rasulova[1]
[1]Andijan state university named after Z.M. Babur, Andijan, Uzbekistan
[2]Research Institute of Semiconductor and Microelectronics Physics at the National University of Uzbekistan, Tashkent
**Corresponding Author e-mail: aboboevscp@gmail.com*
Received June 16, 2025; revised October 28, 2025; in final form February 2, 2026; accepted February 17, 2026

This paper deals with the influence of impurity atoms on optical properties of single crystal silicon doped with nickel and copper during high-temperature diffusion doping. And also, the processes of formation of various chemical compounds with participation of oxygen and carbon atoms with atoms of nickel, copper and silicon. By means of FTIR spectrometry and X-ray diffraction analysis it was revealed that the concentration of optically active oxygen and carbon in the volume of silicon samples doped with nickel and copper significantly increases compared to the original samples.
Keywords: *Silicon; Nickel; Copper; Diffusion; Impurity; Oxygen; Carbon; Clusters*
PACS: 78.30.Am

INTRODUCTION

The control and characterization of background impurities such as oxygen and carbon in silicon single crystals is a critical task for modern microelectronics and optoelectronic device fabrication. These impurities, particularly when optically active, can significantly alter the electrical, optical, and structural properties of silicon, affecting charge carrier lifetime, recombination rates, and overall device efficiency [1]. Optically active oxygen and carbon atoms are known to interact with substitutional or interstitial impurities and contribute to the formation of electrically active complexes and extended defects, especially under thermal or radiation processing conditions [2].

Fourier-transform infrared (FTIR) spectroscopy remains a powerful and non-destructive analytical tool for the precise quantification of light elements such as oxygen and carbon in silicon matrices. Its high sensitivity to vibrational modes of impurity atoms enables accurate detection of characteristic absorption peaks corresponding to bond-specific interactions [3]. In particular, absorption at 1106 cm^{-1} is attributed to interstitial oxygen (O_i) stretching modes, while peaks in the 607–620 cm^{-1} region correspond to substitutional carbon (Cs) modes [4].

In the present study, we aimed to determine the concentration of optically active oxygen and carbon in both intrinsic n-type silicon and in silicon samples doped with transition metals such as nickel and copper. The samples were analyzed using a Fourier-transform infrared spectrometer FSM 2201, operating in the range 370–7800 cm^{-1} with a spectral resolution of 1 cm^{-1}. A DLATGS pyrodetector was employed for enhanced signal sensitivity. The oxygen and carbon concentrations were calculated from the respective IR absorption intensities at room temperature, applying standard calibration methods [5].

To complement the FTIR analysis and gain deeper insight into the structural rearrangements induced by metallic dopants, we also conducted X-ray diffraction (XRD) studies. These investigations were essential for identifying the formation of metallic impurity complexes, dislocation loops, or secondary phase precipitates within the silicon lattice. The XRD measurements were performed using a high-resolution Malvern Panalytical Empyrean diffractometer with CuKα radiation ($\lambda = 0.15405$ nm), operated in step-scan mode to ensure accurate peak identification and lattice parameter extraction [6].

Such integrated spectroscopic and diffraction-based analysis enables a more comprehensive understanding of impurity-induced modifications in silicon, which is crucial for the optimization of material parameters in semiconductor device engineering.

MATERIALS AND METHODS

Growing silicon single crystals by the Czochralskii method, which is the most frequently used in modern semiconductor production, involves a number of important parameters, such as melt temperature, drawing speed, rotation speed of the crystal and seed, composition and purity of the initial polysilicon, mainly determine the quality of the obtained single crystal. In the technological process of growing single crystals of silicon, depending on the conditions of growth, to exclude the penetration of oxygen and carbon atoms in the composition of the growing material is virtually impossible.

Cite as: S.Z. Zainabidinov, N.A. Turgunov A.Y. Boboev, Sh.K. Akbarov, R.M. Turmanova, Abdukakhor Arikov, M.O. Kuchkarova, B. Tolanova, M.B. Rasulova, East Eur. J. Phys. 1, 203 (2026), https://doi.org/10.26565/2312-4334-2026-1-20

Therefore, in the volume of single crystalline silicon, obtained by this method, oxygen and carbon atoms are present in high enough concentrations up to 10^{17}-10^{18}cm^{-3}. These two contaminating impurities in single crystals of silicon are called background impurities, because when using the existing installations of the Czochralski method, their entry into the melt can not be excluded. Numerous studies have shown that oxygen and carbon atoms participate in complexation processes in single crystal silicon [7]. Often extensive precipitates or microinclusions of impurity atoms [8-11], which are formed during very large-scale or ultra-large-scale integrated fabrication, can be critical to device quality and performance. Oxygen precipitates can be useful by allowing the deposition of transition metals and strengthening the wafer by preventing plastic deformation during processing. However, if they form in active regions, they act as defects, degrading device performance [12].

RESULTS AND DISCUSSION

Initial n-Si samples and doped n-Si <Ni,Cu> samples were fabricated for the studies. As an initial sample for experiments, single-crystalline silicon of KEF grade, grown by the Czochralski method, with a resistivity of 0.3 Ohm·cm was used. The samples prepared in the form of a rectangular parallelepiped with dimensions 10x5x2 mm were pre-cleaned by chemical methods [13]. Using a VUP-4 vacuum sputtering system unit, in which the vacuum value was 10^{-4}Torr, nickel atoms were deposited on the previously prepared silicon samples on one side by sputtering with a thickness of 0.4 μm. And on the other side, copper atoms with a thickness of 0.6 μm were deposited on the same samples. Simultaneous diffusion of nickel and copper atoms in silicon was carried out in a horizontal SUOL-4 furnace at temperature T=1473 K for 5 hours. The furnace temperature was controlled within ±3 K using a platinum-platinum-rhodium thermocouple. After diffusion annealing, the samples were cooled by rapid cooling method, where the cooling rate was υ_{col}=200 K/s. Fig. 1. shows a fragment and spectrograms of the change in the concentration of optically active oxygen in the original sample and in the n-Si <Ni,Cu> sample

Calculations of the value of optically active oxygen concentration were carried out using the following formula [14]:

$$N_O^{opt} = 3.3 \cdot 10^{17} \cdot \frac{1}{d} ln \frac{I}{I_0}, \quad (1)$$

Where: I and I_0 are the intensities of incident and transmitted light, d is the thickness of the sample

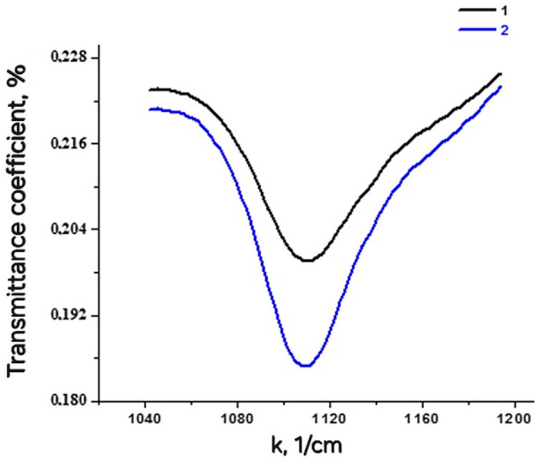

Figure 1. Dependence of transmittance on wavenumber (k, cm^{-1}): 1 - n-Si; 2 - n-Si<Ni,Cu>

The concentration of optically active oxygen in the original sample and in the n-Si< Ni,Cu> samples is n = 2.5·10^{17}cm^{-3} and n= 3.9·10^{17}cm^{-3}, respectively. Calculations show that the concentration of optically active oxygen in the n-Si<Ni,Cu> samples is 1.6 times higher compared to the original samples.

This means that in the process of diffusion at T=1473 K oxygen atoms form a bond with impurity atoms, forming a metal oxide. Because of this, the concentration of optically active oxygen in the doped samples increases.

Fig. 2. shows fragments of IR spectrograms of the change in the concentration of optically active carbon in the original n-Si sample and in the n-Si <Ni,Cu> sample.

The concentration of optically active carbon was calculated by the following formula [14]:

$$N_C^{opt} = 1{,}1 \cdot 10^{17} \cdot \frac{1}{d} ln \frac{I}{I_0}, \quad (2)$$

Where: d-thickness of the sample, I - and I_0- of incident and transmitted light.

The results obtained showed that the concentration of optically active carbon in the original sample and in the n-Si< Ni,Cu> samples respectively are n= 6.6·10^{17}cm^{-3} and n= 8.84·10^{17}cm^{-3}. From the results obtained, it is found that the value of optically active carbon concentration in the n-Si<Ni,Cu> samples is 1.33 times more as compared to the original sample.

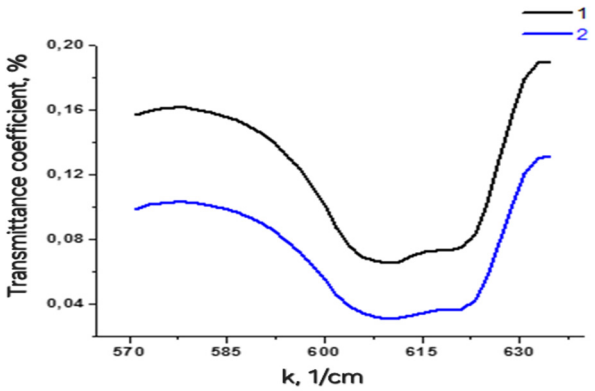

Figure 2. Graphs of dependence of transmission coefficient on the wave vector: 1 – n-Si, 2 – n-Si<Ni,Cu>

In order to further clarify and confirm the presented results, we carried out X-ray diffraction analyses of all samples. The obtained results were analyzed as follows. In Fig. 3. shows the X-ray diffraction patterns of the original sample and the n-Si <Ni,Cu> sample. Using the obtained results, the interplanar distance in the crystal can be determined from the Wolf-Bragg equation [15].

$$n\lambda = 2dsin\theta, \tag{3}$$

where d is the interplanar distance, θ is the Wolf-Bragg angle n-order of diffraction maximum, λ = 0.15405 nm is the wavelength of CuK_α-radiation.

The average size of crystallites of different planes was determined by Scherrer's formula [15]:

$$L = \frac{K\lambda}{\beta cos\theta}, \tag{4}$$

Where, K is the dimensionless particle shape factor (Scherrer's constant); λ = 0.15405 nm - wavelength of CuK_α-radiation; β - reflex width at half-height, θ - Wolf-Bragg angle,L - average crystallite size (nm).

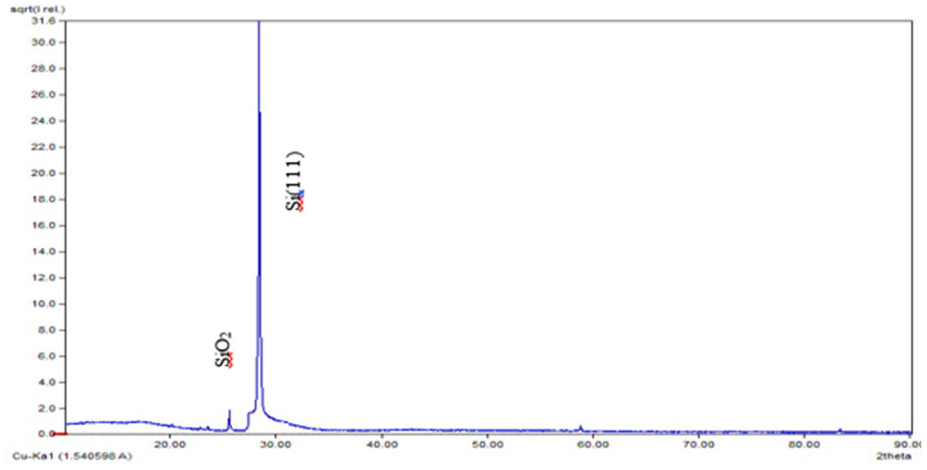

a)

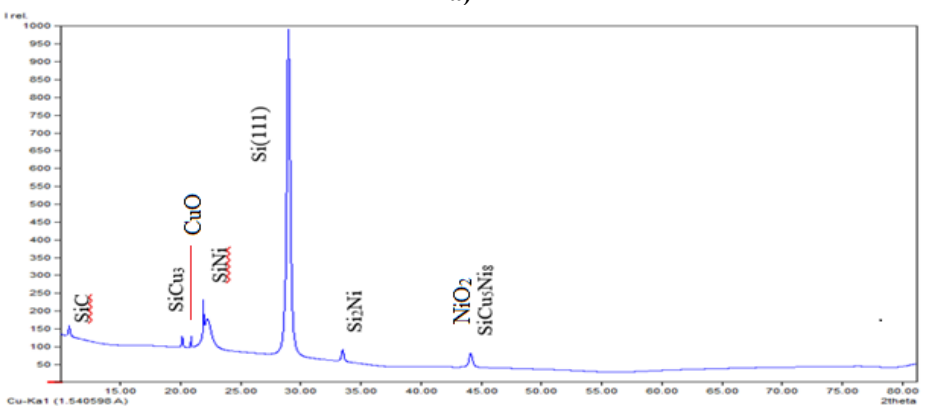

b)

Figure 3. Plots of the dependence of the transmittance coefficient on the wave vector for the samples: 1 – n-Si; 2 – n-Si<Ni,Cu>

The largest peak of them corresponds to single-crystalline silicon with crystal orientation (111). In this reflection, the L value and the d value are 0.474 nm and 1.84 nm, respectively. From this calculation, it can be seen that the L value decreases almost 6 times and the d value increases almost 3 times compared to the same reflex in the original sample. These results indicate that the crystal lattice is deformed due to the penetration (introduction) of impurity atoms. The reflex observed at an angle of 10.77° , corresponds to the SiC compound. In the X-ray diagram, the third peak by order number corresponds to the copper oxide compound CuO. It reflects at an angle of 20.88° and its L and d values are 2.805 nm and 1.27 nm, respectively. And one more peak corresponds to the compound of oxygen to metal $NiO_2$and it reflects at an angle of 44.12° [16].

As can be seen from the results of X-ray diffraction analysis, several kinds of clusters involving impurity atoms of nickel and copper were formed in the silicon crystal after diffusion. In addition, from the results of X-ray diffraction analysis, the formation of various chemical compounds of oxygen atoms, carbon atoms with nickel or copper atoms, as well as with silicon atoms is observed. Consequently, it appears that in the process of high-temperature diffusion annealing, oxygen atoms form chemical compounds with the main impurity atoms and move to an optically active state. For this reason, an increase in the optically active oxygen concentrations was observed in the Fourier spectroscopy analysis compared to the original sample.

Thus, the results obtained by determining the concentration of optically active background impurities in the original samples n-Si and in samples n-Si<Ni,Cu> showed that during high-temperature diffusion doping of silicon with nickel and copper, the concentration of optically active oxygen and carbon in the volume of samples increases significantly. This increase is due to the formation of complexes of oxygen and carbon atoms with atoms of the main impurities, after which they pass to the optically active state.

CONCLUSIONS

As can be seen from the results of X-ray diffraction analysis, several types of clusters containing nickel and copper impurity atoms formed in the silicon crystal after diffusion. In addition, from the results of X-ray diffraction analysis, the formation of various chemical compounds of oxygen atoms, carbon atoms with nickel or copper atoms, as well as with silicon atoms, is observed. Consequently, it appears that during high-temperature diffusion annealing, oxygen atoms form chemical compounds with the main impurity atoms and become optically active. For this reason, an increase in the optically active oxygen concentrations was observed in the Fourier spectroscopy analysis compared to the original sample.

Thus, the results obtained by determining the concentration of optically active background impurities in the original samples n-Si and in samples n-Si<Ni,Cu> showed that during high-temperature diffusion doping of silicon with nickel and copper, the concentration of optically active oxygen and carbon in the volume of samples increases significantly. This increase is due to the formation of complexes of oxygen and carbon atoms with atoms of the main impurities, after which they pass to the optically active state.

Funding

The present research work was financed under the project FZ-292154210 granted by the Ministry of Innovative Development of the Republic of Uzbekistan

ORCID

S.Z. Zainabidinov, https://orcid.org/0000-0003-2943-5844; **N.A. Turgunov,** https://orcid.org/0000-0003-3481-5622
A.Y. Boboev, https://orcid.org/0000-0002-3963-708X; **Sh.K. Akbarov,** https://orcid.org/0009-0008-4193-8659
R.M.Turmanova, https://orcid.org/0009-0005-7346-0571; **A. Artikov,** https://orcid.org/0009-0001-3911-3999
M.O. Kuchkarova, https://orcid.org/0009-0005-4053-0414; **B. Tolonova,** https://orcid.org/0009-0004-4944-1672
M.B. Rasulova, https://orcid.org/0009-0003-1068-7651

REFERENCES

[1] S.Z. Zainabidinov, Sh.K. Akbarov, N.A. Turgunov, N.B. Khaytimmetov, and R.M. Turmanova, "Formation of impurity accumulations in silicon doped with nickel and copper," E3S Web of Conferences. **632**, 03004 (2025). https://doi.org/10.1051/e3sconf/202563203004

[2] S.Z. Zaynabidinov, A.Y. Boboev, N.Y. Yunusaliyev, and M.B. Rasulova, "X-ray diffraction analysis, optical characteristics and electro-physical properties of the n-ZnO/p-NiO structure grown by the spray pyrolysis method," New Materials, Compounds and Applications, **8**(3), 411–421 (2024). https://doi.org/10.62476/nmca83411

[3] Y. Yamashita, *et al*., "Effect of metal impurities on recombination lifetime in Si," J. Appl. Phys. **127**, 075701 (2020). https://doi.org/10.1063/1.5140424

[4] S. Sarti, *et al*., "FTIR characterization of carbon in silicon," Materials Science in Semiconductor Processing, **21**, 78–83 (2014).

[5] M. Fahelelbom, A. Saleh, M. M. A. Al-Tabakha, and A. A. Ashames, "Recent applications of quantitative analytical FTIR spectroscopy in pharmaceutical, biomedical, and clinical fields: A brief review," Rev. Anal. Chem. **41**(1), 21–33 (2022). https://doi.org/10.1515/revac-2022-0030

[6] J.H. Linn, and K.L. Hanley, "Quantitative infrared spectroscopy of interstitial oxygen in silicon wafers using multivariate calibration," Applied Spectroscopy, **47**(12), 2102–2107 (1993). https://doi.org/10.1366/0003702934066361

[7] J. Kozuch, K. Ataka, and J. Heberle, "Surface-enhanced infrared absorption spectroscopy," Nat. Rev. Methods Primers, **3**, 1 (2023). https://doi.org/10.1038/s43586-023-00253-8

[8] B. Talanin, and I. Talanin, "High-temperature precipitation of impurities in metals," Physics of the Solid State, **64**(3), 340–346 (2022). https://doi.org/10.1134/S1063783422030270.

[9] G. Kissinger, D. Kot, F. Bärwolf, and M. Lisker, "Investigation of the Impact of Amorphous Silicon Layers Deposited by PECVD and HDP-CVD on Oxide Precipitation in Silicon," Materials Science in Semiconductor Processing, **164**, 107614 (2023). https://doi.org/10.1016/j.mssp.2023.107614
[10] N.A. Turgunov, E.Kh. Berkinov, and R.M. Turmanova, "Accumulations of impurity Ni atoms and their effect on the electrophysical properties of Si," E3S Web of Conferences, **402**, 14018 (2023).
[11] N.A. Turgunov, S.K. Akbarov, N.B. Khaytimmetov, and R.M. Turmanova, "Influence of accumulation of impurity atoms Ni and Fe on the electrophysical properties of Si single crystals," J. Nano Electron. Phys. **16**(1), 01004 (2024). https://doi.org/10.21272/jnep.16(1).01004
[12] D. Firsov, S. Khakhulin, and O. Komkov, "Fourier-transform infrared reflection anisotropy spectroscopy of semiconductor crystals and structures: Development and application in the mid-infrared," Appl. Spectrosc. **1**(4), 1–12 (2023).
[13] N.Y. Yunusaliyev, "The gas-sensitive properties of tin dioxide films" East Eur. J. Phys. **4**, 439 (2024), https://doi.org/10.26565/2312-4334-2024-4-5
[14] A. Janotti and C.G. Van de Walle, "Fundamentals of zinc oxide as a semiconductor," Reports on Progress in Physics, **72**(12), 126501 (2009). https://doi.org/10.1088/0034-4885/72/12/126501
[15] S. Zaynabidinov, *et al*., "X-ray diffraction and electron microscopic studies of the ZnO(S) metal oxide films obtained by the ultrasonic spray pyrolysis method," Herald of the Bauman Moscow State Tech. Univ., Ser. Nat. Sci. **1**, 78 (2024). https://doi.org/10.18698/1812-3368-2024-1-78-92
[16] M. Kooti, and M. Jorfi, "Synthesis and characterization of nanosized NiO_2 and NiO using Triton X-100," Open Chemistry, **6**(1), 186–192 (2008). https://doi.org/10.2478/s11532-008-0005-9

ВПЛИВ ДОМІШКОВИХ КЛАСТЕРІВ НА ОПТИЧНІ ВЛАСТИВОСТІ КРЕМНІЮ, ЛЕГОВАНОГО НІКЕЛЕМ ТА МІДДЮ

Сіраджідін З. Зайнабідінов[1], Н.А. Тургунов[2], Акрамжон Й. Бобоєв[1], Шухратжон К. Акбаров[1], Раймаш М. Турманова[2], Абдукахор Аріков[1], Мукаддас О. Кучкарова[1], Бахріхон Толанова[1], Мархабо Б. Расулова[1]

[1]*Андижанський державний університет імені З.М. Бабура, Андижан, Узбекистан*

[2]*Науково-дослідний інститут фізики напівпровідників та мікроелектроніки Національного університету Узбекистану, Ташкент*

У цій статті розглядається вплив домішкових атомів на оптичні властивості монокристалічного кремнію, легованого нікелем та міддю, під час високотемпературного дифузійного легування. А також процеси утворення різних хімічних сполук за участю атомів кисню та вуглецю з атомами нікелю, міді та кремнію. За допомогою ІЧ-спектрометрії з перетворенням Фур'є та рентгеноструктурного аналізу було виявлено, що концентрація оптично активного кисню та вуглецю в об'ємі зразків кремнію, легованих нікелем та міддю, значно зростає порівняно з вихідними зразками.

Ключові слова: *кремній; нікель; мідь; дифузія; домішка; кисень; вуглець; кластери*

EAST EUROPEAN JOURNAL OF PHYSICS. 1. 208-215 (2026)
DOI:10.26565/2312-4334-2026-1-21 ISSN 2312-4334

COMPOSITION AND RADIATION-INDUCED VARIATIONS OF THERMAL CONDUCTIVITY IN $Sn_{1-x}Tb_xSe$ SOLID SOLUTIONS

T.A. Jafarov[1], H.A. Aslanov[1], A.M. Allahverdiyev[1], O.M. Gasanov[1], J.I. Huseynov[1]*, Kh.A. Adgezalova[1], G.A. Garashova[1], I.I. Abbasov[2]

[1]*Azerbaijan State Pedagogical University, Az-1000, Baku, Uz Hajibeyli Str.68, Azerbaijan*
[2]*Azerbaijan State Oil and Industry University,* Az-1010, *Baku, Azadlıq Avenue 20, Azerbaijan*
Corresponding Author email: jahangirhuseynov1958@gmail.com
Received December 4, 2025; revised January 15, 2026; accepted January 25, 2026

In this work, the structural, physicochemical, and thermal transport properties of $Sn_{1-x}Tb_xSe$ ($0 \le x \le 0.05$) alloys were investigated with respect to terbium concentration and γ-irradiation dose. X-ray diffraction and DTA analyses confirmed the formation of orthorhombic substitutional solid solutions following Vegard's law, with a slight increase in lattice parameters and microhardness as Tb content increased. The introduction of Tb atoms into the SnSe matrix enhances phonon–defect scattering due to mass fluctuations and lattice distortions, resulting in a pronounced reduction in thermal conductivity, particularly at low doping levels ($x \le 0.02$). Thermal conductivity measurements performed after γ-irradiation (0–6.5 Mrad, ^{60}Co source) revealed a general decreasing trend for all compositions. In undoped SnSe, the relative decrease reached ~6%, while in Tb-doped samples, the sensitivity to irradiation was significantly reduced. For doses above 5 Mrad, the dependence k(D) is well described by a linear model with high correlation coefficients. These results demonstrate that Tb incorporation not only suppresses phonon transport, enhancing thermoelectric potential, but also increases the radiation resistance of SnSe-based materials.
Keywords: *Thermal conductivity; Phonon scattering; Radiation resistance; γ-irradiation; Solid solutions; Orthorhombic structure; Defect formation; Thermoelectric materials; Lattice distortion; Mass fluctuation scattering*
PACS: 71.20.Nr, 72.20.Pa, 61.72.-y

1. INTRODUCTION

Compounds of the A_4B_6 type ($A = Ge, Sn, Pb$; $B = S, Se, Te$) crystallize in an orthorhombic layered structure (space group *Pnma*), characterized by alternating atomic double layers held together by relatively weak interlayer interactions. This layered configuration gives rise to pronounced anisotropy in their mechanical and electro-optical properties: elastic moduli and dielectric permittivity differ significantly along and across the layers [1]. Electronic structure calculations show that these compounds exhibit narrow or medium band gaps with an indirect transition, making them promising semiconductor materials [2].

A_4B_6 materials exhibit distinct optical responses: calculated functions of dielectric permittivity, energy loss, and the effective number of valence electrons confirm their potential application in optoelectronic devices such as photovoltaic cells, photodetectors, and elements of flexible electronics [3]. Their structural and electronic characteristics also enable control over the anisotropy of charge transport within functional layers.

Tin selenide ($SnSe$) crystals possess a wide range of optical and photoelectric properties determined by their anisotropic layered structure and narrow band gap ($\sim 1.0\ eV$), making them promising materials for infrared optoelectronics [4, 5]. Due to their strong absorption in the visible and near-infrared regions, $SnSe$ can be effectively utilized as a photonic absorber in solar cells and photodetectors [6]. The high carrier mobility and stability of its crystal lattice further enhance its potential for use in photodetectors, solar energy converters, and energy storage devices [7, 8]. Moreover, the combination of high thermoelectric efficiency and sensitivity to light irradiation makes $SnSe$ a versatile material for multifunctional energy-efficient sensors [9].

Enhancement of the thermoelectric parameters of $SnSe$ crystals can be achieved by introducing various dopant impurities, which modify the carrier concentration and phonon-scattering behavior. Doping with rare-earth elements helps optimize the balance between electrical conductivity and thermal conductivity, thereby improving the thermoelectric efficiency of the material [10, 11].

The study of the combined effects of doping and ionizing radiation is a relevant research direction aimed at developing stable and highly efficient thermoelectric materials based on $SnSe$. Alloys of the type $Tb_xSn_{1-x}Se$, derived from $SnSe$, are considered promising thermoelectric materials due to their high Seebeck coefficient and low thermal conductivity. In this work, the dependence of the thermal conductivity of these alloys on the *Tb* content and absorbed dose of gamma irradiation is investigated.

2. EXPERIMENTAL SECTION

For the synthesis of $Sn_{1-x}Tb_xSe$ alloys, high-purity starting materials were used: tin of grade "B4-000", selenium of grade "OC417-4", and chemically pure terbium (99.98%). The synthesis was carried out in evacuated quartz ampoules at a pressure of $0.1333\ Pa$ by a two-stage direct fusion method.

Cite as: T.A. Jafarov, H.A. Aslanov, A.M. Allahverdiyev, O.M. Gasanov, J.I. Huseynov, Kh.A. Adgezalova, G.A. Garashova, I.I. Abbasov, East Eur. J. Phys. 1, 208 (2026), https://doi.org/10.26565/2312-4334-2026-1-21

At the first stage, the ampoule containing the mixture was heated at a rate of $4-5\ ^\circ C$ per minute up to the melting point of selenium and held at this temperature for $3-4\ hours$. Subsequently, the temperature was gradually increased to $950-1000\ ^\circ C$ (depending on the alloy composition) and maintained for $8-9\ hours$ [12].

The interaction in the $SnSe-TbSe$ system was studied using differential thermal analysis (DTA), X-ray phase analysis (XRD), microstructural analysis (MSA), as well as through measurements of microhardness and density [13]. Thermal effects and phase transitions of the obtained samples were investigated by DTA using a *PerkinElmer Simultaneous Thermal Analyzer STA 6000* (USA). Nitrogen was used as the purge gas at a flow rate of 20 mL/s, and the samples were heated up to the melting temperature at a rate of $5\ ^\circ C/min$.

X −ray diffraction (XRD) analysis was performed on a *Rigaku Miniflex* diffractometer operating at 30 kV and 10 mA, using CuKα radiation (λ = 1.5406 Å). The diffraction patterns were recorded within the 2θ range of 0–80° [14]. The morphology and microcomposition of the sample surfaces were examined using a *JEOL JSM-6610LV* scanning electron microscope (Japan).

The thermal conductivity of the investigated samples was measured by an absolutely steady-state method according to the procedure described in [15]. This method provides high accuracy in determining the thermal conductivity coefficient by establishing a stable temperature gradient between the heated and cooled ends of the sample. The measurement error did not exceed 4.2%, confirming the reliability of the obtained experimental data.

For irradiation of samples with different compositions, an ionizing γ-radiation source based on the isotope ^{60}Co was used, with a dose rate of $0.6\ Gy/s$ and photon energy of $1.25\ MeV$. During irradiation, the samples were exposed to radiation at the given dose rate and various absorbed doses for durations of $\boldsymbol{t} = 5, 10, 15, 20, 25$ and $30\ hours$. After irradiation, the thermal conductivity of the samples was measured at a temperature of $\boldsymbol{T} = 300\ K$. A comparative analysis of results obtained before and after irradiation enabled evaluation of the material's radiation resistance.

3. RESULTS AND DISCUSSION

3.1. Physicochemical Analysis

The thermograms of the $Tb_xSn_{1-x}Se$ alloys exhibit distinct peaks upon heating and cooling, corresponding to melting and solidification temperatures, which indicates the formation of congruently melting alloys. Partial substitution of Sn with Tb leads to a decrease in the melting temperature due to lattice deformation and weakening of interatomic bonds. At a $TbSe$ content up to $0.03\ mol.\%$, the microhardness of the samples reaches approximately $500\ MPa$.

Analysis of X −ray diffraction (XRD) patterns shows that the sample is single-phase and exhibits a preferred crystal orientation. Indexing of the diffraction peaks corresponds to an orthorhombic symmetry with space group $D_2h^{16}-Pcmn$ (Fig. 1). Within the composition range $0 \le x \le 0.05$, no noticeable shift of diffraction lines is observed, but their intensity changes, indicating the formation of solid solutions based on $SnSe$. Substitution of Sn atoms with rare-earth elements of larger ionic radii causes a reduction in reflection intensity and a linear increase in lattice parameters, with no deviation from Vegard's law detected.

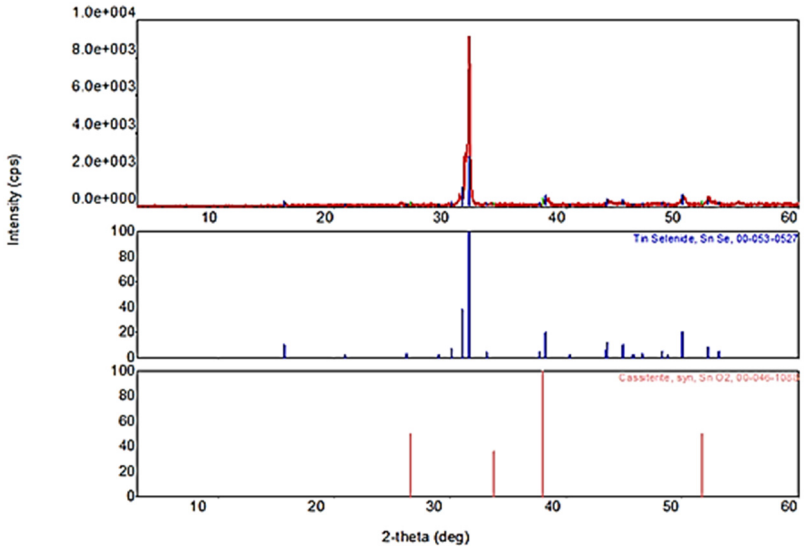

Figure 1. X-ray diffraction spectrum of crystals $Tb_xSn_{1-x}Se$:x = 0.0025. Below are X-ray diffraction patterns of SnSe and SnO for comparison

X −ray structural analysis reveals that the incorporation of terbium selenides leads to an increase in the unit cell parameters of $SnSe$ as the Tb concentration rises. This results in enhanced scattering of charge carriers due to lattice distortions, which correlates with the observed decrease in the thermal conductivity of the alloys [16]. At the same time, the density of $Tb_xSn_{1-x}Se$ compounds remain nearly constant, suggesting that Tb atoms occupy interstitial positions and generate Frenkel-type defects [17].

The increase in lattice parameters and the consistent substitution of *Sn* atoms by *Tb,* along with adherence to Vegard's law, indicate the formation of a substitutional solid solution based on *SnSe*. According to $X-$ray diffraction and pycnometric measurements, the solubility limit of $TbSe$ in $SnSe$ at room temperature is about 5 $mol.\%$.

Comprehensive physicochemical analysis demonstrates that the $Tb_xSn_{1-x}Se$ solid solutions retain an orthorhombic symmetry similar to that of the parent $SnSe$ compound. With increasing $TbSe$ content, a slight increase in lattice parameters, density, and microhardness is observed, along with a shift of thermal effects toward lower temperatures. The difference in electronic configurations between *Sn* and *Tb* atoms leads to distortions in the $SnSe$ crystal lattice upon substitution; however, its fundamental structure remains preserved [18].

Atomic force microscopy (AFM) studies of the surface morphology of $Tb_xSn_{1-x}Se$ crystals reveal a distinctly nonuniform surface with an average roughness of about 25 nm. Such microrelief structures are associated with weak van der Waals interlayer interactions typical of layered compounds. The cleavage of these crystals leads to the formation of separate atomic clusters and microsteps, giving the surface an uneven, wave-like texture. $X-$ray microanalysis (Fig. 2) enabled determination of the phase composition and spatial distribution of the constituent elements. It was found that the surface remains chemically homogeneous overall, although a slight excess of selenium content is observed within the homogeneity region of the $SnSe$ compound.

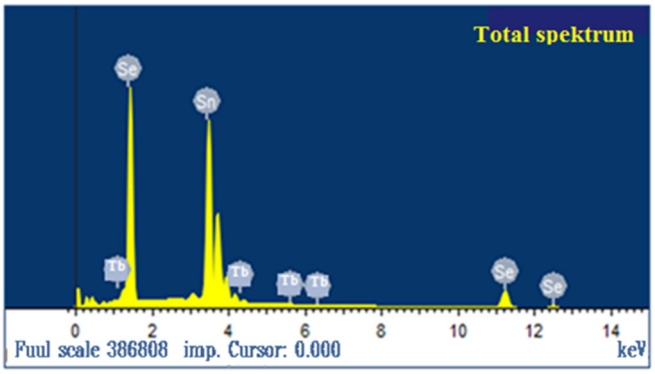

Element	Weight %	Atomic %
Sn L	59.69	49.72
Se L	39.90	50.03
Tb L	0.41	0.25
Total	100	100

Figure 2. X-ray microanalysis of the crystal surface $Tb_xSn_{1-x}Se$:(x=0,005)

3.2. Dependence of Thermal Conductivity on Composition

The thermal conductivity of the system alloys $Sn_{1-x}Tb_xSe$ at room temperature was experimentally determined, and its dependence on the molar fraction of Tb atoms was investigated. According to the experimental results, a clear dependence of the thermal conductivity coefficient (k) on the molar content of Tb was established (Fig. 3).

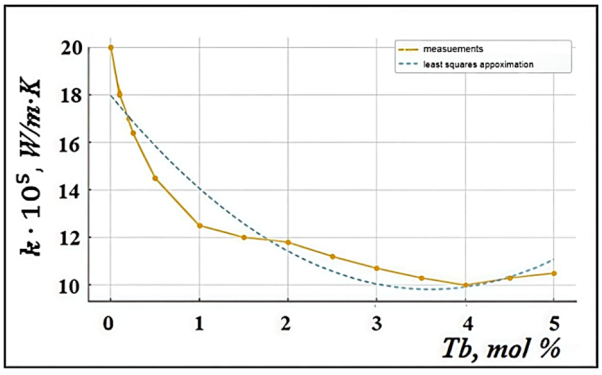

Figure 3. Composition dependence of thermal conductivity in $Sn_{1-x}Tb_xSe$ system alloys

As seen from the graph, the thermal conductivity decreases with increasing Tb concentration, and this reduction is particularly sharp up to approximately 2 $mol\%$. Such behavior is primarily attributed to the increase in defect density and mass fluctuation within the crystal lattice caused by the substitution of Tb atoms into the $SnSe$ matrix. The introduction of Tb enhances phonon scattering [19]. The appearance of Tb nuclei and atoms with different masses reduces the average phonon mean free path, leading to a decrease in thermal conductivity. The rate of reduction is especially high at low Tb concentrations, since the initial doping introduces new scattering centers in the lattice, sharply decreasing the phonon mean free path and consequently the thermal conductivity.

A slight increase in thermal conductivity observed in the range of 4–5 mol%$(10.0 - 10.5) \times 10^{-5} W \cdot m^{-1} \cdot K^{-1}$,is statistically insignificant and most likely results from measurement uncertainties or microstructural variations between samples. The weak increase in this range may also be associated with the formation of a secondary phase or local ordering of the crystal structure at higher Tb contents. Such a dependence can be explained by changes in the material's heat transport mechanisms as the composition changes.

Overall, the conducted studies show that the incorporation of Tb atoms into the $SnSe$ matrix significantly enhances phonon scattering mechanisms, resulting in a pronounced decrease in thermal conductivity. Thus, with increasing Tb concentration in $Sn_{1-x}Tb_xSe$ alloys, heat transfer becomes limited by diffusive phonon scattering, which is of both scientific and practical importance for improving the thermoelectric efficiency of such materials.

In solids, thermal conductivity depends on multiple parameters, and the total thermal conductivity coefficient can be represented as the sum of several major components, which are separated according to the nature of heat carriers in the material [20]:

$$k_{tot} = k_{ph} + k_{el} + k_{ex} + k_{maq} + k_f + k_{bp}$$

For semiconductors, the thermal conductivity is usually expressed as the sum of two main parts [21]:

$$k_{tot} = k_{ph} + k_{el},$$

where k_{ph} −is the phonon (lattice) contribution, i.e., the heat flux carried by atomic vibrations (phonon propagation), and k_{el} − is the electronic contribution, i.e., the heat flux carried by free charge carriers (electrons and holes).

The electronic thermal conductivity can be approximately estimated using the Wiedemann–Franz law [22]:

$$k_{el} = L\sigma T,$$

where L −is the Lorenz constant ($\approx 2.44 \cdot 10^{-8} W\Omega K^{-2}$for ideal metals, but variable for semiconductors depending on band structure), $\sigma$is the electrical conductivity, and T is the absolute temperature.

Calculations show that in $SnSe$ −based semiconductors, heat transport is predominantly phononic, and the low thermal conductivity of such compounds is mainly due to strong phonon scattering [23]. The partial substitution of Sn atoms by Tb atoms break the local symmetry of the crystal lattice and creates point defects. These defects increase the probability of elastic phonon scattering, thereby reducing the thermal conductivity.

The mechanism of phonon–defect scattering can be described by the Clemens model [24]. According to this model, the average phonon lifetime limited by point-defect scattering decreases as follows:

$$\tau_{pd}^{-1} \propto \Gamma\omega^4,$$

where $\Gamma = {}_i f_i(1 - M_i/M_{av})^2$is the mass-fluctuation parameter, $\omega$is the phonon frequency, M_i and M_{av} are the atomic masses of the components and their average atomic mass, respectively.

The substitution of Sn atoms with Tb introduces differences not only in mass but also in elastic modulus, which shortens the phonon mean free path and lowers the thermal conductivity. This model successfully explains the sharp decline in thermal conductivity observed in the range of $0 - 3\ mol\%\ Tb$.To provide a more complete description of heat transport in the alloys, the Callaway model [25] was employed. According to this model, the thermal conductivity is determined by the combined influence of several scattering mechanisms. The total phonon relaxation rate is given by Matthiessen's rule [26]:

$$\tau_C^{-1} = \tau_U^{-1} + \tau_B^{-1} + \tau_{pd}^{-1},$$

where τ_U^{-1} − corresponds to Umklapp scattering processes, τ_U^{-1} −represents boundary scattering, and τ_{pd}^{-1} − accounts for point-defect scattering.

As the Tb concentration increases, the intensity of point-defect scattering rises (i.e., τ_{pd}^{-1}increases), which shortens the total phonon lifetime and leads to a monotonic decrease in the thermal conductivity of the samples.

The observed compositional dependence of thermal conductivity can also be explained by the Clemens–Abeles alloy model, which attributes the enhanced phonon scattering to increasing differences in the masses and radii of the constituent atoms, resulting in reduced thermal conductivity [27].

According to the experimental data, the slight rise in thermal conductivity at $4 - 5\ mol\%$ Tb, although statistically insignificant, may be related to local microstructural modifications or the formation of a secondary phase (e.g., Tb_2Se_3).

In conclusion, the obtained experimental results demonstrate that the thermal conductivity of $Sn_{1-x}Tb_xSe$ alloys is primarily governed by phonon–defect scattering mechanisms. Increasing Tb concentration enhances lattice disorder, decreases the phonon mean free path, and consequently reduces the overall thermal conductivity. This relationship is fully consistent with both the Clemens and Callaway models.

3.3. Dependence of Thermal Conductivity on the Absorbed Radiation Dose

To investigate the effect of ionizing radiation on the thermal conductivity of the $Sn_{1-x}Tb_xSe$ alloy system, samples with compositions $x = 0;\ 0.001;\ 0.01;\ 0.025;$ and 0.05 were synthesized and subjected to γ −irradiation in the dose

range of $0 - 6.5\ Mrad$. For each dose, the thermal conductivity (k) was measured, and the obtained results are summarized in Table 1.

It follows from Table 1 that within the investigated dose interval ($0 - 6.5\ Mrad$), the thermal conductivity of $Sn_{1-x}Tb_xSe$ alloys under γ-irradiation exhibits a general decreasing trend for all compositions. The largest relative change is observed in the undoped sample ($x = 0$), where$\Delta k/k_0 \approx -6\%$. This indicates that in pure $SnSe, \gamma$ −irradiation enhances phonon scattering more strongly than in doped alloys. With increasing Tb concentration, the decrease in k becomes progressively weaker, reaching only -1.38% at $x = 0.05$. This effect can be attributed to the fact that Tb incorporation initially suppresses phonon scattering in the crystal lattice, partially compensating for the influence of additional radiation-induced defects.

Table 1. Thermal conductivity of $Sn_{1-x}Tb_xSe$ system alloys at different absorption doses

Absorbed dose D, Mrad	COMPOSITIONS				
	x=0	*x=0.001*	*x=0.01*	*x=0.025*	*x=0.05*
	k·10^{-5}, W/(m^{-1}K^{-1})	**k·10^{-5}, W/(m^{-1}K^{-1})**	**k·10^{-5}, W/(m^{-1}K^{-1})**	**k·10^{-5}, W/(m^{-1}K^{-1})**	**k·10^{-5}, W/(m^{-1}K^{-1})**
0	20	18	12.5	11.2	14.5
1	20	18	12.5	11.2	14.5
2	20	18	12.5	11.2	14.5
3	20	18	12.5	11.2	14.5
4	20	18	12.5	11.2	14.5
5	19.8	17.9	12.5	11.2	14.5
5,5	19.5	17.7	12.4	11.2	14.5
6	19.2	17.4	12.3	11.1	14.4
6.5	18.8	17.1	12.2	11.0	14.3

The dependences of thermal conductivity on the γ-irradiation dose for different compositions are shown in Figure 4. These plots demonstrate that the $k(D)$ behavior is consistent with a radiation defect accumulation model, in which increasing defect concentration enhances phonon scattering. At low doses, k remains nearly constant; however, once a threshold dose is reached, thermal conductivity begins to decrease monotonically.

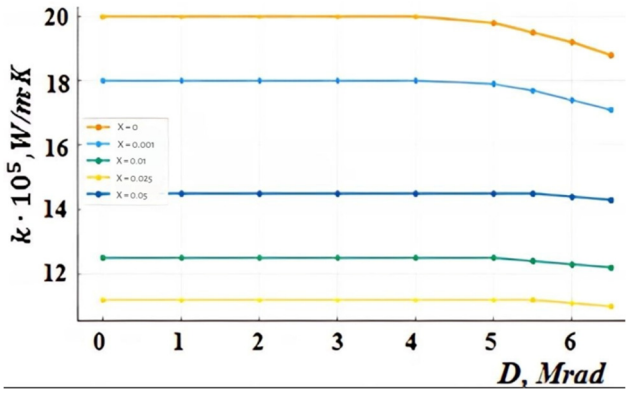

Figure 4. Dependence of thermal conductivity in $Sn_{1-x}Tb_xSe$ system alloys on absorption dose

Mathematically, this behavior can be described using two main approaches:

1. Exponential saturation model:$N(D) = N_\infty(1 - e^{-\sigma D})$ −where *N(D)* is the defect concentration increasing with dose *D* and approaching saturation. The corresponding expression for thermal conductivity is [28]:

$$k(D) = k_\infty + (k_0 - k_\infty)e^{-\alpha D}$$

where $k_0 = k(0), k_\infty -$ is the asymptotic value at large doses, and α is the accumulation-rate parameter. This model is often applied to describe the influence of vacancy (or cluster) buildup on phonon scattering.

2. Threshold-linear (empirical) model: For cases where the material remains nearly unchanged at low doses and shows an approximately linear decrease beyond a threshold [29]:

$$k(D) = \begin{cases} k_0 \ D \le D_{th} \\ a + bD \ D > D_{th} \end{cases}$$

where D_{th} is the threshold dose ($\approx 5\ Mrad$), a is the extrapolated initial value, and $b < 0$ is the slope characterizing the sensitivity of thermal conductivity to radiation dose.

This model is convenient for limited dose ranges exhibiting a clear defect activation threshold (e.g., defect clustering or local structural transitions). In studies of ionizing radiation effects, this empirical approach is frequently employed for analyzing low- and medium-dose regimes.

Experimental data for $Sn_{1-x}Tb_xSe$ alloys show that within $D = 0-5\ Mrad$, no significant change in k occurs. However, at $D = 5-6.5\ Mrad$, the decrease becomes pronounced. The analysis indicates that in this active region, $k(D)$ is well described by a linear dependence,$(k(D) = a + bD)$ (Figure 5). The obtained parameters and statistical measures are given in Table 2.

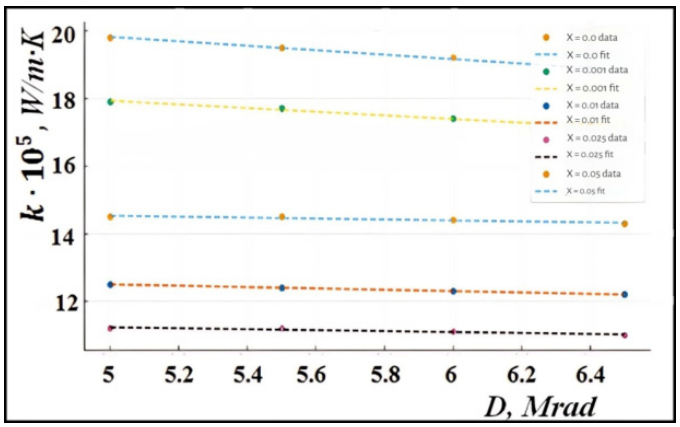

Figure 5. Active-range (5.0-6.5 Mrad) with linear fits

Table 2. Linear approximation parameters and statistical indicators

Composition	Slope b (k per Mrad)	Slope standard error	Intercept A (k units)	Intercepts	R^2	RMSE
x=0	−0.6600	0.0346	23.1200	0.2001	0.9945	0.0274
x=0.001	−0.5400	0.0346	20.6300	0.2001	0.9918	0.0274
x=0.01	−0.2000	0.0000	13.5000	0.0000	1.0000	0.0000
x=0.025	−0.1400	0.0346	11.9300	0.2001	0.8909	0.0274
x=0.05	−0.1400	0.0346	15.2300	0.2001	0.8909	0.0274

As seen from Table 2, the correlation coefficient $R^2 \approx 0.99$ for most compositions, indicating excellent agreement between the experimental data and the linear model. This confirms that the decrease in thermal conductivity follows an almost perfectly linear law. In particular, for $x = 0.01$, the coefficient $R^2 = 1.0000$, showing an ideal fit.

For all compositions, the slope b is negative $(b < 0)$, meaning that thermal conductivity decreases with increasing γ-irradiation dose. Moreover, as the Tb content increases, the absolute value of b decreases, indicating a reduction in the sensitivity of thermal conductivity to radiation. The low standard errors of the slopes $(\sim 0.03-0.04)$ and small RMSE values $(0.027-0.03)$ confirm the statistical reliability and accuracy of the linear fit.

Thus, for all $Sn_{1-x}Tb_xSe$ alloys, the thermal conductivity decreases with increasing γ −irradiation dose, with the strongest effect observed in pure $SnSe$. As Tb concentration increases, the alloys' radiation resistance increases, and the rate of decrease in k weakens. Experimental results indicate that within $D = 0-5\ Mrad$, $k$remains nearly constant, whereas for $D > 5\ Mrad$, it follows a clear linear dependence described by $k(D) = a + bD$. The reduction in the absolute value of negative slopes with higher Tb content reflects the suppression of phonon scattering by Tb ions and partial compensation for radiation-induced defects [30].

CONCLUSIONS

The structural and thermal analyses performed on $Sn_{1-x}Tb_xSe$ alloys demonstrate that terbium incorporation leads to the formation of stable substitutional solid solutions with orthorhombic symmetry preserved across the studied composition range. Increasing Tb content results in moderate lattice expansion, microhardness growth, and enhanced defect-induced phonon scattering, which collectively cause a significant reduction in thermal conductivity, especially at low dopant concentrations.

The study of γ-irradiation effects in the dose range $0-6.5\ Mrad$ revealed that thermal conductivity decreases for all compositions, with the strongest degradation ($\approx 6\%$) observed in undoped $SnSe$. For alloys with higher Tb content, the reduction becomes progressively weaker, indicating improved radiation resistance. For irradiation doses above $5\ Mrad$, thermal conductivity follows a nearly perfect linear decay, accurately described by empirical $k(D) = a + bD$ relations with high correlation coefficients.

Overall, the obtained results confirm that Tb doping effectively suppresses phonon transport while simultaneously enhancing the radiation stability of $SnSe$ −based materials, making $Sn_{1-x}Tb_xSe$ alloys promising candidates for thermoelectric and radiation-resistant semiconductor applications.

ORCID

O.M. Gasanov, https://orcid.org/0000-0003-4888-7686; **J.I. Huseynov,** https://orcid.org/0000-0002-4498-2400;
I.I. Abbasov, https://orcid.org/0000-0001-8111-2642

REFERENCES

[1] H. Koc, S. Simsek, S. Palaz, O. Oltulu, A.M. Mamedov, and E. Ozbay, "Mechanical, electronic, and optical properties of the A4B6 layered ferroelectrics: ab initio calculation," Phys. Status Solidi C, **12**(6), 651–658 (2015). https://doi.org/10.1002/pssc.201400245

[2] L.T. Nguyen, and G. Makov, "Lone-Pair Origins of Polymorphism: Sn Monochalcogenides as a Case Study," Chemistry of Materials, **36**(11), 5487–5499 (2024).https://doi.org/10.1021/acs.chemmater.4c00409

[3] Y. Xu, H. Zhang, H. Shao, *et al*., "Electronic, transport and optical properties of monolayer α and βGeSe: A first-principles study," Phys. Rev. B, **96**, 245421 (2017). https://doi.org/10.1103/PhysRevB.96.24542

[4] L.D. Zhao, S.H. Lo, Y. Zhang, *et al.* "Ultralow thermal conductivity and high thermoelectric figure of merit in SnSe crystals," Nature, **508**, 373–377 (2014). https://doi.org/10.1038/nature13184

[5] Y. Yu, T. Xiong, Z. Guo, *et al*. "Wide-spectrumpolarization-sensitiveandfast-responsephotodetectorbasedon 2D group IV-VI semiconductor tin selenide," Fundamental Research, **2**(6), 985-992, (2022). https://doi.org/10.1016/j.fmre.2022.02.008

[6] Z. Liang, R. Hao, H. Luo, Z. He, L. Su, and X. Fan, "Enhancing the photo-response performance of SnSe-based photoelectrochemical photodetector via Ga doping," Journal of Materials Chemistry C, **12**(8), (2024). https://doi.org/10.1039/D3TC03937D

[7] K. Mukai, R. Wanibuchi, and Y. Nunomura, "Improved performance of solar cells using chemically synthesized SnSe nanosheets as light absorption layers," J. Mater. Sci: Mater. Electron. **35**, 680 (2024).https://doi.org/10.1007/s10854-024-12366-1

[8] B. Qin, D. Wang, T. Hong, *et al*. "High thermoelectric efficiency realized in SnSe crystals via structural modulation," Nat. Commun. **13**(14), 1366 (2023). https://doi.org/10.1038/s41467-023-37114-7

[9] G. Shi, and E. Kioupakis, "Quasiparticle band structures and thermoelectric transport properties of p-type SnSe," J. Appl. Phys. **117**, 065103 (2015). https://doi.org/10.1063/1.4907805

[10] Sh.S. Ismailov, M.A. Musaev, I.I. Abbasov, *et al*. "Effect of doping level and compensation on thermal conductivity in $Ce_xSn_{1-x}Se$ solid solutions," Low Temp. Phys. **46**, 1114–1120 (2020). https://doi.org/10.1063/10.0002155

[11] J.I. Huseynov, and T.A. Jafarov, "The Influence of γ-Irradiation on Thermo emf and Heat Conduction of $Ln_{0.01}Sn_{0.99}Se$ (LnPr, Tb, Er) Monocrystals, World Journal of Condensed Matter Physics, **4**(1) 5 (2014). https://doi.org/10.4236/wjcmp.2014.41001

[12] J.I. Huseynov, M.I. Murguzov, and S.S. Ismayilov, "Specific features of self-compensation in $Er_xSn_{1-x}Se$ solid solutions," Semiconductors, **47**, 323–326 (2013). https://doi.org/10.1134/S106378261303010X

[13] I.I. Aliev, J.I. Huseynov, M.I. Murguzov, *et al*. "Phase relations and properties of alloys in the SnSe-DySe system," Inorg. Mater. **50**, 237–240 (2014).https://doi.org/10.1134/S0020168514030029

[14] I.I. Abbasov, Sh.S. Ismailov, and V.A. Abdurahmanova, "Concentration dependences of electrical conductivity and the Hall effect of the $Ce_xSn_{1-x}Se$ single crystals," Low Temperature Physics, **45**, 1277–1280 (2019). https://doi.org/10.1063/10.0000209

[15] I. Huseynov, M.I. Murquzov, R.F. Mamedova, and Sh.S. Ismailov, "Thermal Conductivity and Thermal EMF of Materials for Thermal Energy Converters," in: *TPE-06 3rd Intern. Conf. on Technical and Physical Problems in Power Engineering*, (Ankara, 2008).

[16] J.I. Huseynov, M.I. Murguzov, Sh.S. Ismailov, R.F. Mamedova, and E.M. Gojayev, "On the thermopower and thermomagnetic properties of $Er_xSn_{1-x}Se$ solid solutions," Semiconductors, **51**(2), 153-157 (2017). https://doi.org/10.1134/S1063782617020075

[17] J.I. Huseynov, M.I. Murguzov, and S.S. Ismayilov, "Specific features of self-compensation in $Er_xSn_{1-x}Se$ solid solutions," Semiconductors,**47**, 323–326 (2013). https://doi.org/10.1134/S106378261303010X

[18] O.M. Hasanov, C.I. Huseynov, H.A. Aslanov, *et al*. "Galvanomagnetic Properties of $Gd_xSn_{1-x}Se$ Solid Solutions," Journal of Baku Engineering University – Physics, **8**(2), 81-90 (2024).https://doi.org/10.30546/09081.2024.102.7068

[19] W.-Y. Lyu, W.D. Liu, M. Li, *et al*. "The effect of rare earth element doping on thermoelectric properties of GeTe," Chemical Engineering Journal, **446(**Part 1), 137278, (2022). https://doi.org/10.1016/j.cej.2022.137278

[20] *Thermal Conductivity: Theory, Properties, and Applications*, edited by Terry M. Tritt, (Springer US, New York, 2004). https://doi.org/10.1007/b136496

[21] Q. Zheng, A.B. Mei, M. Tuteja, *et al*. "Phonon and electron contributions to the thermal conductivity of VN_x epitaxial layers Phys. Rev. Materials,**1**, 065002 (2017). https://doi.org/10.1103/PhysRevMaterials.1.065002

[22] V.N. Glazkov, L. Ginzburg, and A. Orlov, "Wiedemann-Franz law demonstration in a student practicum," Am. J. Phys. **85**, 473-477 (2017).https://doi.org/10.1119/1.4982787

[23] D.I. Huseynov, M.I. Murguzov, and S.S. Ismailov, "Thermal conductivity of $Er_xSn_{1-x}Se$ ($x \leq 0.025$) solid solutions," Inorg. Mater. **44**, 467–469 (2008).https://doi.org/10.1134/S0020168508050063

[24] R. Gurunathan, R. Hanus, M. Dylla, *et al*. "Analytical Models of Phonon–Point-Defect Scattering," Phys. Rev. Applied, **13**, 034011 (2020). https://doi.org/10.1103/PhysRevAppleid.13.034011

[25] J. Callaway, "Model for Lattice Thermal Conductivity at Low Temperatures," Phys. Rev. **113**, 1046, (1959). https://doi.org/10.1103/PhysRev.113.1046

[26] T. Feng, B. Qiu, X. Ruan, "Coupling between phonon-phonon and phonon-impurity scattering: A critical revisit of the spectral Matthiessen's rule," Phys. Rev. B, **92**, 235206 (2015). https://doi.org/10.1103/PhysRevB.92.235206

[27] B. Abeles, "Lattice Thermal Conductivity of Disordered Semiconductor Alloys at High Temperatures," Phys. Rev. **131**, 1906 (1963). https://doi.org/10.1103/PhysRev.131.1906

[28] Y. Zhao, D. Liu, J. Chen, *et al*. "Engineering the thermal conductivity along an individual silicon nanowire by selective helium ion irradiation," Nat. Commun.**8**, 15919 (2017). https://doi.org/10.1038/ncomms15919

[29] W. Zhao, Y-H. Li, H-Z. Ma, *et al*. "Dependence of irradiation defects evolution on dose rate and PKA energy spectrum in tungsten," Nuclear Materials and Energy, **43**, 101956 (2025). https://doi.org/10.1016/j.nme.2025.101956

[30] J.I. Huseynov, and T.A. Jafarov, "Effect of γ-ray radiation on electrical properties of heat-treated $Er_xSn_{1-x}Se$ single crystals," Semiconductors, **46**, 430–432 (2012). https://doi.org/10.1134/S1063782612040082

СКЛАД ТА РАДІАЦІЙНО-ІНДУКОВАНІ ЗМІНИ ТЕПЛОПРОВІДНОСТІ У ТВЕРДИХ РОЗЧИНАХ $Sn_{1-x}Tb_xSe$

Т.А. Джафаров[1], Г.А. Асланов[1], А.М. Аллахвердієв[1], О.М. Гасанов[1], Дж.І. Гусейнов[1], Х.А. Адгезалова[1], Г.А. Гарашова[1], І.І. Аббасов[2]

[1]Азербайджанський державний педагогічний університет, Az-1000, Баку, вул. Уз Гаджибейлі, 68, Азербайджан

[2]Азербайджанський державний університет нафти та промисловості, Az-1010, Баку, проспект Азадлик, 20, Азербайджан

У цій роботі досліджували структурні, фізико-хімічні та термотранспортні властивості сплавів $Sn_{1-x}Tb_xSe$ ($0 \le x \le 0,05$) залежно від концентрації тербію та дози γ-опромінення. Рентгенівська дифракція та ДТА-аналіз підтвердили утворення орторомбічних твердих розчинів заміщення згідно із законом Вегарда, з незначним збільшенням параметрів кристалічної решітки та мікротвердості зі збільшенням вмісту Tb. Введення атомів Tb у матрицю SnSe посилює розсіювання фононів-дефектів через флуктуації маси та спотворення кристалічної решітки, що призводить до помітного зниження теплопровідності, особливо при низьких рівнях легування ($x \le 0,02$). Вимірювання теплопровідності, проведені після γ-опромінення (0–6,5 Мрад, джерело ^{60}Co), виявили загальну тенденцію до зниження для всіх складів. У нелегованому SnSe відносне зниження досягло ~6%, тоді як у зразках, легованих Tb, чутливість до опромінення значно знизилася. Для доз вище 5 Мрад залежність k(D) добре описується лінійною моделлю з високими коефіцієнтами кореляції. Ці результати демонструють, що включення Tb не тільки пригнічує транспорт фононів, посилюючи термоелектричний потенціал, але й підвищує радіаційну стійкість матеріалів на основі SnSe.

Ключові слова: *теплопровідність; розсіювання фононів; радіаційна стійкість; γ-опромінення; тверді розчини; орторомбічна структура; утворення дефектів; термоелектричні матеріали; спотворення кристалічної решітки; розсіювання флуктуацій маси*

EAST EUROPEAN JOURNAL OF PHYSICS. **1.** 216-220 (2026)
DOI:10.26565/2312-4334-2026-1-22 ISSN 2312-4334

ACOUSTIC PROPERTIES OF TRIGLYCINE SULPHATE CRYSTALS WITH *α*-ALANINE IMPURITY

E.U. Arzikulov[1,2,3]*, F.A. Salaxitdinov[1], Wang Yujin[2], Shaowei Lu[3], Teng Liu[3], Zhisheng Nong[3], M.D. Toshboyev[1], G.G. Gulyamov[1], N. Mamatkulov[4]

[1]*Samarkand State University named after Sharof Rashidov, 140104, 15, University Blvd., Samarkand, Republic of Uzbekistan*
[2]*State Key Laboratory of Precision Welding & Joining of Materials and Structures, School of Material Science and Engineering, Harbin Institute of Technology, Yikuang Street, Nangang District, Harbin 150001, China*
[3]*School of Material Science and Engineering, Shenyang Aerospace University, 37, Daoyi South Avenue, Shenyang, China*
[4]*Samarkand State University Veterinary Medicine, Livestock and Biotechnologies, 140003, 77, Mirzo Ulugbek Str., Samarkand, Republic of Uzbekistan*
**Corresponding Author e-mail: eshkuvata@gmail.com*
Received December 12, 2025; accepted January 20, 2026

The frequency- and concentration-dependent absorption coefficients of longitudinal and transverse ultrasonic waves in pure and α-alanine-doped triglycine sulfate (α-TGS) crystals (α-alanine content in crystals is: 5, 10, 15, 20, 25, 30, and 35 mol%) grown from solution at room temperature were studied. It is established that absorption coefficients of ultrasonic waves in *α*-TGS crystals with L and S polarization with the increase in concentration of *α*-alanine about 1.57 and 1.88 times decrease, and propagation velocity increases by 3.24 and 13.38%, respectively. Decrease of absorption coefficients of transverse ultrasonic waves caused by elastic scattering of phonons on impurity, i.e., decrease of *τ*, at the corresponding dispersive properties of a phonon subsystem.
Keywords: *Triglycine sulfate; Ultrasonic waves; Velocity of elastic wave; Absorption coefficient; Ferroelectric; Phase transition; Phonon; α-alanine*
PACS: 43.35. Ae, 43.35. Bf, 43.35. Cg, 77.84. -s

INTRODUCTION

Triglycine sulfate (TGS) crystals are model and well-studied ferroelectric crystals [1, 2]. The first works devoted to growing and studying the physical properties of these crystals date back to the middle of the last century [3] and continue to the present day [4-9]. Interest in these crystals is mainly associated with the possibility of creating radiation detectors based on them over a wide spectral range, including the infrared, as substrates for vidicon materials, good prospects for use in various microelectronics devices, and pyroelectric sensors [10, 11], etc.

The dielectric, structural, acoustic and other properties of pure [12] and doped with various impurities [13-17] TGS crystals have been studied quite well. It is known that impurity atoms in crystals affect their acoustic properties, in particular the absorption coefficient and the speed of propagation of ultrasonic waves [18, 19]. Interest in these studies is driven by both the study of the influence of impurities on the ultrasonic properties of TGS crystals and the great potential for their practical use. On the other hand, TGS crystals are a convenient model system for studying the role of structural imperfections in the physical properties of ferroelectrics [14, 15, 17]. The introduction of impurities makes it possible to regulate a number of properties of crystals, and in particular, and most importantly, it allows one to stabilize spontaneous polarization due to the formation of internal fields [17, 20]. In this regard, it is of significant interest to study the acoustic properties of TGS crystals doped with *α*-alanine (*α*–TGS), namely, the effect of impurities on the propagation and attenuation speeds of ultrasonic waves in them.

This work presents the results of studies of the frequency and concentration dependences of the absorption coefficient of longitudinal and transverse ultrasonic waves in nominally pure and *α*-alanine-doped *α*–TGS crystals (α-alanine content in the crystals: 5, 10, 15, 20, 25, 30, and 35 mol% %) grown from solution at room temperature, i.e. in the ferroelectric phase. Indeed, the *α*-TGS crystal is one of the currently very well-known model ferroelectrics with a second-order phase transition, in which, due to the strong anisotropy of the relaxation mechanism of absorption and dispersion of ultrasonic waves [21], both relaxation and actual critical (fluctuation) phenomena occur. However, in most studies [22], ultrasonic anomalies in the region of structural phase transition are considered, while the effect of *α*-alanine on ultrasonic properties in *α*-TGS crystals in the ferroelectric phase has not been studied.

MATERIAL AND METHODS

To carry out ultrasonic studies, an acousto-optical installation was used [23], operating in a pulsed mode and consisting of a system for excitation of ultrasonic waves and a system for recording continuous He-Ne laser radiation with a wavelength $\lambda_0 = 632.8\ nm$ diffracted by ultrasonic waves. High-frequency longitudinal and transverse ultrasonic waves with frequencies in the range of 0.2-1.2 GHz were excited using quartz piezo transducers *x* or *y* slice, 70-100 μm

Cite as: E.U. Arzikulov, F.A. Salaxitdinov, W. Yujin, S. Lu, T. Liu, Z. Nong, M.D. Toshboyev, G.G. Gulyamov, N. Mamatkulov, East Eur. J. Phys. 1, 216 (2026), https://doi.org/10.26565/2312-4334-2026-1-22

thick. The studied samples were parallelepipeds with an average size of 8×9×10 mm, oriented along the main crystallographic axis [001]. The attenuation coefficient of ultrasonic waves was determined by the Bragg diffraction of light on ultrasonic waves [23] based on the dependence of the intensity of diffracted light I and on the distance to the transducer x_1 and x_2 using the following formula:

$$\alpha, cm^{-1} = \frac{1}{x_1 - x_2} 10lg \frac{I(x_1)}{I(x_2)}. \quad (1)$$

The accuracy in determining the attenuation coefficient was ~5%. At the same time, the speed of propagation of ultrasonic waves was determined from measurements of the angle of Bragg diffraction of light by the following formula:

$$\upsilon = \frac{\lambda_0 \nu}{2sin\theta}, \quad (2)$$

where $\lambda_0 -$ is the wavelength of laser radiation, $\nu -$ is the frequency of ultrasonic waves, and is the angle $\theta -$ is the Bragg diffraction angle.

RESULTS AND DISCUSSIONS

The experimentally obtained results of the attenuation coefficient and speed of ultrasonic waves propagating along the [001] crystallographic direction at a frequency of 500 MHz in doped and nominally pure α-TGS crystals at room temperature are given in Table 1.

Table 1. Concentration dependence of the attenuation coefficient and propagation velocity of ultrasonic waves to TGS crystals at temperature T = 300 K.

α-alanine content in TGS, %	$q \parallel z$		$\upsilon \times 10^5\ cm/s$	
	α_l	α_s	υ_l	υ_s
TGS pure	22.2	35	3.858	1.985
α–TGS, 5 %	20.7	32.1	3.876	2.032
α–TGS, 10 %	19.1	29	3.898	2.078
α–TGS, 15 %	18.1	26.1	3.925	2.110
α–TGS, 20 %	17.2	23.1	3.951	2.140
α–TGS, 25 %	16.2	21.5	3.962	2.171
α–TGS, 30 %	15.4	20.1	3.973	2.203
α–TGS, 35 %	14.3	18.5	3.983	2.250

As can be seen from Table 1, the attenuation coefficients of ultrasonic waves with L and S polarization decrease by approximately 1.57 and 1.88 times, respectively, with increasing α-alanine concentration, and the propagation speed increases by 3.24 and 13.38 %, respectively. The concentration dependence curves of the absorption coefficient and the propagation speed of ultrasonic waves are described by curves of the following form:

$$\alpha_l = -60.61346 + \frac{82.8359}{(1 + (c/533.7909) \cdot 0.830231)};$$

$$\alpha_s = 9.232921 + \frac{25.733609}{(1 + (c/23.32901) \cdot 1.382119)};$$

$$\upsilon_l = 4.019122 - \frac{0.160101}{(1 + (c/17.87642) \cdot 1.819346)};$$

$$\upsilon_s = 4.022538 - \frac{2.037637}{(1 + (c/265.7397) \cdot 0.9357489)},$$

where c the α-alanine content is in %.

The study showed that in pure TGS crystals the attenuation of ultrasonic waves is proportional to the square of the frequency, and in α-TGS the attenuation of longitudinal ultrasonic waves decreases by approximately 20 %, and the nature of the frequency dependence remains quadratic. The attenuation coefficient of transverse ultrasonic waves is very sensitive to the admixture of α-alanine and in some samples the attenuation coefficient is almost halved compared to pure TGS crystals. As for the frequency dependence of the attenuation of these waves, it is observed that it is proportional to the square of their frequency. It was also shown that the attenuation of ultrasonic waves in TGS and α-TGS crystals is practically independent of temperature, with the exception of the region of the ferroelectric phase transition [30] observed in them at a temperature of T = 54°C. In Figure 1 shows the concentration dependence of the attenuation of ultrasonic waves in α-TGS crystals.

As can be seen from Fig. 1, with an increase nonlinear in the concentration of α-alanine in TGS crystals, the attenuation coefficient of ultrasonic waves of both polarizations decreases (Fig. 2).

It should be assumed that the decrease in the attenuation coefficient of ultrasonic waves in nominally pure and doped α-TGS ferroelectric crystals is associated with a decrease in the phonon relaxation time [20].

A theoretical consideration of the attenuation of longitudinal and transverse elastic waves in crystals with impurities was carried out in [24], where, under the condition $\Omega\tau \ll 1$, for crystals with impurities, the relaxation time is taken as:

$$\tau = \left(\tau_i^{-1}(k_T) + \tau_l^{-1}(k_T)\right)^{-1}, \tag{3}$$

where, k_T – is the wave vector of thermal phonons: τ_i – is the relaxation time associated with inelastic phonon scattering; τ_l – is the relaxation time associated with elastic scattering by impurities.

Taking into account the relationship between the indicated relaxation times, an expression for determining the attenuation coefficient of transverse elastic waves is obtained in the following form:

$$\alpha = \beta(\Omega^2 T)\rho v^2 \sum_{\vec{k}j} C(\vec{k},j)\tau(\vec{k},j)\gamma^2(\vec{k},j), \tag{4}$$

where, β – is a numerical factor of the order of unity, the value of which depends on the type of local equilibrium distribution of thermal phonons; Ω and v – frequency and speed of ultrasonic waves; $C(\vec{k},j)$ – heat capacity of the $(\vec{k},j)$ phonon branch; γ – effective anharmonicity constant, depending on the degree of order of the crystal.

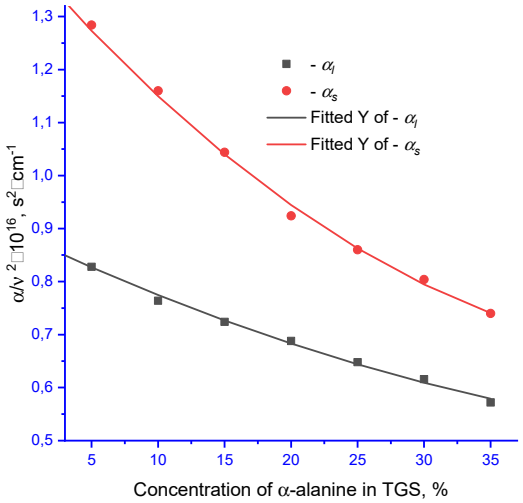

Figure 1. Concentration dependence of α/v^2 values in α–TGS for longitudinal and shear vibrations

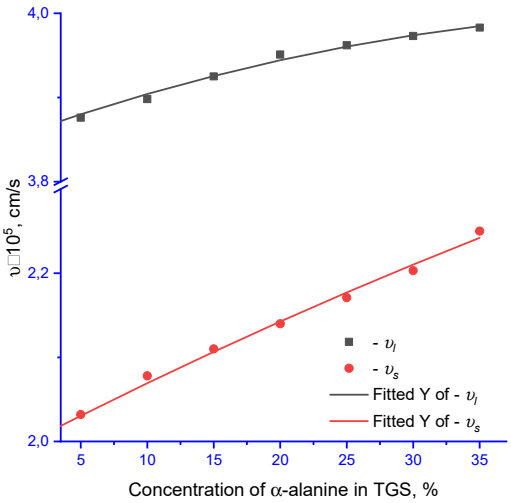

Figure 2. Concentration dependence of the propagation speed of longitudinal and shear ultrasonic waves in α-TGS

A theoretical consideration of the attenuation of longitudinal and transverse elastic waves in crystals with impurities was carried out in [24], where, under the condition $\Omega\tau \ll 1$, for crystals with impurities, the relaxation time is taken as:

$$\tau = \left(\tau_i^{-1}(k_T) + \tau_l^{-1}(k_T)\right)^{-1}, \tag{3}$$

where, k_T – is the wave vector of thermal phonons: τ_i – is the relaxation time associated with inelastic phonon scattering; τ_l – is the relaxation time associated with elastic scattering by impurities.

Taking into account the relationship between the indicated relaxation times, an expression for determining the attenuation coefficient of transverse elastic waves is obtained in the following form:

$$\alpha = \beta(\Omega^2 T)\rho v^2 \sum_{\vec{k}j} C(\vec{k},j)\tau(\vec{k},j)\gamma^2(\vec{k},j), \tag{4}$$

where, β – is a numerical factor of the order of unity, the value of which depends on the type of local equilibrium distribution of thermal phonons; Ω and v – frequency and speed of ultrasonic waves; $C(\vec{k},j)$ – heat capacity of the $(\vec{k},j)$ phonon branch; γ – effective anharmonicity constant, depending on the degree of order of the crystal.

CONCLUSIONS

It has been established that with an increase in the concentration of α-alanine in TGS crystals, the attenuation coefficient of ultrasonic waves of both polarizations decreases nonlinearly, while the speed of propagation increases nonlinearly.

The concentration dependences of the attenuation coefficient and propagation velocity of ultrasonic waves of both polarizations in TGS crystals with an admixture of α-alanine can be approximated by the following expressions:

$$\alpha_l = -60.61346 + \frac{82.8359}{(1 + (c/533.7909) \cdot 0.830231)};$$

$$\alpha_s = 9.232921 + \frac{25{,}733609}{(1 + (c/23.32901) \cdot 1.382119)};$$

$$v_l = 4.019122 - \frac{0.160101}{(1 + (c/17.87642) \cdot 1.819346)};$$

$$v_s = 4.022538 - \frac{2.037637}{(1 + (c/265.7397) \cdot 0.9357489)},$$

where c the α-alanine content is in %.

It has been established that the attenuation coefficients of ultrasonic waves with L and S polarization decrease by approximately 1.57 and 1.88 times, respectively, with increasing α-alanine concentration, and the propagation speed increases by 3.24 and 13.38 %, respectively.

According to (4), it follows that a decrease in the attenuation coefficient of transverse ultrasonic waves can be due to elastic scattering of phonons on impurities, i.e., a decrease in, with the corresponding dispersion properties of the phonon subsystem. Thus, according to equation (4), a decrease in α_l, and α_s may be due to a decrease in the effective anharmonicity constant γ of crystal lattice vibrations under the influence of defects.

ORCID

Eshkuvat U. Arzikulov, https://orcid.org/0000-0001-9179-3402; **Wang Yujin,** https://orcid.org/0000-0002-8710-1108

REFERENCES

[1] M.E. Lines, and A.M. Glass, *Principles and Applications of Ferroelectrics and Related Materials*, (OUP Oxford, Science, 2001).
[2] B.A. Strukov, and A.P. Levanyuk, *Ferroelectric Phenomena in Crystals*, (Springer, Geydelberg, 1998).
[3] H. Toyada, Sh. Waku, and H. Hirabayshi, "Structure of Ferroelectric Domains in Triglycine Sulphate," Journal of the Physical Society of Japan, **14**(8), 1003-1011 (1959). https://doi.org/10.1143/jpsj.14.1003
[4] M.B. Dung, and H.T. Nguyen, "Influence of Gamma Irradiation on Properties of Ferroelectric Composite from Cellulose Nanoparticles and Triglycine Sulfate," Materials Transactions, **60**(9), 1902-1907 (2019). https://doi.org/10.2320/matertrans.mt-m2019139
[5] S. Goel, N. Sinha, A. Hussain, A.J. Joseph, H. Yadav, and B. Kumar, "Sunset yellow dyed triglycine sulfate single crystals: enhanced thermal, mechanical, optical and di-/piezo-/ferro-/pyro-electric properties," Journal of Materials Science: Materials in Electronics, **29**(16), 13449–13463 (2018). https://doi.org/10.1007/s10854-018-9470-9
[6] B. Mytsyk, N. Demyanyshyn, A. Erba, V. Shut, S. Mozzharov, Y. Kost, O. Mys, and R. Vlokh, "Piezo-optic and elasto-optic properties of monoclinic triglycine sulfate crystals," Journal of Applied Optics, **56**(34), (2017). https://doi.org/10.1364/ao.56.009484
[7] O. Krupych, M. Kostyrko, D. Adamenko, I. Skab, and R. Vlokh, "Tracing of optic axis with an acouto-optically diffracted beam: generation of vector-vortex beam in triglycine sulphate crystals," J. Phys. Opt. **21**, (2020). https://doi.org/.3116/16091833/21/1/1/2020
[8] M.J. Ibrahim, and T.M. Ai-Saadi, "Investigating the Effect of Doping and Sulfuric Acid (H2SO4) on the Growth and Properties of a Triglycine Sulphate (TGS) Crystal," IOP Conf. Ser.: Mater. Sci. Eng. **871**, 012082 (2020). https://doi.org/10.1088/1757-899x/871/1/012082
[9] R. Raja, V. Santhanam, D. Vedhavalli, and P.K. Nathan, "Investigation on mechanical, dielectric and thermal properties of aluminum doped TGS single crystal," International Journal of Material Science, **12**(2), 185-196 (2017). https://www.ripublication.com/ijoms17spl/ijomsv12n2spl_22.pdf
[10] E. Theocharous, "Absolute linearity measurements on a gold-black-coated deuterated L-alanine-doped triglycine sulphate pyroelectric detector," Applied Optics, **47**(21), 3731-3736 (2008). https://doi.org/10.1364/ao.47.003731
[11] V.Yu. Kurlyak, V.Yo. Stadyuk, B.V. Andriyevsky, M.O. Romanyuk, Z.O. Kohut, and V.M. Gaba, "Optical properties of D-serine doped TGS crystals for pyroelectric sensors," Material Science-Poland, **33**(4), 692-698 (2015). https://doi.org/10.1515/msp-2015-0105
[12] R.B. Lal, and A.K. Batra, "Growth and properties of triglycine sulfate (TGS) crystals: Review," Ferroelectrics, **142**(1), 51-82 (1993). http://dx.doi.org/10.1080/00150199308237884
[13] H.V. Alexandrru, "Pure and Doped Triglycine Sulfate Crystals Growth and Characterization," Interdisciplinary Transport Phenomena: Ann: N. Y. Acad. Sci. **1161**, 387-396 (2009). https://doi.org/10.1111/j.1749-6632.2008.04080.x
[14] N.V. Belugina, R.V. Gainutdinov, A.L. Tolstkhina, V.V. Dolbinina, N.I. Sorokina, and O.A. Alekseeva, "Nanorelief of the Natural Cleavage Surface of Triglycine Sulphate Crystals with Substitutional and Interstitial Impurities," Crystallography Reports, **56**(6), 1070-1076 (2011). https://doi.org/10.1134/s1063774511030047
[15] V.N. Shut, I.F. Kashevich, and S.R. Syrtsov, "Ferroelectric properties of triglycine sulfate crystals with non-uniform distribution of chromium impurity," Physics of the Solid State, **50**(16), 115-118 (2008). (in Russian)
[16] V. Windsh, I. Rakhimov, V.M. Sarnatsky, E.V. Charnaya, and V.A. Shutylov, "Ultrasonic studies of the structural phase transition in impurity TGS crystals," Physics of the Solid State, **27**(6), 1671-1674 (1985). (in Russian)
[17] A.L. Tolstikhina, N.V. Belugina, R.V. Gainutdinov, E.S. Ivanova, A.K. Lashkova, V.N. Shut, I.F. Kashevich, *et al*., "Domain structure and properties of triglycine sulfate crystals layer-by-layer doped with D, L-α- and L-α-alanine impurity," Crystallography, **61**(6). 975-981 (2016). https://doi.org/10.1134/s106377451606016x

[18] T.Ch. Upadhyay, and A. Nautiyal, "Effect of Electric Field on Dielectric and Acoustic Properties of triglycine Sulphate Crystal," AIP Conference Proceedings, **1372**, 1 (2011). https://doi.org/10.1063/1.3644410
[19] E.V. Charnaya, and I. Rakhimov, "Acoustic studies of imperfect TGS crystals," Ferroelectrics, **112**(1), 45-54 (1990). https://doi.org/10.1080/0015019900-8012784
[20] E.V. Charnaya, A.A. Kuleshov, A.K. Radzhabov, I.K. Rakhimov, and L.A. Shuvalov, "Frequency-independent order parameter relaxation time in TGS crystals," Ferroelectrics, **143**(1), 143-148 (1993). https://doi.org/10.1080/001501-99308008323
[21] S.N.Drozhdin, O.M. Golitsyna, A.I. Nikishina, F.A. Tuma, and D.P. Tarasov, "Relaxation of the Domain Structure in Triglycine Sulphate and Deuterated Triglycine Sulfate Crystals in the Couse of Polarization Switching," Physics of the Solid State, **48**(3), 532-536 (2006). (in Russian)
[22] A. Levanyuk, "On the phenomenological theory of sound absorption near the points of second-order phase transitions," JETP, **49**, 1304 (1985). (in Russian)
[23] F.A. Salakhitdinov, E.V. Charnaya, and V.A. Shutilov, "Absorption of high-frequency ultrasound during phase transition in triglycine sulfatem" in: *IV All-Russian Symp. on Physics of Acoustohydrodynamic Phenomena and Optoacoustics*, (Ashgabat, 1985), pp. 69.
[24] Yu.A. Logachev "Difference in absorption of longitudinal and transverse sound in impurity crystals," Physics of the Solid State **15**(11), 3454-3455 (1973). (in Russian)

АКУСТИЧНІ ВЛАСТИВОСТІ КРИСТАЛІВ ТРИГЛІЦИН СУЛЬФАТУ З ДОМІШКОЮ α АЛАНІНУ

Є.У. Арзікулов[1,2,3], Ф.А. Салахітдінов[1], Ван Юйджін[2], Шаовей Лу[3], Тен Лю[3], Чжишен Нонг[3], М.Д. Тошбоєв[1], Г.Г. Гулямов[1], Н. Маматкулов[4]

[1]Самаркандський державний університет імені Шарофа Рашидова, 140104, бульвар Університету, 15, Самарканд, Республіка Узбекистан
[2]Державна ключова лабораторія прецизійного зварювання та з'єднання матеріалів і конструкцій, Школа матеріалознавства та інженерії, Харбінський технологічний інститут, вулиця Ікуан, район Нанган, Харбін 150001, Китай
[3]Школа матеріалознавства та інженерії, Шеньянський аерокосмічний університет, проспект Даої Саут, 37, Шеньян, Китай
[4]Самаркандський державний університет ветеринарної медицини, тваринництва та біотехнологій, 140003, вул. Мірзо Улугбека, 77, Самарканд, Республіка Узбекистан

Досліджено частотну та концентраційну залежність коефіцієнта поглинання поздовжніх та поперечних ультразвукових хвиль у чистих та легованих α-аланін-тригліцинсульфаті (α-TGS) кристалах (вміст α-аланіну в кристалах: 5, 10, 15, 20, 25, 30 та 35 мол.%), вирощених з розчину за кімнатної температури. Встановлено, що коефіцієнти поглинання ультразвукових хвиль у кристалах α-TGS з L та S поляризацією зі збільшенням концентрації α-аланіну приблизно в 1,57 та 1,88 раза зменшуються, а швидкість поширення збільшується на 3,24 та 13,38% відповідно. Зменшення коефіцієнтів поглинання поперечних ультразвукових хвиль, спричинене пружним розсіюванням фононів на домішці, тобто зменшення τ, при відповідних дисперсійних властивостях фононної підсистеми.

Ключові слова: *тригліцинсульфат; ультразвукові хвилі; швидкість пружної хвилі; коефіцієнт поглинання; сегнетоелектрик; фазовий перехід; фонон, α-аланін*

East European Journal of Physics. 1. 221–227 (2026)
DOI: 10.26565/2312-4334-2026-1-23 ISSN 2312-4334

FIRST-PRINCIPLES INVESTIGATION OF THE ELECTRONIC PROPERTIES OF MONOLAYER MoS_2 USING DFT-BASED QuantumATK SIMULATIONS

Makhkam Khalilloev[1*], **Bahor Jabbarova**[1], **Asrorbek Hasanov**[1], **Ghayrat Ibodullaev**[2], **Atabek Atamuratov**[1]

[1]*Department of Physics, Urgench State University, 14,Kh.Alimdjan Str., Urgench, 220100, Uzbekistan*
[2]*Department of Physics and Mathematics, Urgench State Pedagogical Institute 1-A, Gurlan str, Urgench city, 220100, Uzbekistan*
[*]*Corresponding Author e-mail: x-mahkam@urdu.uz*

Received August 28, 2025; revised February 12, 2026, accepted February 14, 2026

In this work, the electronic properties of monolayer molybdenum disulfide (MoS_2) were investigated using density functional theory (DFT) within the QuantumATK simulation environment. The band structure and density of states (DOS) calculations reveal that MoS_2 possesses a direct band gap of 1.74 eV and an indirect band gap of 1.27 eV. Further analysis including partial DOS and charge density distribution was performed to examine the orbital contributions and bonding characteristics. The influence of biaxial strain (±3%) on the electronic structure was also studied, showing a tunable band gap behavior. These results provide valuable insight into the electronic characteristics of MoS_2 and support its potential applications in nanoelectronic and flexible device technologies.

Keywords: *Density Functional Theory; QuantumATK; Band Structure; Density of States; 2D Materials*

PACS: 71.15.Mb, 73.22.-f, 71.20.Nr, 62.25.-g, 68.43.Bc

1. INTRODUCTION

Two-dimensional (2D) transition metal dichalcogenide monolayers, particularly molybdenum disulfide (MoS_2), have emerged as promising semiconducting materials due to their unique electronic properties and potential applications in nanoelectronics and optoelectronic devices [1]. Unlike bulk MoS_2, which exhibits an indirect band gap of approximately 1.2 eV [2], monolayer MoS_2 transitions to a direct band gap semiconductor with typical values around 1.8–1.9 eV at the K point of the Brillouin zone [3]. This direct gap offers significant advantages in optoelectronics, such as efficient light emission and detection [4].

Several first-principles DFT studies have focused on the electronic structure of monolayer MoS_2. Most report a direct band gap in the range of 1.8–1.9 eV within the PBE-GGA approximation, whereas many-body GW or hybrid functional calculations predict higher values (up to ~ 2.3 eV) [5]. Moreover, the effects of biaxial strain on the band gap have been widely explored; in particular, a tensile strain typically reduces the gap by 60–90 meV per percent [6].

In addition to band gap modulation, orbital-resolved analyses such as partial density of states (PDOS) and electron density distribution have been used to understand bonding characteristics in MoS_2 [7, 8]. These tools offer insight into the contribution of Mo-d and S-p orbitals, and into the spatial distribution of electron localization, which are important for understanding electronic transport and material interactions.

While previous works have provided valuable data on the electronic properties of MoS_2, many are limited to band structure and DOS analyses, lacking complementary studies on charge density or strain-dependent electronic descriptors.

In this context, our study presents a comprehensive first-principles analysis of pristine monolayer MoS_2. Using DFT-based QuantumATK simulations, we investigate the band structure, total and partial DOS, electron density distribution, and the effect of ±3% biaxial strain on the band gap. Our findings aim to deepen the understanding of how structural deformation influences the electronic behavior of MoS_2, thus supporting future applications in flexible nanoelectronic devices.

2. COMPUTATIONAL METHOD

The structural and electronic properties of monolayer molybdenum disulfide (MoS_2) were investigated using first-principles calculations within the framework of density functional theory (DFT), as implemented in the QuantumATK simulation package. The Localized Atomic Orbital (LCAO) method was employed with the Medium basis set and norm-conserving pseudopotentials. Exchange-correlation interactions were treated using the Generalized Gradient Approximation (GGA) in the form of the Perdew–Burke–Ernzerhof (PBE) functional [9].

The initial structure of monolayer MoS_2 was constructed based on experimental lattice constants and relaxed by geometry optimization using the Quasi-Newton minimization algorithm until the maximum force on atoms was less than 0.01 eV/Å. A vacuum spacing of 20 Å was introduced along the z-direction to eliminate interlayer interactions due to periodic boundary conditions. The final optimized structure is shown in Fig. 1.

Cite as: M. Khalilloev, B. Jabbarova, A. Hasanov, G. Ibodullaev, A. Atamuratov, East Eur. J. Phys. 1, 221 (2025), https://doi.org/10.26565/2312-4334-2026-1-23

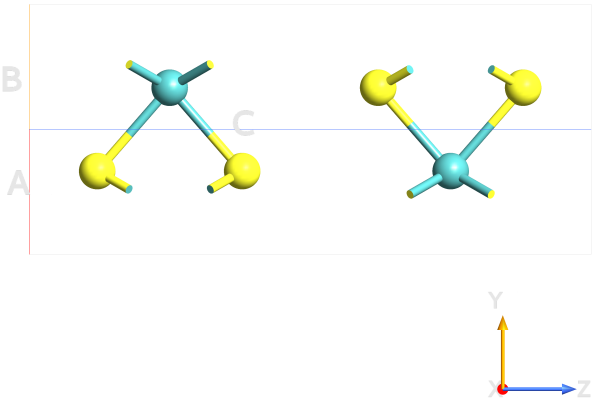

Figure 1. Relaxed atomic structure of monolayer MoS_2

The self-consistent field (SCF) procedure was enabled with a maximum of 100 iterations and energy tolerance of 10^{-5} eV. The Poisson equation for electrostatic potential was solved using the Fast Fourier Transform (FFT) solver. The k-point sampling of the Brillouin zone was performed using the Monkhorst–Pack scheme with a grid of 15×15×1 for the 2D periodic system. The mesh cutoff energy was set to 150 Hartree to ensure high numerical accuracy.

3. RESULTS AND DISCUSSION

3.1. Band Structure Analysis

The calculated electronic band structure of monolayer MoS_2 is presented in Fig. 2, where both direct and indirect band gap transitions are indicated with arrows. The results show that monolayer MoS_2 exhibits a direct band gap of 1.74 eV at the K-point, which aligns with many DFT-based predictions using the GGA-PBE approximation [9, 10]. Additionally, an indirect band gap of 1.27 eV was observed between the Γ-point (valence band maximum) and the K-point (conduction band minimum). These results demonstrate the quasi-direct nature of the band structure of monolayer MoS_2, and are in good agreement with previously reported theoretical values ranging from 1.7 to 1.9 eV [11, 12].

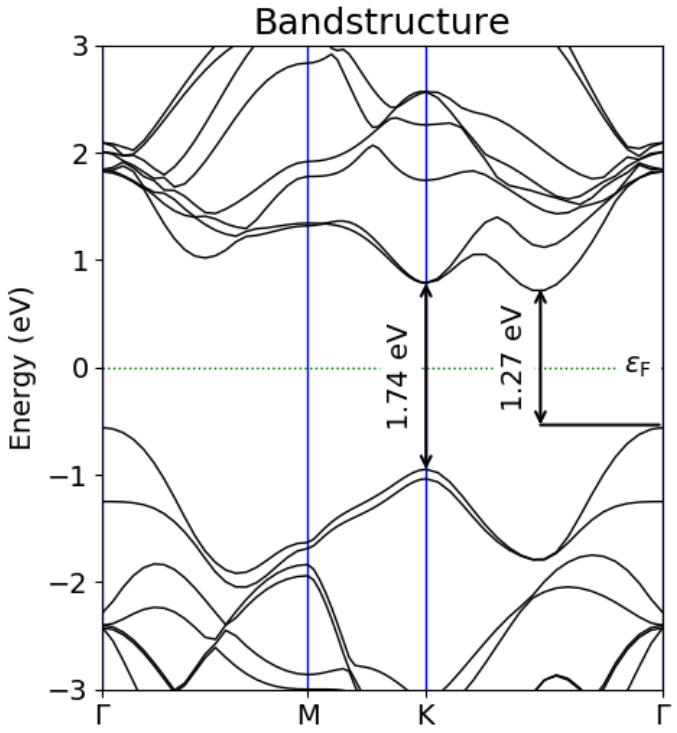

Figure 2. Calculated band structure of monolayer MoS_2 showing both direct (1.74 eV) and indirect (1.27 eV) band gaps

To support these values, the valence band maximum (VBM) and conduction band minimum (CBM) were extracted

from the band structure. The VBM is located at –0.56045 eV, and the CBM is at +0.71831 eV relative to the Fermi level, yielding a calculated gap of 1.2787 eV, which corresponds to the indirect transition. This supports the existence of a strong direct transition while also revealing possible indirect behavior, depending on external factors like strain or substrate effects.

Fig. 2. Electronic band structure of monolayer MoS_2. Both direct (1.74 eV) and indirect (1.27 eV) band gaps are marked with arrows.

3.2. Total Density of States (DOS)

The total density of states (DOS) of monolayer MoS_2 is shown in Fig. 3, where the Fermi level is aligned at 0 eV. The DOS plot clearly confirms the presence of a band gap around the Fermi level, with no electronic states in the energy range between the valence and conduction bands. The band gap value inferred from the DOS plot is approximately 1.27 eV, which is consistent with the band structure analysis discussed above.

Both spin-up and spin-down components were calculated within a spin-polarized framework. The two spin channels fully overlap, indicating the absence of exchange-induced spin polarization and confirming a non-magnetic ground state. Spin–orbit coupling (SOC) effects were not included in the present calculations; therefore, possible SOC-induced band splittings, known to occur in monolayer MoS_2, are beyond the scope of this work.

Although only the total DOS is discussed here, future analysis of the partial DOS (PDOS) will help identify the orbital contributions of the Mo (d-orbitals) and S (p-orbitals) atoms. Preliminary expectations suggest dominant Mo-4d and S-3p contributions near the band edges [13, 14].

Fig. 3. Total density of states (DOS) of monolayer MoS_2. The band gap of ∼ 1.27 eV is indicated with an arrow. Fermi level is set at 0 eV.

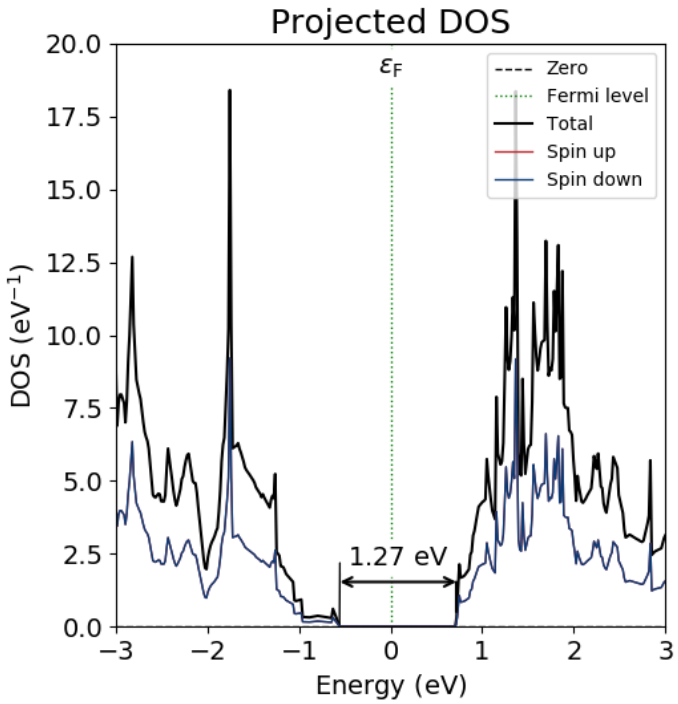

Figure 3. Total density of states (DOS) of monolayer MoS_2. The band gap of 1.27 eV is indicated

3.3. Partial Density of States (PDOS) Analysis

To gain deeper insight into the electronic structure of monolayer MoS_2, the projected density of states (PDOS) was computed and is shown in Fig. 4. The graph highlights the orbital contributions from Mo d-orbitals and S s+p orbitals. The Fermi level (ε_F) is set to 0 eV, and the calculated band gap (Eg) is clearly visible, measuring approximately 1.27 eV, consistent with previous band structure and total DOS results.

As evident from Fig. 4, the valence band maximum (VBM) is primarily composed of S 3p states, while the conduction band minimum (CBM) is dominated by Mo 4d states. This is in agreement with earlier theoretical findings, where Mo-d orbitals govern the conduction characteristics and S-p orbitals contribute to valence behavior [15, 16].

The strong contribution of Mo d-states near the conduction band edge suggests that the conduction mechanism in MoS_2 is primarily controlled by the transition metal atom. Conversely, the sulfur atoms influence the valence characteristics, which is vital for tuning optical and electronic transitions in device applications.

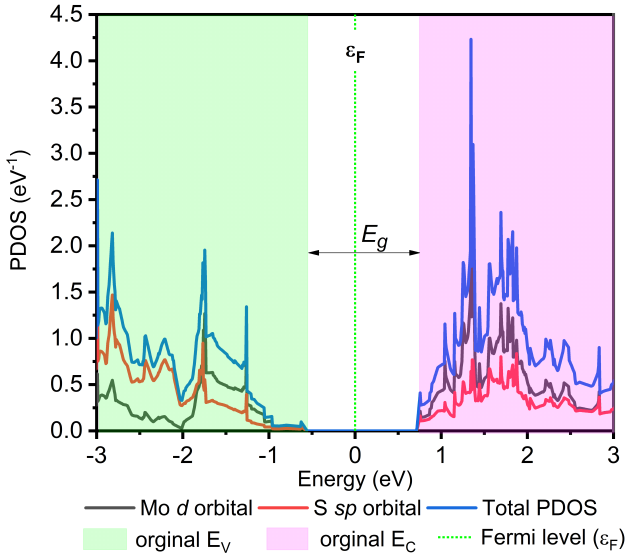

Figure 4. PDOS of monolayer MoS_2 showing total DOS, Mo d- and S s+p orbital contributions. The Fermi level ($\varepsilon_F = 0$ eV) and band gap ($E_g \approx 1.27$ eV) are indicated.

These orbital insights provide important guidelines for future work involving doping, strain engineering, or heterostructure design, where band alignment and charge transfer are sensitive to atomic orbitals.

Fig. 4. Partial density of states (PDOS) of monolayer MoS_2 showing contributions from Mo-d, S-sp orbitals. The band gap ($E_g \approx 1.27$ eV) and Fermi level (ε_F) are indicated. Color shading marks valence (E_V) and conduction (E_C) regions.

3.4. Electron Charge Density Distribution

To analyze the spatial distribution of electrons in the MoS_2 monolayer, the total electron charge density was calculated based on the self-consistent field (SCF) results. The charge density map is visualized in Fig. 5, showing a cross-sectional view along the XZ plane of the relaxed atomic structure. As observed in Fig. 5, the electron density is strongly localized around the Mo–S bonds, indicating a high degree of covalent bonding between molybdenum and sulfur atoms. The central regions of high density (colored red and green) represent the bonding areas, while the outer blue regions correspond to low-density vacuum or interlayer spacing.

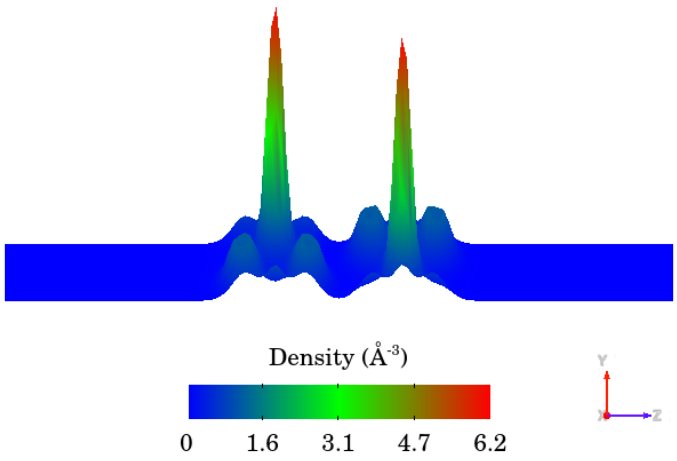

Figure 5. Electron charge density distribution of monolayer MoS_2 plotted along the XZ plane. The red and green regions indicate high electron accumulation, particularly around the Mo–S bonds, while blue areas correspond to low electron density. The color scale represents the charge density in A^{-3}

This distribution aligns well with the partial density of states (PDOS) results, where Mo-d and S-p orbitals are the

dominant contributors near the valence and conduction band edges. The symmetry and uniformity of the electron cloud also indicate structural relaxation and convergence of the optimized geometry.

Understanding the electron density map is crucial for identifying chemical reactivity zones, adsorption behavior, and defect sensitivity, which are significant in the design of optoelectronic and sensing devices based on MoS_2 and other 2D materials.

3.5. Strain Effect on the Electronic Properties

To understand the influence of biaxial mechanical deformation on the electronic properties of monolayer MoS_2, a series of calculations were performed by applying strain in the range of –3% to +3%. At each strain level, the lattice constant a was adjusted according to the equation (1):

$$a = a_0 \times (1 + \varepsilon) \tag{1}$$

where a_0=3.1604 Å and ε is the applied strain in percentage.

For each applied biaxial strain value, the in-plane lattice parameters were modified according to Eq. (1), while all internal atomic coordinates were fully relaxed under fixed strained lattice constants until the force convergence criterion (0.01 eV/Å) was satisfied. The vacuum spacing (20 Å), k-point mesh (15×15×1), mesh cutoff energy (150 Hartree), and SCF convergence parameters were kept unchanged for all strain configurations to ensure methodological consistency and reliable comparison of the calculated electronic properties.

The computed direct and indirect band gap values under various strain conditions are presented in Fig. 6 and summarized in Table 1. The results indicate that the band gap decreases almost linearly with increasing tensile strain, while compressive strain slightly enhances the band gap.

Table 1. Calculated direct and indirect band gaps of monolayer MoS_2 under various biaxial strain levels.

Strain (%)	Direct Band Gap (eV)	Indirect Band Gap (eV)
–3	2.1169	1.4879
–2	1.9853	1.5209
–1	1.8476	1.3042
0	1.7364	1.2787
+1	1.6286	1.1425
+2	1.5289	0.9527
+3	1.4366	0.7747

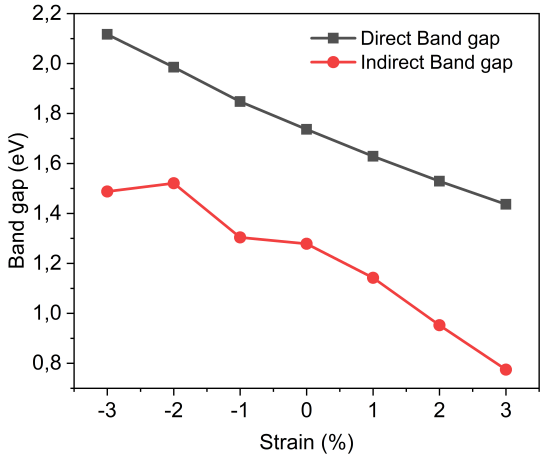

Figure 6. Variation of direct and indirect band gaps of monolayer MoS_2 under biaxial strain from –3% to +3%. The band gaps were extracted from calculated band structures at each strain level.

Specifically, the direct band gap decreased from 2.12 eV (–3%) to 1.44 eV (+3%), and the indirect band gap reduced from 1.49 eV to 0.77 eV. At 0% strain, the direct gap is 1.7364 eV and the indirect gap is 1.2787 eV, consistent with the earlier band structure results. This trend agrees with previous theoretical studies [1, 2], which report that tensile strain weakens interatomic interactions, narrowing the band gap. Furthermore, the transition from indirect to more pronounced

indirect band gap under large tensile strain suggests strain-induced electronic phase tunability, making MoS_2 a promising material for flexible electronics and strain-engineered devices.

4. CONCLUSIONS

In this study, the electronic properties of monolayer MoS_2 were systematically investigated using the density functional theory (DFT) approach implemented in QuantumATK with the LCAO basis set. The structural optimization was followed by calculations of the band structure, density of states (DOS), projected density of states (PDOS), charge density, and the effects of biaxial strain on the band gap.

The calculated band structure revealed that monolayer MoS_2 possesses a direct band gap of 1.74 eV and an indirect band gap of 1.27 eV, which is in good agreement with previously reported theoretical values. The total and partial DOS analysis showed that the Mo-d and S-p orbitals are the dominant contributors near the Fermi level, confirming the strong covalent interaction between the atoms. The charge density distribution further illustrated the bonding characteristics and electron localization along the Mo–S bonds.

The influence of biaxial strain on the electronic structure was also explored. It was found that increasing tensile strain led to a gradual decrease in both direct and indirect band gaps, with values ranging from 2.12 eV to 1.44 eV (direct) and 1.49 eV to 0.77 eV (indirect) over a strain range of –3% to +3%. These findings demonstrate the potential of strain engineering for tuning the electronic properties of 2D materials such as MoS_2.

Overall, the results confirm that monolayer MoS_2 exhibits tunable electronic behavior, making it a promising candidate for future applications in nanoelectronics, optoelectronics, and flexible device technologies.

Acknowledgments

The authors declare that there is no conflict of interest regarding the publication of this paper.

ORCID

Makhkam Khalilloev, https://orcid.org/0000-0001-5497-6410; **Bahor Jabbarova**, https://orcid.org/0000-0003-1181-5195; **Asrorbek Hasanov**, https://orcid.org/0009-0008-7976-667X; **Ghayrat Ibodullaev**, https://orcid.org/0009-0002-2324-959X; **Atabek Atamuratov**, https://orcid.org/0000-0003-2173-3783

REFERENCES

[1] K. F. Mak, C. Lee, J. Hone, J. Shan, and T. F. Heinz, "Atomically Thin MoS_2: A New Direct-Gap Semiconductor," Phys. Rev. Lett. **105**, 136805 (2010). https://doi.org/10.1103/PhysRevLett.105.136805

[2] A. Ramasubramaniam, "Large excitonic effects in monolayers of molybdenum and tungsten dichalcogenides," Phys. Rev. B, **86**, 115409 (2012). https://doi.org/10.1103/PhysRevB.86.115409

[3] J. Shi, T. Yu, M. Yang, *et al.*, "First-principles study of MoS_2 under strain," Superlattices Microstruct. **185**, 107912 (2023). https://doi.org/10.1016/j.spmi.2023.107912

[4] J. Kang, S. Tongay, J. Zhou, J. Li, and J. Wu, "Band offsets and heterostructures of two-dimensional semiconductors," Appl. Phys. Lett. **102**, 012111 (2013). https://doi.org/10.1063/1.4774090

[5] S. I. Sim, D. K. Lim, Y. M. Kim, *et al.*, "Photoluminescence of monolayer MoS_2 fabricated by chemical vapor deposition method," J. Korean Phys. Soc. **66**, 1789–1794 (2015). https://doi.org/10.3938/jkps.66.1789

[6] H. Fang, S. Chuang, T. C. Chang, K. Takei, T. Takahashi, and A. Javey, "High-performance single layered WSe_2 p-FETs with chemically doped contacts," Nano Lett. **12**, 3788–3792 (2012). https://doi.org/10.1021/nl301702r.

[7] L. Yu, Y. Chen, W. Zhang, P. Yang, and X. Feng, "Spin-Orbit-Coupling-Governed Optical Absorption in Bilayer MoS_2 via Strain, Twist, and Electric Field Engineering," Nanomaterials, **15**(14), 1100 (2025)/ https://doi.org/10.3390/nano15141100

[8] H. Rezania, M. Abdi, and B. Astinchap, "The effects of spin-orbit coupling on optical properties of monolayer MoS_2 due to mechanical strains," Sci. Rep. **13**, 1159 (2023). https://doi.org/10.1038/s41598-023-28258-z

[9] L. Yu, Y. Chen, W. Zhang, P. Yang, and X. Feng, "Spin-Orbit-Coupling-Governed Optical Absorption in Bilayer MoS_2 via Strain, Twist, and Electric Field Engineering," Nanomaterials, **15**(14), 1100 (2025). https://doi.org/10.3390/nano15141100

[10] W.-J. Lan, H.-X. Li, T. Du, X. Lin, and F. Pan, "Strain modulation on electronic structures and magnetic properties of Fe-doped monolayer 2H-MoS_2: A first-principles study," Eur. Phys. J. B, **98**, 24 (2025). https://doi.org/10.1140/epjb/s10051-025-00872-y

[11] H. Gan, G. Zhou, H. Zhang, and X. Hua, "Strain engineering of electronic and thermoelectric properties in MoS_2/WSe_2 bilayer heterostructure," Chem. Phys. **599**, 112859 (2025). https://doi.org/10.1016/j.chemphys.2025.112859

[12] A. Samy, S. Zeng, M. D. Birowosuto, and A. El Moutaouakil, "A review on MoS_2 properties, synthesis, sensing applications and challenges," Crystals, **11**(4), 355 (2021). https://doi.org/10.3390/cryst11040355

[13] B. Radisavljevic, A. Radenovic, J. Brivio, V. Giacometti, and A. Kis, "Single-layer MoS_2 transistors," Nat. Nanotechnol. **6**, 147–150 (2011). https://doi.org/10.1038/nnano.2010.279

[14] Q. Yue, S. Chang, J. Kang, X. Zhang, and S. Qin, "Mechanical and electronic properties of monolayer MoS_2 under elastic strain," Phys. Lett. A, **376**, 1166–1170 (2012). https://doi.org/10.1016/j.physleta.2012.02.021

[15] B. K. Ismaylov, K. A. Ismailov, N. F. Zikrillaev, A. E. Atamuratov, S. V. Koveshnikov, Z. T. Kenzhaev, M. M. Khalilloev, and P. K. Dilimbetov, "Investigation of the behavior of nickel impurity atoms in the silicon lattice based on first principles," East European Journal of Physics, (3), 48 (2025). https://doi.org/10.26565/2312-4334-2025-3-48

[16] T. Li, and G. Galli, "Electronic properties of MoS_2 nanoparticles," J. Phys. Chem. C, **111**, 16192–16196 (2007). https://doi.org/10.1021/jp0743773.

ДОСЛІДЖЕННЯ ЕЛЕКТРОННИХ ВЛАСТИВОСТЕЙ МОНОШАРУ MoS_2 З ПЕРШИХ ПРИНЦИПІВ ЗА ДОПОМОГОЮ DFT-МОДЕЛЮВАННЯ В QuantumATK

Махкам Халіллоєв[1], **Бахор Джаббарова**[1], **Асрор Хасанов**[1], **Гайрат Ібодуллаєв**[2], **Атабек Атамуратов**[1]

[1]*Кафедра фізики, Ургенчський державний університет, вул. Х. Алімджана, 14, м. Ургенч, 220100, Узбекистан*

[2]*Кафедра фізики та математики, Ургенцький державний педагогічний інститут, вул. Гурлан, 1-А, Ургенч, 220100, Узбекистан*

У цій роботі електронні властивості моношару дисульфіду молібдену (MoS_2) досліджувалися з використанням теорії функціоналу густини (DFT) у середовищі моделювання QuantumATK. Розрахунки зонної структури та густини станів (DOS) показали, що MoS_2 має прямий заборонений зонний проміжок шириною 1,75 еВ та непрямий — 1,44 еВ. Додатково було проведено аналіз часткової густини станів (PDOS) та розподілу густини заряду з метою вивчення внеску орбіталей та характеристик хімічного зв'язування. Також було досліджено вплив біаксіального механічного напруження (±3%) на електронну структуру, що продемонструвало можливість керування шириною забороненої зони. Отримані результати надають цінну інформацію про електронні властивості MoS_2 та підтверджують його перспективність для застосування в наноелектроніці та гнучких електронних пристроях.

Ключові слова: *теорія функціонала густини; QuantumATK; зонна структура; густина станів; двовимірні матеріали*

East European Journal of Physics. 1. 228-232 (2026)
DOI:10.26565/2312-4334-2026-1-24 ISSN 2312-4334

STUDY OF THE FORMATION OF RADIATION DEFECTS IN IRRADIATED SILICON SAMPLES, DOPED WITH CHROMIUM ATOMS

Sh.I. Nabiyev[1], Kh.N. Bozorov[1], A. Nasritdinov[1], R.G. Ikramov[1], M.A. Yuldoshev[2]*, N.A. Sattarov[3], U. Edilboyev[4], S.M. Adilkhan[5], S.A. Tursinbaev[6], A.E. Otarbaev[6], S.M. Kasimov[6]

[1]Namangan State Technical University, Uzbekistan
[2]Turan International University, Namangan, Uzbekistan
[3]Kimyo International University in Tashkent, Uzbekistan
[4]Tashkent Institute of Irrigation and Agricultural Mechanization Engineers, National Research University, Uzbekistan
[5]Institute of Nuclear Physics ARKAE, Almaty, Kazakhstan
[6]Nukus State Pedagogical Institute Named After Ajiniyaz, Nukus, Uzbekistan
**Corresponding Author e-mail: murod.yuldoshev1993@gmail.com*
Received January 6, 2026, revised February 13, 2026; accepted February 20, 2026

This work presents an investigation of radiation-induced defect formation in single-crystal n-type silicon doped with chromium (n-Si<Cr>) using positron annihilation spectroscopy. The initial silicon samples, phosphorus-doped during crystal growth, were subsequently modified by chromium diffusion and then irradiated with 2 MeV protons at a beam current of 0.5 μA using the EG-5 accelerator facility. The measurements revealed the formation of characteristic radiation-induced vacancy-type defects, including A-centers, E-centers, divacancies, and their stable complexes. A comparative analysis of chromium-doped and undoped samples demonstrated a pronounced difference in the accumulation rate of these defects. It was established that the presence of chromium atoms in the bulk of n-type silicon significantly suppresses radiation defect formation: the concentration of vacancy-related defects in n-Si<Cr> was found to be approximately 1.5–2 times lower than in the reference n-Si samples irradiated under identical conditions. These results confirm that chromium doping enhances the radiation resistance of silicon and can be considered an effective approach for modifying semiconductor materials intended for operation in environments with high radiation exposure.
Keywords: *Semiconductor; Silicon; Chromium; Doping; Irradiation; Proton; Positron annihilation*
PACS: 78.30. Am

INTRODUCTION

The complex theoretical and practical research on semiconductor materials is of great interest to researchers [1-3]. As a result of research, various diode structures and devices based on them can be seen [4-7].

The study of radiation-induced defects in silicon (Si) and doped silicon materials is an important direction in modern semiconductor science and technology. Under proton irradiation, atoms of the crystal lattice are displaced from their lattice sites, leading to the formation of vacancies, interstitial atoms, and their complexes. These defects have a significant impact on the electronic properties of the material, including electrical conductivity, charge carrier concentration, and electron mobility, which are directly related to the functional characteristics of semiconductor devices, especially those operating under extreme radiation conditions [8-10].

Of particular interest are doped silicon systems such as n-Si<Cr>, where the presence of chromium impurities can substantially alter the formation and evolution of radiation defects. Impurities can interact with vacancies and interstitial atoms, promoting the formation of complex defects with different energy characteristics and enhanced stability. This makes doped materials especially attractive for studies aimed at improving the radiation hardness of semiconductor devices [11, 12].

A key tool for investigating such defects is positron annihilation spectroscopy (PAS), which provides high sensitivity to vacancies and their complexes. This method allows not only the quantitative determination of defect concentrations but also the characterization of their nature and size, as well as the evaluation of the dynamics of changes in the crystal structure under proton irradiation. Owing to these capabilities, PAS has become a standard technique for studying radiation effects in semiconductors [13].

The comprehensive use of experimental data makes it possible to obtain a deep understanding of the processes of formation and evolution of radiation defects in n-Si and n-Si<Cr>. Analysis of the obtained results provides not only fundamental knowledge about the interaction of protons with the crystal lattice but also practical information for the development of semiconductor materials with enhanced resistance to ionizing radiation. These data are of great importance for space electronics, nuclear power engineering, and other fields where the reliability of semiconductor devices critically depends on their radiation stability [14].

The aim of the present work is to study radiation-induced defect formation in n-Si and n-Si<Cr> silicon single crystals using positron annihilation spectroscopy.

Cite as: Sh.I. Nabiyev, Kh.N. Bozorov, A. Nasritdinov, R.G. Ikramov, M.A. Yuldoshev, N.A. Sattarov, U. Edilboyev, S.M. Adilkhan, S.A. Tursinbaev, A.E. Otarbaev, S.M. Kasimov, East Eur. J. Phys. 1, 228 (2026), https://doi.org/10.26565/2312-4334-2026-1-24

In solid-state spectroscopy, once a positron has thermalized, it is treated as a point-like particle that remains within the solid until it annihilates or becomes trapped. During its lifetime in the lattice, the positron diffuses through the crystal, tending to avoid the positively charged atomic nuclei and therefore occupying interstitial regions. Because the positron wave function becomes strongly localized at defect sites, changes in defect structure can be qualitatively inferred from the S–W plot, as discussed in Refs. [15, 16]. However, direct comparison of absolute S and W parameters obtained from different spectrometers is discouraged, since these values are influenced by the instrument's energy resolution and the specific window settings used during their evaluation (Fig. 1).

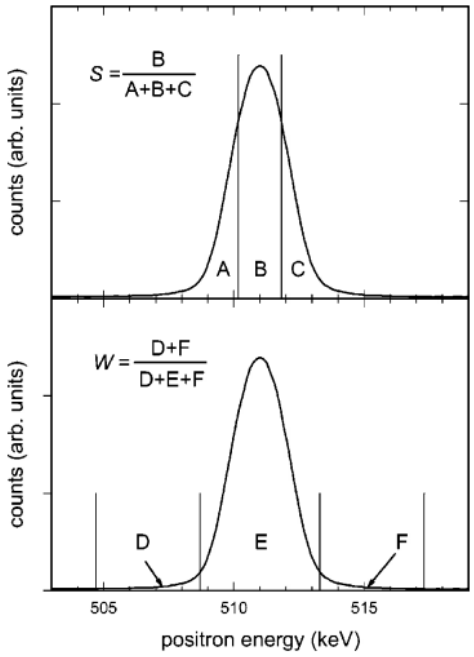

Figure 1. Dependence of parameters S and W on the positron energy with corresponding energy windows, used in the analysis of the positron annihilation peak at 511 keV

EXPERIMENTAL PART

The samples investigated in this study were n-type silicon wafers (KEF-20) with dimensions of 1.5×7×14 mm and a resistivity of 20 Ω·cm. These wafers were obtained from silicon single crystals grown by the Czochralski technique. Chromium was introduced into the silicon by diffusion, using a metallic chromium layer deposited on the wafer surface and sealed in evacuated quartz ampoules. The diffusion process was carried out at 1200 °C for 2 hours, followed by cooling according to the thermal treatment procedures described in Refs. [17, 18]. The concentration of phosphorus dopant in the initial n-type silicon crystals was 4.5×10^{14} at/cm³.

After surface cleaning, the chromium-doped silicon samples were irradiated with 2 MeV protons at a beam current of 0.5 μA to achieve a total fluence of 5.1×10^{14} particles/cm². The irradiation procedures were performed using the "EG-5" electrostatic accelerator at the Frank Laboratory of Neutron Physics (FLNP), Joint Institute for Nuclear Research (JINR).

Radiation-induced structural defects in the samples were examined using positron annihilation spectroscopy, specifically by analyzing the Doppler broadening of the 511 keV gamma line. The measurements were conducted using a positron beam facility with adjustable implantation energy for depth profiling, located at the Laboratory of Nuclear Problems, JINR.

RESULTS AND DISCUSSIONS

Figure 2 illustrates the variation of the S parameter as a function of positron implantation energy for n-Si and n-Si<Cr> samples following proton irradiation at room temperature. A distinct increase in the S parameter is observed in the shallow region corresponding to positron energies of 0.1–2 keV (Fig. 2, curve 1). For positron energies in the range of 3–17 keV, which probe deeper into the samples, the S parameter decreases below its initial value in the irradiated n-Si. Previous studies [19] on irradiated n-Si and n-Si<Pt> demonstrated that positron annihilation behavior differs significantly between n-Si<Cr> and n-Si<Pt> samples, indicating a dependence on the impurity type of doping.

The S parameter of the irradiated n-Si<Cr> sample is lower than that of the irradiated n-Si sample (Fig. 2, red curve). An increase in S is observed in the shallow region corresponding to positron energies of 0.05–1.8 keV. At greater depths, corresponding to implantation energies of 1.8–23 keV, the S parameter falls below the bulk value.

The S parameter reflects the fraction of positron annihilations occurring with valence electrons [20]. In these materials, it is also necessary to consider the contribution of positronium annihilation, which can affect the measured S

values. However, the influence of parapositronium annihilation can be accounted for by comparing S with the W parameter, which represents positron annihilation with core (nuclear) electrons. In the absence of parapositronium effects, the S and W profiles should exhibit opposite trends, as illustrated in Fig. 3.

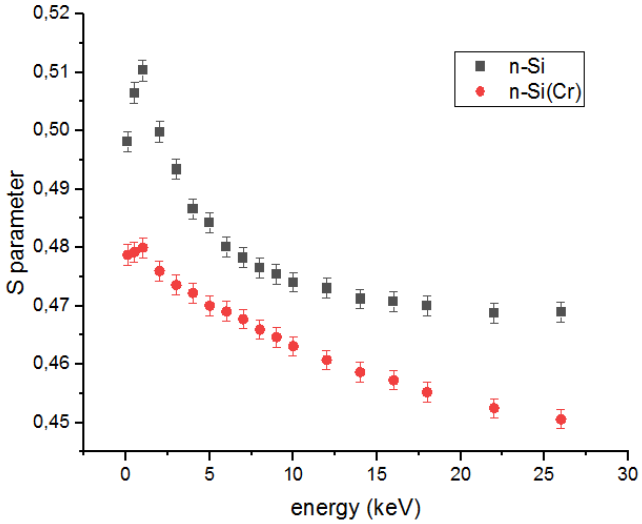

Figure 2. Variation of the S parameter as a function of positron implantation energy (corresponding depth) for irradiated silicon samples: n-Si (1) and n-Si<Cr> (2)

When comparing n-Si and n-Si<Cr>, it is evident that defect concentration decreases with increasing positron energy, indicating that defects are more prevalent near the surface. In Fig. 2, the implantation profiles suggest partial "healing" of defects throughout the depth of n-Si. In contrast, the n-Si<Cr> samples display both radiation-induced defects and additional structural defects caused by mechanical stress, which are more clearly reflected in the S parameter.

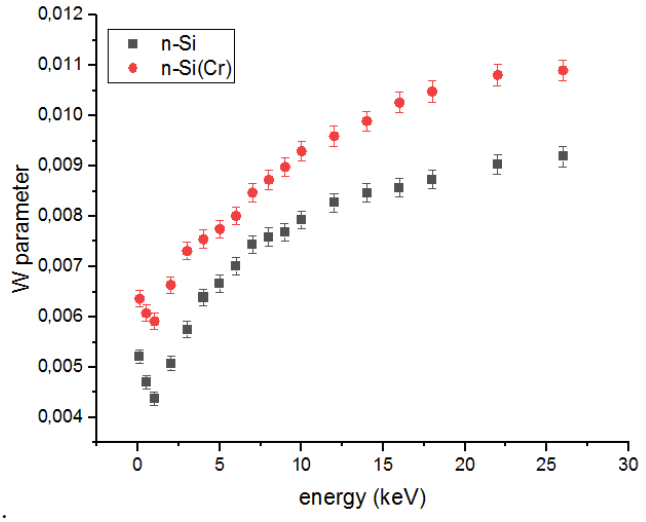

Figure 3. Variation of the W parameter as a function of positron implantation energy (corresponding depth) for irradiated silicon samples: n-Si (1) and n-Si<Cr> (2)

It is well established [21, 22] that the primary effect of radiation on semiconductors is the formation of radiation-induced defects, particularly vacancies. These defects commonly include oxygen-vacancy complexes (Oi–V, A-centers), divacancies (V–V), and phosphorus-vacancy complexes (P_S–V, E-centers).

Doping of monocrystalline silicon with chromium significantly affects the behavior of radiation-induced defects formed during proton irradiation. In particular, the presence of Cr atoms contributes to a reduction in the concentration of key point defects, such as A-centers, E-centers, and divacancies. This effect is achieved through the formation of stable "defect–Cr" complexes, which hinder the migration and aggregation of vacancies and interstitial silicon atoms, while also accelerating the recombination of free vacancies and interstitials. Thus, Cr simultaneously acts as a "trap" for radiation defects and a catalyst for their annihilation, leading to decrease in defect concentration compared to initial silicon and enhancing the material's radiation tolerance [23].

As noted in [24], real solids always contain some intrinsic defects, which disrupt the perfect translational symmetry of the lattice and the electronic band structure. In such regions, the local potential for positrons can decrease significantly,

allowing individual positrons to become trapped. This trapping typically occurs at open-volume defects, such as vacancies, vacancy clusters, dislocations, and certain types of precipitates. Positrons can also localize near negatively charged foreign atoms (planar traps), although this effect is mainly observed at low temperatures due to minor reductions in positron potential. Additionally, vacancies in semiconductors can carry an electric charge, creating a long-range potential that attracts or repels positrons.

According to [25], open-volume defects exhibit a lower local electron density than an ideal crystal because atomic cores and core electrons are absent. Consequently, the positron annihilation rate decreases in these regions. Positron annihilation techniques generally assume that a positron trapped in a specific defect interacts primarily with the electrons in that defect. This interaction determines a characteristic annihilation probability, the reciprocal of which defines the positron lifetime in the defect. The lifetime describes how long positrons remain in a particular defect type before annihilation.

The small spatial extent of deep traps restricts the number of positron states that can be occupied and limits capture according to energy selection rules. In larger or more extended defect centers, capture is mainly limited by positron diffusion. Measurable positron trapping occurs only if defects are sufficiently dense; the average distance between defects of the same type must be smaller than the positron diffusion length in a defect-free lattice. As the density of defects increases, the S parameter correspondingly rises due to enhanced positron localization [26].

Based on these studies [21–27], it can be inferred that proton irradiation at 2 MeV generates radiation defects in both n-Si and n-Si<Cr> samples, predominantly associated with vacancies (A-centers, E-centers, divacancies, etc.). However, the concentration of vacancy-related defects in irradiated n-Si is approximately 1.5 times higher than in irradiated n-Si<Cr>. This indicates that chromium doping reduces the formation of radiation defects in the silicon lattice.

CONCLUSIONS

Positron annihilation spectroscopy measurements have shown that irradiation with 2 MeV protons at a fluence of 5.1×10^{14} cm^{-2} leads to the formation of vacancy-type radiation defects in both n-Si and n-Si<Cr> samples, including A-centers, E-centers, divacancies, and their complexes. However, a comparative analysis revealed a pronounced difference in defect concentration: in undoped n-Si, the density of these defects after irradiation is nearly 1.5 times higher than in chromium-doped n-Si samples.

This observation indicates that chromium atoms play a stabilizing role in the silicon crystal lattice, effectively reducing the accumulation of radiation-induced damage. Chromium doping partially suppresses the formation of vacancy-related complexes, thereby enhancing the radiation tolerance of the material.

Overall, the present results demonstrate the strong potential of chromium-doped silicon for use in microelectronic devices and structures intended to operate in high-radiation environments. These findings also contribute to a deeper understanding of radiation damage mechanisms in doped semiconductors and open new prospects for the development of more reliable and radiation-resistant semiconductor technologies.

ORCID

Murodjon A. Yuldoshev, https://orcid.org/0000-0002-9722-9439; **Nosirbek A. Sattarov,** https://orcid.org/0009-0005-0506-0269
Saltanat M. Adilkhan, https://orcid.org/0009-0003-5096-502X; **Unarbek Edilboyev,** https://orcid.org/0009-0004-6983-8482

REFERENCES

[1] M. Akramov, B. Eshchanov, S. Usanov, Sh. Norbekov, and D. Matrasulov, "Second-harmonic generation in branched optical waveguides: Metric graphs-based approach," Physics Letters A, **524**, 129827 (2024). https://doi.org/10.1016/j.physleta.2024.129827
[2] J.R. Yusupov, M. Ehrhardt, Kh.Sh. Matyokubov, and D.U. Matrasulov, "Driven transparent quantum graphs," Physica Scripta, **100**(7), (2025). https://doi.org/10.1088/1402-4896/ade014
[3] N.Yu. Sharibaev, A.Q. Ergashov, S.B. Fazliddinov, R.G. Ikramov, M.A. Yuldoshev, and A.A. Abdulxayev, "Photoelectric characteristics of TiO_2-based on thin-film solar elements with ruthenium (II) compounds," Journal of Ovonic Research, **21**(6), (2025). https://doi.org/10.15251/JOR.2025.216.859
[4] W.A. Mussawi, N.S.S. Singh, S.G. Waheedullah, E. Muniyandy, B. Madaminov, S. Usanov, M. Latipova, H.A. El-Sabbani, M.A. Diabk, A. Smerat, Sh.M. Qasim, "Design and supported gold nanoparticles over the modified magnetic iron oxide nanoparticles as an effective nanocatalyst for Suzuki-Miyaura reactions," Journal of Organ-ometallic Chemistry 1042, 123863 (2025). https://doi.org/10.1016/j.jorganchem.2025.123863
[5] Sh.B. Utamuradova, Z.T. Azamatov, A.I. Popov, M.R. Bekchanova, M.A. Yuldoshev, and A.B. Bakhromov, "Study of Optical, Electrophotographic and Holographic Parameters of As-Se Condensates from the Prehistory of the Original Bulk Materials," East Eur. J. Phys. (3), 278 (2024). https://doi.org/10.26565/2312-4334-2024-3-27
[6] F.A. Giyasova, A.Z. Rakhmatov, Kh.N. Bakhronov, M.A. Yuldoshev, F.A. Giyasov, A.N. Olimov, and N.A. Sattarov, "Physical Principles of Photocurrent Generation in a Silicon-Based Photodiode Structure with a Schottky Barrier," East Eur. J. Phys. (4), 397 (2025), https://doi.org/10.26565/2312-4334-2025-4-38
[7] F.A. Giyasova, Kh.N. Bakhronov, M.A. Yuldoshev, I.B. Sapaev, R.G. Ikramov, F.A. Giyasov, M.R. Bekchanova, *et al*., "Study of the Influence of Temperature on the Transitions of the CdS/Si/CdTe Heterosystem," East Eur. J. Phys. (4), 461 (2025). https://doi.org/10.26565/2312-4334-2025-4-47
[8] Sh. B. Utamuradova, D.A. Rakhmanov, and A.S. Abiyev, "Investigation of Sensitive Thermal Sensors Based on Si<Pt> and Si<Pd>," East Eur. J. Phys. (3), 375 (2024). https://doi.org/10.26565/2312-4334-2024-3-45
[9] M, Golosov, V. Lozanov, and N. Baklanova, "The study of the iridium – silicon carbide reaction by Raman and IR spectroscopy," Materials Today: Proceedings, **25**, 352-355 (2019). https://doi.org/10.1016/j.matpr.2019.12.088

[10] P.R. Berger, G. Gulyamov, M.G. Dadamirzaev, M.K. Uktamova, and S.R. Boidedaev, Romanian Journal of Physics, 69, 609 (2024), https://doi.org/10.59277/RomJPhys.2024.69.609
[11] A.A. Lebedev, and V.V. Kozlovskiy, "On comparison of the radiation resistance of silicon and silicon carbide," Semiconductors, **48**(10), 1329–1331 (2014). https://doi.org/10.1134/S1063782614100170
[12] Sh.B. Utamuradova, Sh.Kh. Daliev, D.A. Rakhmanov, A.B. Uteniyazova, and A.S. Abiyev, "Raman Spectroscopy of Gamma-Irradiated Silicon Doped with Rhodium," East Eur. J. Phys. (4), 696 (2025). https://doi.org/10.26565/2312-4334-2025-4-75
[13] A.A. Istratov, H. Hieslmair, and E.R. Weber, "Iron contamination in silicon technology," Appl Phys A, **70**, 489–534 (2000). https://doi.org/10.1007/s003390051074
[14] Sh.B. Utamuradova, Sh.Kh. Daliev, D.A. Rakhmanov, A.S. Doroshkevich, I.G. Genov, P.L. Tuan, and A. Kirillov, Euroasian physical technical journal, **20**(3(45)), 35–42 (2023). https://doi.org/10.31489/2023No3/35-42
[15] M.K. Uktamova, Sh. Mamadaliev, "Three-dimensional modeling of the relationship between static tunneling and the optical absorption coefficient in tunnel diodes," Results in optics. Vol 22, 100950 (2026). https://doi.org/10.1016/j.rio.2025.100950
[16] Sh.B. Utamuradova, F.A. Giyasova, K.N. Bakhronov, M.A. Yuldoshev, M.R. Bekchanova, and B. Ismatov, "Current Transfer Mechanism in a Thin-Based Heterosystem Based on A^2B^6 Compounds," East Eur. J. Phys. (3), 325-335 (2025). https://doi.org/10.26565/2312-4334-2025-3-31
[17] I. Pintilie, G. Lindström, A. Junkes, and E. Fretwurst, "Radiation-induced point- and cluster-related defects with strong impact on damage properties of silicon detectors," Nuclear Instruments and Methods in Physics Research A, **611**, 52–68 (2009). https://doi.org/10.1016/j.nima.2009.09.065
[18] F.A. Giyasova, and M.A. Yuldoshev, "Investigation of temporal characteristics of photosensitive heterostructures based on gallium arsenide and silicon," Chalcogenide Letters, 22(2), 123–129 (2025). https://doi.org/10.15251/CL.2025.222.123
[19] Sh.B. Utamuradova, S.A. Muzafarova, A.M. Abdugofurov, K.M. Fayzullaev, E.M. Naurzalieva, and D.A. Rakhmanov, Applied Physics, (4), 81-86 (2021). https://applphys.orion-ir.ru/appl-21/21-4/PF-21-4-81.pdf
[20] F.A. Selim, "Positron annihilation spectroscopy of defects in nuclear and irradiated materials- a review," Materials Characterization, **174**, 110952 (2021). https://doi.org/10.1016/j.matchar.2021.110952
[21] V.A. Kozlov, and V.V. Kozlovskiy, Semiconductors, **35**(7), (2001), http://journals.ioffe.ru/articles/viewPDF/37060
[22] M.G. Dadamirzaev, M.K. Uktamova, S. Rakhmanova, G.A. Ibadullayev, East Eur. J. Phys. 4, 675 (2025), https://doi.org/10.26565/2312-4334-2025-4-73
[23] Sh.B. Utamuradova, Kh.S. Daliev, Sh.Kh. Daliev, and K.M. Fayzullaev, Applied Physics, (6), 90–95 (2019). (in Russian)
[24] F. Tuomisto, *Springer Handbook of Crystal Growth, Defects and Characterization*, (Springer-Verlag, New York, 2010). http://dx.doi.org/10.1016/B978-0-12-396489-2.00002-3
[25] R.S. Brusa, C. Macchi, S. Mariazzi, and G.P. Karwasz, "Porosity of Low-Materials Studied by Slow Positron Beam," Acta physica polonica A, **107**(4), 702 (2005). https://www.researchgate.net/publication/241562432
[26] M.A. Huis, A. Veen, H. Schut, C.V. Falub, S.W.H. Eijt, and P.E. Mijnarends, "Positron confinement in embedded lithium nanoclusters," Physical review B, **65**, 085416 (2002). https://doi.org/10.1103/PhysRevB.65.085416
[27] S.F. Samadov, N.V.M. Trung, A.A. Sidorin, S.I. Ibragimova, S.H. Jabarov, M.A. Yuldoshev, O.S. Orlov, *et al*., "Effect of Zn and Fe doping on vacancy cluster formation in Cu–In–Se system," Micro and Nanostructures, **209**, 208451 (2026). https://doi.org/10.1016/j.micrna.2025.208451

ДОСЛІДЖЕННЯ УТВОРЕННЯ РАДІАЦІЙНИХ ДЕФЕКТІВ В ОПРОМЕНЕНИХ ЗРАЗКАХ КРЕМНІЮ, ЛЕГОВАНИХ АТОМАМИ ХРОМУ

Ш.І. Набієв[1], Х.Н. Бозоров[1], А. Насрітдінов[1], Р.Г. Ікрамов[1], М.А. Юлдошев[2], Н.А. Саттаров[3], У. Едільбоєв[4], С.М. Адільхан[5], С.А. Турсинбаєв[6], А.Е. Отарбаєв[6], С.М. Касімов[6]

[1]Наманганський державний технічний університет, Узбекистан
[2]Міжнародний університет Туран, Наманган, Узбекистан
[3]Міжнародний університет Кімьо в Ташкенті, Узбекистан
[4]Ташкентський інститут інженерів іригації та механізації сільського господарства, Національний дослідницький університет, Узбекистан
[5]Інститут ядерної фізики АРКАЕ, Алмати, Казахстан
[6]Нукусський державний педагогічний інститут імені Аджиніяза, Нукус, Узбекистан

У цій роботі представлено дослідження радіаційно-індукованого дефектоутворення в монокристалі n-типу кремнію, легованого хромом (n-Si<Cr>), за допомогою позитронно-анігіляційної спектроскопії. Вихідні зразки кремнію, леговані фосфором під час росту кристалів, згодом модифікували дифузією хрому, а потім опромінювали протонами з енергією 2 МеВ при струмі пучка 0,5 мкА за допомогою прискорювальної установки EG-5. Вимірювання виявили утворення характерних радіаційно-індукованих дефектів вакансійного типу, включаючи А-центри, Е-центри, дивакансії та їх стабільні комплекси. Порівняльний аналіз легованих хромом та нелегованих зразків продемонстрував помітну різницю в швидкості накопичення цих дефектів. Було встановлено, що присутність атомів хрому в об'ємі n-типу кремнію значно пригнічує радіаційне дефектоутворення: концентрація дефектів, пов'язаних з вакансіями, в n-Si<Cr> виявилася приблизно в 1,5–2 рази нижчою, ніж у еталонних зразках n-Si, опромінених за ідентичних умов. Ці результати підтверджують, що легування хромом підвищує радіаційну стійкість кремнію та може вважатися ефективним підходом до модифікації напівпровідникових матеріалів, призначених для експлуатації в середовищах з високим радіаційним впливом.

Ключові слова: *напівпровідник, кремній, хром, легування, опромінення, протон, анігіляція позитронів*

EAST EUROPEAN JOURNAL OF PHYSICS. 1. 233-240 (2026)
DOI:10.26565/2312-4334-2026-1-25 ISSN 2312-4334

FEATURES OF THE THERMAL BEHAVIOR AND PHASE FORMATION OF $BiFeO_3$ USING PRECURSORS ACTIVATED BY SOLAR MELTING

M.S. Payzullakhanov[1,2], F.A. Giyasova[3], M.A. Yuldoshev[4]*, Ch.X. Toshpulatov[5], R.U. Ernazarov[5], F.A. Giyasov[3], A. Urishev[6], A.D. Paluanova[7]

[1]Institute of Materials Science, Academy of Sciences of the Republic of Uzbekistan. Tashkent, Uzbekistan
[2]Fergana State Technical University, Uzbekistan
[3]Kimyo International University in Tashkent, Uzbekistan
[4]Turan International University, Namangan, Uzbekistan
[5]Tashkent branch of Samarkand State University of Veterinary Medicine, Animal Husbandry and Biotechnology, Uzbekistan
[6]Tashkent Institute of Irrigation and Agricultural Mechanization Engineers, National Research University, Uzbekistan
[7]Nukus State Pedagogical Institute, Uzbekistan
**Corresponding Author e-mail: murod.yuldoshev1993@gmail.com*
Received December 1, 2025; revised January 16, 2026; accepted January 30, 2026

The effect of pretreatment of Bi_2O_3 and Fe_2O_3 oxides on the synthesis and structural characteristics of bismuth ferrite $BiFeO_3$ was studied. It was found that $BiFeO_3$ formation begins at 790÷850 °C, and decomposition occurs above ~920 °C. Preliminary melting of the oxides in a solar furnace shifts the thermal effects to higher temperatures and increases the thermodynamic stability of the phase. X-ray phase analysis revealed the formation of a perovskite-like structure with orthorhombic distortion, high crystallinity, and a crystallite size of 40±10 nm. Phase analysis confirmed an increase in the content of the main phase to 97 % and a decrease in the impurity phase $Bi_2Fe_4O_9$. The obtained results confirm the efficiency of preliminary solar melting of oxides for the synthesis of high-quality ceramic materials based on $BiFeO_3$.
Keywords: *Solar furnace; Synthesis; Bismuth ferrite; Phase; Diffusion; Microstructure; Analysis; Temperature; Thermal effect*
PACS: 68.37.Hk, 78.70.Ck, 77.84.-s

INTRODUCTION

Multiferroic materials, which combine spontaneous polarization and magnetic ordering in a single structure, are of significant interest for modern electronics, spintronics, and sensor technologies [1-3]. Among these compounds, bismuth ferrite $BiFeO_3$ (BFO), which exhibits ferroelectric and antiferromagnetic properties at room temperature, has attracted particular attention. Due to its high Néel temperature (≈370 °C) and Curie point (≈820 °C), $BiFeO_3$ is considered a promising material for the creation of energy-efficient multifunctional devices, piezoelectric transducers, and photocatalytic systems [4-6].

Despite its high functional characteristics, obtaining single-phase bismuth ferrite $BiFeO_3$ remains a complex task. With traditional synthesis methods, secondary phases such as $Bi_2Fe_4O_9$ and $Bi_{25}FeO_{39}$ are typically formed from an oxide mixture of Bi_2O_3 and Fe_2O_3, thereby reducing the material's electrical and magnetic properties [7-10]. Attempts to eliminate their formation by changing the stoichiometry of the initial components, by introducing excess Bi_2O_3, also do not result in obtaining a single-phase compound [11]. The phase composition and morphology of the samples are significantly affected by the composition and dispersion of the precursors, the degree of their homogenization, and the heat treatment conditions [12]. As noted in [13], the difficulties in synthesizing single-phase bismuth ferrite are due to the peculiarities of the phase diagram of the Bi_2O_3-Fe_2O_3 system, which includes several stable compounds, as well as the high volatility of Bi_2O_3 at temperatures above the melting point [14] and the thermodynamic instability of $BiFeO_3$ in air in the absence of an equilibrium melt [15]. A comparison of literature data [13,16,17] indicates that obtaining single-phase $BiFeO_3$ by solid-phase synthesis is practically impossible.

In recent years, considerable attention has been paid to solution combustion synthesis (SCS) methods based on the exothermic reaction between metal nitrates and organic fuels (glycine, urea, citric acid, etc.) [18,19]. These methods allow the production of nanodispersed powders in a short time at temperatures of 500÷600 °C. However, the unevenness of the thermal field and the rapid evolution of gases lead to the formation of a porous structure and secondary phases, as well as to contamination of the product with carbon residues [20,21].

An alternative approach to synthesizing oxide materials is the use of concentrated solar radiation (CSR). The use of a solar furnace provides local heating up to 2000÷2500 °C and a heating rate up to 200 °C/s, enabling melting and crystallization without external fuel [22, 23]. In [24], it was shown that melting the oxide precursors Bi_2O_3 and Fe_2O_3 at the focus of a solar furnace leads to the formation of dense, homogeneous $BiFeO_3$ structures with a low coefficient of thermal expansion and high chemical resistance. Solar synthesis is environmentally friendly, highly energy-efficient, and allows the production of materials with minimal secondary-phase content [25].

Cite as: M.S. Payzullakhanov, F.A. Giyasova, M.A. Yuldoshev, Ch.X. Toshpulatov, R.U. Ernazarov, F.A. Giyasov, A. Urishev, A.D. Paluanova, East Eur. J. Phys. 1, 233 (2026), https://doi.org/10.26565/2312-4334-2026-1-25

As a result of the above, traditional methods for synthesizing bismuth ferrite – both thermal (solid-phase reactions at temperatures below the melting point) and chemical (solution reactions) – fail to produce single-phase $BiFeO_3$. Therefore, the use of solar technologies based on exposure to concentrated, high-density light is of scientific interest. In this approach, synthesis is performed from a melt formed under the influence of concentrated solar radiation, where phase formation occurs directly in the melt, and the resulting state is fixed by quenching.

Combining fuel precursors with high-energy solar heating opens the prospect of creating next-generation multiferroic materials. This approach combines the chemical homogeneity of the precursors with the high thermal efficiency of a solar furnace, facilitating the formation of dense single-phase structures with improved physical, mechanical, and functional properties. This study examines the influence of concentrated solar radiation parameters and the composition of fuel precursors on the structure formation, phase composition, and properties of bismuth ferrite ($BiFeO_3$).

The aim of this study is to determine the effect of pre-melting Bi_2O_3 and Fe_2O_3 oxides in a solar furnace on the structure formation, phase composition, and properties of $BiFeO_3$, and to compare the results with traditional solid-phase synthesis to optimize the conditions for producing a single-phase material.

EXPERIMENTAL SAMPLES AND MEASUREMENT METHODS

To determine the influence of the microstructural state of the components (Bi_2O_3 and Fe_2O_3 oxides) on the synthesis process and properties of bismuth ferrite, the starting components were melted in a small-sized solar installation — a small solar furnace (SSF) with a high degree of concentration [26]. The technological route included the following operations: grinding of the starting components → mixing → molding → melting → quenching. The density of the concentrated flux was 450 W/cm², enabling local heating of the sample to temperatures exceeding the melting points of the components. The exposure in the molten state was 15 minutes, which contributed to the complete homogenization of the oxide mass. The resulting melts were quenched in water at a cooling rate of about 10^4 °C/s, thereby fixing the system's nonequilibrium state and preventing phase separation.

The solidified samples were ground in a ball mill under wet conditions for 10 hours at a material:water:grinding media weight ratio of 1:1:1. After grinding, the powder was sieved through a 0.05 mm sieve to ensure a uniform particle size distribution. A Bi_2O_3+Fe_2O_3 mixture was prepared from the resulting fused oxides in a strictly stoichiometric ratio corresponding to the $BiFeO_3$ composition. The prepared powder was pressed into tablets under a 1-ton load on a C-100 hydraulic press. The resulting pressed samples were heat-treated in a resistance electric furnace with silicate heaters at various temperatures. These samples were designated as type A.

For comparative analysis, bismuth ferrite was also synthesized without the solar melting step, directly from the starting mixture of Bi_2O_3 and Fe_2O_3 oxides. The resulting samples, which underwent standard heat treatment, were designated type B and used as controls.

In this study, modern physicochemical methods were used to analyze the pyroxene materials, ensuring high accuracy and minimal error in the comprehensive assessment of their properties. The phase and thermal characteristics of oxide systems and man-made rock waste were investigated using differential thermal analysis (DTA) and thermogravimetric analysis (TGA). Experiments were conducted on a Q-1500 D derivatograph in the temperature range of 100÷1000 °C at a heating rate of 15°C/min. This allowed for simultaneous recording of mass changes and thermal effects, as well as identification of the nature of phase transformations, dehydration processes, and thermal decomposition of the studied samples.

To identify the phase composition, X-ray diffraction (XRD) was performed on a DRON-3M diffractometer with a copper anode (CuKα radiation).

The physical characteristics of the samples were assessed using density parameters. The apparent density (ρ_{app}) was determined by hydrostatic weighing in octane, and the X-ray density (ρ_x) was calculated using the expression [27]:

$$\rho_x = 1.66 \times M / V, \quad (1)$$

where, M is the mass of the formula unit (g), V is the volume of the unit cell of the perovskite structure (Å^3).

Relative density (ρ_{rel}) was calculated as the ratio $\rho_{kak}/\rho_x p$, expressed as a percentage:

$$\rho_{rel} = (\rho_{app} / \rho_x) \times 100\%. \quad (2)$$

To assess the packing density of the crystal lattice, the structural looseness parameter (ω) was additionally calculated using the formula [28]:

$$\omega = M / (n\rho), \quad (3)$$

where, M is the molecular mass of the compound, n is the number of structural units (atoms, ions or complexes) in the formula cell, ρ is the density of the material.

RESULTS AND DISCUSSION

The DTA curves of a mixture of bismuth and iron oxides (Bi_2O_3 + Fe_2O_3), obtained for samples subjected and not subjected to melting in a solar furnace, in the temperature range of 100÷1000 °C, are shown in Fig. 1.

As is well known, such m-n-n^+-m structures are often used to study transient effects and rectification characteristics.

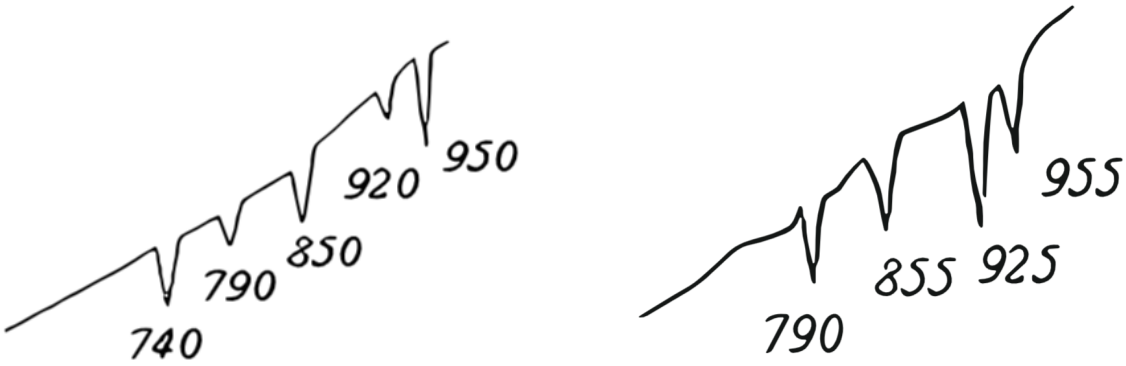

a b

Figure 1. DTA of a Bi_2O_3 + Fe_2O_3 mixture in the temperature range of100÷1000°C
a) components not subjected to melting in a solar furnace; b) components melted in a solar furnace

From Fig. 1a, it follows that in the first case five endothermic peaks are recorded on the DTA curve, the nature of the dependence indicating the sequential occurrence of a number of endothermic processes as the temperature increases. The endothermic effect observed at a temperature of about 740 °C corresponds to the polymorphic transformation of bismuth oxide (Bi_2O_3) – the transition of the low-temperature β-modification to the high-temperature δ-form, which is consistent with the literature data [4, 29] on the behavior of this compound upon heating. At ~790 °C, an endothermic peak is observed, associated with the melting of the eutectic mixture in the Bi_2O_3-Fe_2O_3 system and the onset of interaction of oxides with the formation of primary $BiFeO_3$ crystals. A further increase in temperature to ~850 °C is accompanied by intense formation of the $BiFeO_3$ phase due to the activation of diffusion processes between the melt components. At temperatures of 920÷950 °C, endothermic effects are observed, indicating the decomposition of bismuth ferrite with the formation of secondary phases, mainly $Bi_2Fe_4O_9$ and $Bi_{25}FeO_{39}$. The results of thermal analysis show that the synthesis of bismuth ferrite ($BiFeO_3$) from the initial mixture of Bi_2O_3 and Fe_2O_3 oxides begins in the range of 790÷850 °C, while the thermal stability of the resulting compound is maintained up to approximately 920 °C, after which its partial decomposition begins [30].

A comparison of the obtained thermograms (Fig. 1 a and b), reveals the influence of preliminary melting of the oxide precursors on the thermal behavior of the Bi_2O_3-Fe_2O_3 system. While the mixture that has not been subjected to solar melting is characterized by a sequential occurrence of endothermic processes with pronounced decomposition of bismuth ferrite at temperatures above 900 °C, in the case of pre-melted components, a shift in the temperature effects and a decrease in their intensity are observed. This indicates a change in the mechanism of oxide interaction and an increase in the stability of the resulting $BiFeO_3$ phase [31–33].

Fig. 1b shows the DTA curve of a mixture of bismuth and iron oxides (Bi_2O_3+Fe_2O_3), pre-melted in a solar furnace, recorded in the temperature range of 100÷1000 °C. The nature of the thermogram differs significantly from the similar dependence for the initial unmelted components, which indicates a change in the physicochemical properties of the system under the influence of concentrated solar radiation. In the temperature range of about ~790 °C, a weak endothermic effect is observed, corresponding to the onset of interaction of the oxides, accompanied by activation of their surface and the nucleation of the bismuth ferrite phase $BiFeO_3$. A more intense endothermic peak at ~855 °C reflects the main stage of $BiFeO_3$ formation associated with the melting of the eutectic mixture and diffusion redistribution of the components [34,35]. The endothermic effects at 925 and 955 °C are due to the partial decomposition of $BiFeO_3$ with the formation of secondary phases $Bi_2Fe_4O_9$ and $Bi_{25}FeO_{39}$. However, the intensity of these effects is significantly lower than for unmelted samples, indicating an increase in the thermal stability of bismuth ferrite synthesized from the solar-melted mixture. The DTA results indicate that preliminary melting of the initial bismuth and iron oxides (Bi_2O_3 and Fe_2O_3) in a solar furnace promotes a more complete reaction of bismuth ferrite $BiFeO_3$ formation, as well as an increase in the stability of its phase over a wider temperature range. This is due to an increase in the chemical activity of the components after solar melting, which ensures more intense interaction between them [36]. Additionally, it was established that the endothermic effects corresponding to phase transformations shift to the region of higher temperatures by approximately 50 °C, which indicates an improvement in the thermodynamic stability of the system and the formation of a more stable $BiFeO_3$ structure.

Diffraction peaks in the range 2θ ≈ 20÷60°, characteristic of the perovskite-like structure of $BiFeO_3$, are shown in Fig. 2.

The X-ray diffraction pattern of bismuth ferrite $BiFeO_3$ synthesized at 885 °C shows phase X, corresponding to a solid solution of $Bi_2Fe_4O_9$, which is [Fe_2O_3 2$BiFeO_3$]. Bismuth ferrite was synthesized by a solid-phase reaction from the initial oxides Bi_2O_3 and Fe_2O_3. After mixing and molding, the samples were calcined at 885 °C for 2 hours. X-ray diffraction analysis was performed using CuKα radiation (λ=1.5406 Å) in the angular range 2θ=20÷60°. Interplanar distances were determined according to Bragg's law [37]:

$$d=\lambda/2\sin\theta, \quad (4)$$

The lattice parameters were calculated using the pseudocubic structure approximation:

$$a=d\,(h^2+k^2+l^2)^{1/2}, \quad (5)$$

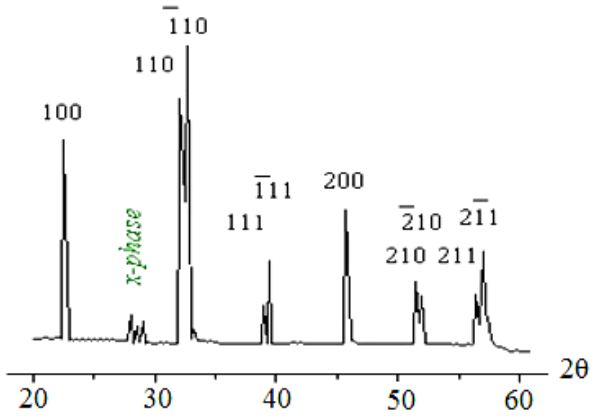

Figure 2. X-ray diffraction pattern of $BiFeO_3$ calcined at 885°C

The presence of narrow and distinct maxima indicates a high degree of crystallinity of the sample. In the range of angles 2θ=20÷60°, distinct and intense diffraction maxima are observed, corresponding to reflections from the planes (100), (110), (–110), (111), (–111), (200), (210), (–210), and (211). The set of registered reflections indicates the formation of a perovskite-like structure of bismuth ferrite with an orthorhombic distortion of the unit cell, belonging to the space group R3c. The calculated interplanar distances and lattice parameters are presented in Table 1.

Table 1. Lattice parameters of $BiFeO_3$ calcined at 885°C

Reflex (hkl)	2θ (°)	d (Å)	Pseudocubic constant a (Å)
(100)	22.6	3.931	3.931
(110)	31.6	2.829	4.001
(111)	39.8	2.263	3.920
(200)	46.5	1.964	3.928

Bismuth ferrite is characterized by an orthorhombic distortion of the perovskite cell [38] and temperature-dependent nonstoichiometry [39], which complicates the synthesis of a single-phase compound. In the studied sample, a high degree of crystallinity is achieved at a temperature of 885 °C, and a stable $BiFeO_3$ phase is formed without signs of secondary compounds. The average lattice parameter, calculated from the main diffraction peaks, is a=3.94±0.04 Å, which corresponds to the values characteristic of an orthorhombically distorted perovskite. The X-ray density of bismuth ferrite, calculated based on the structural parameters, is $\rho=8.39$ g/cm^3. The obtained data confirm the formation of phase-pure $BiFeO_3$ with a stable crystalline structure and a high degree of ordering of the atomic lattice.

The absence of additional reflections characteristic of Bi_2O_3, Fe_2O_3 oxides or $Bi_2Fe_4O_9$ phases indicates the formation of single-phase $BiFeO_3$. The presence of a weakly expressed signal, designated as the x-phase, may be associated with an insignificant content of the transition phase; however, its intensity is low and does not significantly affect the overall phase composition. The shape and width of the peaks indicate a high degree of crystallinity of the material. Narrow and symmetrical maxima reflect the growth of crystallites at the optimal synthesis temperature. The average crystallite size can be calculated using the Scherrer formula [40], where $K \approx 0.9$:

$$D = K\cdot L/\beta\cdot\cos\theta, \quad (6)$$

Experimental FWHM values (0.2±0.05°) were used to estimate the crystallite size, yielding an approximate size of D=40±10 nm.

These results indicate that at 885 °C, an optimal balance is achieved between the diffusion rate and the stability of the $BiFeO_3$ phase, ensuring the formation of a structurally ordered material without secondary phases.

The microstructure of $BiFeO_3$ heat-treated at 885 °C is shown in Fig. 3. Scanning electron microscopy (SEM) analysis indicates the formation of a fine-grained, porous structure characteristic of partially sintered perovskite materials.

As shown in Figure 3a, the type A sample exhibits a fine-grained, porous structure with an uneven particle distribution. The average grain size is 0.5÷1.5 μm, and they are agglomerated into larger conglomerates. The grains are predominantly rounded, have poorly defined grain boundaries, and a smooth surface without faceting, indicating incomplete completion of the crystallization and sintering processes. The microstructure contains micropores of 2÷3 μm in

size, distributed over the surface of the material. The presence of porosity and intergranular defects indicates limited crystallite growth under the given heat treatment conditions and is associated with insufficient temperature or duration of calcination, which prevents the formation of a dense polycrystalline matrix. This morphology can lead to a decrease in the density and electrical strength of the material, but simultaneously increases the number of interphase boundaries, which has a positive effect on the dielectric characteristics due to increased polarization in the grain boundary regions [41, 42]. In general, the type A microstructure reflects the early stage of $BiFeO_3$ sintering and is formed at relatively low temperatures, when diffusion processes are not yet sufficiently intense. However, the presence of pores negatively affects the density and electrical strength of the sample, which requires optimization of the synthesis temperature regime. Consequently, the type A $BiFeO_3$ microstructure is characterized by fine grain size, moderate porosity, and surface heterogeneity, indicating incomplete completion of the sintering and crystallization stages under the given heat treatment conditions [43].

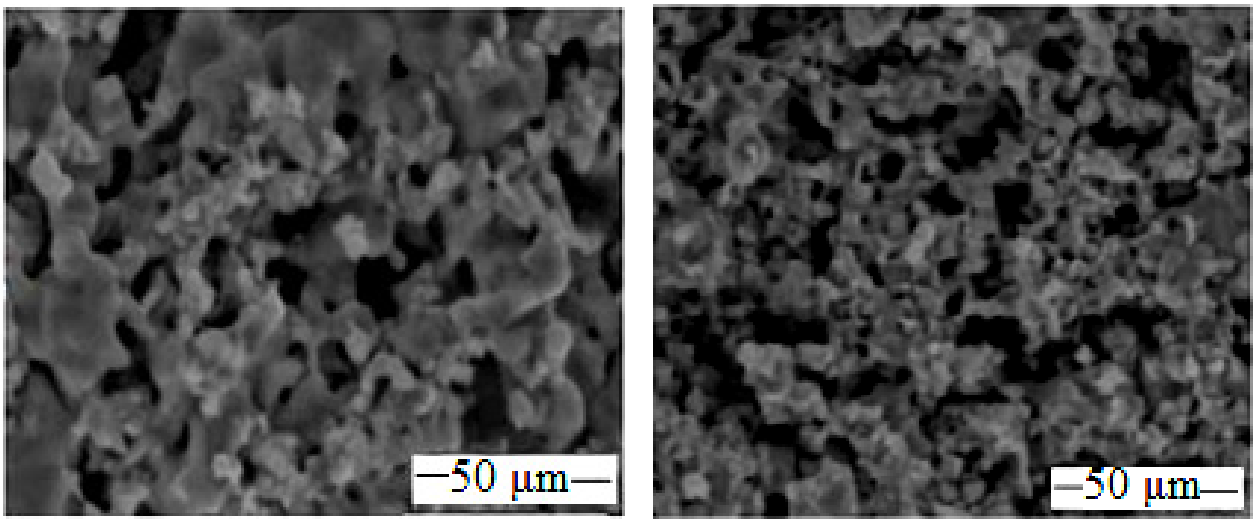

a b

Figure 3. SEM images of the $BiFeO_3$ microstructure surface:
a) type A; b) type B

The type B microstructure (Fig. 3b) has a denser and more uniform structure with clearly distinguishable grains. The average grain size increases to 1.5÷3.0 μm, indicating the occurrence of crystallite growth and coalescence processes. Pores are practically absent, the sample surface becomes smoother, and the grains form a compact matrix. This microstructure is formed at higher heat treatment temperatures, ensuring complete sintering and improved physical and mechanical properties [44]. Comparative analysis shows that an increase in the synthesis temperature promotes grain coarsening and decreases porosity, which is associated with the activation of diffusion processes in the solid phase. The evolution of the microstructure from type A to type B reflects the transition from a partially sintered state to a dense polycrystalline structure characteristic of the thermodynamically stable $BiFeO_3$ phase. Such changes have a direct impact on the functional properties of the material – an increase in density and grain size can contribute to an increase in electrical conductivity and a reduction in dielectric losses.

The values of apparent density (ρ_{app}), porosity (P), relative density (ρ_{rel}), structural looseness (ω), and the coefficient of linear thermal expansion (α) for two types of ceramic bismuth ferrite samples prepared from different starting components and synthesized by different methods are given in Table 2.

Table 2. Density and thermal parameters of ceramic bismuth ferrite samples

Samples	P_{app}, g/cm^3	P, %	P_{rel}, %	ω	α.10^6, K^{-1}
A-type	5.40	36	64.36	7.36	13.4
B-type	4.87	42	58.04	11.44	11.9

Type A samples exhibit higher apparent density (5.40 g/cm³) and relative density (64.36%) compared to type B samples (4.87 g/cm³ and 58.04%). Accordingly, the porosity of sample A is lower (36%) compared to B (42%), and the structural looseness is also lower and is 7.36 compared to 11.44. The difference in the structural looseness of the samples is due to the fact that the preliminary melting of oxides in a solar furnace promotes the formation of bismuth ferrite with a denser and more uniform crystalline structure, which is confirmed by the increased density and uniform microstructural structure of type A samples. The coefficient of linear thermal expansion α for samples A is higher (13.4×10^{-6} K^{-1}) than for samples B (11.9×10^{-6} K^{-1}). This is due to lower porosity and a denser crystalline structure, which ensures more pronounced thermal mobility of the lattice upon heating [45, 46]. It should be noted that the sintering of bismuth ferrite is somewhat improved when it is synthesized from pre-melted oxides. The processing of the starting components has a significant impact on the density characteristics and thermal stability of $BiFeO_3$ ceramic samples, which should be taken into account when developing materials with specified physical and mechanical properties [47-49].

Data on the phase composition of bismuth ferrite obtained from Fe_2O_3 and Bi_2O_3 oxides with different pre-treatments are given in Table 3.

Table 3. Results of bismuth ferrite synthesis depending on the pre-treatment of Fe_2O_3 and Bi_2O_3 components

Pretreatment of Fe_2O_3 and Bi_2O_3 components	Technological mode	Phase composition, %	
		$BiFeO_3$	$Bi_2Fe_4O_9$
not melted in a solar furnace	885 ^{0}C, 5 hours	88	12
melted in a solar furnace		97	3

The data show that the samples synthesized from molten oxides contain significantly less $Bi_2Fe_4O_9$ impurity phase (3%), whereas in the samples obtained from unmelted oxides, the content of the impurity phase reaches 12%. This difference may be due to the increased reactivity of the molten oxides, which accelerates the formation of the main $BiFeO_3$ phase and simultaneously promotes the appearance of the $Bi_2Fe_4O_9$ impurity phase at a lower temperature [50]. Preliminary melting of the oxides in a solar furnace ensures the formation of bismuth ferrite with a higher degree of purity and a smaller amount of secondary phases during synthesis at 885 °C for 5 hours. These results indicate the importance of choosing the form of the starting components for the synthesis of $BiFeO_3$ with high phase purity, which is important for optimizing the physical and chemical properties of the resulting material.

CONCLUSIONS

The conducted studies have shown that the thermal behavior of the Bi_2O_3-Fe_2O_3 system and the formation of bismuth ferrite depend significantly on the pretreatment of the starting oxides. It was found that the synthesis of $BiFeO_3$ from the starting materials begins at 790-850 °C, while its decomposition occurs at temperatures above ~920 °C. Preliminary melting of the oxides in a solar furnace leads to a shift in the thermal effects to higher temperatures and an increase in the thermodynamic stability of the resulting phase. X-ray diffraction analysis of samples calcined at 885 °C confirmed the formation of a perovskite-like structure with orthorhombic distortion and a high degree of crystallinity. The calculated lattice parameters and X-ray density correspond to the values for stable $BiFeO_3$, and the absence of reflections from secondary phases indicates the production of a phase-pure material. The average crystallite size, determined using the Scherrer formula, was 40±10 nm, which confirms the nanocrystalline nature of the formed structure.

Microstructural analysis revealed differences between samples obtained from molten and unmelted oxides. Type A material is characterized by a fine-grained, porous structure corresponding to the early stage of sintering, while type B samples exhibit a dense, homogeneous polycrystalline matrix with coarse grains. These differences are consistent with the density characteristics: type A samples have lower porosity and higher density. Phase analysis confirmed that the use of pre-melted oxides increases the content of the main $BiFeO_3$ phase to 97 % and reduces the proportion of the $Bi_2Fe_4O_9$ impurity phase. This is due to the increased reactivity of the oxides after solar melting and more complete solid-phase interaction.

Thus, solar pre-melting of Bi_2O_3 and Fe_2O_3 oxides is an effective technological approach that significantly increases the phase purity, crystallinity, and structural homogeneity of bismuth ferrite, as well as improves its physicochemical and functional properties. The obtained results confirm the potential of this method for creating high-quality $BiFeO_3$-based ceramic materials.

ORCID

Feruza A. Giyasova, https://orcid.org/0000-0003-0746-4986; **Murodjon A. Yuldoshev,** https://orcid.org/0000-0002-9722-9439
Farkhod A. Giyasov, https://orcid.org/0009-0003-9882-0655

REFERENCES

[1] Shuai Dong, Hongjun Xiang and Elbio Dagotto, "Magnetoelectricity in multiferroics: a theoretical perspective," National Science Review, **6,** 629-641 (2019). https://doi.org/10.1093/nsr/nwz023
[2] Sh.B. Utamuradova, Z.T. Azamatov, A.I. Popov, M.R. Bekchanova, M.A. Yuldoshev, and A.B. Bakhromov, East Eur. J. Phys. (3), 278 (2024). https://doi.org/10.26565/2312-4334-2024-3-27
[3] Yu. Gao, M.Yu. Gao, and Yu. Lu, "Two-dimensional multiferroics," Nanoscale, **13**, 19324-19340, (2021). https://doi.org/10.1039/d1nr06598j
[4] G. Catalan, and J.F. Scott, "Physics and Applications of Bismuth Ferrite," Advanced Materials, **21**(24), 2453-2556, (2009). https://doi.org/10.1002/adma.200802849
[5] B. Xu, D. Wang, J. Íñiguez, and L. Bellaiche, "Finite-Temperature Properties of Rare-Earth-Substituted $BiFeO_3$ Multiferroic Solid Solutions," Advanced Functional Materials, **25**(4), 497-650 (2015). https://doi.org/10.1002/adfm.201403811
[6] S. Zheng, J. Wang, J. Zhang, H. Ge, Z. Chen, and Y.F. Gao, "The structure and magnetic properties of pure single phase $BiFeO_3$ nanoparticles by microwave-assisted sol-gel method," Journal of Alloys and Compounds, **735**, 945-949, (2018). https://doi.org/10.1016/j.jallcom.2017.10.133
[7] S.F. Samadov, N.V.M. Trung, A.A. Sidorin, S.I. Ibragimova, S.H. Jabarov, M.A. Yuldoshev, O.S. Orlov, Y.I. Aliyev, Micro and Nanostructures 209 (2026) 208451, (2026). https://doi.org/10.1016/j.micrna.2025.208451

[8] A. Perejón, E. Gil-González, P.E. Sánchez-Jiménez, A.R. West, and L.A. Pérez-Maqueda, "Electrical properties of bismuth ferrites: $Bi_2Fe_4O_9$ and $Bi_{25}FeO_{39}$," Journal of the European Ceramic Society, **39**(2-3), 330-339 (2019). https://doi.org/10.1016/j.jeurceramsoc.2018.09.008
[9] A. Kirsch, G.B. Strapasson, N.L.M. Gogolin, M.C. Videbæk, S. Banerjee, H.N. Bordallo, and K.M. Ø. Jensen, "Control of Crystallization Pathways in the $BiFeO_3$-$Bi_2Fe_4O_9$ System," Chem. Mater. **37**, 338-348, (2025). https://doi.org/10.1021/acs.chemmater.4c02656
[10] A. Makridis, E. Myrovali, D. Sakellari, and M. Angelakeris, "Tuning the Structural and the Magnetic Properties of $BiFeO_3$ Magnetic Nanoparticles," Physica status solidi (b), **257**(6), (2020). https://doi.org/10.1002/pssb.202000005
[11] A.G. Monteduro, S.R.Ch. Leo, Sh. Karmakar, F. Sirsi, A. Leo, V. Tasco, M. Esposito, *et al*., "Dielectric and Ferroelectric Response of Multiphase Bi-Fe-O Ceramics," Physica status solidi (a), Vol. 216, Issue **3,** (2019). https://doi.org/10.1002/pssa.201800584
[12] G. Clarke, A. Rogov, S. McCarthy, L. Bonacina, Yu. Gun'ko, Ch. Galez, R.Le. Dantec, *et al*., "Preparation from a revisited wet chemical route of phase-pure, monocrystalline and SHG-efficient $BiFeO_3$ nanoparticles for harmonic bio-imaging," Scientific Reports, **8**, 10473 (2018). https://doi.org/10.1038/s41598-018-28557-w
[13] S.M. Selbach, M.A. Einarsrud, and T. Grande, "On the Thermodynamic Stability of $BiFeO_3$," Chemistry of Materials, **21**(1), 169-173 (2009). https://doi.org/10.1021/cm802607p
[14] F. Schröder, N. Bagdassarov, F. Ritter, and L. Bayarjargal, "Temperature dependence of Bi_2O_3 structural parameters close to the α-δ phase transition," Phase Transitions, **83**(5), 311-325 (2010). https://doi.org/10.1080/01411591003795290
[15] C. Wesley, L. Bellcase, J.S. Forrester, E.C. Dickey, I.M. Reaney, and J.L. Jones, "Solid state synthesis of $BiFeO_3$ occurs through the intermediate $Bi_{25}FeO_{39}$ compound," Journal of the American Ceramic Society, (2023). https://doi.org/10.1111/jace.19702
[16] R. Palai, R.S. Katiyar, H. Schmid, P. Tissot, S.J. Clark, J. Robertson, S.A. T. Redfern, *et al*., "β phase and γ-β metal-insulator transition in multiferroic $BiFeO_3$," Phys. Rev. B, **77**, 014110 (2008). https://doi.org/10.1103/PhysRevB.77.014110
[17] W. Song, D. Zhang, Z. Sun, B. Han, L.-J. He, and X. Wang, "Preparation and characterization of multiferroic $BiFeO_3$," in: *IEEE 10th International Conference on the Properties and Applications of Dielectric Materials*, (2012). https://doi.org/10.1109/ICPADM.2012.6318899
[18] A. Varma, A.S. Mukasyan, A.S. Rogachev, and K.V. Manukyan, "Solution Combustion Synthesis of Nanoscale Materials," Chem. Rev. **116**, 14493-14586, (2016). https://doi.org/10.1021/acs.chemrev.6b00279
[19] F. Siddique, S. Gonzalez-Cortes, A. Mirzaei, T. Xiao, M.A. Rafiq, and X. Zhang, "Solution combustion synthesis: the relevant metrics for producing advanced and nanostructured photocatalysts," Nanoscale, **14**, 11806-11868 (2022). https://doi.org/10.1039/D2NR02714C
[20] N. Asefi, M. Hasheminiasari, and S.M. Masoudpanah, "Photocatalytic properties of $BiFeO_3$ powders synthesized by the mixture of CTAB and Glycine, Scientific Reports, **13**, 12338 (2023). https://doi.org/10.1038/s41598-023-39622-4
[21] M.M. Suleimanova, M.U. Nosirova, H.T. Yusupov, and Kh.Yu. Rakhimov, "Wave-packet dynamics in monolayer graphene with periodic scattering potentials," Physica B: Condensed Matter, **714**, 417484 (2025). https://doi.org/10.1016/j.physb.2025.417484
[22] J. Rodriguez, I. Cañadas, and E. Zarza, "New PSA high concentration solar furnace SF40," AIP Conf. Proc. **1734**, 070028 (2016). https://doi.org/10.1063/1.4949175
[23] L.G. Rosa, "Solar Heat for Materials Processing: A Review on Recent Achievements and a Prospect on Future Trends," Chem. Engineering, **3**, 83 (2019). https://doi.org/10.3390/chemengineering3040083
[24] Y. Zhuang, X. Pan, X. Liu, and K. Chen, "Effect of Cooling Rate on the Crystalline Morphology of Bi_2O_3-Fe_2O_3 Pseudo-Binary System," Physica status solidi (a), **220**(9), (2023). https://doi.org/10.1002/pssa.202200838
[25] G. Levêque, R. Bader, W. Lipinski, and S. Haussener, "High-flux optical systems for solar thermochemistry," Solar Energy, **156**, 133-148 (2017). https://doi.org/10.1016/j.solener.2017.07.046
[26] M.S. Paizullakhanov, R.Yu. Akbarov, Zh.Z. Shermatov, O.T. Razhamatov, F. Ernazarov, M. Sulaimanov, N. Karshieva, *et al.*, "Small solar furnace for processing and melting of materials," in: *Collection of materials of the international scientific and technical conference "Actual problems of the energy complex: production, transmission and ecology*," (Karshi, 2024), pp. 533-538.
[27] V. Nicola, Y. Scarlett, and I.C. Madsen, "Quantification of phases with partial or no known crystal structures," Powder Diffraction, **21**(4), 278–284 (2016). https://doi.org/10.1154/1.2362855
[28] H.T. Costi, R. Dall'Agnol, M. Pichavant, and O.T. Ramo, "The peralkaline tin-mineralized madeira cryolite albite-rich granite of Pitinga, Amazonian craton, Brazil: petrography, mineralogy and crystallization processes," The Canadian Mineralogist, (2009). https://doi.org/10.3749/canmin.47.6.1301
[29] M.S. Paizullakhanov, and I.G. Atabaev, "BiFeO Synthesized on the Solar Furnace," Materials Research Letters, **1**(2), 1-4 (2017).
[30] M.S. Bernardo, "Synthesis microstructure and properties of $BiFeO_3$-based multiferroic materials: A review," Boletin de la Sociedad Espanola de Ceramica y Vidrio, **53**(1), 1-14, (2014). https://doi.org/10.3989/cyv.12014
[31] R. Haumont, I.A. Kornev, S. Lisenkov, L. Bellaiche, J. Kreisel, and B. Dkhil, "Phase stability and structural temperature dependence in powdered multiferroic $BiFeO_3$," Phys. Rev. B, **78**, 134108 (2008). https://doi.org/10.1103/PhysRevB.78.134108
[32] M.S. Paizullakhanov, A.A. Xolmatov, and M.M. Sobirov, "Magnetic materials synthesized in the sun furnace," International Journal of Advanced Research in Science, Engineering and Technology, **7**(4), 13499-13505 (2020).
[33] Kh. Bakhronov, O. Ergashev, G'. Ochilov, N. Esonkulova, A. Ganiev, N. Akhmedova, and O. Ochilova, "Study of isotherm, thermodynamic characteristics and sorption mechanism of toluene adsorption on zeolite CsZSM-5 by adsorption-calorimetric method. Edelweiss Applied Science and Technology, **8**(6), 6959-6966 (2024). https://doi.org/10.55214/25768484.v8i6.3508
[34] C.M. Suarez, S. Hernández, and N. Russo, "$BiVO_4$ as photocatalyst for solar fuels production through water splitting: A short review," Applied Catalysis A General, **504**, (2014). https://doi.org/10.1016/j.apcata.2014.11.044
[35] J. Matrasulov, J.R. Yusupov, and A.A. Saidov, "Fast forward evolution in heat equation: Tunable heat transport in adiabatic regime," Nanosystems: Phys. Chem. Math. **14**(4), 421-427 (2023). https://doi.org/10.17586/2220-8054-2023-14-4-421-427
[36] O.R. Furtado, "Metal oxides and the thermochemical storage of solar energy," in: Chimica Oggi - Chemistry Today, **37**(2), 6-18 (2019). http://hdl.handle.net/10400.9/3187

[37] H. Liu, and X. Yang, "Structural, dielectric, and magnetic properties of $BiFeO_3$ -$SrTiO_3$ solid solution ceramics," Ferroelectrics, **500**(1), 310-317 (2016). https://doi.org/10.1080/00150193.2016.1230445
[38] M.A. Rusho, T.A. Ahmed, L.H. Saleh, S.W. Ghori, E. Muniyandy, S. Usanov, M. Latipova, *et al.*, "Design and synthesis of decorated palladium nanoparticles on chitosan-tannic acid modified magnetic nanoparticles and evaluation of its catalytic application in the Heck coupling reactions," Journal of Organometallic Chemistry, **1039**, 123773 (2025). https://doi.org/10.1016/j.jorganchem.2025.123773
[39] N. Lomanova, M.V. Tomkovich, V.V. Sokolov, and V.V. Gusarov, "Special features of formation of nanocrystalline $BiFeO_3$ via the glycine-nitrate combustion method," Russian Journal of General Chemistry, **86**(10), 2256-2262 (2016). https://doi.org/10.1134/S1070363216100030
[40] B. Wang, and D.A. Hall, "Structural evolution in $BiFeO_3$-$BaTiO_3$ ceramics via quenching strategy," Journal of Alloys and Compounds, **1044**, 184439 (2025). https://doi.org/10.1016/j.jallcom.2025.184439
[41] Z. Zeng, Q. Zhang, H. Wu, and M. Lan, "Influence of calcination temperature on structure and multiferroic properties of barium ferrite ceramics," Processing and Application of Ceramics, **16**(2), 106-114 (2022). https://doi.org/10.2298/PAC2202106Z
[42] Sh.B. Utamuradova, F.A. Giyasova, K.N. Bakhronov, M.A. Yuldoshev, M.R. Bekchanova, and B. Ismatov, "Current Transfer Mechanism in A Thin-Based Heterosystem Based on A^2B^6 Compounds," East Eur. J. Phys. (3), 325-335 (2025). https://doi.org/10.26565/2312-4334-2025-3-31
[43] Z. Cen, Y. Huabin, C. Zhou, and Q. Zhou, "Effect of sintering temperature on microstructure and piezoelectric properties of Pb-free $BiFeO_3$-$BaTiO_3$ ceramics in the composition range of large $BiFeO_3$ concentrations," Journal of Electroceramics, **31**(1-2), (2013). https://doi.org/10.1007/s10832-013-9803-2
[44] D. Szalbot, J.A. Bartkowska, K.Feliksik, and M. Bara, "Correlation Between Structure, Microstructure and Dielectric Properties of $Bi_7Fe_3Ti_3O_21$ Ceramics Obtained in Different Conditions," Archives of Metallurgy and Materials, **65**(2), 879 (2020). https://doi.org/10.24425/amm.2020.132834
[45] E. Gil-Gonzalez, A. Perejon, P.E. Sánchez-Jiménez, and M.J. Sayagues, "Phase-pure $BiFeO_3$ produced by reaction flash-sintering of Bi_2O_3 and Fe_2O_3," Journal of Materials Chemistry A, **6**(13), (2017). https://doi.org/10.1039/C7TA09239C
[46] F.A. Giyasova, and M.A. Yuldoshev, "Investigation of temporal characteristics of photosensitive heterostructures based on gallium arsenide and silicon," Chalcogenide Letters, 22(2), 123–129 (2025). https://doi.org/10.15251/CL.2025.222.123
[47] F.A. Giyasova, Kh.N. Bakhronov, M.A. Yuldoshev, I.B. Sapaev, R.G. Ikramov, F.A. Giyasov, M.R. Bekchanova, M.M. Qaxxarov, H.O Abdullayev, East Eur. J. Phys. 4, 461 (2025). https://doi.org/10.26565/2312-4334-2025-4-47
[48] F.A. Giyasova, A.Z. Rakhmatov, Kh.N. Bakhronov, M.A. Yuldoshev, F.A. Giyasov, A.N. Olimov, N.A. Sattarov, East Eur. J. Phys. 4, 397 (2025). https://doi.org/10.26565/2312-4334-2025-4-38
[49] N.Yu. Sharibaev, A.Q. Ergashov, S.B. Fazliddinov, R.G. Ikramov, M.A. Yuldoshev, A.A. Abdulxayev, Journal of Ovonic Research. Vol.21, No.6, (2025). https://doi.org/10.15251/JOR.2025.216.859
[50] C. Wesley, L. Bellcase, J.S. Forrester, E.C. Dickey, I.M. Reaney, and J.L. Jones, "Solid state synthesis of $BiFeO_3$ occurs through the intermediate $Bi_{25}FeO_{39}$ compound," Journal of the American Ceramic Society, **107**(6). 3716-3723 (2024). https://doi.org/10.1111/jace.19702

ОСОБЛИВОСТІ ТЕПЛОВОЇ ПОВЕДІНКИ ТА ФАЗОУТВОРЕННЯ $BiFeO_3$ З ВИКОРИСТАННЯМ ПРЕКУРСОРІВ АКТИВОВАНИХ СОНЯЧНИМ ПЛАВІННЯМ

М.С. Пайзуллаханов[1,2] Ф.А. Гіясова[3], М.А. Юлдошев[4], Ch.X. Тошпулатов[5], Р.У. Ерназаров[5], Ф.А. Гіясов[3], А. Урішев[6], А.Д. Палуанова[7]

[1]Інститут матеріалознавства Академії наук Республіки Узбекистан. Ташкент, Узбекистан
[2]Ферганський державний технічний університет, Узбекистан
[3]Міжнародний університет Кімьо в Ташкенті, Узбекистан
[4]Міжнародний університет Туран, Наманган, Узбекистан
[5]Ташкентський філіал Самаркандського державного університету ветеринарної медицини, тваринництва та біотехнології, Узбекистан
[6]Ташкентський інститут інженерів іригації та механізації сільського господарства, Національний дослідницький університет, Узбекистан
[7]Нукусський державний педагогічний інститут, Узбекистан

Досліджено вплив попередньої обробки оксидів Bi_2O_3 та Fe_2O_3 на синтез та структурні характеристики фериту вісмуту $BiFeO_3$. Було виявлено, що утворення $BiFeO_3$ починається при 790÷850 °C, а розкладання відбувається вище ~920 °C. Попереднє плавлення оксидів у сонячній печі зміщує теплові ефекти в бік вищих температур та підвищує термодинамічну стабільність фази. Рентгенофазовий аналіз виявив утворення перовскітоподібної структури з орторомбічним спотворенням, високою кристалічністю та розміром кристалітів 40±10 нм. Фазовий аналіз підтвердив збільшення вмісту основної фази до 97 % та зменшення домішкової фази $Bi_2Fe_4O_9$. Отримані результати підтверджують ефективність попереднього сонячного плавлення оксидів для синтезу високоякісних керамічних матеріалів на основі $BiFeO_3$.

Ключові слова: *сонячна піч; синтез; ферит вісмуту; фаза; дифузія; мікроструктура; аналіз; температура; тепловий ефект*

EAST EUROPEAN JOURNAL OF PHYSICS. 1. 241-246 (2026)
DOI:10.26565/2312-4334-2026-1-26 ISSN 2312-4334

INFLUENCE OF PbTe ADDITION ON THE ELECTRIC CHARGE AND HEAT TRANSPORT IN $AgSbSe_2$

A.A. Saddinova[1], R.I. Selim-zadeh[1], A.E. Babayeva[1], A.A. Orujova[2]
[1]Institute of Physics Ministry of Science and Education Republic of AzerbaijanAZ-1143, Azerbaijan
[2]Mingachevir State University, Az-4500, Azerbaijan
**Corresponding Author email: a.saddinova@physics.science.az*
Received November 30, 2025; revised January 9, 2026; in final form January 12, 2026; accepted January 30, 2026

The aim of this study is to investigate the influence of PbTe addition on the thermoelectric properties and band parameters of $AgSbSe_2$ at temperatures below room temperature. For this purpose, the polycrystalline $(AgSbSe_2)_x(PbTe)_{1-x}$ (x = 1; 0.9; 0.85) samples were prepared by direct fusion method. The temperature dependences of electrical conductivity, Seebeck coefficient, and thermal conductivity of $(AgSbSe_2)_x(PbTe)_{1-x}$ (x = 1; 0.9; 0.85) samples were investigated in the temperature range 80-350K. The value of electrical conductivity of PbTe added samples decreased compared to $AgSbSe_2$. Simultaneously, the inversion of the sign of Seebeck coefficient ($n \rightarrow p$) in $(AgSbSe_2)_x(PbTe)_{1-x}$ (x=0.9; 0.85) solid solutions at temperatures of T > 110K was observed. It was determined that the effective mass of holes value in $(AgSbSe_2)_x(PbTe)_{1-x}$ (x=0.9; 0.85) solid solutions increased compared to $AgSbSe_2$. It has been found that the lattice thermal conductivity of $(AgSbSe_2)_x(PbTe)_{1-x}$ (x=0.9; 0.85) solid solutions decreases significantly with increasing PbTe amount in $AgSbSe_2$.
Keywords: *Thermoelectric material;Electrical conductivity; Seebeck coefficient;Thermal conductivity;Effective mass*
PACS: 71.20.Nr, 72.20.Pa, 72.15.Eb

INTRODUCTION

Binary silver selenide and related ternary semiconductor materials have a number of valuable functional properties and are effective, environmentally friendly compounds. Based on these properties, these materials are intensively studied by many researchers [1-5].

A number of important functional properties of compounds with the general formula $A^IB^{IV}X^{VI}$ (A-Ag, Cu; B-Si, Ge, Sn; X-Se, S) have been extensively studied. In particular, numerous studies have been conducted on the photo-electrical properties of chalcogenide glasses containing Ag such as photodoping, photovoltage, and photochemical modification [6-9].

Among these functional properties, one of the most interesting is ionic conductivity. As is known, ionic conductors are promising materials for the preparation of ion batteries. Possible crystallochemical conditions for the formation of the superionic state have been shown in studies [10-18]. Many articles have provided detailed information on the ionic conductivity of binary compounds formed with Ag^+ and Cu^+ chalcogenides [19-21].

The ternary semiconductor $AgSbSe_2$ is considered a promising thermoelectric materials due to its thermoelectric properties, and particularly its very low lattice thermal conductivity [22, 23]. $AgSbSe_2$ features a strong anharmonic bonding arrangement associated with the Sb $5s^2$ lone pair, which leads to strong phonon-phonon interactions that reduce the lattice thermal conductivity [24]. Additionally, $AgSbSe_2$ is a narrow-bandgap semiconductor exhibiting p-type conductivity with a favourable valence-band structure composed of multiple flat valleys, potentially leading to a high effective mass of holes and thus the high value of the Seebeck coefficient. The band gap values of $AgSbSe_2$ measured by various methods are in the range of 0.3-1.1 eV [25-27]. This intrinsically low thermal conductivity and the appropriate electronic band structure make $AgSbSe_2$ a promising candidate for thermoelectric applications in the intermediate temperature range (500-700K) [28-30]. On the other hand, among the traditional thermoelectric materials, PbTe and its alloys are considered as excellent thermoelectric materials that operate in the medium and high temperature range (400 K - 800K) [31]. The crystal structure of I-V-VI_2 group compounds ($AgSbSe_2$, $AgSbTe_2$ etc.) is very similar to that of IV-VI group compounds (PbTe, PbSe, etc.) and all these compounds crystallize in NaCl structure. Therefore, these materials may be used to prepare solid solutions based on I-V-VI_2 group compounds [32, 33].

Investigations of $AgSbSe_2$ were mainly carried out above room temperature to enhance its thermoelectric properties [28-30]. Also, the kinetic properties of $AgSbSe_2$ and its solid solutions, their electronic structure, mechanisms of electric charge and heat transport have been little studied at low temperatures [34]. In this study, to address these questions experimentally, we synthesized $(AgSbSe_2)_x(PbTe)_{1-x}$ (x = 1; 0.9; 0.85) samples and investigated the influence of PbTe on the thermoelectric properties and band parameters of $AgSbSe_2$ at the temperature range of 80-350K.

EXPERIMENTAL METHOD

Synthesis. Polycrystalline $(AgSbSe_2)_x(PbTe)_{1-x}$ (x = 1; 0.9; 0.85) bulk samples were prepared using a direct fusion method together with mechanical pressing. The constituent elements Ag, Sb, Se, Pb, Te (99,99% purity) in stoichiometric ratios were sealed in evacuated quartz tubes under a pressure value of 10^{-4} Torr. The tubes were placed in furnace and

Cite as:A.A. Saddinova, R.I. Selim-zadeh, A.E. Babayeva, A.A. Orujova, East Eur. J. Phys. 1, 241 (2026), https://doi.org/10.26565/2312-4334-2026-1-26

heated slowly (1 K/min) up to 1000 K ($AgSbSe_2$ melting point: 908 K) over a period of 12 hours. Then tubes were maintained at this temperature for 10 hours and gradually cooled to room temperature at the same rate. The obtained ingots were ground into fine powders to eliminate pores. Then the powders were pressed (under a pressure of 500 MPa) to form bulk samples with dimensions of 12×5.2×2.4 mm^3.

Powder X-ray diffraction. Powder X-Ray diffraction (PXRD) analysis was conducted using a Bruker D8 Advance diffractometer with a CuKα anode (λ = 0.1542 nm), operating at 40 kV and 40 mA. The lattice constants were calculated using the Rietveld method with EVA and TOPAS software.

Carrier concentration. The values of carrier concentration and Hall mobility at room temperature were derived from Hall coefficient measurements using by the Van der Pauw method (in direct current and 0,32 T magnetic field) on the HL5500PC Hall Effect Measurement System.

Electrical transport. The thermoelectric properties were measured simultaneously from liquid nitrogen temperature to 350K in direct current using four-probe potentiometric method.

RESULTS AND DISCUSSION

Structural characterization

Figure 1 displays the PXRD patterns for $(AgSbSe_2)_x(PbTe)_{1-x}$ (x = 1; 0.9; 0.85) samples. The results of X-ray analysis revealed that all samples were single-phase with a cubic NaCl-type structure (Fm3m), with no impurity phases observed.

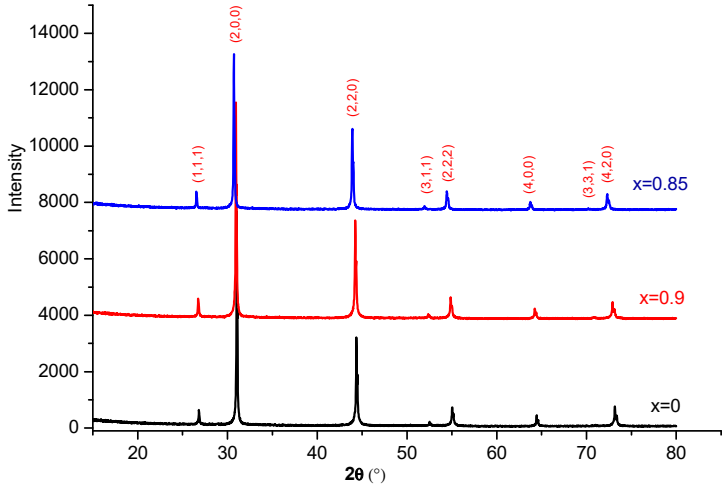

Figure 1. Powder XRD patterns of $(AgSbSe_2)_x(PbTe)_{1-x}$ (x = 1; 0.9; 0.85)

As seen in Figure 2, the linear expansion in the lattice constants with increasing PbTe concentrations follows the Vegard's law for the $(AgSbSe_2)_x(PbTe)_{1-x}$ (x = 1; 0.9; 0.85) samples. The ionic radius of Pb (Te) is larger than of Sb. Therefore, as larger Pb (Te) is introduced in the place of smaller Sb, the unit cell undergoes a systematic expansion, leading to an increase in the lattice parameter [29].

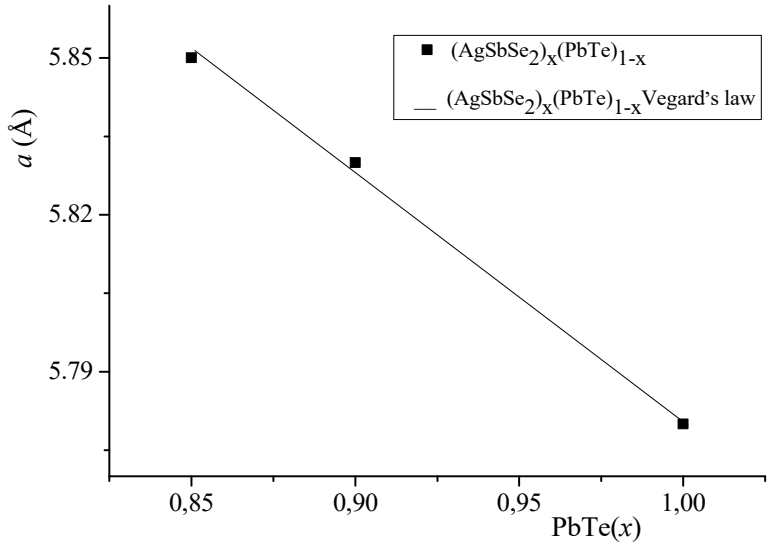

Figure 2. Composition (x) dependence of lattice constants for $(AgSbSe_2)_x(PbTe)_{1-x}$ (x = 1; 0.9; 0.85), and a straight line indicates Vegard's law for solid solution

Electrical transport properties

The temperature dependence of electrical conductivity (σ) of $(AgSbSe_2)_x(PbTe)_{1-x}$ (x=1; 0.9; 0.85) samples over the 80-350 K range is presented in Figure 3.

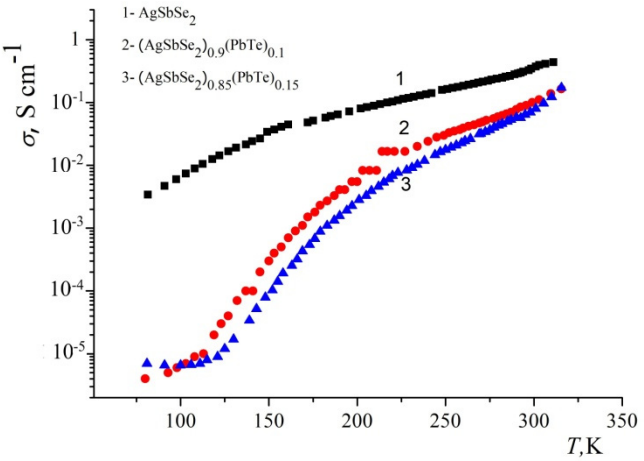

Figure 3. Temperature dependence of the electrical conductivity of $(AgSbSe_2)_x(PbTe)_{1-x}$ (x = 1; 0.9; 0.85) solid solutions

As observed in Fig. 3, the value of σ at below room temperatures is relatively small and exponentially increases with temperature. However, the value of electrical conductivity of all samples increases with rising temperature. Additionally, we observed a decrease in the electrical conductivity of PbTe added samples compared to $AgSbSe_2$. At room temperature, the measured values of σ for $(AgSbSe_2)_x(PbTe)_{1-x}$ (x = 1; 0.9; 0.85) solid solutions are 0.4 $S \cdot cm^{-1}$, 0.11 $S \cdot cm^{-1}$ and 0.09 $S \cdot cm^{-1}$, respectively.

The addition of PbTe to $AgSbSe_2$ lead to partial compensation of electroactive acceptor centers, resulting in a decrease in hole concentration p. Hall measurements at room temperature indicate positive sign of the Hall coefficient (R_H) for all samples. This indicates that the majority carriers are holes and the samples exhibit p-type conduction. The carrier concentrations of $(AgSbSe_2)_x(PbTe)_{1-x}$ (x=1; 0.9; 0.85) solid solutions, estimated from measurements of the R_H ($p=1/eR_H$, where e is the elementary charge) at room temperature, are $5.6 \cdot 10^{17}$ cm^{-3}, $4.8 \cdot 10^{16}$ cm^{-3} and $3.7 \cdot 10^{16}$ cm^{-3}, respectively. Furthermore, the addition of PbTe to $AgSbSe_2$most likely increases the number of defects in the crystal lattice. This leads to an increase in the scattering centers of charge carriers and, as a result, to a decrease in the Hall mobility μ ($\mu=\sigma/pe$). The Hall mobilities of $(AgSbSe_2)_x(PbTe)_{1-x}$(x=1; 0.9; 0.85) solid solutions at room temperature are 4.2 $cm^2/V \cdot s$, 3 $cm^2/V \cdot s$ and 2.3 $cm^2/V \cdot s$, respectively. Thus, we assume that these two factors together cause a decrease in the electrical conductivity of $(AgSbSe_2)_x(PbTe)_{1-x}$(x=0.9; 0.85) solid solutions.

The temperature dependence of the Seebeck coefficient (S) of $(AgSbSe_2)_x(PbTe)_{1-x}$ (x=1; 0.9; 0.85) solid solutions in the 80-350K range is presented in Figure 4.

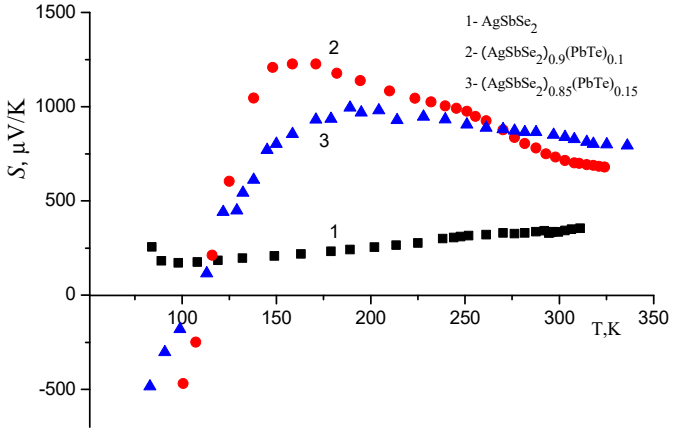

Figure 4. Temperature dependence of the Seebeck coefficient in $(AgSbSe_2)_x(PbTe)_{1-x}$ (x = 1; 0.9; 0.85) solid solutions

As is known, $AgSbSe_2$ is a p-type semiconductor [22-24]. As can be seen in Fig. 4, $AgSbSe_2$ exhibits p-type conductivity in the temperature range of 80-350K. However, in the $(AgSbSe_2)_x(PbTe)_{1-x}$ (x = 0.9; 0.85) solid solutions, the sign of the Seebeck coefficient is negative at temperatures below 110 K, indicating n-type conductivity. It is possible that the addition of PbTe to the $AgSbSe_2$ leads to the formation of shallow donor levels. The ionization of these donor centers leads to a significantly increase in the contribution of electrons in the Seebeck coefficient compared to $AgSbSe_2$.

Consequently, for $(AgSbSe_2)_x(PbTe)_{1-x}$ (x = 0.9; 0.85) solid solutions, the sign of Seebeck coefficient is negative at temperatures below 110K (Fig. 4). At T>110K the Seebeck coefficient changes its sign ($n \rightarrow p$) and becomes positive. Such a change of sign is also manifested at temperature dependence of Hall coefficient. The increase in hole concentration, most likely resulting from the ionization of deep acceptor centers as temperature rises, leads to the change in the sign of the Seebeck coefficient. Moreover, the values of Seebeck coefficient in $(AgSbSe_2)_x(PbTe)_{1-x}$ (x = 0.9; 0.85) solid solutions are larger than $AgSbSe_2$ (350 μV/K), at room temperature, and the values of S are 701 μV/K and 828 μV/K, respectively. The increase in the Seebeck coefficient for $(AgSbSe_2)_x(PbTe)_{1-x}$ (x=0.9; 0.85) solid solutions compared to $AgSbSe_2$ most probably may be explained by the increased density of states effective mass for holes $m^*_{h,dos}$. Assuming a single parabolic band model with acoustic phonon scattering (r=0, where r is scattering factor), we calculated the values of effective mass of holes m^*_p using the following equations (1)-(3) based on the values of S and hole concentrations p [35]:

$$p = \frac{(2m^*_p k_B T)^{3/2}}{3\pi^2\hbar^3} F_{3/2}(\eta^*) \quad (1)$$

$$m^*_p = \frac{(3\pi^2\hbar^3)^{3/2}}{2k_B T[F_{3/2}(\eta^*)]^{3/2}} \quad (2)$$

$$F_r(\eta) = \int_0^\infty \left(-\frac{\partial f_0}{\partial x}\right) x^r dx \quad (3)$$

where, η^* is the reduced Fermi energy, $F_r(\eta)$ - the r^{th}- order Fermi integral, k_B- the Boltzmann constant, $\hbar$ - the reduced Planck's constant ($\hbar=h/2\pi$), e- elementary charge.

From these calculations, the value of effective mass for holes m^*_p at room temperature for $(AgSbSe_2)_x(PbTe)_{1-x}$ (x=1; 0.9; 0.85) solid solutions were found to be $m^*_p = 0.13m_0$, $m^*_p = 3.82m_0$, and $m^*_p = 3.98m_0$, respectively. We suppose that with increasing temperatures, the high-density charge carriers resulting from the addition of PbTe into $AgSbSe_2$ may be redistributed among multiple energy states within the valence band. This could potentially lead to changes in the electronic band structure that could affect the material's properties. In work [36] the authors suggest that such redistribution of the density of states of charge carriers leads to an increase in the effective coverage of bands. An increase in the number of charge carriers in the multiple degenerate valence bands can cause a higher value of their density of states effective mass m^*. This, is in turn, lead to an increase in the Seebeck coefficient, since S is directly related to m^* by the equation of $S = \frac{8\pi^2 k_B^2}{3eh^2} m^* T \left(\frac{\pi}{3n}\right)^{2/3}$ [37]. Additionally, the increase in the values of m^*_p due to the amount of PbTe also results in decreased Hall mobility, leading to a decrease in the value of electrical conductivity (σ) in the $(AgSbSe_2)_x(PbTe)_{1-x}$ (x = 0.9; 0.85) solid solutions compared to the pristine $AgSbSe_2$ sample. This confirms earlier discussed results on electrical conductivity and Hall mobility.

We have also investigated the thermal conductivity (k) of the $(AgSbSe_2)_x(PbTe)_{1-x}$ (x = 1; 0.9; 0.85) solid solutions in the temperature range of 80-350K. The obtained result is shown in Figure 5.

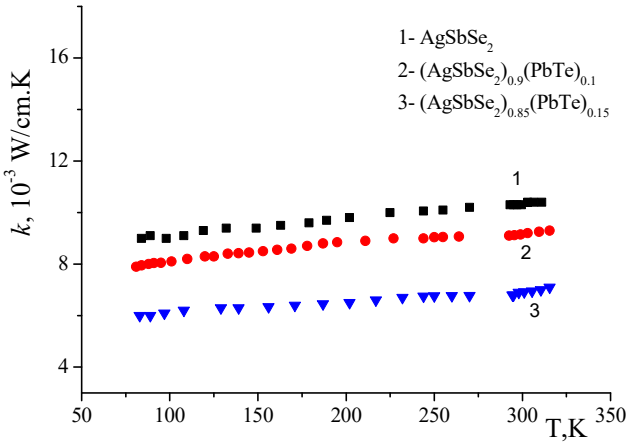

Figure 5. Temperature dependence of thermal conductivity of $AgSbSe_2$ and $(AgSbSe_2)_x(PbTe)_{1-x}$ (x = 0.9; 0.85) solid solutions

As can be seen from Fig 5, the values of thermal conductivity of $(AgSbSe_2)_x(PbTe)_{1-x}$ (x = 0.9; 0.85) significantly decreased compared to $AgSbSe_2$. We have calculated the electronic contribution in thermal conductivity k_{el} using the Wiedemann-Franz law: $k_{el}=L_0\sigma T$, where $L_0 = 2.44 \cdot 10^{-8}$ W·Ω/K^2 is Lorentz number [25], and, for all three samples, k_{el} is not more than 2%. The obtained lattice thermal conductivity k_{lat} values of $(AgSbSe_2)_x(PbTe)_{1-x}$ (x=1; 0.9; 0.85) are low and 0.85 W/m·K, 0.78 W/m·K and 0.57 W/m·K, respectively.

The main reason for the low thermal conductivity of $AgSbSe_2$ and other compounds of the I-V-VI_2 group is most likely the disorder of their structure [38]. Moreover, the point defects which exist in the crystal lattice and structural components may cause low thermal conductivity of $AgSbSe_2$. As mentioned above, $AgSbSe_2$ crystallize in disordered

NaCl type structure. In such structure, the random distribution of non-chalcogenide atoms may cause energetically favorable (Ag^{+}–Sb^{3+}) and unfavorable (Ag^{+}–Ag^{+} and Sb^{3+}–Sb^{3+}) states of Ag^{+} and Sb^{3+} ions in the Ag/Sb sublattice [39, 40]. Therefore, the presence of regions with orderly and disorderly distributions of Ag and Sb atoms in $AgSbSe_2$, high anharmonicity of the Sb-Se bonding arrangement [29], displacement of atoms and deformation of crystal lattice leads to the formation of phonon scattering centers. Consequently, the k_{lat} value decreases due to increasing phonons scattering.

Furthermore, it is known that silver chalcogenides are high-ionic-conductivity materials [41, 42]. The silver ions leave their positions as the temperature increases, and intensifying more energetically favorable state of the crystal lattice. As a result, the defects in the crystal structure insignificantly decrease and thermal conductivity slightly increase with rising temperature. Simultaneously, also this factor causes the distortion of the crystal lattice and as a result, the k_{lat} value decreases caused by increasing phonons scattering.

Thus, all mentioned above factors most probably collectively lead to a decrease of the k_{lat} value of $AgSbSe_2$ due to increasing phonons scattering. The addition of PbTe to $AgSbSe_2$ increases the disorder of the crystal lattice, which ultimately leads to a significant decrease in the lattice thermal conductivity in $(AgSbSe_2)_x(PbTe)_{1-x}$ (x=0.9; 0.85) solid solutions.

CONCLUSIONS

In summary, we observed that the electrical conductivity of $(AgSbSe_2)_x(PbTe)_{1-x}$ (x = 0.9; 0.85) solid solutions decreased compared to $AgSbSe_2$ in the 80-350 K temperature range. Simultaneously, the inversion of the sign of Seebeck coefficient ($n \rightarrow p$) of $(AgSbSe_2)_x(PbTe)_{1-x}$ (x=0.9; 0.85) at temperatures of T>110K occurred most likely due to the ionization of deep acceptor centers. Additionally, we observed higher values of the hole effective mass in $(AgSbSe_2)_x(PbTe)_{1-x}$ (x=0.9; 0.85) compared to $AgSbSe_2$, which is due to the increase in redistribution of the density of states of charge carriers in the multiple energy states of the valence band. This enhances the Seebeck coefficient value of $(AgSbSe_2)_x(PbTe)_{1-x}$ (x=0.9; 0.85) solid solutions. Moreover, the strong phonon-phonon interactions due to the high anharmonicity in the Sb-Se bonding arrangement, effective scattering of phonons by the disordered crystal lattice and point defects lead to the low lattice thermal conductivity k_{lat} of the $(AgSbSe_2)_x(PbTe)_{1-x}$ (x=0.9; 0.85) solid solutions compared to pristine $AgSbSe_2$.

The results obtained in this study provide directions for future research- including nanostructuring, doping, band convergence, and defect engineering to enhance the properties of thermoelectric materials.

Declarations

- Funding: The authors did not receive support from any organization for the submitted work.
- Financial interests: The authors have no relevant financial or non-financial interests to disclose.
- Conflict of interest: The authors declare that they have no conflict of interest.
- Author contribution: The authors contributed equally to this work.

Data Availability Statement

Due to privacy and ethical restrictions, the data used in this study cannot be shared publicly. However, the analyzed data are available to the researcher from the corresponding author on reasonable request with appropriate ethical approval.

ORCID

A.A. Saddinova, https://orcid.org/0009-0005-9967-3575; **R.I. Selim-zadeh,** https://orcid.org/0009-0007-3649-5390
A.E. Babayeva, https://orcid.org/0009-0001-0286-5783; **A.A. Orujova,** https://orcid.org/0009-0007-7254-9499

REFERENCES

[1] C. Yang, Y. Luo, Y. Xia, L. Xu, Z. Du, Z. Xan, X. Li, and J. Cui, ACS Appl. Mater. Interfaces. **13**(47), 56329 (2021). https://doi.org/10.1021/acsami.1c17548
[2] M. Jin, S. Lin, W. Li, Z. Chen, R. Li, X. Wang, Y. Chen, and Y. Pei, Chemistry of Materials, **31**(7), 2603 (2019). https://doi.org/10.1021/acs.chemmater.9b00393
[3] B. Jiang, P. Qiu, E. Eikeland, H. Chen, Q. Song, D. Ren, T. Zhang, *et al*., Journal of Materials Chemistry C, **5**(4), 943 (2017). https://doi.org/10.1039/C6TC05068A
[4] B. Jiang, P. Qiu, H. Chen, Q. Zhang, K. Zhao, D. Ren, X. Shi, and L. Chen, Chem. Commun. **53**, 11658 (2017). https://doi.org/10.1039/C7CC05935C
[5] D. Frank, B. Gerke, M. Eul, R. Pöttgen, and A. Pfitzner, Chem. Mater. **25**(11), 2339(2013). http://dx.doi.org/10.1021/cm401057u
[6] L.V. Piskach, O.V. Parasyuk, I.D. Olekseyuk, Y.E. Romanyuk, S.V. Volkov, and V.I. Pekhnyo, Journal of Alloys and Compounds,**421**(1-2), 98(2006). https://doi.org/10.1016/j.jallcom.2005.11.056
[7] A.E. Owen, A.P. Firth, and P.J.S. Ewen, Philosophical Magazine B, **52**(3), 347(1985). https://doi.org/10.1080/13642818508240606
[8] K. Tanaka, Journal of Non-Crystalline Solids, **170**(1), 27(1994). https://doi.org/10.1016/0022-3093(94)90099-X
[9] T. Kawaguchi, K. Tanaka, and S.R. Elliott, *Handbook of Advanced Electronic and Photonic Materials and Devices,* edited by H.S. Nalwa (Academic Press, 2001), vol. 5, pp. 91-117. https://doi.org/10.1016/B978-012513745-4/50044-5
[10] A.V. Kolobov, and S.R. Elliott, Advances in Physics, **40**(5), 625(1991). https://doi.org/10.1080/00018739100101532
[11] R.M. Sardarly, N.N. Hajiyeva, N.A. Aliyeva, S.M. Gahramanova, and R.A. Mammadov, Problems of Atomic Science and Technology, **152**(4), 23(2024). https://doi.org/10.46813/2024-152-023

[12] L.S. Parfen'eva, A.I. Shelykh, I.A. Smirnov, A.V. Prokof'ev, W. Assmus, H. Misiorek, J. Mucha, *et al*., Phys. Solid State, **45**(11), 2093 (2003). https://doi.org/10.1134/1.1626742
[13] O.Z. Alekperov, A.I. Najafov, E. Nakhmedov, O.A. Samedov, N.A. Aliyeva, and G. Jafarova, Journal of Applied Physics, **123**(13), 135701 (2018). https://doi.org/10.1063/1.5018128
[14] R.M. Sardarly, F.T. Salmanov, N.A. Aliyeva, R.N. Mehdiyeva, and S.M. Gakhramanova, Moderin Physics Letters B, **35**(33), 2150504 (2021). https://doi.org/10.1142/S0217984921505047
[15] R.M. Sardarli, F.T. Salmanov, N.A. Aliyeva, and R.M. Abbasli, Modern Physics Letters B, **34**(11), 2050113 (2020). https://doi.org/10.1142/S0217984920501134
[16] N.N. Gadzhieva, G.B. Akhmedova, and R.A. Mammadov, Problems of Atomic Science and Technology (PAST),**152**(4), 20(2024). https://doi.org/10.46813/2024-152-020
[17] F.T. Salmanov, R.M. Sardarly, R.M. Mukhtarov, N.A. Aliyeva, R.A. Mammadov, and Z.Q. Zeynalova, Problems of Atomic Science and Technology, **156**(2), 49 (2025). https://doi.org/10.46813/2025-156-049
[18] R.M. Sardarli, O.A. Samedov, A.P. Abdullayev, E.K. Huseynov, F.T. Salmanov, N.A. Alieva, and R.Sh. Agaeva, Semiconductors,**47**(5), 707(2013). https://doi.org/10.1134/S1063782613050199
[19] R.M. Sardarly, M.B. Babanly, N.A. Aliyeva, L.F. Mashadiyeva, R.A. Mamadov, G.M.Ashirov, A.A. Saddinova, and S.Z. Damirova, East European Journal of Physics,(1), 233(2025). https://doi.org/10.26565/2312-4334-2025-1-24
[20] R.M. Sardarly, G.M. Ashirov, L.F. Mashadiyeva, N.A. Aliyeva, F.T. Salmanov, R.Sh. Agayeva, R.A. Mamedov. and M.B. Babanly, Modern Physics Letters B, **36**(32n33), 2250171 (2022). https://doi.org/10.1142/S0217984922501718
[21] M. Onoda, H. Wada, A. Sato, and M. Ishii,Journal of Alloys and Compounds, **383**(1-2), 113(2004). https://doi.org/10.1016/j.jallcom.2004.04.018
[22] Y. Sun, F. Guo, H. Qin, W. Cai, and J. Sui, J. All. Compd. **859**,157844 (2021). https://doi.org/10.1016/j.jallcom.2020.157844
[23] X. Tan, J. Ding, H. Luo, O. Deliare, J. Yang, Z. Zhou, J. Lan, *et al*., ACS Appl. Mater. Interfaces, **12**(37), 41333(2020). https://doi.org/10.1021/acsami.0c10508
[24] Y. Liu, D. Cadavid, M. Ibanez, J.D. Roo, S. Ortega, O. Dobrozhan, M.V. Kovalenko, and A. Cabot, J. Mater. Chem. C, **4**(21), 4756(2016). https://doi.org/10.1039/C6TC00893C
[25] S.N. Guin, A. Chatterjee, D.S. Negi, R. Datta, and K. Biswas, Energy Environ. Sci. **6**(9), 2603 (2013). https://doi.org/10.1039/C3EE41935E
[26] V. Jovovic, and J.P. Heremans, Phys. Rev. B, **77**(24), 245204 (2008). https://doi.org/10.1103/PhysRevB.77.245204
[27] S.S. Ragimov, V.E. Bagiyev, A.I. Aliyeva, and A.A. Saddinova, Semiconductors, **55**(12), 928 (2021). https://doi.org/10.1134/S106378262104014X
[28] D. Li, X.Y. Qin, T.H. Zou, J. Zhang, B.J. Ren, C.J. Song, Y.F. Liu, *et al*.,J. Alloys Compd. **635**, 87 (2015). https://doi.org/10.1016/j.jallcom.2014.11.081
[29] S.N. Guin, A. Chatterjee, and K. Biswas, RSC Advances,**4**(23), 11811 (2014). https://doi.org/10.1039/C4RA00969J
[30] X.C. Liu, Y.M. Wang, M.L. Qi, and M.Y. Pan,J. Solid State Chem. **288,** 121454 (2020). https://doi.org/10.1016/j.jssc.2020.121454
[31] H. Fan, T. Su, H. Li, Y. Zheng, Sh. Li, M. Hu, H. Ma, and X. Jia, Mater. Sci.-Pol. **33**(1), 152 (2015). https://doi.org/10.1515/msp-2015-0004
[32] Y. Xiao, and L.-D. Zhao, Quantum Materials, **3**(55), 1 (2018). https://doi.org/10.1038/s41535-018-0127-y
[33] H.Z. Wang, Q.Y. Zhang, B. Yu, H. Wang, W. Liu, G. Chen, and Z. Ren, JMR. **26**(7), 912(2011). https://doi.org/10.1557/jmr.2010.96
[34] T.N. Asokan, K.S. Urmila, R. Jacob, R.R. Philip, G.S. Okram, V. Ganesan, and B. Pradeep, J. Semicond. **35**(5), 052001 (2014). http://dx.doi.org/10.1088/1674-4926/35/5/052001
[35] B.M. Askerov, *Electron transport phenomena in semiconductors*, (Singapore, World Scientific, 1994).
[36] Y. Pei, X. Shi, A. LaLonde, H. Wang, L. Chen, and G.J. Snyder, Nature. **473**(7345), 66(2011). https://doi.org/10.1038/nature09996
[37] G.J. Snyder, and E.S. Toberer, Nature Materials, **7**(2), 105 (2008). https://doi.org/10.1038/nmat2090
[38] S.S. Ragimov, A.E. Babayeva, and A.I. Aliyeva, Low Temp. Phys. **44**(11), 1195 (2018). https://doi.org/10.1063/1.5062157
[39] L.H. Ye, K. Hoang, A.J. Freeman, S.D. Mahanti, J. He, T.M. Tritt, and M.G. Kanatzidis, Phys. Rev. B, **77**(24), 245203 (2008). https://doi.org/10.1103/PhysRevB.77.245203
[40] J.R. Sootsman, D.Y. Chung, and M.G. Kanatzidis, Angew. Chem. Int. Ed. **48**(46), 8616 (2009). https://doi.org/10.1002/anie.200900598
[41] M. Marple, D.C. Kaseman, S. Kim, and S. Sen. J. Mater. Chem. A, **4**(3), 861(2016). https://doi.org/10.1039/C5TA07301D
[42] S. Miyatani. J. Phys. Soc. Jpn. **50**(10), 3415 (1981). https://doi.org/10.1143/JPSJ.50.3415

ВПЛИВ ДОДАВАННЯ PbTe НА ЕЛЕКТРИЧНИЙ ЗАРЯД ТА ТЕПЛОПЕРЕНОС В $AgSbSe_2$

А.А. Саддинова[1], Р.І. Селім-заде[1], А.Є. Бабаєва[1], А.А. Оруджова[2]
[1]Інститут фізики Міністерства науки і освіти Азербайджанської Республіки, AZ-1143, Азербайджан
[2]Мінгачевірський державний університет, Az-4500, Азербайджан

Метою цього дослідження є вивчення впливу додавання PbTe на термоелектричні властивості та параметри зон $AgSbSe_2$ за температур нижче кімнатної. Для цього методом прямого сплавлення було виготовлено полікристалічні зразки $(AgSbSe_2)_x(PbTe)_{1-x}$ (x = 1; 0,9; 0,85). Досліджено температурні залежності електропровідності, коефіцієнта термоЕРС та теплопровідності зразків $(AgSbSe_2)_x(PbTe)_{1-x}$ (x = 1; 0,9; 0,85) в діапазоні температур 80-350 K. Значення електропровідності зразків з додаванням PbTe зменшилося порівняно з $AgSbSe_2$. Одночасно спостерігалася інверсія знака коефіцієнта термоЕРС (n→p) у твердих розчинах $(AgSbSe_2)_x(PbTe)_{1-x}$ (x = 0,9; 0,85) за температур T>110K. Було визначено, що значення ефективної маси дірок у твердих розчинах $(AgSbSe_2)_x(PbTe)_{1-x}$ (x = 0,9; 0,85) збільшується порівняно з $AgSbSe_2$. Було виявлено, що ґраткова теплопровідність твердих розчинів $(AgSbSe_2)_x(PbTe)_{1-x}$ (x = 0,9; 0,85) значно зменшується зі збільшенням кількості PbTe в $AgSbSe_2$.

Ключові слова: *термоелектричний матеріал; електропровідність; коефіцієнт Зеєбека; теплопровідність; ефективна маса*

EAST EUROPEAN JOURNAL OF PHYSICS. 1. 247-255 (2026)
DOI:10.26565/2312-4334-2026-1-27 ISSN 2312-4334

INVESTIGATION OF THE PHYSICAL PROPERTIES OF Yb^{3+} DOPED $ZnFe_2O_4$ NANOPOWDERS SYNTHESIZED BY SOL GEL METHOD

M. Guettaf[1]*, S. Saadi[2], D. Mouattah[3], A. Kezzim[1], I. Lanez[1], B. Rekik[1]
[1]*Laboratory of Physical-Chemical Inorganic Materials and their applications (LPCMIA), Saad Dahleb University-Blida 1, BP270 09000, Blida, Algeria*
[2]*Laboratory of Applied Chemistry and Materials (LabCAM), University of M'hamed Bougara of Boumerdes, Avenue de l'Indépendance, Boumerdes, 35000. Algeria*
[3]*Laboratory Physico- Chemistry of Materials (LPCM), University of Amar Telidji, BP37G 03000, Laghouat, Algeria*
**Corresponding author e-mail: guettaf_mohamed@univ-blida.dz*
Received July 7, 2025; revised December 20, 2025; accepted January 16, 2026

$ZnFe_{2-x}Yb_xO_4$ with (x = 0, 0.01, 0.02, 0.03, 0.05, 0.07, and 0.09) have been successfully synthesized by the sol-gel method at 750°C. X-ray diffraction results showed a single phase and crystalline nanopowders of spinel-type structure with cubic symmetry and space group. The lattice parameters increase with Yb^{3+} concentrations. The BET specific area of $ZnxFe_{2-x}Yb_xO_4$ (x = 0.03) was determined to be the larger 13.59 m^2/g. The crystallite size was determined by Rietveld to be in the range of 29-104 nm. FTIR spectra showed two strong absorption bands, a common characteristic of the spinel structure. Further, the shifting of the lower absorption band toward a higher frequency confirms that Yb^{3+} ions predominantly replaced Fe^{3+} ions in octahedral sites. The formation of the spinel phase in the samples was also validated by Raman scattering, with asymmetric broadening, and a systematic shift in the Raman spectra was observed as a function of Yb3+ concentration. Scanning electron microscopy SEM showed that powders consist of micrometric aggregation of smaller particles. EDS examinations verified that the chemical elements Zn, Fe, Yb, and O are present in all samples. The direct bandgap energy values are calculated by Tauc's plot, and it indicates a semiconductor character of our compound, revealing an increase and enhancement in bandgap energy values from 1.82 to 2.4 eV with Yb^{3+} substitution.
Keywords: *Ytterbium; Zinc ferrite nanopowders; XRD; Raman; Bandgap energy*
PACS: 75.50.Gg , 78.20.-e, 81.20.Fw

1. INTRODUCTION

The synthesis of nanostructured materials with controlled composition and improved chemical-physical properties is one of the most interesting fields of materials science. Spinel compounds with excellent chemical stability and optical properties have attracted the attention of many researchers in various technological applications such as cancer treatment [1], medicinal chemistry and pharmacology [2,3], photo catalyst in wastewater treatment [4-6] H_2-generation under visible irradiation [7, 8], lithium-ion batteries [9-11] and gas-sensing devices [12,13]. The spinel ferrite oxides are a new family of magnetic nanomaterials, in which ferric ions "Fe^{3+}" play a prominent role as a principal cation in their composition [14]. This family of magnetic nanoparticles shows impressive properties which proved to be promising nanomaterials used in a variety of magnetic applications such as magnetic resonance imaging [15,16] and magnetic hyperthermia [17, 18]. The molecular formulas of spinel ferrites are represented by MFe_2O_4 (M is a divalent ion, such as Ni^{2+}, Mg^{2+}, Zn^{2+}, Co^{2+}, etc.). The unit cell has two distinct internal sites with a total of 96 sites, of which 64 are tetrahedral A-sites and 32 are octahedral B-sites. The structure attributes of spinel ferrites are intricately influenced by magnetic interactions and the distribution of cations across B and A sites [19]. Zinc ferrite bulk material $ZnFe_2O_4$ has a normal spinel structure, where divalent cations $Zn^{2+}$are located on the tetrahedral sites while trivalent cations Fe^{3+} are located at the octahedral sites [20]. Zinc ferrite nanoparticles doped with transition metals are being studied widely by various research groups [21-23]. Recently, the substitution of rare-earth elements in zinc ferrite was also studied in numerous research such as ytterbium (Yb^{3+}), Neodymium (Nd^{3+}) Lutetium (Lu^{3+}) substitution [24-26]. Rare earth ions are one of the most excellent substituents to further improve zinc ferrite properties. They play a major part in the enrichment of their electromagnetic characteristics [27,28]. Trivalent rare-earth dopants prefer a cubic crystallization system occupying the octahedral sites due to their larger ionic radius [29]. In fact, the ionic radius of rare earth elements is larger than Fe^{3+} which leads to a structural distortion of the spinel ferrite [30]. The substitution of the host iron ion (3d) in coordination number CN = 8 by rare earth cations (4f) results in structural distortions and thus significantly modifying the structural properties and optical ones of the ferrite nanoparticles through the coupling of the 3d-4f electron [31].

The aim of this study is to synthesize $ZnFe_{2-x}Yb_xO_4$ with x= 0, 0.02, 0.03, 0.05, 0.07, and 0.09 pure phase using the sol-gel method at 750°C. The works ought to improve structural, morphological and optical properties via Yb^{3+}-substitution process. Extensive characterization with various technics including XRD, FTIR, BET, SEM and diffuse reflectance were interested in investigating the impact of ytterbium concentrations on enhancement bandgap energy of the $ZnFe_{2-x}Yb_xO_4$ compounds.

Cite as: M. Guettaf, S. Saadi, D. Mouattah, A. Kezzim, I. Lanez, B. Rekik, East Eur. J. Phys. 1, 247 (2026), https://doi.org/10.26565/2312-4334-2026-1-27

2. EXPERIMENTAL

2.1. Synthesis

Yb^{3+} doped $ZnFe_2O_4$ were synthesized by sol-gel method using zinc nitrate $Zn(NO_3)_2.6H_2O$, iron nitrate $Fe(NO_3)_3.9H_2O$ purchased from Alfa Aesar. Ytterbium nitrate $Yb(NO_3)_3.5H_2O$ with 99.9 % and citric acid $C_6H_8O_7$ were supplied from Sigma-Aldrich with 99.9% purity. First, $Zn(NO_3)_2.6H_2O$, $Fe(NO_3)_39.H_2O$, and $Yb(NO_3)_3.5H_2O$, in their respective stoichiometry were dissolved in 10 mL of deionized water which were then mixed. After continuous stirring for 30 min at room temperature, a citric acid $C_6H_8O_7$, as a complexity agent, was added to the solution which was then heated at 85°C under magnetic stirring until a gel formed. The resultant gel was dried at 80 °C for 48 hours. Then, the generated powders were ground in an agate mortar and heat-treated at 750 °C for 8 hours in a tube oven in the air (4 h, 5 °C/min). The procedure is illustrated in figure 1.

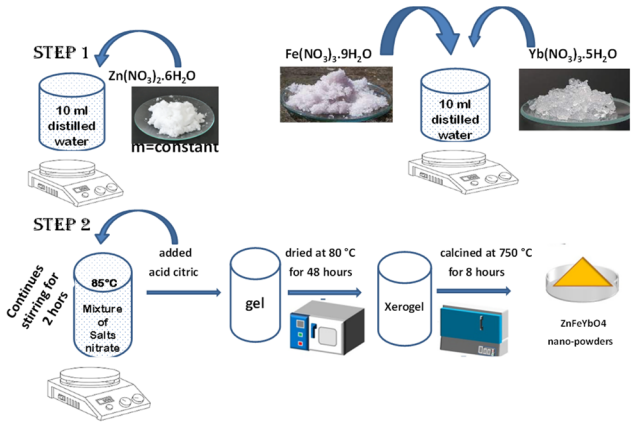

Figure 1. Different steps of synthesis of $ZnFe_{2-x}Yb_xO_4$ (x=0 0.01 0.02, 0.03 0.05 0.07 and 0.09) nanoparticles by sol-gel method

2.2 Characterizations

The identifications of $ZnFe_{2-x}Yb_xO_4$ phases were done by using X-ray diffraction (XRD). The patterns were recorded with Brüker D8 Phaser X-ray diffractometer equipped with Cu Kα radiation (λCu = 1.5418 Å) in the 2θ range (10–70°). Raman spectra for samples were recorded on a Horiba Jobin Yvon Lab Ram high-resolution spectrometer in backscattering geometry in the range 100–1000 cm^{-1} with a He-Ne laser excited with wavelength 532nm, grating 1800 lines/mm, slit 100, power at sample of 0.4 and 1.0 mW, and acquisition 20 s/5 cycles. Jasco FT/IR-4200 was used for Fourier Transform Infrared spectroscopy over the range 400–4000 cm^{-1}.The morphology of the nanopowders was investigated using a scanning electron microscope (SEM-EDS) on a Quattro SEM FEG. The BET surface area, pore-volume and pore size distributions were investigated via N_2 sorption performed on a BET ASAP 2020 PLUS 2.00 instrument. The grain size distribution was measured using the Mastersizer 2000, Malvern laser instrument. The different grain sizes were dispatched among various classes and used to evaluate the most relevant statistical diameters. The band gap energies Eg of the $ZnFe_{2-x}Yb_xO_4$ nanomaterials were determined from the Tauc relation using the diffuse reflectance data recorded on a optima SP-3000nano spectrophotometer between (200–800 nm.

3. RESULTS AND DISCUSSIONS

3.1. Structural properties

XRD patterns of Yb^{3+} doped $ZnFe_2O_4$ samples synthesized at 750°C using sol-gel method are shown in Figure 2a. The results indicate that all the samples crystallize in a cubic spinel structure according to JCPDS card no. 22-1012 with the space group: Fd-3m [32,33]. All diffraction peaks were indexed and matched to a single phase without the detection of any peaks attributed to the formation of secondary phases. As a result, Yb^{3+} atoms are assumed to be efficiently incorporated into the lattice within the studied range. Figure 2b shows that the Yb^{3+} substitution causes a shift of the XRD peaks towards to the lower diffraction angles values. The extent of the peak shift is dependent on the Yb^{3+} content. The same behaviour was observed upon substituting Yb3+ in cobalt ferrite nanoparticles [34]. This may be attributed to the ionic radius of Yb3+ (0,85 Å), which is larger than that of Fe3+ (0,64 Å), causing an increase in the interplanar spacing and a subsequent decrease in the diffraction angle as the lattice parameter increases [35].

Beyond a certain concentration of Yb^{3+}, the single-phase domain of the solid solution becomes poly-phase by the appearance of new peaks due to the high Yb^{3+}/Fe^{3+} ratio, indicating the formation of secondary phases ytterbium oxide (Yb_2O_3) and ytterbium iron perovskite ($YbFeO_3$), which crystallized in cubic phase (JCPDS file no. 43-1037) and orthorhombic structure (JCPDS file no. 047-0070) respectively. We are confirmed by preparing samples with higher concentrations of Yb^{3+} showing that the limiting solubility for this compound is when the concentration of Yb^{3+} is located belongs to 10% and 20% (Figure 2c). Consequently, it can be seen that the maximum solubility limit of Yb^{3+} ions in the $ZnFe_2O_4$ crystal structure lies between 10% and 20%.

The lattice parameter *a* is sensitive to the composition of the solid solution (Figure 3). At first sight, the substitution of Yb^{3+} with greater ionic radii in place of Fe^{3+} at octahedral site causes expansion of crystalline structure which resulted

into increase in lattice parameters. However, a close examination reveals that a x = 0, 0.01 and 0.02 concentrations are formed, indicating that the parameter *a* is not affected by the little amount of Yb^{3+} substitution, and then a decrease at x=0.05 after which it increases and reaches a maximum at x = 0.09. The lattice parameters are calculated by Rietveld refinement program. Clearly, the lattice parameter of the doped samples is higher than that of the undoped original compound and increases with increasing Yb^{3+} incorporation. This behavior is associated with the larger ionic radius of ytterbium (r=0.87A°) in octahedral coordination compared to iron (r=0.65A°). The considerable difference in ionic radii between Yb^{3+} and Fe^{3+} leads to a deviation from Vegard's law, which explains the non-linear increase in the lattice parameter with increasing dopant concentration [36].

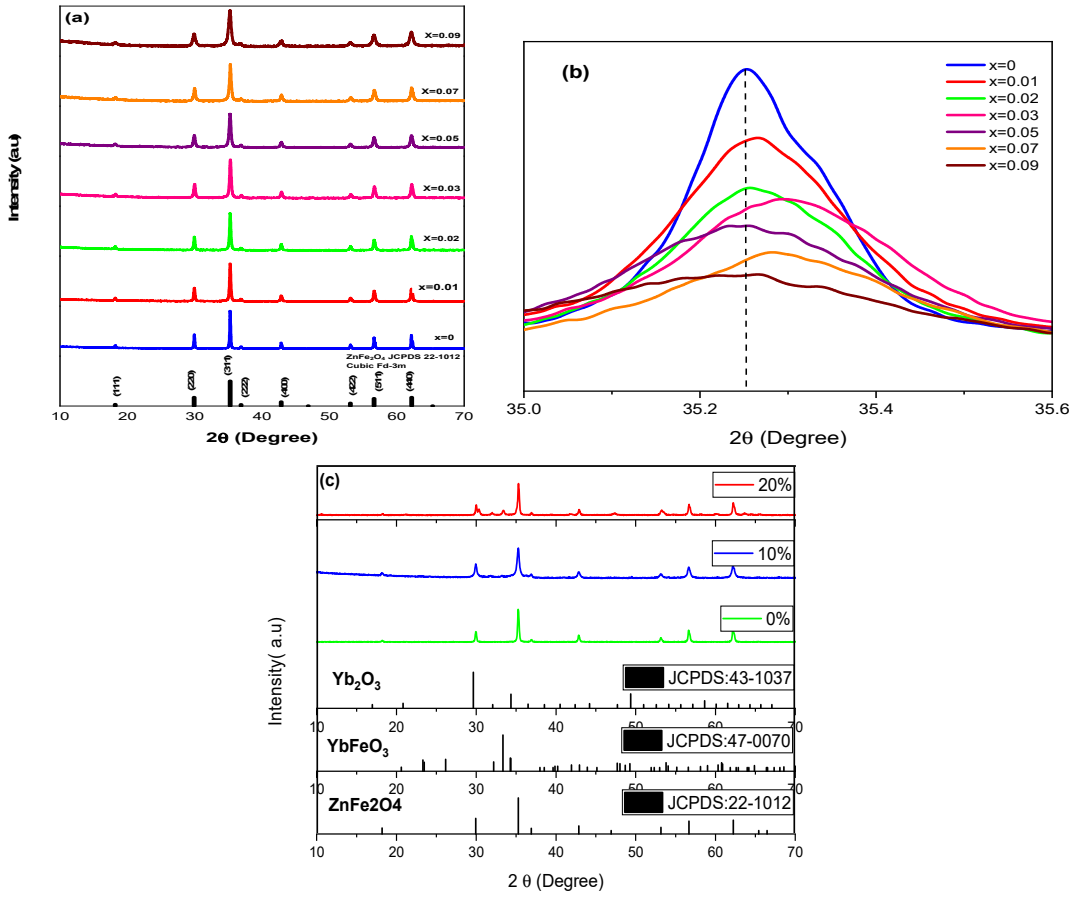

Figure 2. (a) X-ray diffraction patterns of $ZnFe_{2-x}Yb_xO_4$ (x= 0, 0.01, 0.02, 0.03, 0.05, 0.07, and 0.09), (b) expanded view of 2θ diffraction peak between 35 and 35.6, and (c) the solubility limit of Yb^{3+} ions in $ZnFe_2O_4$ nanopowders

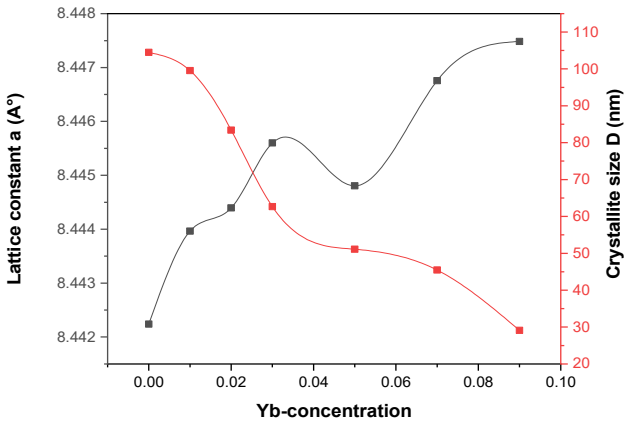

Figure 3. Composition dependence of the lattice parameters and crystallite size (D) of $ZnFe_{2-x}Yb_xO_4$ (x=0, 0.01, 0,02,0.03, 0.05, 0.07, 0.09)

The calculated values for the lattice constant (a) and cell volume (V) are shown in Table 1. The obtained values of the lattice constant (a = 8.442 Å), for $ZnFe_2O_4$ (x=0) are in good agreement with the earlier reported values (a = 8.44 Å) [37, 38].

Table 1. Lattice parameters, Crystallite size, cell volume and surface area of $ZnFe_{2-x}Yb_xO_4$ compounds

x	Lattice constant *a* (A°)	cell volume *V*(A°^{3})	Crystallite size *D Rietveld refinement* (nm)	Crystallite size *D Scherrer* (nm)	XRD density ρ (g/ cm^3)	S_{BET} (exp) (m^2/g)	D_{BET} (nm)
0	8.44224	601.690	104.49645	70.025	5.33	6.415	175.47
0.01	8.44397	602.060	99.57471	44.962	5.35	/	/
0.02	8.4444	602.152	83.40205	43.137	5.38	/	/
0.03	8.4456	602.409	62.64066	32.075	5.40	13.589	81.765
0.05	8.44481	602.240	51.09478	27.275	5.43	/	/
0.07	8.44676	602.657	45.45637	30.062	5.50	11.388	95.794
0.09	8.44749	602.813	29.09815	18.85	5.55	/	/

In Table 1 is also shown the average crystallite size (D_{XRD}) which are evaluated from the width at mid-height β (β, radians) of the most intense peak using Debye Scherrer's formula [39]:

$$D = \frac{k\lambda}{\beta \cdot cos\theta}. \quad (1)$$

Where is a shape factor (taken as 0.94 for spherical crystallites), λ represents the X-ray wavelength, and θ signifies Bragg's angle. Moreover, crystallite size D was calculated by the Rietveld method, and by comparison with Scherer, the Rietveld method appeared to give better results.

As a results, Yb^{3+} content increases, the diameter is also found to decrease due to the larger ionic radii of the dopant. The average crystallite sizes were found to be between 29 and 104 nm. The theoretical value of X-ray density ρ (as mentioned in Table 1) increases as the Yb^{3+} concentration increases in the samples, and it was calculated through the following formula:

$$\rho = \frac{8M}{N_A a^3}. \quad (2)$$

Where a is the lattice parameter, N_A represents Avogadro's number, and M indicates the molecular weight of the synthesized samples.

To determine the specific surface area and the pore size distribution of the synthesized samples, we have used the BET method. According to the nitrogen sorption data, the surface areas of $ZnFe_2O_4$ replaced with Yb^{3+} at composition values of 0, 0.03, and 0.07 is 6.415, 13.589, and 11.388 m^2/g, respectively. Specific surface area is highly affected by the substitution ratio. The highest surface area is attributed to the sample with composition x = 0.03 with a value of 13.589 m^2/g. whereas the average particle size D_{BET}, was determined using the following formula:

$$D_{BET} = \frac{6}{\rho \times s_{BET}}. \quad (3)$$

It should be noted that the sample with x = 0.03 has the smallest average particle size (81.765 nm, from Table 1) compared to x = 0 and 0.07. This confirms that the specific surface area and the particle size are inversely related to each other [40].

3.2. Vibrational properties

In order to explain the cation distribution at tetrahedral and octahedral sites in ferrites samples which are known to be sensitive to infrared in the 400-700 cm^{-1} range where the characteristic metal-oxygen bands appear [41]. Figure 4 shows FTIR spectra of the $ZnYb_xFe_{2-x}O_4$ nanopowders after calcination at 750°C.

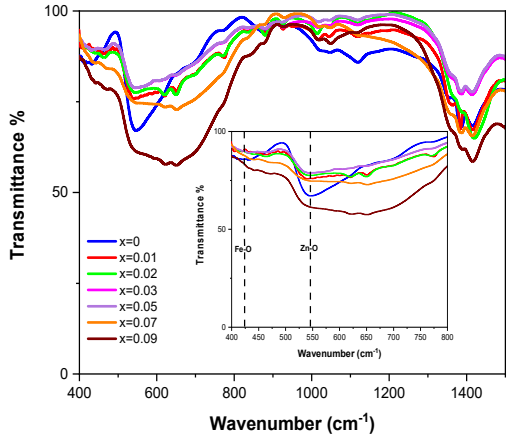

Figure 4. FTIR spectra $ZnFe_{2-x}Yb_xO_4$ (x = 0, 0.01, 0.02, 0.03, 0.05, 0.07, and 0.09)

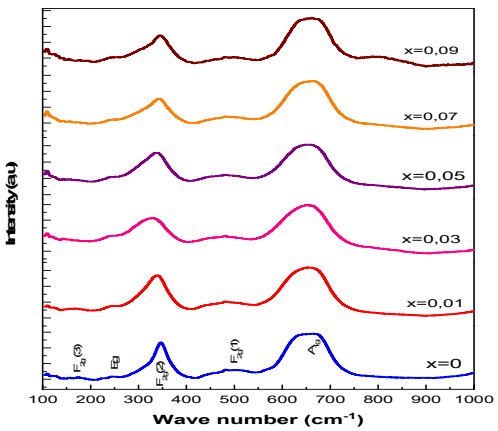

Figure 5. Raman measurements of the $ZnFe_{2-x}Yb_xO_4$ (x = 0 0.01 0.03 0.05 0.07 and 0.09) nanoparticles under an excitation λ_{ex} = 532nm

All spectra show two noticeable strong bands, common characteristics of spinel structure, where the first around 400-450 cm^{-1} characteristic of octahedral coordinated Fe-O, and the second is more intense in the range 530-600 cm^{-1} associated with the vibrations of the tetrahedral coordinated Zn-O.

The absorption band of octahedral coordination shifts toward higher frequency for the substituted samples, whereas that of tetrahedral varies more less and remains nearly constant (Figure 4). The shifting toward to the higher frequency confirms that Yb^{3+} ions are predominantly replacing Fe^{3+} ions at octahedral sites. This was found with ytterbium doping [42]. Furthermore, an absorption band occurs at 1420 cm^{-1} because of the existence of O–H stretching vibration of free water molecules [43].

The nanopowders $ZnFe_{2-x}Yb_xO_4$ with (x=0 0.01 0.03 0.05 0.07 and 0.09) have been characterized by Raman scattering in the range of 100 to 1000 cm^{-1} at the wavelength excitation λ_{ex} =532nm which crystallize in cubic ferrites. Figure 5 shows Raman spectra which indicate the strongest active mode at 655cm^{-1} corresponding to A_g symmetric stretching mode which it associated to vibration of Zn-O in tetragonal site, in other hand the Fe-O vibrations were attributed at 165-250 and 355 cm^{-1} on octahedral site corresponding to: translational movement of the assembly tetrahedron; F_{2g} (1), symmetric bending; E_g and asymmetric bending; F_{2g} (2) respectively, while the F_{2g} (3) mode at 480 cm^{-1} is the second order active mode Raman. The intensity peaks related to the concentration of Yb^{3+} may be due to the electronegativity values of ytterbium doping as a rare earth and to the length of vibrating bond of ytterbium with environmental atoms in the polyhedron [44-47].

3.3. Morphological properties

Scanning electron microscopy (SEM) images of the oxides with compositions x = 0, 0.01, 0.02, 0.03, 0.05, 0.07, and 0.09 are shown in Figure 6. It depicts all powders that consist of micrometric aggregation of smaller particles. The existence of a high-density agglomeration indicates that pore-free crystallites are present on the surface. Nonetheless, for x = 0.02, 0.07, and 0.09, the morphological study reveals the presence of pores and voids due to gases emitted during the synthesis process [48]. Micrographs of $ZnFe_2O_4$ samples containing ytterbium are not homogeneous and consist of both monolithic, massive pieces and grains connected by bridges. The samples' irregular shape could result from mechanical grinding [49].

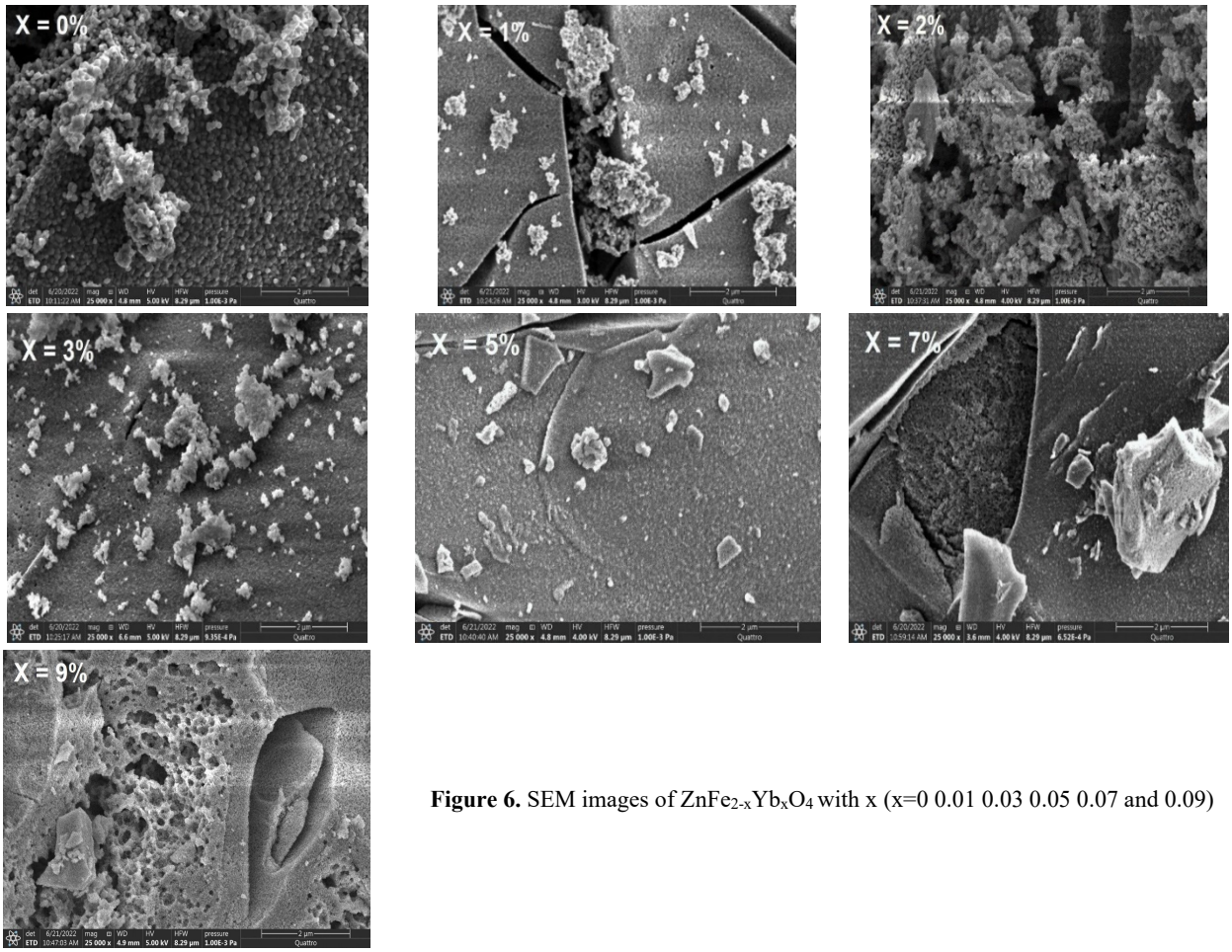

Figure 6. SEM images of $ZnFe_{2-x}Yb_xO_4$ with x (x=0 0.01 0.03 0.05 0.07 and 0.09)

Energy dispersive X-rays analysis was applied to provide the elemental identification and quantitative compositional in formation. Figure 7 shows that all the elements are present, no additional peaks are observed indicating the purity of the nanopowders.

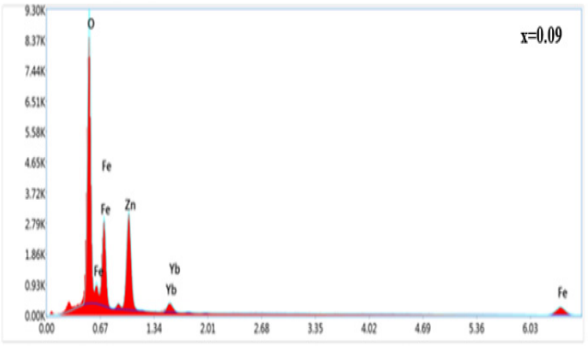

Figure 7. EDS analysis for x=0.09

3.4. Optical properties

The optical properties of Yb^{3+}substituted $ZnFe_2O_4$ spinel nanoparticles were determined using UV–vis analysis.

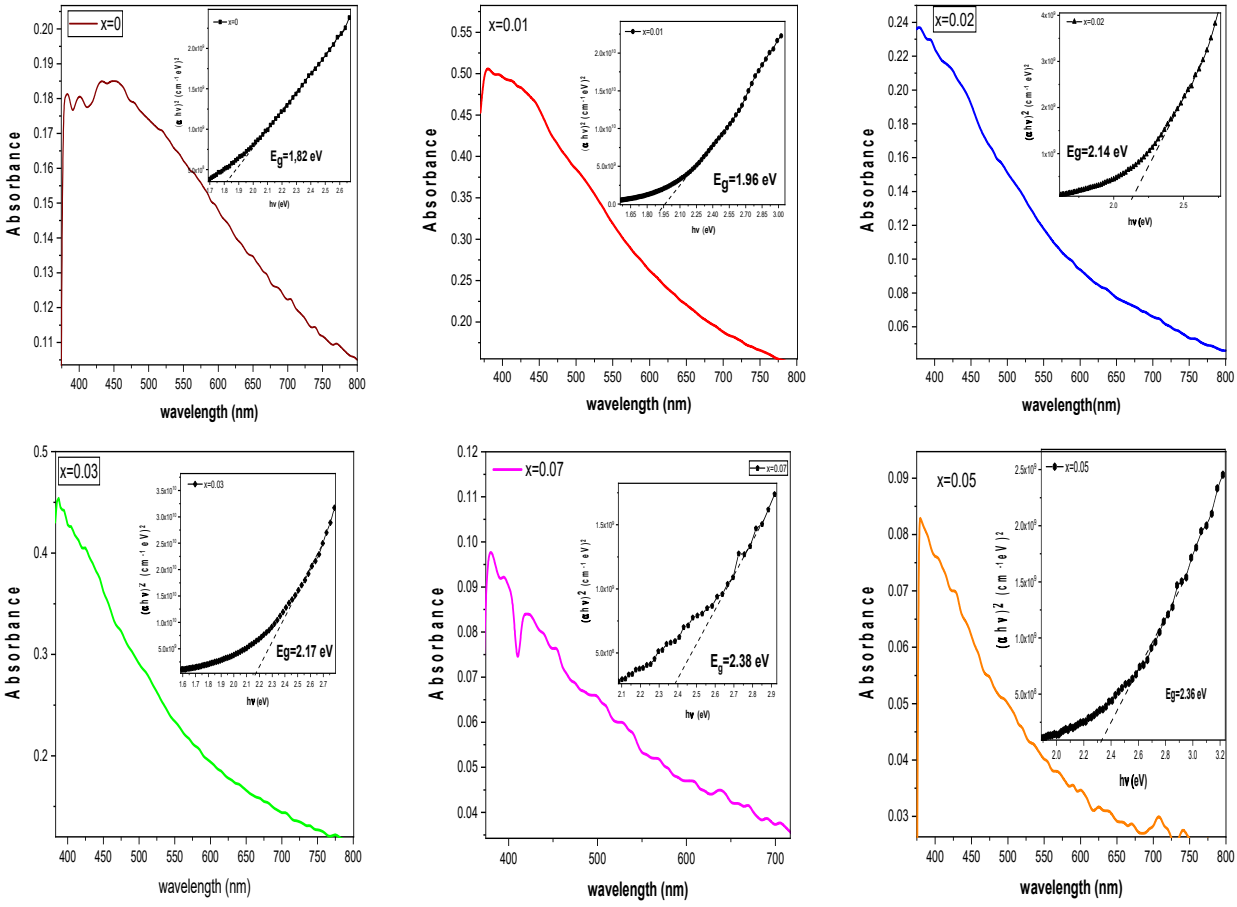

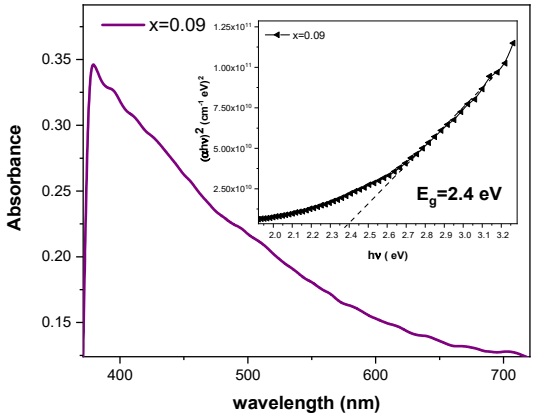

Figure 8. Energy gap E_g of $ZnFe_{2-x}Yb_xO_4$ with (x=0 0.01 0.03 0.05 0.07 and 0.09)

Figure 8 shows the energy gap E_g of $ZnFe_{2-x}Yb_xO_4$ at different ratios, which is calculated using the well-known Tauc relation:

$$(\alpha h\nu)^n = A(h\nu - E_g) \quad (4)$$

Where α is the absorption coefficient, $h\nu$ is the photon energy (eV), A is proportionality constant and n are either 2 or 1/2 for direct and indirect transitions, respectively. By extrapolating the linear part of the curve on the energy axis, more reliable values of the gap were determined.

For all samples, the diffuse reflectance spectra exhibit a steep shape of absorption bands characteristic of direct transitions (Figure 8), with an appropriate adjustment for $n = 2$ and is the energy required for electrons to be excited from the top of the valence band (VB) to the bottom of the conduction band (CB) without phonon assistance.

The calculated gaps depend on the Yb^{3+} concentration and increase monotonically with Yb3+ substitution into the crystal lattice, corroborating the existence of a solid solution. This result can be explained by the fact that the Yb^{3+} ions substitution process requires a higher energy level to excite an electron from the valence band to the conduction band, thus increasing the energy band gap of the doped-zinc ferrite. The obtained bandgap energy values for $ZnFe_{2-x}Yb_xO_4$ nanoparticles are comparable to those reported in the literature [35,50-51].

CONCLUSIONS

In the present work, Yb^{3+} doped $ZnFe_2O_4$ with (x= 0, 0.01, 0.02, 0.03, 0.05, 0.07, and 0.09) have been successfully synthesized by the sol-gel method at 750°C for 8 hours. The obtained powders were then analysed for their structural, morphological, and optical properties. XRD patterns show that $ZnFe_{2-x}Yb_xO_4$ samples are single-phase and crystallize in cubic symmetry with good crystallinity. As the ytterbium ion content increased, the lattice constant increased, whereas the crystallite size decreased from 29 to 104 nm. The specific surface area of the Brunauer–Emmett–Teller (BET) of the $Zn_xFe_{2-x}Yb_xO_4$ (x=0.03) was determined to be the larger 13.59m^2/g. FTIR analysis shows that the substitution of ytterbium ions shifts the lower band absorption towards the higher frequency side, indicating the occupancy of Yb^{3+} ions in octahedral sites. The appearance of all active modes in the Raman spectra shows that the structure of spinel ferrite was not changed by the insertion of ytterbium. The SEM images show that the samples are agglomerated and irregular in shape, which could be due to mechanical grinding. The identification and quantitative composition in formation were determined by energy dispersive X-rays (EDS), confirming that all samples contain Zn, Fe, Yb and O without any additional elements. The narrow-bandgap energy is found to be dependent on the ytterbium content and increases monotonically from 1.82 to 2.4 eV with Yb3+ substitution, corroborating the existence of the $ZnFe_{2-x}Yb_xO_4$ samples.

Acknowledgments

The authors thank the General Directorate of Scientific Research and Technological Development (DGRSDT) for providing the financial support the chemical and physical analysis. Additionally, the authors thank CRAPC LAGHOUAT for physical and chemical examinations. The authors also give acknowledgement to researchers of Laboratory of Physical-Chemical Inorganic Materials and Their Applications (LPCMIA) at Saad Dahleb Blida 1 university, Algeria's.

ORCID

Mohammed Guettaf, https://orcid.org/0009-0005-3875-3782; **Souad Saadi,** https://orcid.org/0009-0002-0633-9294
Dalila Mouattah, https://orcid.org/0009-0000-0941-7740; **Amina Kezzim,** https://orcid.org/0000-0001-6638-0809
Imane Lanez, https://orcid.org/0000-0001-6758-9583; **Brahim Rekik,** https://orcid.org/0000-0003-4944-3390

REFERENCES

[1] Gao J, Si F, Wang F, Li Y, Wang G, Zhao J, Ma Y, Yu R, Li Y, Jin C, Li D 2023 *Solid State. Sci.* **135** 107066 https://doi.org/10.1016/j.solidstatesciences.2022.107066
[2] Rahimi S, Nezhad S. M, Zare, E. N, Pourmousavi S. A, Boroujerdian M, Hosseini S 2023 *Inorganic Chemistry Communications* **158** 111556. https://doi.org/10.1016/j.inoche.2023.111556
[3] P. Abishad, M. Jayashankar, A. Hezam, B.S. Srinath, N.V. Kurkure, S.B. Barbuddhe, and R.D.B, Vergis, J. Nano-Structures & Nano-Objects, **37**, 101112 (2024). https://doi.org/10.1016/j.nanoso.2024.101112
[4] R. Jasrotia, Suman, A. Verma, R. Verma, J. Ahmed, S.K. Godara, G. Kumar, *et al*., J. Water Process Eng. **48**,102865 (2022). https://doi.org/10.1016/j.jwpe.2022.102865
[5] M.A. Gavrilova, D.A. Gavrilova, S.K. Evstrop'ev, and N.V. Nikonorov, Russian Journal of Inorganic Chemistry, 1 (2024). https://doi.org/10.1134/S0036023623602994
[6] R. Jasrotiaa, N. Jaswal, J. Prakasha, C.C. Kit, J. Singhd, and A. Kandwal, Journal of Magnesium and Alloys, **12**, 490 (2024). https://doi.org/10.1016/j.jma.2024.02.006
[7] A. Boujemaa, R. Bouareb, S. Saadi, A. Bouguelia, and M. Trari, Applied Energy, **86**, 1080 (2009). https://doi.org/10.1016/j.apenergy.2008.06.007
[8] S. Attia, N. Helaïli, Y. Bessekhouad, and M. Trari, A: Chemistry, **426**, 113745 (2022). https://doi.org/10.1016/j.jphotochem.2021.113745
[9] Y. Qu, D. Zhang, X. Wang, H. Qiu, T. Zhang, M. Zhang, G. Tian, *et al*., J. Alloys Compd. **721**, 697 (2017). https://doi.org/10.1016/j.jallcom.2017.06.031
[10] D. Zhang, C. Zhang, H. Xu, Z. Huo, X. Shi, B. Luo, G. Liu, *et al*., Journal of Alloys and Compounds, **987**, 174212 (2024). https://doi.org/10.1016/j.jallcom.2024.174212

[11] L. Dong, Z. Wang, C. Mi, W. Zhao, C. Qin, C. Luo, and Z. Wang, Materials Today Chemistry, **35**, 101853 (2024). https://doi.org/10.1016/j.mtchem.2023.101853
[12] A.S. Mokrushin, N.P. Simonenko, T.L. Simonenko, E.P. Simonenko, V.G. Sevast'yanov, and N.T. Kuznetsov, Russ. J. Inorg. Chem. **66**, 1425 (2021). https://doi.org/10.1134/S0036023621090060
[13] R. Prakshale, S. Bangale, M. Kamble, and S. Sonawale, Micro and Nanostructures, **189**, 207820 (2024). https://doi.org/10.1016/j.micrna.2024.207820
[14] O.D. Dastjerdi, H. Shokrollahi, and S. Mirshekari, Inorganic Chemistry Communications, **153**, 110797 (2023). https://doi.org/10.1016/j.inoche.2023.110797
[15] J. Wan, X. Jiang, H. Li, and K.J. Mater. Chem. **22**, 13500 (2012). https://doi.org/10.1039/C2JM30684K
[16] B. Hu, Y. Cui, X. Yang, X. Xu, B.J. Janani, and A. Fakhri, Surfaces and Interfaces, **33**, 102226 (2022). https://doi.org/10.1016/j.surfin.2022.102226
[17] M. Srivastava, S.K. Alla, S.S. Meena, N. Gupta, R.K. Mandala, and N.K. Prasad, New J. Chem. **42**(9), 7144 (2018). https://doi.org/10.1039/C8NJ00547H
[18] M. Tahir, M. Fakhar-e-Alam, M. Asif, M.J. Iqbal, A. Abbas, M. Hassan, *et al*., Heliyon, **10**, (2024) https://doi.org/10.1016/j.heliyon.2024.e24792
[19] E.A. Alghamdi, and R. Sai, Results in Physics, **59**, 107549 (2024). https://doi.org/10.1016/j.rinp.2024.107549
[20] M. Madhu, A.V. Rao, D. Parajuli, S.Y. Mulushoa, and N. Murali, Inorganic Chemistry Communications, **143**, 109818 (2022). https://doi.org/10.1016/j.inoche.2022.109818
[21] H.M.N.H.K. Asghar, M. Khalid, Z.A. Gilani, M. Shifa, A. Parveen, M.S. Ahmed, J.K. Khan, *et al*., Optical and Quantum Electronics, **53**, 677 (2021). https://doi.org/10.1007/s11082-021-03299-8
[22] G.R. Vasudha, N. Yerol, E. Jomy, and K.V. Anupriya, Materials Today: Proceedings, **2023**, (2023). https://doi.org/10.1016/j.matpr.2023.06.333
[23] R.V. Bharathi, M.K. Raju, P.S.V. Shanmukhi, M.G. Kiran, N. Murali, D. Parajuli, T.W. Mammo, and K. Samatha, Inorganic Chemistry Communications, **158**, 111713 (2023). https://doi.org/10.1016/j.inoche.2023.111713
[24] P. Naik, R.B. Tangsali, S.S. Meena, and S.M. Yusuf, Materials Chemistry and Physics, **191**, 215 (2017). https://doi.org/10.1016/j.matchemphys.2017.01.032
[25] H. Javeda, F. Iqbalb, P.O. Agboolac, M.A. Khanb, M.F. Warsia, and I. Shakird, Ceramics International, **45**, 11125 (2019). https://doi.org/10.1016/j.ceramint.2019.02.176
[26] S. Nadaf, B. Chethan, K.M. Swathi, S.S. Laxmeshwar, J. Angadi, K. Manjunatha, V. Molahalli, *et al*., Ceramics International, (2024). https://doi.org/10.1016/j.ceramint.2024.04.045
[27] S.E. Jacobo, S. Duhalde, and H.R. Bertorello, Journal of Magnetism and Magnetic Materials, **276**, 2253 (2004). https://doi.org/10.1016/j.jmmm.2003.12.564
[28] M.M. Baig, S. Zulfiqar, M.A. Yousuf, M. Touqeer, S. Ullah, P.O. Agboola, M.F. Warsi, and I. Shakir, Ceram. Int. **46**, 23208 (2020). https://doi.org/10.1016/j.ceramint.2020.06.103
[29] P. Priyadharshini, and K. Pushpanathan, Chemical Physics Impact, **6**, 100201 (2023). https://doi.org/10.1016/j.chphi.2023
[30] M. Choupani, and A, Gholizadeh, Journal of rare earth, (2023). https://doi.org/10.1016/j.jre.2023.06.011
[31] M. Vucinic-Vasic, E.S. Bozin, L. Bessais, G. Stojanovic, U. Kozmidis-Luburic, M. Abeykoon, B. Jancar, *et al*., J. Phys. Chem. C, **117**, 12358 (2013). https://doi.org/10.1021/jp403459t
[32] G. Wang, Y. Ma, Y. Tong, X. Dong, and M. Li, J. Intell. Mater. Syst. Struct. **28**(17), 2331 (2017). https://doi.org/10.1177/1045389X16685449
[33] J.N. Baby, C. Lavanya, S. Wang, B. Sriram, A. Anantharaman and M. George, New J. Chem. 45 (2021) 10049–10056. https://doi.org/10.1039/D1NJ01367J
[34] H. Ghorbani, M. Eshraghi, A.S. Dodaran, P. Kameli, S. Protasowicki, and D. Vashaee, Materials Research Bulletin, **147**, 111642 (2022). https://doi.org/10.1016/j.materresbull.2021.111642
[35] M.R. Rather, A.M, Sultan, S. Khalid, S. Abass, and R. Samad, Journal of Sol-Gel Science and Technology, **1,** (2024). https://doi.org/10.1007/s10971-024-06362-4
[36] S.R. Naik, and A.V. Salker, Journal of Alloys and Compounds, **600**, 137 (2014). http://dx.doi.org/10.1016/j.jallcom.2014.02.101
[37] A. Hakimyfard, and S. Mohammadi, Adv. Powder Technol. **30**, 1257 (2019). https://doi.org/10.1016/j.apt.2019.04.005
[38] D.D. Andhare, S.A. Jadhav, M.V. Khedkar, S.B. Somvanshi, S.D. More, and K.M. Jadhav, Journal of Physics: Conference Series, **1644**, 012014 (2020). https://doi.org/10.1088/1742-6596/1644/1/012014
[39] N Koriche, A. Bouguelia, and M. Trari, International Journal of Hydrogen Energy, **80**, 272 (2006). https://doi.org/10.1016/j.ijhydene.2004.06.011
[40] Z. Li, G. Chen, X. Tian, and Y. Li, Res. Bull. **43**, 1781 (2008). https://doi.org/10.1016/j.materresbull.2007.07.010
[41] S. Saadi, A. Kezzim, A. Irekti, M.S. Nas, and M. Guettaf, Russ. J. Gen. Chem. **94**, 1207 (2024). http://dx.doi.org/10.1134/S1070363224050189
[42] A.B. Gadkari, T.J. Shinde, and P.N. Vasambekar, Materials Chemistry and Physics, **114**, 505 (2009). https://doi.org/10.1016/j.matchemphys.2008.11.011
[43] S. Yuvaraj, S. Revathi, A. Kumar, G. Anitha, A.M. Al-Enizi, B. Pandit, R. Revathi, *et al*., Optical Materials, **145**, 114423 (2023). https://doi.org/10.1016/j.optmat.2023.114423
[44] A. Aslam, N.A. Morley, N. Amin, M.I. Arshad, M.A. Nabi, A. Ali, K. Mahmood, *et al*., Physica B: Physics of Condensed Matter, **601**, 412565 (2021). https://doi.org/10.1016/j.physb.2020.412565
[45] N.B. Singh, and A. Agarwal, Materials Today: Proceedings, **5**, 9148 (2018). https://doi.org/10.1016/j.matpr.2017.10.035
[46] A. Manohar, C. Krishnamoorthi, K.C.B. Naidu, and C. Pavithra, Applied Physics A, **125**, (2019). https://doi.org/10.1007/s00339-019-2760-0
[47] Z.Ž. Lazarević, Č. Jovalekić, A. Milutinović, D. Sekulić, V.N. Ivanovski, A. Rečnik, B. Cekić, and N.Ž. Romčević, Journal of Applied Physics **113**, 187221 (2013). http://dx.doi.org/10.1063/1.4801962
[48] N.M. Deraz, Journal of Alloys and Compounds, **501**(2), 317 (2010). https://doi.org/10.1016/j.jallcom.2010.04.096

[49] C. Aziz, and B. Azhdar, Journal of Magnetism and Magnetic Materials, **542**, 168577 (2022). https://doi.org/10.1016/j.jmmm.2021.168577
[50] R.S. Yadav, I. Kuřitka, J. Vilcakova, P. Urbánek, M. Machovsky, M. Masař, and M. Holek, Journal of Physics and Chemistry of Solids, **110**, 87 (2017). https://doi.org/10.1016/j.jpcs.2017.05.029
[51] M. Shobana, T. Raguram, N. Eswaramoorthy, G. Cárdenas-Jirón, K. Granados-Tavera, and A.N. Alodhayb, *et al*., Ceramics International, **51**(5), (2025). https://doi.org/10.1016/j.ceramint.2024.12.119

ДОСЛІДЖЕННЯ ФІЗИЧНИХ ВЛАСТИВОСТЕЙ НАНОПОРОШКІВ $ZnFe_2O_4$, ЛЕГОВАНИХ Yb^{3+}, СИНТЕЗОВАНИХ ЗОЛЬ-ГЕЛЬ МЕТОДОМ

М. Геттаф[1], С. Сааді[2], Д. Муаттах[3], А. Кеззім[1], І. Ланез[1], Б. Рекік[1]

[1]Лабораторія фізико-хімічних неорганічних матеріалів та їх застосування (LPCMIA), Університет Саада Далеба, Бліда 1, BP270 09000, Бліда, Алжир

[2]Лабораторія прикладної хімії та матеріалів (LabCAM), Університет Мхамеда Бугари в Бумердесі, Авеню де л'Індепенданс, Бумердес, 35000. Алжир

[3]Лабораторія фізико-хімії матеріалів (LPCM), Університет Амар Теліджі, BP37G 03000, Лагуат, Алжир

$ZnFe_{2-x}Yb_xO_4$ з (x = 0, 0,01, 0,02, 0,03, 0,05, 0,07 та 0,09) були успішно синтезовані золь-гель методом при 750°C. Результати рентгенівської дифракції показали однофазні та кристалічні нанопорошки зі структурою шпінелі з кубічною симетрією та просторовою групою . Параметри решітки збільшуються зі збільшенням концентрації Yb^{3+}. Питома площа $Zn_xFe_{2-x}Yb_xO_4$ за методом BET (x = 0,03) була визначена як більша з них і становить 13,59 м²/г. Розмір кристалітів, визначений Рітвельдом, знаходиться в діапазоні 29-104 нм. ІЧ-спектри з Фур'є показали дві сильні смуги поглинання, що є загальною характеристикою структури шпінелі. Крім того, зміщення нижньої смуги поглинання в бік вищої частоти підтверджує, що іони Yb3+ переважно заміщують іони Fe^{3+} в октаедричних позиціях. Формування шпинельної фази у зразках також було підтверджено за допомогою комбінаційного розсіювання з асиметричним розширенням, і спостерігався систематичний зсув у спектрах комбінаційного розсіювання як функція концентрації Yb^{3+}. Скануюча електронна мікроскопія SEM показала, що порошки складаються з мікрометричної агрегації дрібніших частинок. EDS-дослідження підтвердили, що хімічні елементи Zn, Fe, Yb та O присутні у всіх зразках. Значення прямої енергії забороненої зони розраховані за графіком Таука, і це вказує на напівпровідниковий характер нашої сполуки, демонструючи збільшення та посилення значень енергії забороненої зони від 1,82 до 2,4 еВ із заміщенням Yb^{3+}.

Ключові слова: *ітербій; нанопорошки фериту цинку; рентгенівська дифракція; Раман; енергія забороненої зони*

East European Journal of Physics. 1. 256-260 (2026)
DOI:10.26565/2312-4334-2026-1-28 ISSN 2312-4334

ENHANCING THE YIELD OF CARBON NANOTUBES THROUGH THE NANOCATALYST-SUBSTRATE INTERFACE

Ilyos J. Abdisaidov*, Sevara G. Gulomjanova, Ilyos Kh. Khudaykulov, Khatam B. Ashurov
Institute of Ion-Plasma and Laser Technologies named after U.A. Arifov, Academy of Sciences of the Republic of Uzbekistan, 100125, Durmon yuli st. 33, Tashkent, Uzbekistan
**Corresponding Author-mail: ilyos.abdisaidov@gmail.com*
Received August 24, 2025; revised December 19, 2025; accepted January 19, 2026

In this study, the effect of the nanocatalyst/substrate interface on the yield and quality of carbon nanotubes (CNTs) synthesized by chemical vapor deposition (CVD) was investigated. Nickel oxide (NiO) nanoparticles were prepared using the sol–gel spin-coating method and deposited as thin films with different masses (66 mg, 99 mg, and 132 mg) on SiO_2/Si substrates with an identical surface area of 12,56 cm^2. The NiO nanoparticle thin films on the substrate surface were then placed into a CVD reactor and reduced in a hydrogen atmosphere, resulting in the formation of nickel nanoparticles that acted as active catalysts during CNTs synthesis. Ethanol vapor was used as the sole carbon source without any carrier gas, which enabled precise and comparative evaluation of the CNTs yield. X-ray diffraction (XRD) and Raman spectroscopy were employed to characterize the obtained CNTs. XRD results showed that CNTs with high crystallinity were produced when a 51,7 mg catalyst thin film was used. Raman spectroscopy confirmed the presence of RBM, G, D, and G′ peaks characteristic of CNTs structures. Increasing the catalyst mass led to a rise in RBM frequency and a decrease in CNTs diameter. However, an increase in catalyst mass also caused a reduction in CNTs yield. The highest yield (445%) was observed for Ni nanocatalysts with a mass of 51,7 mg. These findings demonstrate that the thickness of the catalyst layer and its surface distribution density on the substrate play a crucial role in determining the growth efficiency and structural quality of CNTs.
Keywords: *Carbon nanotubes; NiO catalyst; Sol-gel method; CVD; Substrate–nanocatalyst interface; RBM; Yield*
PACS: 61.46-w, 61.46.+w, 61.46.Np

INTRODUCTION

CNTs are nanoscale materials characterized by high strength, light weight, and unique electronic, thermal, and optical properties. They possess significant potential for application in future technologies, particularly in nanoelectronics, sensing, energy storage devices, hydrogen energy, biomedicine, and nanocomposites [1–3]. The synthesis of CNTs has attracted considerable attention from researchers, especially vertically aligned nanotubes, which offer major technological advantages. However, achieving high-quality growth and high productivity requires the synergistic interaction of multiple factors, notably the nature of the catalyst, the substrate material, synthesis conditions, and the properties of the interface [4, 5].

The growth of CNTs is typically carried out using the CVD method, in which nanoparticles of the nanocatalyst play an active role on the substrate surface. The nanocatalyst-substrate interface (i.e., the interaction between them, contact angle, surface energy, and structural stability) determines the growth mechanism and type of CNTs (single-walled or multi-walled) [6,7].

Several studies have shown that the smaller the contact angle at the interface, the better the spreading of catalyst particles on the substrate, which ensures their superior thermal stability [8]. This is a critical condition for the aligned and continuous growth of nanotubes. For example, in CNTs synthesized on SiO_2/Si substrates using Ni or Fe catalysts, interfacial forces and excess charge distribution in the substrate directly influenced growth efficiency [9–11].

Additionally, the presence of an intermediate oxide layer (e.g., Al_2O_3, MgO, and TiO_2) on the substrate can prevent catalyst agglomeration and maintain its activity over an extended period [12]. In such cases, the interface between the substrate surface and the catalyst acts as an active site. Certain studies have also revealed that the presence of Na^+ or Mg^{2+} ions in the substrate composition can affect the catalytic process, as these ions participate in diffusion processes and alter the electronic structure of the interface [13].

The size, distribution, and isolated positioning of catalyst particles on the substrate surface are also of critical importance. Their activity depends not only on chemical composition but also on the binding forces with the substrate and the interface energy [14]. Therefore, engineering the nanocatalyst-substrate interface becomes essential for controlling the synthesis process. Recent research has demonstrated that improving the interface can significantly enhance the yield of carbon nanotubes [15].

This study focuses specifically on analyzing the properties of the nanocatalyst–substrate interface to improve the growth and efficiency of carbon nanotubes.

EXPERIMENTAL PROCEDURE

a) Catalyst preparation.

The synthesis of NiO nanoparticles was carried out using the sol-gel spin coating method, a schematic of the synthesis process is shown in Figure 1.

Cite as: I.J. Abdisaidov, S.G. Gulomjanova, I.Kh. Khudaykulov, Kh.B. Ashurov, East Eur. J. Phys. 1, 256 (2026), https://doi.org/10.26565/2312-4334-2026-1-28

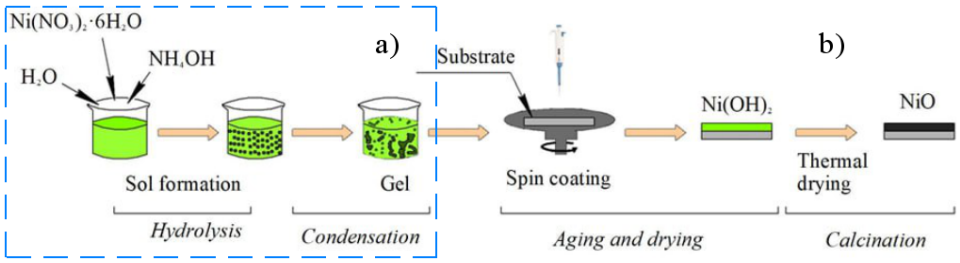

Figure 1. Schematic illustration of the formation of thin NiO layers with varying masses on the substrate surface

As seen in Figure 1, the formation of the NiO layer on the substrate surface consists of two steps:

a) preparation of a metal hydroxide sol using the sol–gel method [16];

b) formation of a thin metal hydroxide film on the substrate surface during the spin-coating process.

Initially, nickel nitrate [$Ni(NO_3)_2 \cdot 6H_2O$], ammonium hydroxide (NH_4OH), and deionized water were used as the starting reagents. An aqueous solution containing $Ni(NO_3)_2 \cdot 6H_2O$ and ammonium hydroxide in a 1:2 molar ratio was prepared and placed in a glass flask. The mixture was continuously stirred for 2 hours at a temperature of 85°C using a magnetic stirrer. After stirring, the resulting suspension was cooled to room temperature and allowed to age for 20 hours. The resultant $Ni(OH)_2$ was then used for the synthesis of carbon nanotubes. $Ni(OH)_2$ was applied onto three SiO_2/Si substrates with identical surface areas (12,56 cm^2) in different masses, and subsequently calcined in a SNOL laboratory furnace at 400°C for 2 hours. This thermal treatment resulted in the formation of a thin NiO layer on the surface of the substrates.

b) Synthesis of carbon nanotubes.

CNTs were synthesized using the CVD method. Ethanol vapor was employed as the hydrocarbon source, and no carrier gas was used to ensure accurate assessment of the ethanol vaporization efficiency and conversion. Nickel (Ni) nanoparticles, which were obtained by hydrogen reduction of the NiO synthesized through the sol-gel spin coating method, served as the catalyst for the CNTs growth. This process was carried out in the temperature range of 200÷400°C at a heating rate of 5°C/min. As a result, thin Ni nanocatalyst layers with different masses (51,7 mg, 77,6 mg, and 103 mg) were formed on the substrate surfaces. The synthesis process was then conducted at 500°C for 0,5 hours.

RESULTS AND DISCUSSION

In this study, the characterization of single-walled carbon nanotube (SWCNTs) samples was performed using XRD in order to acquire indirect information regarding the properties of the catalyst used. The XRD patterns, as shown in Figure 2, were obtained utilizing a Rigaku Smartlab X-ray diffractometer, employing CuKα radiation with a wavelength of 0.15405 nm, along with a Kβ filter to ensure accurate measurements. The experimental setup included a tube current of 50 mA and a tube voltage of 40 kV, optimizing the diffraction process. A range of angular 2θ values between 5° and 100° was explored, with the scanning rate set at 3° per minute. To ensure high precision in the analysis, the resolution of the 2θ scan was consistently maintained at 0.01°, providing a detailed and reliable dataset for subsequent analysis.

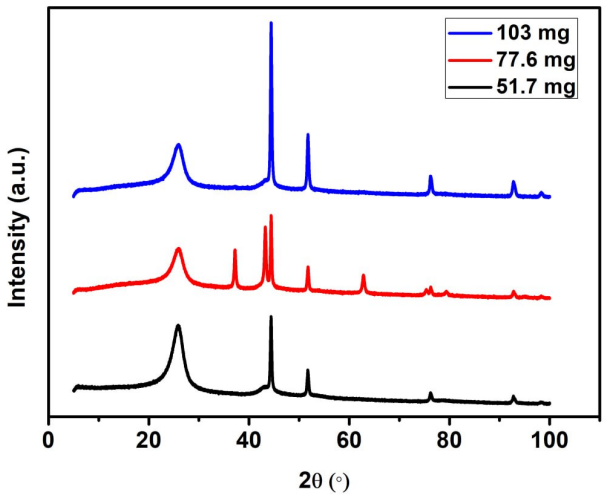

Figure 2. XRD diffractograms of the synthesized CNTs

Figure 2 presents the XRD spectra of CNTs synthesized via the CVD method on SiO_2/Si substrates of identical size, using a Ni nanocatalyst with varying thicknesses. It is important to note that the use of SiO_2/Si substrates - specifically the presence of a natural SiO_2 layer (~360 nm) on the Si surface prevents stress formation on the Si substrate at elevated temperatures and inhibits the formation of nickel silicide [17, 18]. The XRD analysis revealed several peaks

corresponding to the carbon structure, specifically the (002), (101), (201), (020), (222), and (112) planes. Of these, the (002) peak is considered the most significant, while the other peaks are less relevant [19]. This prominent (002) peak is located at approximately 2θ ≈ 25,89°, and its intensity can be used as an indicator of the crystallinity of the CNTs. In addition to the CNTs related peaks, the XRD spectrum also revealed the presence of Ni and NiO phases associated with the catalyst material. At temperatures above 400°C, nickel reacts with oxygen to form NiO, resulting in low-intensity NiO traces appearing in the diffraction spectrum [20]. According to the XRD analysis, a catalyst mass of 51,7 mg corresponding to a specific catalyst layer thickness leads to the formation of CNTs with higher crystallinity.

The samples were analyzed using Raman spectroscopy, produced by Renishaw, UK. Excitation was provided by a RL532 Class 3B laser, with a radiation wavelength of 532 nm. For the measurements, a diffraction grating with a period of 1200 lines/mm was employed to achieve high-resolution spectral data. A standard Renishaw CCD camera detector was utilized to record the Raman spectra, ensuring precise detection of the Raman shifts and providing reliable results for further analysis. Raman spectra were recorded over the range of 100÷3000 cm^{-1} (Figure 3).

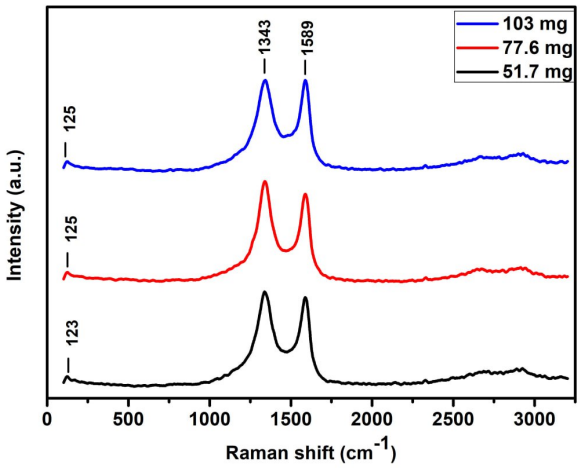

Figure 3. Raman spectrum of carbon nanotubes

From Figure 3, it is established that, with the same process of carbon nanotube growth, the mass of the catalyst does not affect the formation of carbon nanotubes. The peaks that characterize the most important properties of the Raman spectra of SWCNTs are: the RBM, observed in the range of 100÷300 cm^{-1}, the tangential G-band (characterizing the C-C bond) near the frequency of ~1572 cm^{-1} and the D-band caused by defects and disorder near the frequency of ~1300 cm^{-1} and its second-order harmonic (G'-band) in the frequency range of 2600÷2800 cm^{-1} [21]. As can be seen from Figure 3, the peaks characterizing SWCNTs are observed in the frequency ranges indicated above. Of these four properties, RBM is the property that is inversely proportional to the nanotube diameter, according to expression [22].

$$\omega_{RBM} = A/(dt) + B \quad (1)$$

Where: ω_{RBM} is the oscillation frequency, A and B are constants, and dt is the diameter of the carbon nanotube.

In addition, the quality of CNTs is evaluated by the ratio of the intensity of peak D to the intensity of peak G (I_D/I_G) [23]. If $I_D/I_G \approx 1$, it indicates the presence of more defects and low quality, and if $I_D/I_G < 1$, it indicates good quality of the synthesized CNTs. The influence of the catalyst layer, i.e. the mass of the catalyst, on the yield of the CNTs during the synthesis was also studied. The yield of the CNTs is calculated using formula (2) [24].

$$C_{yield} = (m_{tot} - m_{cat})/m_{cat} \cdot 100\% \quad (2)$$

Where: m_{tot} is the total mass, m_{cat} is the mass of the catalyst, C_{yield} is the yield of the CNTs.

In addition, the effect of catalyst layers on the masses of grown CNTs was studied (table 1).

Table 1. Effect of catalyst content on the yield of grown CNTs

Weight of NiO, (mg)	Weight of Ni, (mg)	Substrate	ω_{RBM} (cm^{-1})	I_D/I_G	d_t (nm)	Weight of CNTs, (g)	CNTs yield (%)
66	51.7	SiO_2 /Si	123	1.04	2.11	0.23	445
99	77.6		125	1.13	2.07	0.16	216
132	103		125	1.01	2.07	0.13	126

The analysis of the data in the table allows us to draw the following conclusions. When using the Ni catalyst mass of 51.7 mg, the RBM peak frequency was 123 cm^{-1}, the peak D intensity ratio was 1,04, and carbon nanotubes with a diameter of 2.11 nm and a mass of 0.23 were synthesized. With an increase in the catalyst mass to 77.6 mg, the RBM

peak frequency was 125 cm^{-1}, the peak D intensity ratio was 1.13, the diameter was reduced to 2,07 nm and the mass of the synthesized carbon nanotube was 0,16 grams. With a further increase in the catalyst mass to 103 mg, the RBM peak frequency was 125 cm^{-1}, the peak D intensity ratio was 1.01, the diameter of the carbon nanotubes was reduced to 2.07 nm, and the mass of the synthesized carbon nanotube was 0.13 grams.

The study shows that the catalyst layers affect the properties of the synthesized carbon nanotubes. A large number of catalyst layers increases the RBM peak frequency and decreases the diameter of carbon nanotubes. At the same time, a decrease in the catalyst layers leads to an increase in the mass of the synthesized carbon nanotubes. This conclusion is confirmed by the fact that the yield of CNTs according to formula (2) was also 445%, 216% and 126%, respectively.

CONCLUSIONS

In this study, the influence of the nanocatalyst/substrate interface on the yield and phase quality of CNTs synthesized by the CVD method was determined. During the reduction of NiO nanoparticles – prepared via the sol–gel spin-coating technique and deposited on the substrate surface in different masses - active nickel catalytic centers were formed, which subsequently governed the growth efficiency of the CNTs.

Analyses revealed that increasing the catalyst mass reduces the diameter of single-walled CNTs and increases the RBM frequency, while the overall yield decreases. The highest yield, 445%, was obtained using 51,7 mg of catalyst. XRD and Raman spectroscopy results confirmed that the synthesized nanotubes possessed a crystalline structure and exhibited characteristic vibrational bands. Furthermore, it was demonstrated that, within the substrate/oxide layer/catalyst triple interface, stress relaxation occurred and nickel silicidation was effectively suppressed.

Overall, the findings indicate that the catalyst coating thickness, the thickness of the native oxide layer, and its uniform distribution across the substrate surface play a decisive role in controlling CNTs growth efficiency, diameter, and phase quality.

Acknowledgments

The authors gratefully acknowledge the financial and technical support provided by the Ministry of Higher Education, Science, and Innovation under project number IL-5421101842.

ORCID

Ilyos J. Abdisaidov, https://orcid.org/0000-0001-7473-1074; **Ilyos Kh. Khudaykulov,** https://orcid.org/0000-0002-2335-4456
Khatam B. Ashurov, https://orcid.org/0000-0002-7604-2333

REFERENCES

[1] M. Diarra, *et al*., Physical Review Letters, **109**(18), 185501 (2012). https://doi.org/10.1103/PhysRevLett.109.185501
[2] B. Karakashov, M. Mayne-L'Hermite, and M. Pinault, Nanomaterials, **12**(13), 2300 (2022). https://doi.org/10.3390/nano12132300
[3] X. Zhao, *et al*., Accounts of chemical research, **55**(23), 3334 (2022). https://doi.org/10.1021/acs.accounts.2c00592
[4] D. Hedman, *et al*., Nature Communications, **15**(1), 4076 (2024). https://doi.org/10.1038/s41467-024-47999-7
[5] K. Awasthi, A. Srivastava, and O. N. Srivastava, Journal of nanoscience and nanotechnology, **5**(10), 1616-1636 (2005). https://doi.org/10.1166/jnn.2005.407
[6] E.R. Meshot, *et al*., Acs Nano, **3**(9), 2477 (2009). https://doi.org/10.1021/nn900446a
[7] L. Nánai, *et al*., Scientific Reports, **14**(1), 7307 (2024). https://doi.org/10.1038/s41598-024-57862-w
[8] J. Bora, *et al*., Applied Surface Science, **648**, 158988 (2024). https://doi.org/10.1016/j.apsusc.2023.158988
[9] J. Sengupta, and C. M. Hussain, Biosensors, **15**(5), 296 (2025). https://doi.org/10.3390/bios15050296
[10] S. Zecchi, *et al*., Micromachines, **16**(1), 53 (2024). https://doi.org/10.3390/mi16010053
[11] K.J. Hughes, *et al*., ACS Applied Nano Materials, **7**(16), 18695 (2024). https://doi.org/10.1021/acsanm.4c02721
[12] A. Venkataraman, *et al*., Nanoscale research letters, **14**(1), 220 (2019). https://doi.org/10.1186/s11671-019-3046-3
[13] Y. Hoshino, *et al*., Nuclear Instruments and Methods in Physics Research Section B: Beam Interactions with Materials and Atoms, 282, 125 (2012). https://doi.org/10.1016/j.nimb.2011.08.062
[14] X. Li, *et al*., Scientific Reports, **8**(1), 4349 (2018). https://doi.org/10.1038/s41598-018-22467-7
[15] Y. Lin, *et al*., Nature Electronics, **6**(7), 506 (2023). https://doi.org/10.1038/s41928-023-00983-3
[16] M. Parashar, V.K. Shukla, and R. Singh, Journal of Materials Science: Materials in Electronics, **31**(5), 3729 (2020). https://doi.org/10.1007/s10854-020-02994-8
[17] A.A. Ismatov, C. Romanitan, Kh.B. Ashurov, M.M. Adilov, and A.A. Rahimov, Eurasian Physical Technical Journal, **22**(3(53)), 5 (2025). https://doi.org/10.31489/2025N3/5-13
[18] A.A. Rakhimov, I.K. Khudaykulov, A.A. Ismatov, and M.M. Adilov, East European Journal of Physics, (3), 436-441 (2025). https://doi.org/10.26565/2312-4334-2025-3-47
[19] W.H. Tan, S.L. Lee, and C.T. Chong, Key Engineering Materials, **723**, 470 (2017). https://doi.org/10.4028/www.scientific.net/KEM.723.470
[20] S.P. Chai, S.H.S. Zein, and A.R. Mohamed, Diamond and related materials, **16**(8), 1656 (2007). https://doi.org/10.1016/j.diamond.2007.02.011
[21] Y. Guo, G. Zhai, Y. Ru, C. Wu, X. Jia, Y. Sun, *et al*., AIP Advances, **8**(3), 035111 (2018). https://doi.org/10.1063/1.5020936
[22] L.A. Bokobza, and J. Zhang, Express Polymer Letters, **6**(7), 601 (2012). https://doi.org/10.3144/expresspolymlett.2012.63
[23] A. C. Sparavigna, *et al*., International Journal of Sciences, 13(7), 1-26 (2024). https://doi.org/10.26434/chemrxiv-2024-xw377
[24] F. Taleshi *et al*., Fullerenes, Nanotubes and Carbon Nanostructures, **22**(10), 921 (2014). https://doi.org/10.1080/1536383X.2012.749456

ПІДВИЩЕННЯ ВИХОДУ ВУГЛЕЦЕВИХ НАНОТРУБОК ЧЕРЕЗ ІНТЕРФЕЙС НАНОКАТАЛІЗАТОР-СУБСТРАТ

Ільос Дж. Абдісаїдов, Севара Г. Гуломджанова, Ільос Х. Худайкулов, Хатам Б. Ашуров

Інститут іонно-плазмових та лазерних технологій імені У.А. Аріфова, Академія наук Республіки Узбекистан, 100125, вул. Дурмон йулі, 33, Ташкент, Узбекистан

У цьому дослідженні досліджувався вплив межі розділу нанокаталізатор/субстрат на вихід та якість вуглецевих нанотрубок (CNTs), синтезованих методом хімічного осадження з парової фази (CVD). Наночастинки оксиду нікелю (NiO) були отримані методом золь-гель спін-покриття та нанесені у вигляді тонких плівок з різною масою (66 мг, 99 мг та 132 мг) на підкладки SiO_2/Si з однаковою площею поверхні 12,56 $см^2$. Тонкі плівки наночастинок NiO на поверхні підкладки потім поміщали в CVD-реактор та відновлювали в атмосфері водню, що призводило до утворення наночастинок нікелю, які діяли як активні каталізатори під час синтезу вуглецевих нанотрубок. Пари етанолу використовувалися як єдине джерело вуглецю без будь-якого газу-носія, що дозволило точно та порівняльно оцінити вихід вуглецевих нанотрубок. Для характеристики отриманих вуглецевих нанотрубок використовували рентгенівську дифракцію (XRD) та раманівську спектроскопію. Результати XRD показали, що вуглецеві нанотрубки з високою кристалічністю утворювалися при використанні тонкої плівки каталізатора масою 51,7 мг. Раманівська спектроскопія підтвердила наявність піків RBM, G, D та G′, характерних для структур вуглецевих нанотрубок. Збільшення маси каталізатора призвело до зростання частоти RBM та зменшення діаметра вуглецевих нанотрубок. Однак збільшення маси каталізатора також призвело до зниження виходу вуглецевих нанотрубок. Найвищий вихід (445%) спостерігався для нанокаталізаторів Ni масою 51,7 мг. Ці результати демонструють, що товщина шару каталізатора та його поверхнева щільність розподілу на підкладці відіграють вирішальну роль у визначенні ефективності росту та структурної якості вуглецевих нанотрубок.

Ключові слова: *вуглецеві нанотрубки; NiO-каталізатор; золь-гель метод; CVD; межа між підкладкою та нанокаталізатором; RBM; вихід*

EAST EUROPEAN JOURNAL OF PHYSICS. 1. 261-265 (2026)
DOI:10.26565/2312-4334-2026-1-29 ISSN 2312-4334

FIELD PROPERTIES OF DIODE STRUCTURES BASED ON SOLID SOLUTION "SILICON-TIN"

Khurshidjon M. Madaminov[1]*, Azizbek A. Abdurakhmonov[2], Avazbek Sh. Ikromov[1], Gulkhayot S. Kholyigitova[3]
[1]*Andijan State University, 129 Universitet st., Andijan, Uzbekistan,*
[2]*Ferghana State University, 19 Murabbiylar st., Ferghana, Uzbekistan*
[3]*Andijan State Technical Institute, 56 Boburshokh st., Andijan, Uzbekistan*
**Corresponding Author e-mail: aduxurshid@gmail.com*
Received August 26, 2025; revised December 12, 2025; accepted January 16, 2026

This article presents the results of studies of the conductivity mechanism in pSi-n$Si_{1-\delta}Sn_\delta$ ($0 \le \delta \le 0.04$) structures based on the $Si_{1-\delta}Sn_\delta$ solid solution with base n-layer thicknesses W ≈ 20-30 μm. The studied samples were obtained in a single technological cycle using liquid-phase epitaxy on single-crystal p-Si substrates with the (111) orientation. Experimental and computational studies showed that the Poole-Frenkel effect is observed in pSi-n$Si_{1-\delta}Sn_\delta$ ($0 \le \delta \le 0.04$) structures at room temperature. This circumstance allows the use of high voltage effects on the parameters of various devices based on the solid solution $Si_{1-\delta}Sn_\delta$. Thus, there is interest in using this effect to convert thermal energy into electrical energy via the thermovoltaic effect. Also, results show the potential of using solid solutions $Si_{1-\delta}Sn_\delta$ ($0 \le \delta \le 0.04$), grown on silicon substrates, as an active material in thermal energy converters.
Keywords: *Liquid-phase epitaxy; Current-voltage characteristic; Field mechanism; Frenkel coefficient; Activation of charge carriers; Concentration of ionized traps; Thermovoltaic effect*
PACS: 73.40.Lq, 77.55.df, 61.82.Fk

INTRODUCTION

Recently, the study of electrophysical processes in semiconductor solid solutions of the $A^{IV}B^{IV}$ type has become increasingly relevant [1]. Analysis of the results of the studies showed that such solid solutions are promising for the creation of lasers, light modulators, photoconverters, and other functional devices [2].

It is known that by changing the zone structure parameters of solid solutions, it is possible to create new, more effective materials for various technological fields with the required combinations of physical characteristics [3-5].

One way to change the band structure of semiconductors is to apply a high voltage to the sample (the Poole-Frenkel effect). The effect is that when sufficiently large electric fields are applied to the semiconductor sample, the activation energy for electrons from the electron energy levels decreases due to the additional energy imparted by the field.

The semiconductor compound $Si_{1-x}Sn_x$, belonging to the above-mentioned type $A^{IV}B^{IV}$, has a number of distinctive properties that allow them to be used in the manufacture of various semiconductor devices [6-8], while the temperature range of their operation depends on the activation energy of charge carriers [9-10]. Thus, it is of interest to study the possibility of changing the activation energy of electrons by the action of electric fields, i.e. the presence of the Poole-Frenkel effect [11-12] and its parameters of solid solutions $Si_{1-\delta}Sn_\delta$ [13-14]. Based on this, this work is devoted to studying the influence of the base region thickness on the electrical conductivity and on the shape of the potential well-formed near the impurity centers in pSi-n$Si_{1-\delta}Sn_\delta$ structures.

MATERIALS AND METHODS

Formation of solid solutions of $Si_{1-\delta}Sn_\delta$. The possibility of forming solid substitution solutions of $A^{IV}B^{IV}$ molecules is determined by their charge states and geometric dimensions, as well as the type of crystal lattices of the components of solid solutions. Academician M.S. Saidov proposed the conditions for the formation of continuous substitution solid solutions in the following form [15-16]

$$\Delta z = \sum_{i=1} z_i^m - \sum_{i=1} z_i^n = 0, \quad (1)$$

$$\Delta r = \sum_{i=1} r_i^m - \sum_{i=1} r_i^n \le 0{,}1 \sum_{i=1} r_i^m, \quad (2)$$

where z_i^m, z_i^n – valence, r_i^m, r_i^n – covalent radius of the atoms of the solvent m and dissolved n chemical element or elements that form the molecules of the solvent and dissolved compounds, respectively, *i=1, 2, 3, 4.*

When the dissolving and solute elements or molecules are isovalent with each other, they are electrically neutral and condition (1) is fulfilled. It is known that the solubility of an atomic or molecular compound of a dissolved

Cite as: Kh.M. Madaminov, A.A. Abdurakhmonov, A.Sh. Ikromov, G.S. Kholyigitova, East Eur. J. Phys. 1, 261 (2026), https://doi.org/10.26565/2312-4334-2026-1-29

component of solid solutions depends on its comparative size with the corresponding size of the solvent. The closer the corresponding sizes of atoms or molecules of the components of solid solutions, the weaker the energy of elastic deformations of the crystal lattice, and the greater the mutual solubility of the solution-forming components, and therefore, the greater the crystalline perfection of solid solutions. When the difference in the sum of the covalent radii of the atoms of the molecules of the solution-forming components is greater than 10%, the formation of solid substitution solutions of these components is insignificant [16].

The sum of the valences of the atoms of the Si_2 and SiSn molecules is equal, and the conditions of electroneutrality (1) are satisfied for them:

$$\Delta z = (z_{Si} + z_{Si}) - (z_{Si} + z_{Sn}) = 0 \tag{3}$$

where z_{Si} and z_{Sn} are the valences of silicon and tin atoms, respectively. The sums of the covalent radius of the atoms of the Si_2 and Sn molecules have close values, then from condition (2) we can obtain:

$$\Delta r = \left|(r_{Si} + r_{Si}) - (r_{Si} + r_{Sn})\right| = \left|2{,}34\overset{0}{A} - 2{,}51\overset{0}{A}\right| \approx 0{,}073 \cdot (r_{Si} + r_{Si}) < 0{,}1(r_{Si} + r_{Si}) \tag{4}$$

Where r_{Si} and r_{Sn} covalent radius of silicon and tin atoms according to Pauling, respectively [17]. From (4) it is evident that the difference in the sums of the covalent radii of the atoms of the Si_2 and SiSn molecules is about 7.3%, therefore, these components satisfy the condition for the formation of a continuous substitution solid solution presented in [18].

Substitution of Si_2 by a SiSn molecule does not strongly deform the crystal lattice, while the energy of elastic distortions of the crystal lattice will be insignificant and the substitution solid solution in the form of $Si_{1-\delta}Sn_\delta$ is a stable solid phase. The spatial configuration of two stable tetrahedral bonds of the $Si_{1-\delta}Sn_\delta$ solid solution is shown in Fig. 1.

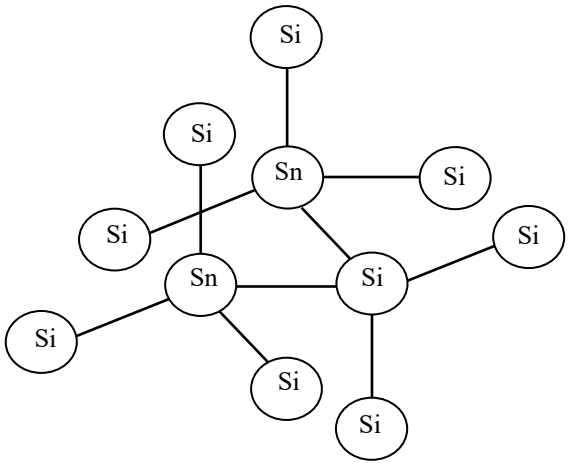

Figure 1. Hypothetical crystal lattice of the solid solution $Si_{1-\delta}Sn_\delta$

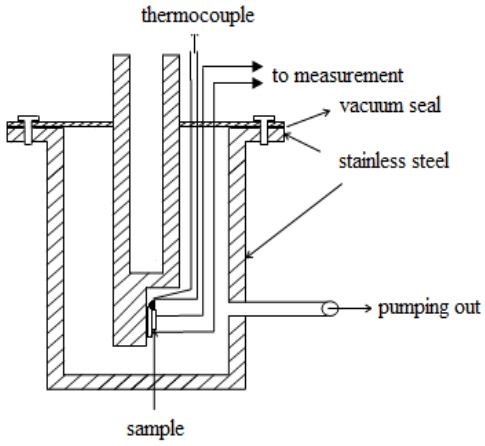

Figure 2. Metal cryostat for taking measurements

Sample preparation and research methods. Solid solutions of $Si_{1-\delta}Sn_\delta$ were grown by liquid-phase epitaxy from a limited volume of tin (Sn) melt solution in a hydrogen atmosphere. Hydrogen was purified by passing through a palladium tube. The film growth process was carried out by forced cooling of the melt solution. Liquid-phase epitaxy was carried out on a vertically positioned quartz reactor with horizontally positioned substrates. To obtain a good interface between the substrate and the epitaxial film, close values of the lattice parameters, thermal expansion coefficients and crystal structure of the substrate and film materials are required [19]. On the other hand, the substrate material must be accessible and well studied. It is known that among elementary semiconductors, silicon and tin are accessible and fairly well studied materials. The linear thermal expansion coefficients of Si and Sn are $4.2 \cdot 10^{-6}$ 1/K [20] and $23.4 \cdot 10^{-6}$ 1/K [21], respectively. Therefore, Si is a suitable material for obtaining a good quality $Si_{1-\delta}Sn_\delta$ solid solution layer.

The elemental chemical compositions of the surface and transverse cleavage of as grown $Si_{1-\delta}Sn_\delta$ solid solution epilayers were studied on a JSM 5910LV X-ray electron probe microanalyzer (JEOL, Japan). It was found that both components are uniformly distributed over the surface, while composition in depth of the film varies within $0 \le \delta \le 0.04$, as in [22].

In addition, it is known that the crystallographic plane with the orientation (111) has two broken bonds, and the plane (100) has one broken bond. Therefore, elementary semiconductors grow well on substrates with the orientation (111), but it is quite difficult to obtain a high-quality film on substrates with the orientation (100) [23]. Therefore, Si washers with the crystallographic orientation (111) and a specific resistance of 1 Ω·cm were used as substrates. The thickness of the film layers varied within 10-40 μm, depending on the growth mode and the thickness of the gap between the substrates. The grown layer thicknesses were determined using a thickness gauge EV-01.

To conduct the studies, pSi-n$Si_{1-\delta}Sn_\delta$ structures were fabricated by growing a solid solution of $Si_{1-\delta}Sn_\delta$ with n-type conductivity and a resistivity of $\rho \approx 0.8$ Ω·cm. When measuring the current-voltage characteristics, samples with a thickness of 10-40 μm of the epitaxial layer of the solid solution were used. Ohmic current-collecting contacts, solid on the back side and quadrangular with an area of 9 mm^2 on the side of the epitaxial layer, were created by vacuum deposition of silver, at a pressure of ~ $1.33 \cdot 10^{-3}$ Pa. The current-voltage characteristics of the pSi-n $Si_{1-\delta}Sn_\delta$ heterostructures were measured in the dark at different values of the thickness of the $Si_{1-x}Sn_x$ epitaxial layer in the forward and reverse directions of the current at bias voltages from -3 to +5 V. For this, the samples were mechanically tightly fixed to a metal cryostat, which was evacuated to a residual pressure of ~ 0.133 Pa (Fig. 2).

As a voltage source we used the B5-11 power supply. The voltage across the sample was measured with the VK7-9 volt-ohmmeter, and the current through the semiconductor structure was measured with the combined device Sh-300. The VK7-9 voltmeter was connected directly to the sample terminal and only in this case we were able to correctly measure the voltage on the sample, since during the measurement a redistribution of the voltage supplied to the circuit between the sample and the divider may occur.

RESULTS AND DISCUSSION

Figure 3 shows the current-voltage characteristics of pSi-n $Si_{1-\delta}Sn_\delta$ structures with different thicknesses of the $Si_{1-\delta}Sn_\delta$ solid solution at room temperature (293 K). From Fig. 3 it is evident that the dependence of the magnitude of the direct current on the applied voltage, for all values of the $Si_{1-\delta}Sn_\delta$ thickness, is nonlinear. The magnitude of the current through pSi-n$Si_{1-\delta}Sn_\delta$ increases and changes by 1-2 orders of magnitude, i.e. the I-V characteristic has a diode character. The following 2 sections are revealed on the current-voltage characteristic: 1 - ohmic $(I \propto U)$ and 2 - the region of sharp current growth $(I \propto U^m,\ m > 1)$. It is evident that the transient voltages from the ohmic region to the sharp current growth decrease as thickness decreases. This proves the presence of the Poole-Frenkel effect in the studied samples.

According to the Poole-Frenkel theory, which explains the Poole-Frenkel effect, the growth of the field dependence of conductivity is represented as [12, 24]

$$\sigma = \sigma_0 \exp(\beta\sqrt{E}), \tag{5}$$

here β - is the Frenkel coefficient and it is determined by the slope of the dependence $\ln\sigma = f(\sqrt{E})$.

Fig. 4 shows the calculated dependences of electrical conductivity at room temperature in coordinates $\ln\sigma = f(\sqrt{E})$ for the region of sharp current growth in the I-V characteristics of the pSi-n$Si_{1-\delta}Sn_\delta$ structure, with a base region thickness of d = 20 μm. From the graphical data, the values of the Frenkel coefficient were determined, which amounted to $\approx 8.7 \cdot 10^{-2} (cm/V)^{1/2}$.

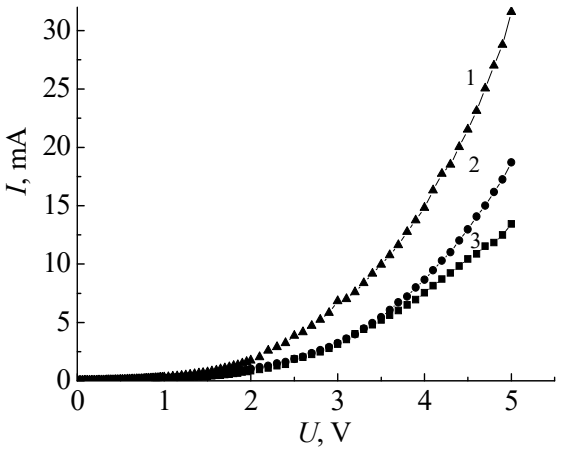

Figure 3. Forward currents of dark I-V characteristics pSi-n$Si_{1-\delta}Sn_\delta$ structures at T=293 K.
Sample thickness, μm: 1 - 20, 2 - 25, 3 – 30

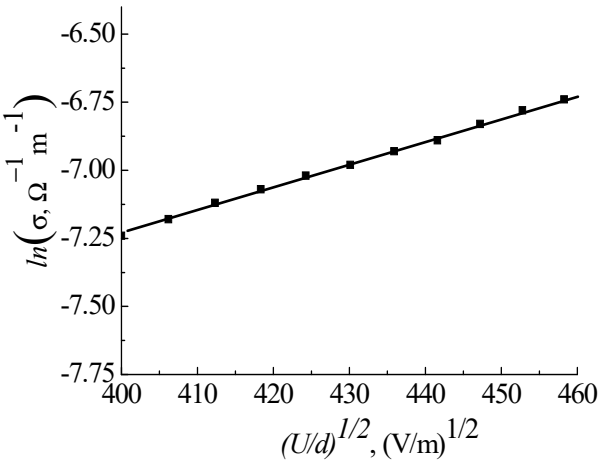

Figure 4. Dependence of electrical conductivity on the electric field, at T=293 K for pSi-n$Si_{1-\delta}Sn_\delta$ structures

It is known that by determining the critical value of the electric field corresponding to the beginning of the nonlinear dependence of electrical conductivity on the applied voltage, according to the expression [12]

$$N_t = \left(\frac{2e}{kT\beta} \sqrt{E_{cr}} \right)^3 \tag{6}$$

It is possible to determine the concentration of defects (N_t) responsible for the conductivity of the pSi-n $Si_{1-\delta}Sn_\delta$ structure.

Based on the values of the critical electric field E_{cr}, at which Ohm's law is violated, the concentrations of ionized centers in the studied structures were determined using formula (6). Based on data from experiments conducted on different samples (with a thickness of d = 20 ÷ 30 μm), the average trap concentration of ~$2{,}4\cdot10^{14}$ cm^{-3} was obtained.

CONCLUSIONS

Thus, pSi-n$Si_{1-\delta}Sn_\delta$ ($0 \le \delta \le 0.04$) structures with base n-layer thicknesses W ≈ 20-30 μm were manufactured in a single technological cycle by the liquid-phase epitaxy method on single-crystal p-Si substrates with the (111) orientation. The study of the conductivity mechanism in pSi-n$Si_{1-\delta}Sn_\delta$ structures based on the solid solution $Si_{1-\delta}Sn_\delta$ obtained by liquid-phase epitaxial was carried out. Based on the analysis of the dependence $\ln\sigma = f(\sqrt{E})$, the value of the Frenkel coefficient β was determined and it was established that the nonlinearity of the current-voltage characteristics of these structures is due to the Poole-Frenkel effect. The concentration of ionized centers (traps), the values N_t of which strongly depend on the field effect, was also estimated.

The experimental and calculated results allow us to conclude that in our experiments at room temperature in pSi-n$Si_{1-\delta}Sn_\delta$ ($0 \le \delta \le 0.04$) structures, the Poole-Frenkel effect is observed. The presence of this effect in the solid solution $Si_{1-\delta}Sn_\delta$ allows us to apply high-voltage effects to the parameters of various devices based on this semiconductor [25]. The most realistic application of the Poole-Frenkel effect in converters of thermal energy into electrical energy together with the thermovoltaic effect seems to be [4, 26-29].

ORCID

Kh.M. Madaminov, https://orcid.org/0000-0003-0117-9316; **A.A. Abdurakhmonov**, https://orcid.org/0009-0007-6758-2585;
A.Sh. Ikromov, https://orcid.org/0009-0009-3145-1326; **G.S. Kholyigitova**, https://orcid.org/0009-0003-4232-4046

REFERENCES

[1] S.Yu. Davydov, "Estimates of the dielectric and optical characteristics for the IV group 3D- and 2D-binary compounds," Physics of the Solid State, **2**(65), 180-184 (2023). http://dx.doi.org/10.21883/PSS.2023.02.55398.491 (in Russian).
[2] Y.M. Basalaev, and E.N. Malysheva, "Electronic structure of single-layer superlattices $(GeC)_1(SiC)_1$, $(SnC)_1(SiC)_1$, and $(SnC)_1(GeC)_1$" Semiconductors **51**, 617–620 (2017). https://doi.org/10.1134/S1063782617050050
[3] P. Lou, and J.Y. Lee, "GeC/GaN vdW Heterojunctions: A Promising Photocatalyst for Overall Water Splitting and Solar Energy Conversion," ACS Appl. Mater. Interfaces, **12**(12), 14289–14297 (2020). https://doi.org/10.1021/acsami.9b20175
[4] A.S. Saidov, A.Y. Leyderman, and A.B. Karshiev, "The thermovoltaic effect in variband solid solution $Si_{1-x}Ge_x$ ($0 \le x \le 1$)," Tech. Phys. Lett. **42**, 725–728 (2016). https://doi.org/10.1134/S1063785016070270
[5] R. Khalil, "Electrical characteristics of (AgNPs-PVA)-based Schottky diode and its application as a low-voltage varistor devices," Physica Scripta, **97**(12), 125832 (2022). https://doi.org/10.1088/1402-4896/aca2f3
[6] H. ElGhonimy, M.R. Abdel-Rahman, M. Hezam, M.A. Alduraibi, N.F. Al-Khalli, and B. Ilahi, "Amorphous SiSn alloy: another candidate material for temperature sensing layers in uncooled microbolometers," Phys. Status Solidi (b), **258** (2021). http://dx.doi.org/10.1002/pssb.202100103
[7] Z. Li, H.-Z. Gao, W.-R. Xu, J.-M. Wang, W. Li, and X.-D. Jiang, "Optoelectronic artificial synapse based on $Si_{1-x}Sn_x$ alloyed film," Vacuum, **6**(212), 112002 (2023). https://doi.org/10.1016/j.vacuum.2023.112002
[8] A.M. Hussain, N. Wehbe, and M.M. Hussain, "SiSn diodes: theoretical analysis and experimental verification," Appl. Phys. Lett. **107**, (2015), https://doi.org/10.1063/1.4929801
[9] A.A. Shiryaev, V.M. Vorotyntsev, and E.L. Shobolov, "Poole-Frenkel Effect and the Opportunity of Its Application for the Prediction of Radiation Charge Accumulation in Thermal Silicon Dioxide," Semiconductors, **52**, 1114–1117 (2018). https://doi.org/10.1134/S1063782618090166
[10] N.D. Zhukov, A.I. Mikhailov, and D.S. Mosiyash, "Mechanism and Features of Field Emission in Semiconductors," Semiconductors, **53**, 321–325 (2019). https://doi.org/10.1134/S1063782619030229
[11] H. Wong, and K. Kakushima, "Poole-Frekel (PL)-MOS: A proposal for the Ultimate Scale of an MOS Transistor", Nanomaterials, **13**(3), 411 (2023). https://doi.org/10.3390/nano13030411
[12] P. Mainali, P. Wagle, C. McPherson, and D.N. McIlroy, "The Impact of Trap-Assisted Tunneling and Poole–Frenkel Emission on Synaptic Potentiation in an α-Fe_2O_3/p-Si Memristive Device," Sci, **5**(1), 3 (2023). https://doi.org/10.3390/sci5010003
[13] Kh.M. Madaminov, "Temperature dependences of the electrophysical properties of the solid solution $Si_{1-x}Sn_x$ ($0 \le x \le 0.04$)," Applied Physics, **1**, 63-68 (2021), https://doi.org/10.51368/1996-0948-2021-1-63-68 (in Russian).
[14] A.S. Saidov, Sh.N. Usmonov, M.U. Kalanov, Kh.M. Madaminov, and D.A. Nishanova, "Effect of Gamma Irradiation on Photoconductivity and Photosensitivity of $Si_{1-x}Sn_x$ Solid Solutions," Applied Solar Energy, **47**(1), 48-51 (2010). https://doi.org/10.3103/S0003701X11010142
[15] A.S. Saidov, D.V. Saparov, Sh.N. Usmonov, A.Sh. Razzakov, and M. Kalanov, "Features of liquid-phase epitaxy of new solid solutions of $(GaAs)_{1-y-z}(Ge_2)_y(ZnSe)_z$ and their photoelectric properties," International Journal of Modern Physics B, **14**(37), 2350132 (2023). https://doi.org/10.1142/S0217979223501321
[16] M.S. Saidov, "New semiconductor materials for thin film solar cells," Applied Solar Energy, **29**(2), 10-14 (1993).
[17] Sh.K. Ismailov, A.S. Saidov, Sh.N. Usmonov, D.V. Saparov, D.O. Eshonkhojaev, U.P. Asatova, and S.G. Bobojanov, "Investigation of the Spectral Photosensitivity of nGaAs-$n^+(GaAs)_{1-x-y}(Ge_2)_x(ZnSe)_y$ Heterostructure Obtained from Bi Solution-Melt," The Transactions of the Korean Institute of Electrical Engineers, **6**(73), 980-986 (2024). https://doi.org/10.5370/KIEE.2024.73.6.980

[18] Kh.M. Madaminov, “Influence of recombination processes on the temperature dependence of the current-voltage characteristics of *p*Si–*n*$(Si_2)_{1-x}(CdS)_x$-structures,” Herald of the Bauman Moscow State Technical University, Series Natural Sciences, **2** (119), 35–51 (2025), EDN: JBOXKK. (in Russian).
[19] S.Z. Zaynabidinov, Kh.M. Madaminov, “Charge transport mechanism in *p*-Si–*n*-$(Si_2)_{1-x}(CdS)_x$ semiconductor structures. Herald of the Bauman Moscow State Technical University, Series Natural Sciences. **4**(91), 58–72 (2020). https://doi.org/10.18698/1812-3368-2020-4-58-72 (in Russian).
[20] T.L. Altshuler, “Thermal Expansion of Silicon Between 293 K and 873 K Using a Capacitor Dilatometer,” Int. J. Thermophys. **44**, 126 (2023). https://doi.org/10.1007/s10765-023-03232-z
[21] C.A. Swenson, “Recommended Values for the Thermal Expasivity of Silicon from 0 to 1000 K,” J. Phys. Chem. Ref. Data, **2**(12), 179-182 (1983). https://doi.org/10.1063/1.555681
[22] A.Sh. Ikromov, A.A. Abdurakhmonov, and Kh.M. Madaminov, “Statical Currents of p-Si–n-$Si_{1-\delta}Sn_\delta$–n^+-$Si_{1-\delta}Sn_\delta$ ($0\leq\delta\leq0.04$)-Structures with Tin Quantum Dots,” East Eur. J. Phys. (3), 309 (2025), https://doi.org/10.26565/2312-4334-2025-3-28
[23] A.M. Pashaev, B.G. Tagiev, and O.B. Tagiev, “Poole-Frenkel effect in chalcogenide semiconductors with various crystalline structures,” Phys. Solid State, **55**, 937–942 (2013). https://doi.org/10.1134/S1063783413050284
[24] N.N. Niftiev, M.A. Alidzhanov, O.B. Tagiev, *et al.* “Electrical properties of $FeIn_2Se_4$ single crystals,” Semiconductors, **37**, 165–167 (2003). https://doi.org/10.1134/1.1548658
[25] Kh.M. Madaminov, **“**Effect of injection phenomena on electrical properties of pSi-n$Si_{1-x}Sn_x$ heterojunctions,” Herald of the Bauman Moscow State Technical University, Series Natural Sciences, **2**(95), 71-84 (2021). https://doi.org/10.18698/1812-3368-2021-2-71-84 (in Russian).
[26] R. Khalil, H. El-Desouky, R. Sobhy, and M.K. El-Mansy, “Electrical characterization of AgNPs-PVA nanocomposites thin film-based heterojunction diode,” Physica Scripta, **98(**4), 045805 (2023). https://doi.org/10.1088/1402-4896/acbe77
[27] Pramod Reddy, Dolar Khachariya, Will Mecouch, M. Hayden Breckenridge, Pegah Bagheri, Yan Guan, Ji Hyun Kim, Spyridon Pavlidis, Ronny Kirste, Seiji Mita, Erhard Kohn, Ramon Collazo, and Zlatko Sitar, “Study on avalanche breakdown and Poole–Frenkel emission in Al-rich AlGaN grown on single crystal AlN,” Appl. Phys. Lett. **119**, 182104 (2021); doi: 10.1063/5.0062831
[28] N.D. Zhukov, A.I. Mikhailov, D.S. Mosiyash, “Mechanism and Features of Field Emission in Semiconductors,” Semiconductors, **53**, 321–325 (2019). https://doi.org/10.1134/S1063782619030229
[29] M.M. Kazanin, V.V. Kaminski, and M.A. Grevtsev, “On the Poole-Frenkel Effect in Polycrystalline Europium Sulfide,” Semiconductors, **53**, 872–874 (2019). https://doi.org/10.1134/S1063782619070121.

ПОЛЬОВІ ВЛАСТИВОСТІ ДІОДНИХ СТРУКТУР НА ОСНОВІ ТВЕРДОГО РОЗЧИНУ "КРЕМНІЙ-ОЛОВО"

Хуршиджон М. Мадамінов[1], Азізбек А. Абдурахмонов[2], Авазбек Ш. Ікромов[1], Гулхаєт С. Холійгітова[3]
[1]Андижанський державний університет, вул. Університетська, 129, Андижан, Узбекистан
[2]Ферганський державний університет, вул. Мураббійлар, 19, Фергана, Узбекистан
[3]Андижанський державний технічний інститут, вул. Бобуршох, 56, Андижан, Узбекистан

У цій статті представлено результати досліджень механізму провідності в структурах pSi-n$Si_{1-\delta}Sn_\delta$ ($0 \leq \delta \leq 0{,}04$) на основі твердого розчину $Si_{1-\delta}Sn_\delta$ з базовою товщиною n-шарів W ≈ 20-30 мкм. Досліджувані зразки були отримані в одному технологічному циклі методом рідкофазної епітаксії на монокристалічних підкладках p-Si з орієнтацією (111). Результати експериментальних та обчислювальних досліджень показали, що ефект Пула-Френкеля спостерігається в структурах pSi-n$Si_{1-\delta}Sn_\delta$ ($0 \leq \delta \leq 0{,}04$) за кімнатної температури. Ця обставина дозволяє використовувати вплив високої напруги на параметри різних пристроїв на основі твердого розчину $Si_{1-\delta}Sn_\delta$. Таким чином, існує інтерес до використання цього ефекту в перетвореній теплової енергії в електричну на основі термовольтаїчного ефекту. Також отримані результати показують потенціал використання твердих розчинів $Si_{1-\delta}Sn_\delta$ ($0 \leq \delta \leq 0{,}04$), вирощених на кремнієвих підкладках, як активного матеріалу в перетворювачах теплової енергії.

Ключові слова: *рідкофазна епітаксія; вольт-амперна характеристика; польовий механізм; коефіцієнт Френкеля; активація носіїв заряду; концентрація іонізованих пасток; термоелектричний ефект*

EAST EUROPEAN JOURNAL OF PHYSICS. 1. 266-273 (2026)
DOI:10.26565/2312-4334-2026-1-30 ISSN 2312-4334

INVESTIGATION OF PHYSICAL, OPTO-ELECTRONICS AND INSULATING PROPERTIES OF PPPCC LIQUID CRYSTAL MOLECULE BY DENSITY FUNCTIONAL THEORY (DFT) METHOD: A THEORETICAL APPROACH

Tikaram, Yogesh Kumar, Narinder Kumar*
Department of physics, School of applied and life sciences (SALS), Uttaranchal University, Dehradun, India-248007
**Corresponding Author email: knarinder7@gmail.com*
Received September 3, 2025; revised January 13, 2026; accepted January 31, 2026

In this paper, we have studied the physical, electro-optical and thermal properties of PPPCC liquid crystal molecule. Density functional theory (DFT) with the B3LYP functional and the 6-31G(d,p) basis set is employed for the optimization and analysis of the p-Propoxyphenyl trans-4-pentylcyclohexanecarboxylate (PPPCC) LC molecule. Various physical properties, such as HOMO-LUMO energy levels, electro-optical properties, and global parameters, are computed and analysed for the PPPCC liquid crystal. We have reported the birefringence of p-Propoxyphenyl trans-4-pentylcyclohexanecarboxylate (PPPCC) liquid crystal under the effect of an external electric field. The UV-Visible analysis leaves a strong peak at 252 nm due to π-π* transitions. HOMO-LUMO band gap found to be 5.1 eV. The maximum stretching was observed at 1000 cm^{-1} due to the C-O stretching caused by the Ether in the PPPCC liquid crystal. The C-C stretching around 1600 cm^{-1} is found due to phenyl group present in PPPCC. The temperature-sensitive birefringence value of PPPCC makes it a suitable choice for modern optical technology applications. The refractive index remains unchanged at large applied electric fields, making it a suitable choice for opto-electronic devices in THz applications. Due to the large band gap, this molecule could be a suitable choice for insulating applications.
Keywords: *PPPCC; Electric field (THz); HOMO-LUMO; UV-Visible; IR; DFT*
PACS: 61.30.-b, 61.30.Dk, 61.30.Jf, 61.30.Gd, 78.30.-j

1. INTRODUCTION

Liquid crystals (LCs) have properties of both solids and liquids. In recent years, LCs have gained the interest of researchers due to their potential applications in display technology. LCs possess a mesomorphic phase due to the molecular arrangement in the compound. Further study of the mesomorphic phase of LCs has led to the development of new materials for optoelectronic applications. Also, understanding the various properties of LCs leads to modifying existing ones. LCs have the property of changing their alignment under an external electric field. This property of LCs is helpful for researchers to develop high-performance display devices [1].

To investigate the various properties of LCs, it is important to understand the structural and chemical properties of the material. Also, it is important to understand the correlation of mesogenic phase of LCs with temperature and chemicals. In general, the shape and size of the molecule influence the property and phase transition behaviour of LC substances [2]. Intra and inter molecular interactions alter the molecular property of the molecule during the LC phase. As a result, vibrational spectroscopy has a high potential for understanding the compound's molecular dynamics. IR spectroscopy is an important tool to reveal the molecular dynamics in the LC molecule [3-6]. Also, molecular polarizability plays an important role to define the opto-electronic properties of LC molecule. Modifying the shape, size and arrangement of atoms in the molecule, researchers can create the new LC molecule with desired opto-electronic properties which is useful for making modern opto-electronic devices such as LCDs [7-10].

In recent years, computational techniques have been modified a lot. Researchers have tested various computational techniques over the past years to investigate properties of LC molecules. Density functional theory (DFT) combined with the B3LYP functional gives good results for LC molecules [11]. This paper reports the molecular conformation, atomic orbital composition, electronic density, HOMO, LUMO, and relative energy gap of the PPPCC LC molecule. This LC molecule is known for its applications in liquid crystal technology applications.

The p-Propoxyphenyl trans-4-pentylcyclohexanecarboxylate (CAS No. 67589-54-2) is an organic compound. This compound has a molecular formula $C_{21}H_{32}O_3$ and a molecular weight of 332.48 g/mol. This compound consists of two groups; propoxyphenyl group and pentyl chain. These groups present in PPPCC LC molecule enhance the thermal stability of the material, makes it suitable for advanced material used in display devices. This compound has a density of 0.996 g/cm^3 and relatively high boiling point, which makes it suitable for high-temperature applications [12]. Further research on this compound continues to explore the tailored properties for advanced opto-electronic devices.

Also, the thermal stability and optical clarity of this compound make it suitable candidate for research in material science, particularly in synthesis of new LC compound with tailored properties. Understanding the various properties of this compound can lead to the advancement in theoretical and applied chemistry [13].

Cite as: Tikaram, Y. Kumar, N. Kumar, East Eur. J. Phys. 1, 266 (2026), https://doi.org/10.26565/2312-4334-2026-1-30

2. COMPUTATIONAL METHODOLOGY

Density functional theory (DFT) techniques using the NWChem Software optimises every molecule with basis set 6-31G** [14]. We are applying the electric field (a.u.) to the liquid crystal compound along the molecular axis (x-axis) and perpendicular axis (y-axis). At the intervals of 0.0020 (a.u.), the applied electric field ranges from 0.0000 (a.u.) to 0.1000 (a.u.), where 1 a.u. = 5.14 x 10^{11} V/m and 1 a.u. = 6.5 x 10^{12} Hz [15]. We have determined the molecular polarizability of the molecule upon the application of an electric field. Extraordinary molecular polarizability (α_e) is measured along the x-axis, whereas ordinary molecular polarizability (α_o) is measured along the y-axis. According to the following equations, we have determined the birefringence, order parameter, refractive index, and magic angle using α_e and α_o. where α, μ, and β stand for the first-order hyper-polarizability, dipole moment, and polarizability components, respectively [16].

$$\alpha = \frac{1}{3}(\alpha_{xx} + \alpha_{yy} + \alpha_{zz})$$

$$\beta = \left[(\beta_{xxx} + \beta_{xyy} + \beta_{xzz})^2 + (\beta_{yyy} + \beta_{xxy} + \beta_{yzz})^2 + (\beta_{zzz} + \beta_{xxz} + \beta_{yyz})^2\right]^{1/2}$$

$$\mu = (\mu_x^{\,2} + \mu_y^{\,2} + \mu_z^{\,2})^{1/2}$$

$$\Delta\alpha = 2^{-1/2}\left[(\alpha_{xx} - \alpha_{yy})^2 + (\alpha_{yy} - \alpha_{zz})^2 + (\alpha_{zz} - \alpha_{xx})^2\right]^{1/2}$$

$$\Delta\tilde{\alpha} = \alpha_e - \alpha_o$$

$$\Delta\tilde{\alpha} = S\Delta\alpha$$

Order Parameter (S):

$$S = \frac{\alpha_e - \alpha_o}{\alpha_e + \alpha_o} \tag{1}$$

Birefringence (Δn):

$$\Delta n = \frac{(\alpha_e - \alpha_o)}{6.3631}\left[R^3 - \left(\frac{2\alpha_o + \alpha_e}{20.244}\right)\right]^{-1} \tag{2}$$

Where, R is the radius of the liquid crystal molecule.

Magic angle (θ):

$$\theta = \cos^{-1}\left[\frac{(2S+1)}{3}\right] \tag{3}$$

Refractive index (n):

$$\alpha = \frac{2\alpha_o + \alpha_e}{3}, \quad \gamma_e = \alpha + \frac{2(\alpha_e - \alpha_o)}{3S}, \quad \gamma_o = \alpha - \frac{(\alpha_e - \alpha_o)}{3S} \quad n_e = \frac{7}{2\sqrt{10}} + \frac{\left(2\sqrt{10}/5\right)\pi N\alpha}{1 - \frac{4\pi N\alpha}{3}} + \frac{\left(4\sqrt{10}/15\right)\pi NS(\gamma_e - \gamma_o)}{1 - \frac{4\pi N\alpha}{3}}$$

$$n_o = \frac{7}{2\sqrt{10}} + \frac{\left(2\sqrt{10}/5\right)\pi N\alpha}{1 - \frac{4\pi N\alpha}{3}} - \frac{\left(2\sqrt{10}/15\right)\pi NS(\gamma_e - \gamma_o)}{1 - \frac{4\pi N\alpha}{3}}$$

$$n = \frac{7}{2\sqrt{10}} + \frac{\left(2\sqrt{10}/5\right)\pi N\alpha}{1 - \frac{4\pi N\alpha}{3}} \tag{4}$$

Where, N is the number of liquid crystal molecules and γ_e, γ_o is representing the extraordinary and ordinary internal field constant. The difference of γ_e-γ_o is to serve the differential molecular polarizability. The n_e and n_o is representing the extraordinary and ordinary refractive index.

Radius of the PPPCC molecule=10.69

Electronegativity (χ):

$$X = \frac{I+A}{2}$$

Hardness (η):

$$\eta = \frac{I-A}{2}$$

Chemical Softness (S):

$$S = \frac{1}{\eta}$$

Chemical Potential (μ):

$$\mu = -X$$

Electrophilicity Index (ω):

$$\omega = \frac{\mu 2}{2\eta}$$

3. RESULTS AND DISCUSSIONS

The optimized structure of PPPCC liquid crystal was obtained by using density functional theory (DFT) through NWChem software are shown in the Figure 1.

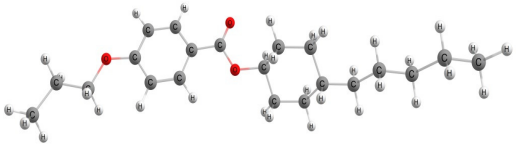

Figure 1. Optimised geometry of PPPCC liquid crystal molecule

3.1 Director angle

The director angle in important parameter of a liquid crystal molecule to understand the various optical parameters. It is the inclination of the long molecular axis over the reference direction of the molecule. The maximum value of director angle of the PPPCC liquid crystal was found to be 58.58^0 whereas the minimum value was found to be 27.47^0. Like other liquid crystal molecules, PPPCC liquid crystal shows magic angle value 54.73^0 as shown in the Figure 2.

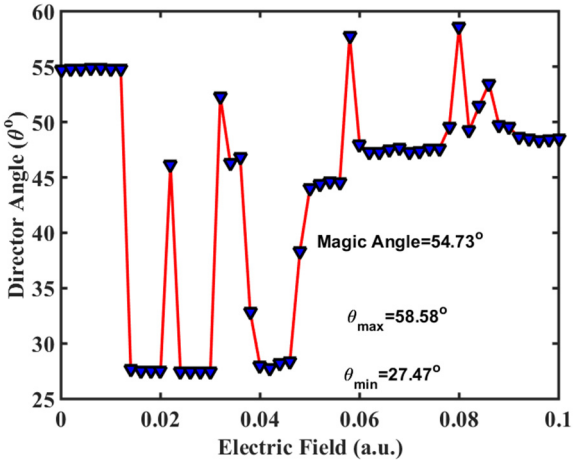

Figure 2. Director Angle of PPPCC liquid crystal molecule

3.2 Refractive index

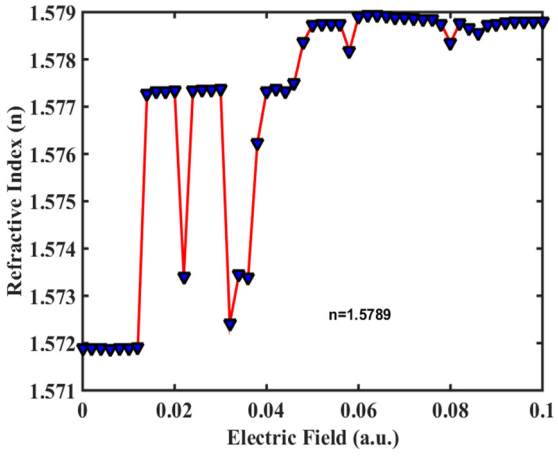

Figure 3. Refractive Index of PPPCC liquid crystal molecule

Liquid crystals are generally anisotropic in nature. This anisotropic nature of liquid crystals is an important feature used in light manipulation applications. Light manipulation is widely used in light moderator applications. This anisotropic nature of liquid crystals provides two refractive indices namely; extra-ordinary refractive index and ordinary refractive index. Refractive index is temperature-dependent property. As the temperature increases, extra-ordinary refractive index decreases whereas ordinary refractive index can either increase or decrease depending on the specific liquid crystal and its phase transitions. Other than temperature, electric field and impurities can also affect the molecular structure of the liquid crystal and hence change the optical parameters [17]. Refractive index of the PPPCC liquid crystal molecule was measured under the effect of external electric field. The average value of

the refractive index of PPPCC is found to be 1.5789. The variation in refractive index as a function of applied electric field is shown in the Figure 3. The nematic phase stability was observed at low THz frequency range in the refractive index characteristics. The refractive index remains constant at the higher frequency, which is suitable for the THz applications.

3.3 Birefringence

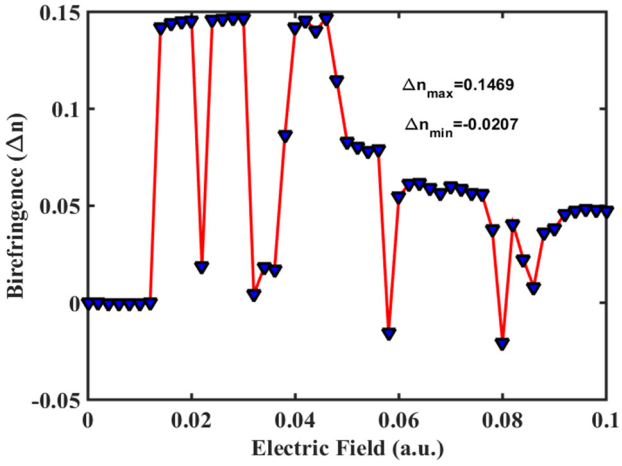

Figure 4. Birefringence of PPPCC liquid crystal molecule

Birefringence is the optical property of a material where the refractive index varies depending on the polarization and propagation direction of light. This anisotropy property of the material is important for display and optical applications. Polarisation Optical Microscope (POM) can be used to analyse the birefringence of the PPPCC liquid crystal molecule. This anisotropic property changes as a function of temperature or electric field. As temperature increases, birefringence decreases. In our study, we found the change in the birefringence of the PPPCC liquid crystal molecule as the external electric field varied as shown on the Figure.4. The maximum and minimum value of the birefringence of the PPPCC molecule were found to be 0.1469 and -0.0207 respectively. Negative value of birefringence is important for opt-electronic applications. This birefringence value makes it suitable for various optical applications. The birefringence of liquid crystals is temperature-dependent, generally exhibiting higher values near their nematic phase transition temperature (T*) [18]. As the temperature increases towards the clearing point, the order parameter decreases, leading to reduced birefringence. The birefringent properties of this compound make it suitable for use in liquid crystal displays (LCDs), tuneable lenses, and other optical devices where precise control over light propagation is necessary. High birefringence enhances contrast and brightness in displays, making it a desirable characteristic.

3.4 Order Parameter

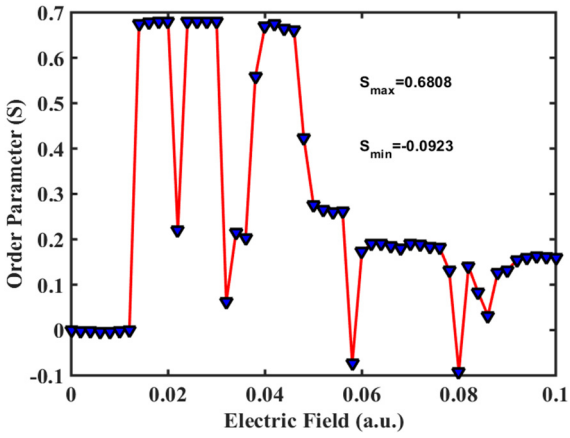

Figure 5. Order Parameter of PPPCC liquid crystal molecule

Order parameter is the angle between the molecular axis and the local director. For completely disordered isotropic liquid, order parameter is S=0 whereas for perfectly ordered liquid crystal, order parameter is S=1. Typical values for liquid crystals range from 0.3 to 0.8 [19]. The value of order parameter varies depending on the temperature or external electric field. In our study, we found the change in the birefringence of the PPPCC liquid crystal molecule as the external electric field varied as shown on the Figure 5.

The maximum and minimum values of the order parameter of PPPCC were found to be 0.6808 and -0.0923 respectively. The value of order parameter varies depending on the temperature and molecular interactions. Generally by increasing the temperature, liquid crystal loss its orientation order and hence order parameter decreases. As temperature increases p-propoxyphenyl trans-4-pentylcyclohexane carboxylate (PPPCC) undergoes phase transitions (e.g., from solid to nematic to isotropic liquid), the order parameter will exhibit distinct changes, providing insight into its molecular alignment and behavior under different conditions. Experimental techniques such as NMR and Raman Scattering can insight the molecular alignment and interactions with the liquid crystal phase.

3.5 IR Analysis

The IR analysis of PPPCC can provide valuable information about its molecular structure and functional group presents in the molecule. The presence of the aromatic ring will show C-H stretching vibrations, typically observed in the range 3000-3100 cm^{-1}. The pentyl chain contributes to C-H stretching vibrations in the region of 2850-2950 cm^{-1}. The carbonyl group from the carboxylic acid derivative will exhibit a strong absorption band in the region of 1700-1750 cm^{-1}. Aromatic C-C stretching vibrations will appear in the range of 1500-1600 cm^{-1}, indicating the presence of the phenyl group. The C-O stretching vibrations in the range of 1000-1300 cm^{-1} is due to the propoxy substitution in the ether

functional group. Also, the vibrations in the range of 675-900 cm^{-1} reveals the bending modes in the aromatic ring. In PPPCC liquid crystal molecule, Out of plane wagging of the hydrogen atom in Benzene found at 823 cm^{-1}, H-atom Rocking in the alkyl chain 972 cm^{-1}, C-O Stretching in either group at 1000 cm^{-1}, C-H wagging at 1246 cm^{-1}, C-H rocking at 1386 cm^{-1}, C-C stretching in benzene ring at 1524 cm^{-1} and C-H stretching in benzene ring at 3027 cm^{-1} as shown in the Figure 6. The obtained vibrational modes of PPPCC liquid crystal matches well with the literature. Various vibrational modes are given in the Table.1.

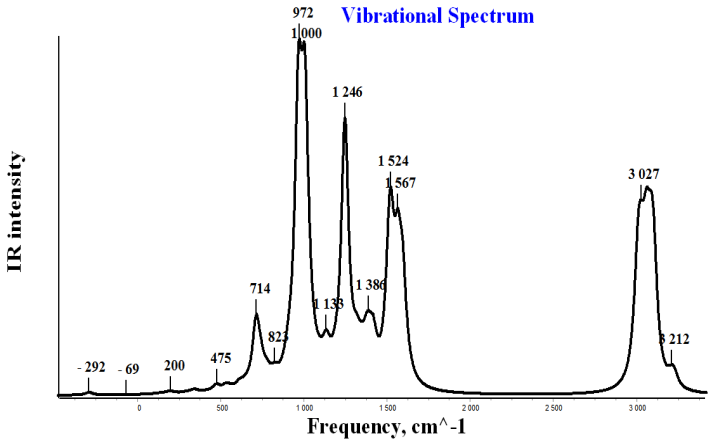

Figure 6. IR Spectrum of PPPCC liquid crystal molecule

Table 1. Vibrational Modes of PPPCC liquid Crystal

S. No.	Frequency (cm^{-1})	Modes of Vibration
1.	823	Out of plane wagging of the hydrogen atom in Benzene
2.	972	H-atom Rocking in the alkyl chain
3.	1000	C-O Stretching
4.	1246	C-H wagging
5.	1386	C-H Rocking
6.	1524	C-C stretching in benzene ring
7.	3027	C-H stretching in benzene ring

3.6 Raman Analysis

The structural and chemical properties of a molecule can be assessed through the vibrational modes present in it. Raman spectroscopy being a non-destructive technique is an important tool to identify the vibrational modes in the molecule. This technique is very useful for the studying the properties of sensitive compounds or those requiring further analysis [20]. For compound PPPCC, Raman spectroscopy can be particularly useful in identifying the functional groups, molecular conformation and interaction within the molecule. In our study, for PPPCC molecule, pentyl group of aromatic ring contributes to the C-H stretching and bending. C=O stretching is due to the carboxylate group. Cyclohexane contribute to the C=O stretching. 3023 cm^{-1} and 3232 cm^{-1} indicates asymmetric stretching of C-H. 1510 cm^{-1} indicates symmetric stretching in C-H. 1182 cm^{-1} indicates the C-C stretching in C-C as shown in the Figure 7. The higher frequency at 3023 cm^{-1} clearly indicates a change in the bonding or molecular interactions of the PPPCC.

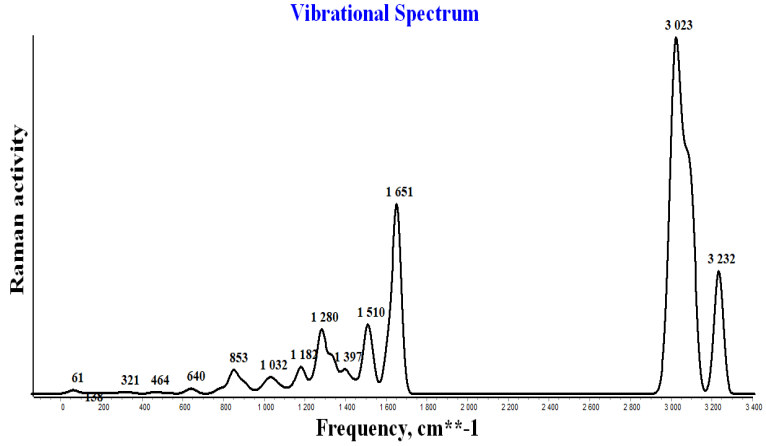

Figure 7. Raman Spectrum of PPPCC liquid crystal molecule

3.7 UV-Visible Analysis

UV-Visible spectroscopy is an efficient technique for determining the conjugated system and functional groups present in the sample. The presence of conjugated double bonds in the molecule will lead to π-π* transitions, which are responsible for light absorption in the UV-Vis range. Whereas the presence of functional groups will lead to n-π* transitions. The π-π* transitions occur at lower wavelengths (nearly 250 nm), whereas n-π* transitions occur at longer wavelengths (nearly 300-400 nm). The ultraviolet-visible (UV-Vis) absorption spectrum of p-propoxyphenyl trans-4-pentylcyclohexanecarboxylate depicts a strong peak at 252 nm, which clearly indicates the π-π* transitions due to the presence of conjugated double bonds in the molecule, as shown in Figure 8. This strong absorption in the UV at 252 nm yields an optical band gap of 4.9 eV.

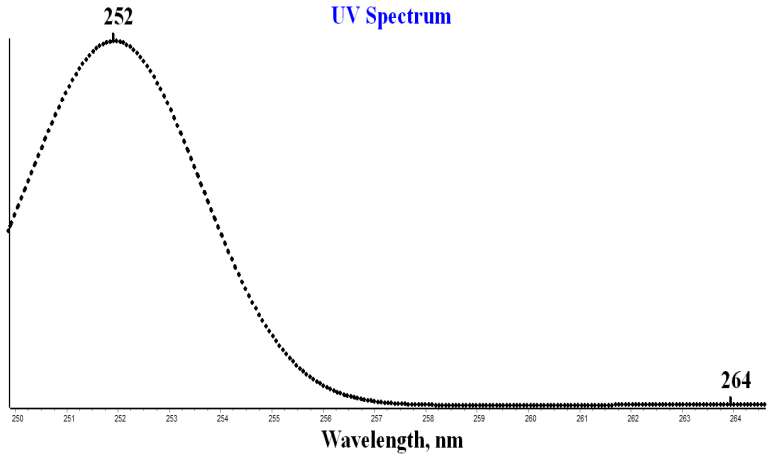

Figure 8. UV-Visible Spectrum of PPPCC liquid crystal molecule

3.8 Frontier Molecular Orbitals (FMO) and Density of States (DOS)

FMO's give insights into the electronic states of the molecule. HOMO-LUMO provides important information about the thermal properties of the molecule [21]. Frontier Molecular Orbitals (FMO) and Density of States (DOS) of the PPPCC molecule are shown in Figure 9. HOMO has a higher density of states (DOS), whereas the LUMO has a lower density of states (DOS). The band gap between HOMO and LUMO is found to be 5.1 eV. High value of the energy band gap leads to the insulating behaviour of the PPPCC molecule.

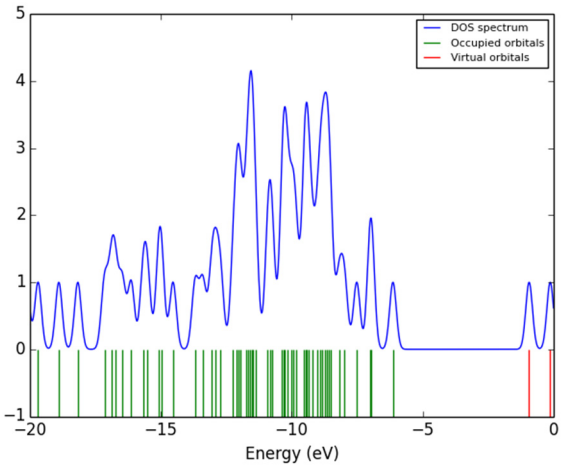

Figure 9. Frontier Molecular Orbitals (FMO's) and Density of States (DOS) of PPPCC liquid crystal molecule

3.9 Global Parameters

The Table 2 presents key electronic parameters that describe an atom or molecule's chemical behavior. The ionization potential (6.13 eV) is the energy needed to remove an electron, while electron affinity (0.93 eV) is the energy change upon gaining an electron. Electronegativity (3.53 eV) indicates the tendency to attract electrons in a bond. Hardness (2.60 eV) measures resistance to changes in electron distribution, with chemical softness (0.38 eV) being its inverse, reflecting how easily the electron cloud can be distorted. Chemical potential (-3.53 eV) shows the tendency of electrons to escape the system; its negative value suggests stability. Lastly, the electrophilicity index (2.39 eV) integrates electronegativity and hardness to quantify the ability to accept electrons. Together, these values provide a concise picture of the species' reactivity and stability in chemical processes.

Table 2. Global parameters of the PPPCC liquid crystal calculated by DFT methodology

Name of the parameter	Value in eV
Ionization Potential (I)	6.13
Electron Affinity (A)	0.93
Electronegativity Index (χ)	3.53
Hardness (η)	2.60
Chemical Softness (S)	0.38
Chemical Potential (μ)	-3.53
Electrophilicity Index (ω)	2.39

CONCLUSIONS

In summary, p-propoxyphenyl trans-4-pentylcyclohexane carboxylate exhibits significant orientational order characterized by its order parameter (S). This parameter varies with temperature and reflects the material's transition between different phases, providing essential insights into its liquid crystal properties and potential applications in display technologies and other optoelectronic devices. The molecular structure of p-propoxyphenyl trans-4-pentylcyclohexanecarboxylate plays a crucial role in determining its physical properties, including thermal stability, optical behaviour, and dielectric characteristics. These properties make it a valuable compound in the field of liquid crystals, particularly for applications in electronic displays where precise control over light manipulation and thermal behavior is required. Understanding these structural influences enables researchers and manufacturers to optimize formulations for enhanced performance in practical applications. In summary, p-propoxyphenyl trans-4-pentylcyclohexane carboxylate likely possesses high birefringence values that are temperature-sensitive, making it valuable for applications in advanced optical technologies. In our study, we found the change in the birefringence of p-Propoxyphenyl trans-4-pentylcyclohexanecarboxylate (PPPCC) liquid crystal under the effect of external electric field. At higher electric field PPPCC possess, negative birefringence, which is suitable for opt-electronic applications. π-π* transitions contribute to a significant peak at 252 nm in UV-Visible region. IR analysis confirms the presence of propoxy and pentyl present in PPPCC liquid crystal. 1000 cm^{-1} due to the C-O stretching caused by Ether in PPPCC liquid crystal. The C-C stretching around 1600 cm^{-1} is found due to phenyl group present in PPPCC. The refractive index remains unchanged for the large value of applied electric field which makes it suitable choice for opto-electronic devices in THz applications. FMO and DOS study depict a large value of energy band gap of 5.1 eV. Due to the high value of band gap this molecule could be a suitable choice for the insulating applications.

The molecular structure impacts the thermal stability and phase transition temperatures. The bulky groups (propoxy and pentyl) present in PPPCC can lower the melting point, facilitating a liquid crystalline state at room temperature. This is crucial for applications in displays that require a stable liquid crystal phase. Also, the arrangement of the propoxyphenyl and pentyl groups within the PPPCC contributes to the high value of birefringence of the material. Birefringence is vital for liquid crystals used in display technologies, as it affects how light is manipulated within the device. The dielectric anisotropy, influenced by the orientation of polar groups within the PPPCC molecule, is essential for liquid crystal applications. The propoxy group introduces polar characteristics that can enhance or reduce dielectric anisotropy depending on its orientation in the liquid crystal matrix. This property is significant for controlling switching speeds in display technologies. The presence of both hydrophobic (pentyl) and hydrophilic (propoxy) components improves solubility across various solvents, enhancing compatibility with other liquid crystal materials. This versatility is essential for formulating liquid crystal mixtures that require specific solubility characteristics. Dipole moment and electrochemical thermal analysis contribute to developing a new, unique optical-based liquid crystalline material. This study helps generate new optoelectronic devices and advanced liquid-crystalline materials.

ORCID

Tikaram, https://orcid.org/0000-0002-8913-0527; **Yogesh Kumar,** https://orcid.org/0009-0000-7856-1340
Narinder Kumar, https://orcid.org/0000-0001-8537-0307

REFERENCES

[1] G.W. Gray, *Molecular Structure and the Properties of Liquid Crystals*, (Academic Press, New York, London, 1962).
[2] S. Chandrasekhar, *Liquid Crystals*, 2nd ed., (Cambridge University Press, Cambridge, 1992); W.R. Krigbaum, Y. Chatani, P.G. Barber, "The crystal structure of p-azoxyanisole," Acta Cryst. **B26**, 97 (1970). https://doi.org/10.1107/s0567740870002005
[3] A. Shukla, R.P. Tiwari, and P.K. Singh, "DFT-Based Study of Physical, Chemical and Electronic Behavior of Liquid Crystals of Azoxybenzene Group: p-azoxyanisole, p-azoxyphenetole, ethyl-p-azoxybenzoate, ethyl-p-azoxycinnamate and n-octyl-p-azoxycinnamate," Online Journal of Chemistry, **1**(1), 18–28 (2021). https://doi.org/10.31586/ojc.2021.010103
[4] A.V. Zakharov, and L.V. Mirantsev, "Dynamic and dielectric properties of liquid crystals," Phys. Solid. State. **45**, 183–188 (2003). https://doi.org/10.1134/1.1537433/METRICS
[5] M. Govindarajan, M. Karabacak, S. Periandy, and S. Xavier, "Vibrational spectroscopic studies, NLO, HOMO-LUMO and electronic structure calculations of α, α, α trichlorotoluene using HF and DFT," Spectrochim Acta - Part A: Mol. Biomol. Spectrosc. **94**, 53–64 (2012). https://doi.org/10.1016/j.saa.2012.03.074
[6] D. Pegu, J. Deb, C. Van Alsenoy, and U. Sarkar, "Theoretical investigation of electronic, vibrational, and nonlinear optical properties of 4-fluoro-4-hydroxybenzophenone," Spectrosc. Lett. **50**, 232–243 (2017). https://doi.org/10.1080/00387010.2017.1308381

[7] L. Sinha, O. Prasad, V. Narayan, S.R. Shukla, Raman, "FT-IR spectroscopic analysis and first-order hyperpolarisability of 3-benzoyl-5-chlorouracil by first principles," Mol. Simul. **37**, 153–163 (2011). https://doi.org/10.1080/08927022.2010.533273.
[8] I. Haller, "Thermodynamic and static properties of liquid crystals," Prog. Solid State Chem. **10**, 103–118 (1975). https://doi.org/10.1016/0079-6786(75)90008-4
[9] P. Upadhyay, M.K. Rastogi, and D. Kumar, "Polarizability study of nematic liquid crystal 4-cyano-4′-pentylbiphenyl (5CB) and its nitrogen derivatives," Chem. Phys. **456**, 41–46 (2015). https://doi.org/10.1016/j.chemphys.2015.03.011
[10] D. de Sarkar, R. Deb, N. Chakraborty, G. Mohiuddin, R.K. Nath, and V.S.R. Nandiraju, "Cholesterol-based dimeric liquid crystals: Synthesis, mesomorphic behaviour of frustrated phases and DFT study," Liq. Cryst. **40**, 468–481 (2013). https://doi.org/10.1080/02678292.2012.757814
[11] D. Bhattacharjee, T.K. Devi, R. Dabrowski, A. Bhattacharjee, Birefringence, polarizability order parameters and DFT calculations in the nematic phase of two bentcore liquid crystals and their correlation, J Mol Liq 272 (2018) 239–252. https://doi.org/10.1016/j.molliq.2018.09.052.
[12] D. Bhattacharjee, T.K. Devi, R. Dabrowski, and A. Bhattacharjee, "Birefringence, polarizability order parameters and DFT calculations in the nematic phase of two bentcore liquid crystals and their correlation," J. Mol. Liq. **272**, 239–252 (2018). https://doi.org/10.1016/J.MOLLIQ.2018.09.052
[13] V.G.K.M. Pisipati, and S.B. Rananavare, "Interdigitated smectic a and b mesophases in higher homologues of the 50.m series," Liq. Cryst. **13**, 757–764 (1993). https://doi.org/10.1080/02678299308027291
[14] M. Govindarajan, S. Periandy, and K. Carthigayen, "FT-IR and FT-Raman spectra, thermo dynamical behavior, HOMO and LUMO, UV, NLO properties, computed frequency estimation analysis and electronic structure calculations on α-bromotoluene," Spectrochim. Acta - Part A: Mol. Biomol. Spectrosc. **97**, 411–422 (2012). https://doi.org/10.1016/j.saa.2012.06.028
[15] D. Bhattacharjee, R. Dabrowski, and A. Bhattacharjee, "Theoretical investigation of nonlinear optical and vibrational properties of two liquid crystalline compounds," J. Mol. Liq. **255**, 80–92 (2018). https://doi.org/10.1016/J.MOLLIQ.2018.01.157
[16] H. Wang, M.Y. Jin, R.C. Jarnagin, T.J. Bunning, W. Adams, B. Cull, Y. Shi, *et al*., "Thermally stable nonlinear optical activity in a smectic-A liquid crystal," Nature, **384**, 244–247 (1996). https://doi.org/10.1038/384244a0
[17] D. Gupta, and A. Bhattacharjee, "Detailed investigation of N-(4-n-pentyl-oxybenzylidene)- 4′-n-hexylaniline liquid crystal molecule," J. Mol. Struct. **1196**, 66–77 (2019). https://doi.org/10.1016/j.molstruc.2019.06.068
[18] E. Apra, E.J. Bylaska, W.A. de Jong, N. Govind, *et. al*. "NWChem: Past, present, and future", The Journal of Chemical Physics, **152**, 184102 (2020). http://dx.doi.org/10.1063/5.0004997
[19] Y. Kumar, and N. Kumar, "Electro-optical Effect of 4-n-alkyl-sulfanyl-4' isothiocyanate-biphenyl Liquid Crystal Homologous Series Under Terahertz Frequency: A Theoretical Approach," Makara Journal of Science, **27**(4), Article 1, (2023). https://doi.org/10.7454/mss.v27i4.1497
[20] N. Kumar, P. Singh, K.B. Thapa, and D. Kumar, "Molecular spectroscopy and adverse optical properties of N-(p-hexyloxy-benzylidene)–ptoluidine(HBT) liquid crystal molecule studied by DFT methodology, IOPSciNotes, **1**, 015202 (2020). https://doi.org/10.1088/2633-1357/ab7f83
[21] T. Orlova, A. Piven, D. Darmoroz, T. Aliev, T.M.T.A. Razik, A. Boitsev, *et al*., "Machine learning for soft and liquid molecular materials," Digital Discovery, **2**, 298-315 (2023). https://doi.org/10.1039/D2DD00132B

ДОСЛІДЖЕННЯ ФІЗИЧНИХ, ОПТОЕЛЕКТРОННИХ ТА ІЗОЛЯЦІЙНИХ ВЛАСТИВОСТЕЙ РІДКОКРИСТАЛІЧНОЇ МОЛЕКУЛИ PPPCC МЕТОДОМ ТЕОРІЇ ФУНКЦІОНАЛА ГУСТИНИ (DFT): ТЕОРЕТИЧНИЙ ПІДХІД

Тікарам, Йогеш Кумар, Наріндер Кумар
Кафедра фізики, школа прикладних та біологічних наук (SALS), Університет Уттаранчал, Дехрадун, Індія-248007

У цій статті ми досліджували фізичні, електрооптичні та теплові властивості рідкокристалічної молекули PPPCC. Теорія функціоналу густини (DFT) з функціоналом B3LYP та базисним набором 6-31G(d,p) використовується для оптимізації та аналізу рідкокристалічної молекули p-пропоксифеніл транс-4-пентилциклогексанкарбоксилату (PPPCC). Для рідкокристалічної молекули PPPCC обчислюються та аналізуються різні фізичні властивості, такі як енергетичні рівні HOMO-LUMO, електрооптичні властивості та глобальні параметри. Ми повідомили про двопроменезаломлення рідкокристалічного p-пропоксифеніл транс-4-пентилциклогексанкарбоксилату (PPPCC) під впливом зовнішнього електричного поля. УФ-видимий аналіз залишає сильний пік при 252 нм через π-π* переходи. Ширина забороненої зони HOMO-LUMO становила 5,1 еВ. Максимальне розтягнення спостерігалося при 1000 см-1 через розтягнення C-O, спричинене ефіром у рідкокристалі PPPCC. Розтягнення C-C близько 1600 см-1 виявлено завдяки фенільній групі, присутній у PPPCC. Температурно-чутливе значення двопроменезаломлення PPPCC робить його придатним вибором для сучасних застосувань в оптичних технологіях. Показник заломлення залишається незмінним у великих прикладених електричних полях, що робить його придатним вибором для оптоелектронних пристроїв у терагерцовому діапазоні. Завдяки великій ширині забороненої зони ця молекула може бути придатним вибором для ізоляційних застосувань.

Ключові слова: *PPPCC; Електричне поле (ТГц); HOMO-LUMO; УФ-видимий діапазон; ІЧ; DFT*

East European Journal of Physics. 1. 274–280 (2026)
DOI: 10.26565/2312-4334-2026-1-31 ISSN 2312-4334

MODELING OF THERMAL EFFECTS IN A POLYIMIDE TARGET UNDER PULSED LASER IRRADIATION

J.O. Sadullayev[1], **M.M. Akhmedov**[1*], **M.E. Vapayev**[1], **I.Y. Davletov**[1], **G.S. Boltaev**[2]
[1]*Department of Electrical Engineering and Power Engineering, Urgench State University named after Abu Raykhan Beruni, Urgench, 220100, Uzbekistan*
[2]*Department of Physics, American University of Sharjah, Sharjah 26666, United Arab Emirates*
[*]*Corresponding Author e-mail: munisbek95@urdu.uz*
Received September 8, 2025; revised December 16, 2025, accepted December 20, 2025

Polyimide is widely valued in modern technology due to its excellent thermal stability and mechanical strength. Understanding how it responds to pulsed laser irradiation is crucial for precise laser-based microfabrication and for interpreting the conditions that can lead to laser induced graphene (LIG) formation. In this study, we use COMSOL Multiphysics to simulate the temperature evolution and heat transfer in a polyimide sample exposed to pulsed laser radiation. The model takes into account temperature dependent thermal properties, laser absorption following the Beer-Lambert law, and the Gaussian energy profile of the laser beam. Our results show how laser fluence and pulse overlap influence heat accumulation within the polymer. While the actual graphene formation process is not modeled here, the thermal analysis provides valuable insight into the photothermal conditions relevant to LIG-related processes.

Keywords: *COMSOL Multiphysics; Thermal properties; Laser radiation; Polyimide*

PACS: 42.70.Hj, 42.62.Fi

1. INTRODUCTION

Polyimide materials have become an integral part of modern materials engineering owing to their outstanding thermal resistance and mechanical stability. These properties make them particularly suitable for applications in aerospace structures, electronic components, and automotive systems, where materials are often exposed to elevated temperatures and harsh operating environments [1, 2]. Despite their robustness, the precise processing of polyimides remains a challenging task, as excessive thermal loading can lead to unwanted material degradation. For this reason, processing techniques that offer both accuracy and controlled energy delivery are of considerable interest. Among such techniques, pulsed laser processing has proven to be an effective tool for polymer modification and micro-scale material treatment. By delivering energy in short, intense pulses, lasers enable localized heating while minimizing damage to surrounding regions [3, 4]. Laser sources such as CO_2 and Nd:YAG lasers are widely employed in materials processing because they provide flexibility in controlling pulse duration, energy density, and interaction time with the target material [2, 5–8]. From a physical perspective, understanding how laser energy is converted into heat and how this heat propagates within a polyimide substrate is essential for achieving reproducible and predictable processing results. However, the quantitative relationship between laser parameters and the resulting thermal distribution is still not fully understood and requires further theoretical and numerical investigation.

At the same time, significant research efforts in laser–matter interaction have been driven by the growing interest in graphene and graphene-related materials. Owing to their exceptional thermal and electrical properties, these materials are being explored for use in energy storage systems, thermoelectric devices, and photothermal applications [9–13]. In particular, laser-induced graphene has attracted attention as a rapid and scalable approach for modifying carbon-rich polymers [10]. Previous studies indicate that laser power, fluence, and irradiation conditions play a decisive role in defining the thermal environment in which structural transformations may occur [11, 12]. Furthermore, investigations of laser-induced plasma formation, surface nanostructuring, and heat accumulation effects have highlighted the importance of accurately describing temperature evolution during pulsed laser irradiation [13–18]. Although the present work does not address the formation or characterization of graphene itself, it focuses on a detailed numerical analysis of thermal processes in a polyimide target exposed to pulsed laser radiation. By modeling heat generation and transport under controlled laser conditions, this study aims to provide a clearer understanding of the thermal response of polyimides, which is a necessary step for interpreting and optimizing laser-based processing techniques, including those related to laser-induced graphene.

2. METHODOLOGY

This work involves modeling the thermal changes that occur when a polyimide material is exposed to laser radiation using COMSOL Multiphysics.

Cite as: J.O. Sadullayev, M.M. Akhmedov, M.E. Vapayev, I.Y. Davletov, G.S.Boltaev, East Eur. J. Phys. 1, 274 (2026), https://doi.org/10.26565/2312-4334-2026-1-31

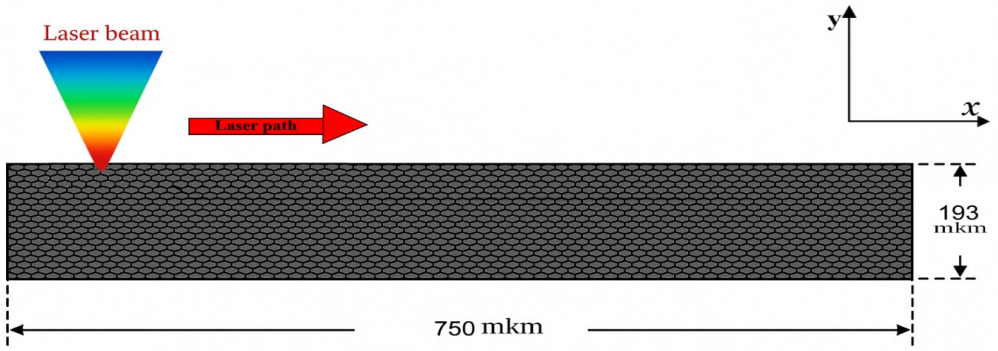

Figure 1. Schematic representation of the 2D-moving laser source simulation.

The parameters of pulsed laser radiation are given in Table 1. The spatial distribution of the incident laser beam on the polyimide surface was modeled, and temperature distribution and heat-related processes were studied. The theoretical model developed is schematically represented in Figure 1. The thermal parameters and geometric dimensions of the polyimide material chosen to model the increase in temperature and the dissipation of heat at the point of impact of the laser beam are given in Table 2.

To better reflect the physical nature of the laser polyimide interaction, the numerical model accounts for the temperature dependence of key thermal properties, including thermal conductivity, heat capacity, and density. Heat transport within the polyimide was described by solving the transient heat conduction equation, while laser irradiation was introduced as a surface heat source with a Gaussian intensity distribution. In addition, reflection losses at the air polyimide interface were considered, and laser energy absorption within the material was evaluated using the Beer–Lambert law. The simulations were carried out under transient conditions in order to capture the time-dependent evolution of temperature during pulsed laser exposure.

Table 1. Laser machining parameters

Nomenclature	Value (units)	Property
f	$10[kHz]$	Number of laser pulses
E_p	$170[\mu J]$	Pulse energy
P_w	250[fs]	Pulse width
D	$150[\mu m]$	Beam diametr
ϵ	0.7	Emissivity
A	0.8	Absorptivity
x_r	$1000[\mu m]$	Reference point to represents the center of the laser beam
x_d	$100[\mu m]$	Standard deviation of the Gaussian laser beam
v	$700mm/s$	Laser scan speed

3. RESULTS AND ANALYSIS

The geometry of the polyimide for modeling was entered into the COMSOL program. The thickness of the polyimide is 168 μm and the density is 1400 kg/m^3. The values of the thermal parameters of the polyimide are given in Table 2. The heat dissipation of the polyimide under the influence of laser radiation was calculated using the Fourier heat transfer equation:

$$\rho C_p \frac{\partial T}{\partial t} = \nabla \cdot (k \nabla T) + q$$

where: ρ is the density of the material, C_p is the heat capacity, k is the thermal conductivity, T is the temperature, and q is the heat source (laser energy). The density, heat capacity, and thermal conductivity vary with temperature.

Table 2. Material properties of polymide parameters

Nomenclature	Value (units)	Property
T_m	723 [K]	Melting temperature
T_v	1173 [K]	Vaporization temperature
L_m	250 [J/g]	Latent heat of melting
L_v	5000 [J/g]	Latent heat of evaporation
β	$5 * 10^-5[1/K]$	Thermal expansion coefficient
γ	$-3 * 10^-4[N/(m * K)]$	Temperature derivative of the surface tension
h_1	$17[W/(m^2 * K)]$	Heat transfer coefficeient
δT	30 [K]	Half-width of the curve
T_a	293.15 [K]	Ambient temperature
T_i	293.15 [K]	Initial temperature
H	$193[\mu m]$	Height of the simple
W	$750[\mu m]$	Simple Width

Table 3. Material properties and heat transfer model equations for polyimide

Name	Equation	No.
Temperature-dependent specific heat at constant pressure (C_p)	$C_p = 1000\left[0.96 + 1.39\left(\frac{T-300}{400}\right) - 0.43\left(\frac{T-300}{400}\right)^2\right]$	1
Governing equation	$\rho C_p \frac{\partial T}{\partial t} = k\left[\left(\frac{\partial^2 T}{\partial x^2}\right) + \left(\frac{\partial^2 T}{\partial y^2}\right)\right]$	2
Beer–Lambert law	$C\frac{\partial T}{\partial t} = \nabla\cdot(k\nabla T) + \alpha(1-R)I_0 e^{-\alpha z}\sum_{n=0}^{4} e^{-2((x-n\delta x)^2+y^2)/w^2}$	3
	$\sum_{n=0}^{4} f(t - nt_{\text{shift}})$	4
Average laser power density in Gaussian distribution	$P_g = A\left[\frac{E_p}{P_w\left(\frac{\pi D^2}{2}\right)}\right]\exp\left[-\left(\frac{(x-x_f)^2}{2\sigma^2}\right)\right]$	5
Analytic function	$\beta = \text{rect}\left(\text{mod}\left(\frac{t}{t_r}\right)\right)$	6
Thermal conductivity (k)	$k = \begin{cases} 0.213 + 3.416\times10^{-5}T, & 200\text{K} < T < 729\text{K} \\ -1.314 + 2.130\times10^{-3}T, & 729\text{K} < T < 1500\text{K} \end{cases}$	7
Reflectivity (R)	$R = \begin{cases} 0.74, & T < 858\text{K} \\ 0.36, & T > 858\text{K} \end{cases}$	8

The relationship between density and temperature is often expressed in terms of the thermal expansion coefficient.

$$\rho(T) = \rho_0 \cdot (1 - \beta(T - T_0))$$

where $\rho(T)$ is the density at temperature T, ρ_0 is the initial density at $T_0 = 293.15\,\text{K}$, and β is the thermal expansion coefficient ($5 \times 10^{-5}\,\text{K}^{-1}$).

Figure 2 shows a graph of the relationship between the density and temperature of polyimide. In this case, the density of polyimide decreases linearly as the temperature increases.

The relationship between the thermal conductivity and temperature of polyimide [8] is given in Equation 6 of Table 3. Polyimide changes in small values from its initial temperature to its melting temperature and increases sharply from the melting temperature to its evaporation temperature (Figure 3). From this we can see that the thermal conductivity is high between the melting and evaporation temperatures of polyimide. This temperature dependent behavior of thermal conductivity provides insight into the thermal regimes that may be relevant for laser induced modification of polyimide based materials

To determine the relationship between the temperature and heat capacity of polyimide, an empirical expression developed by theoretical methods, Equation 1 in Table 3, was used [8]. Using the thermal coefficients of polyimide given in Table 2, a graph of the relationship between heat capacity and temperature was created (Figure 4). In this case, the heat capacity of polyimide increases sharply and begins to decrease when it reaches the evaporation temperature.

By analyzing the temperature dependence of density, thermal conductivity, and heat capacity of polyimide, the present study aims to characterize thermal conditions that are relevant for understanding laser–polymer interaction processes. We define the spatial coherence of laser pulses as the dimensionless number of laser pulses per illuminated [19–22]. The temperature distribution is calculated by the 2D heat transfer equation and the laser pulse acts as a surface heat source, as shown in equation (3) of Table 3. The light reflection coefficient between air and polyimide is calculated and the

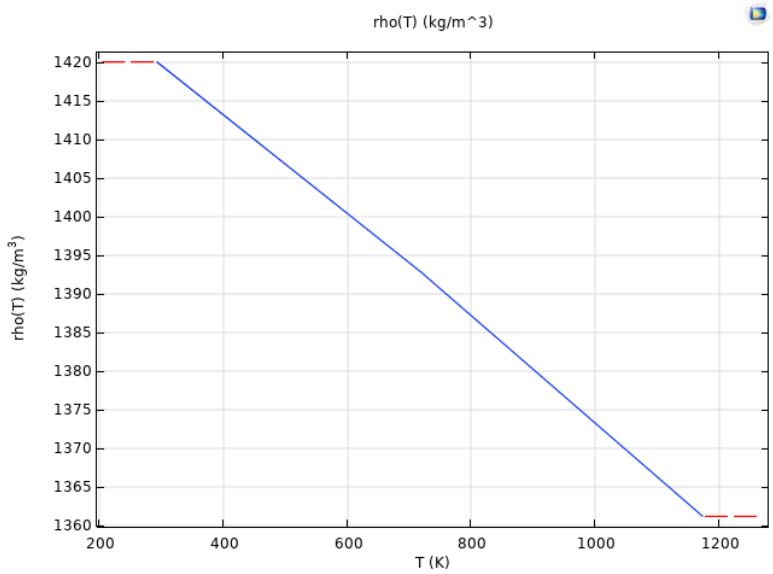

Figure 2. Relationship between density and temperature of polyimide

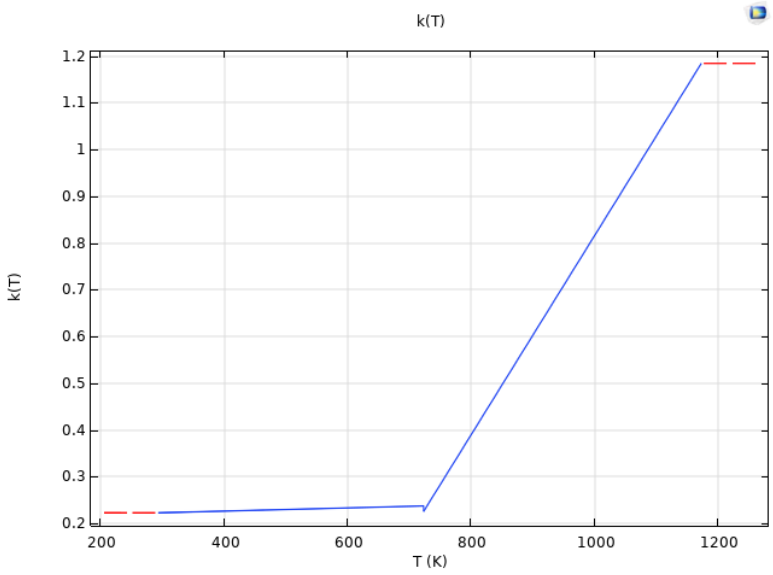

Figure 3. Relationship between temperature and thermal conductivity of polyimide

absorption is based on the Beer-Lambert law. The 2D temperature distribution of the polyimide in the plane is shown in Figures 5(a)–(c). The scanning speed of the laser beam is 40 mm/s and the pulse overlap is 18%, resulting in energy fluxes of (a) 0.7 J/cm^2, (b) 0.9 J/cm^2, and (c) 1 J/cm^2.It should be emphasized that the present analysis is limited to numerical modeling of thermal properties and temperature fields in polyimide under pulsed laser irradiation. While the obtained thermal profiles provide useful insight into temperature regimes relevant to laser–matter interaction in polyimide [23–26], the formation of graphene itself is not directly modeled or experimentally verified in this work [27–30].

4. CONCLUSIONS

In summary, this work presents a numerical study of the thermal behavior of a polyimide target exposed to pulsed laser radiation using COMSOL Multiphysics. The simulations show that the evolution of temperature within the material is mainly controlled by the laser energy flux and the temporal characteristics of the pulses, which together determine the extent of heat accumulation during irradiation. Surface temperature distributions were evaluated for typical processing parameters, including a laser scanning speed of 40 mm/s, a pulse overlap of 18%, and energy flux levels ranging from 0.7 to 1.0 J/cm^2.

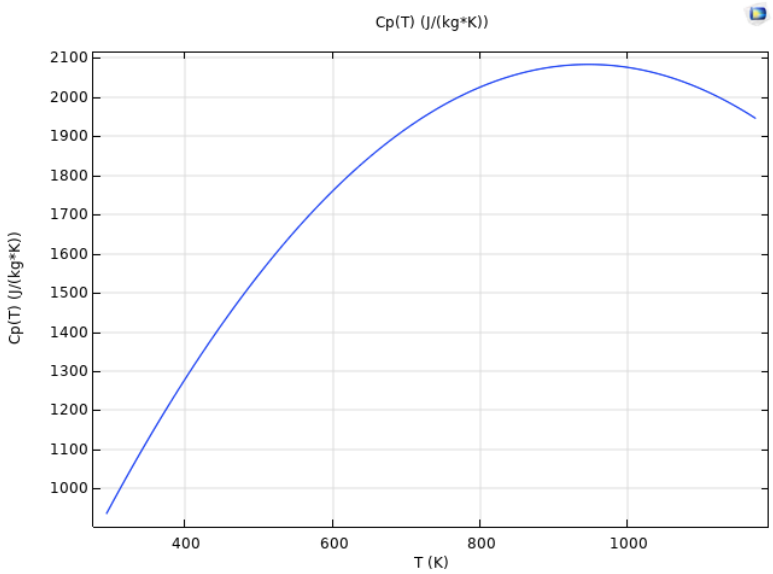

Figure 4. Relationship between heat capacity and temperature of polyimide

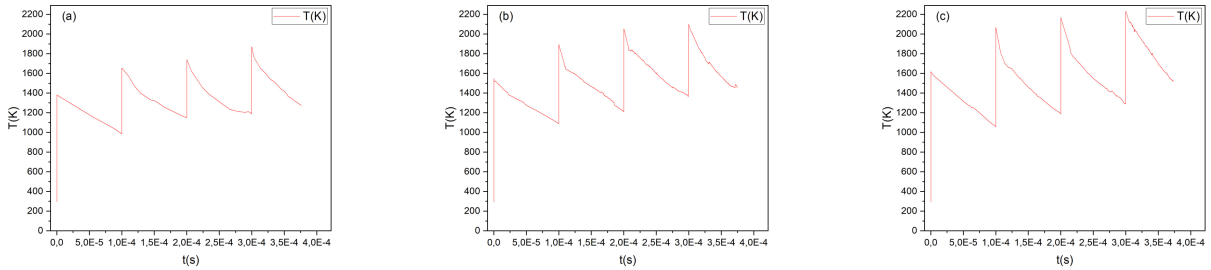

Figure 5. Presents the spatial temperature distribution with an 18.7% overlap between consecutive laser spots for laser fluences of (a) 0.7 J/cm^2, (b) 0.9 J/cm^2, and (c) 1 J/cm^2.

The results indicate that relatively small adjustments in laser parameters can produce noticeable changes in surface temperature, underscoring the need for careful control of processing conditions in applications where high precision is required. While the present study is restricted to numerical modeling and does not include experimental validation, the obtained thermal analysis offers useful guidance for selecting appropriate laser operating regimes and for interpreting heat-related phenomena in polyimide-based materials.

Acknowledgments

We acknowledge the F-FA-2021-510 Grant from the Ministry of Innovative Development of Uzbekistan.

ORCID

J.O. Sadullayev, https://orcid.org/0000-0002-5577-2644; **M.M. Akhmedov**, https://orcid.org/0000-0003-1208-1736;
M.E. Vapayev, https://orcid.org/0009-0007-5194-131X; **I.Y. Davletov**, https://orcid.org/0009-0006-5971-7649;
G.S. Boltaev, https://orcid.org/0000-0003-0354-1251

REFERENCES

[1] X. Ye, *et al*. "A review on the laser-induced synthesis of graphene and its applications in sensors," Journal of Materials Science, **59**(26), 11644-11668 (2024). https://doi.org/10.1007/s10853-024-09883-z

[2] K. Xu, *et al*. "Toward integrated multifunctional laser-induced graphene-based skin-like flexible sensor systems," ACS nano, **18**(39), 26435-26476 (2024). https://doi.org/10.1021/acsnano.4c09062

[3] J. Pola, "Thermal reactive modifications of polymer surfaces by infrared laser radiation," Journal of Analytical and Applied Pyrolysis, **169**, 105819 (2023). https://doi.org/10.1016/j.jaap.2022.105819

[4] D. Shen, X. Zhang, and L. Zhu, "Laser processing for electricity generators: Physics, methods and applications," Nano Energy, **120**, 109182 (2024). https://doi.org/10.1016/j.nanoen.2023.109182

[5] A.K. Singh, *et al*. "Parametric investigation on laser interaction with polyimide for graphene synthesis towards flexible devices," Journal of Physics D: Applied Physics, **56**(1), 015305 (2022). https://doi.org/10.1088/1361-6463/ac9ce7

[6] H.D. Vora, *et al*. "One-dimensional multipulse laser machining of structural alumina: evolution of surface topography," The International Journal of Advanced Manufacturing Technology, **68**(1), 69-83 (2013). https://doi.org/10.1007/s00170-012-4709-8

[7] M.G. Stanford, *et al*. "High-resolution laser-induced graphene. Flexible electronics beyond the visible limit," ACS applied materials.interfaces, **12**(9), 10902-10907 (2020). https://doi.org/10.1021/acsami.0c01377

[8] X. Ruan, *et al*. "Experimental and modeling study of CO_2 laser writing induced polyimide carbonization process," Materials. Design, **160**, 1168-1177 (2018). https://doi.org/10.1016/j.matdes.2018.10.050

[9] Z. Ali, and A. D'Amore, "Fabrication of Synergistically Induced Carbon Fiber/Graphene Reinforced Polydimethylsiloxane Composites with High Thermal Conductivity," Macromolecular Symposia, **413**(4), (2024). https://doi.org/10.13140/RG.2.2.16808.28166

[10] H. Awasthi, *et al*. "Rapidly synthesized laser-induced graphene and its derivatives for miniaturized energy devices: Principles, applications, and challenges," Applied Physics Reviews, **12**(2), (2025). https://doi.org/10.1063/5.0242637

[11] C. Kincal, and N. Solak. "Controlling thermoelectric properties of laser-induced graphene on polyimide," Nanomaterials, **14**(10), 879 (2024). https://doi.org/10.3390/nano14100879

[12] P.C. Wang, *et al*. "Flexible Pressure Sensors Based on Laser-Induced Graphene," in: *Electrochemical Society Meeting Abstracts MA2024-02 2623*, No. 39. (The Electrochemical Society, Inc., 2024). https://doi.org/10.1149/MA2024-02392623mtgabs

[13] H. Wu, *et al*. "Femtosecond Laser Opening Hierarchical Lamination: Micro-Nano Hybrid Scissoring of Three-Dimensional Nitrogen-Doped Graphene for Solar Steam Generation," Nano Letters, **25**(11), 4143-4153 (2025). https://doi.org/10.1021/acs.nanolett.4c04053

[14] A.I. Japakov, *et al*. "The impact of laser radiation frequency on the formation of the main characteristics of ions in a mono-element laser plasma," EPJ Web of Conferences, **318**, 05002 (2025). https://doi.org/10.1051/epjconf/202531805002

[15] M. Akhmedov, *et al*. "Picosecond-pulsed laser ablation of aluminum foils: crater morphology and plasma parameters," Engineering Research Express, **7**(3), 035362 (2025). https://doi.org/10.1088/2631-8695/ae0092

[16] M.E. Vapaev, *et al*. "Laser fluence-dependent LIPSS formed on the surface of niobium alloys." EPJ Web of Conferences, **318**, 05005 (2025). https://doi.org/10.1051/epjconf/202531805005

[17] A.I. Japakov, *et al*. "Spectra of Multiply Charged Ions in Laser Plasma Formed from Gas-Containing Targets," East European Journal of Physics, (3), 490-494 (2023). https://doi.org/10.26565/2312-4334-2023-3-55

[18] G.S. Boltaev, *et al*. "Impact of plasma conditions on the shape of femtosecond laser-induced surface structures of Ti and Ni," Applied Physics A, **128**(6), 488 (2022). https://doi.org/10.1007/s00339-022-05614-w

[19] R. Geremia, D. Karnakis, and D.P. Hand, "The role of laser pulse overlap in ultrafast thin film structuring applications," Applied Physics A, **124**(9), 641 (2018). https://doi.org/10.1007/s00339-018-2045-z

[20] M.R. Bedilov, Kh.B. Beisembaeva, and I.Yu. Davletov, "Effect of γ-radiation-induced defects in glass on laser destruction," Physics of the Solid State, **44**(6), 1093-1097 (2002). https://doi.org/10.1134/1.1485013

[21] M.R. Bedilov, *et al*. "Multiply charged ion spectra of a laser plasmaproduced on both sides of the target," Quantum Electronics, **31**(5), 453 (2001). https://doi.org/10.1070/QE2001v031n05ABEH001977

[22] M.R. Bedilov, R.T. Khaidarov, and I.Yu. Davletov, "Spectra of ions in a four-element laser plasma," Quantum Electronics, **25**(6), 567 (1995). https://doi.org/10.1070/QE1995v025n06ABEH000415

[23] L. Ionel, and C. Viespe, "Numerical Investigation of Enhanced High-Intensity Laser–Matter Interactions in Nanowire-Coated Conical Targets," Nanomaterials, **15**(23), 1763 (2025). https://doi.org/10.3390/nano15231763

[24] G.M. Petrov, *et al*. "Modeling of short-pulse laser-metal interactions in the warm dense matter regime using the two-temperature model," Physical Review E, **103**(3), 033204 (2021). https://doi.org/10.1103/PhysRevE.103.033204

[25] V. Daghigh, H. Daghigh, and R. Harrison, "High-Temperature Polyimide Composites—A Review on Polyimide Types, Manufacturing, and Mechanical and Thermal Behavior," Journal of Composites Science, **9**(10), 526 (2025). https://doi.org/10.3390/jcs9100526

[26] Y. Homma, "Graphene Imaging Using Scanning Electron Microscopy: Mechanism of Secondary Electron Contrast Formation," Crystals, **15**(12), 1025 (2025). https://doi.org/10.3390/cryst15121025

[27] E.A. Danilov, *et al*. "Multicomponent graphene oxide dispersions for thin reduced graphene oxide film formation," Journal of Materials Science, 1-19 (2025). https://doi.org/10.1007/s10853-025-10730-y

[28] B. Kirubasankar, *et al*. "Influence of different electrolytes on the formation of electrochemically exfoliated graphene and their supercapacitor performance," Ionics, **31**(11), 12155-12165 (2025). https://doi.org/10.1007/s11581-025-06687-2

[29] H.J. Choi, *et al*. "Molecular dynamics investigation of biomass-derived laser-induced graphene formation," JMST Advances, **7**(3), 187-193 (2025). https://doi.org/10.1007/s42791-025-00114-3

[30] A. Abbaspourmani, *et al*. "Patterning and nanoribbon formation in graphene by hot punching," Nanotechnology, **36**(11), 115301 (2025). https://doi.org/10.1088/1361-6528/ad9d4c

МОДЕЛЮВАННЯ ТЕПЛОВИХ ЕФЕКТІВ У ПОЛІІМІДНІЙ МІШЕНІ ПІД ВПЛИВОМ ІМПУЛЬСНОГО ЛАЗЕРНОГО ВИПРОМІНЮВАННЯ

Дж.О. Садуллаєв[1], **М.М. Ахмедов**[1], **М.Є. Вапаєв**[1], **І.Й. Давлєтов**[1], **Г.С. Болтаєв**[2]

[1]*Кафедра електротехніки та енергетики, Ургенчський державний університет імені Абу Райхана Беруні, Ургенч, 220100, Узбекистан*

[2]*Кафедра фізики, Американський університет Шарджі, Шарджа 26666, Об'єднані Арабські Емірати*

Поліімід широко цінується в сучасних технологіях завдяки своїй чудовій термостабільності та механічній міцності. Розуміння того, як він реагує на імпульсне лазерне опромінення, має вирішальне значення для точного лазерного мікровиробництва та для інтерпретації умов, які можуть призвести до утворення лазерно-індукованого графену (LIG). У цьому дослідженні ми використовуємо COMSOL Multiphysics для моделювання зміни температури та теплопередачі у зразку поліііміду, що піддається впливу імпульсного лазерного випромінювання. Модель враховує температурно-залежні теплові властивості, поглинання лазера згідно із законом Бера-Ламберта та гауссів енергетичний профіль лазерного променя. Наші результати показують, як лазерний флюенс та перекриття імпульсів впливають на накопичення тепла в полімері. Хоча сам процес утворення графену тут не моделюється, термічний аналіз надає цінну інформацію про фототермічні умови, що стосуються процесів, пов'язаних з LIG.

Ключові слова: *COMSOL Multiphysics; теплові властивості; лазерне випромінювання; поліімід*